UNIVERSITY OF TECHNOLOGY SYDNEY

DOCTORAL THESIS

Optical Transport of Pseudo-Random Coatings

Author:
Marc A. GALÍ LABARIAS

Supervisors:
Assoc. Prof. Matthew D. ARNOLD
Prof. Geoffrey B. SMITH

A thesis submitted in fulfilment of the requirements for the degree of Doctor of Philosophy

in the

Physics Discipline
School of Mathematical and Physical Sciences

February 6, 2019

Declaration of Authorship

I, Marc A. GALÍ LABARIAS, declare that this thesis titled, "Optical Transport of Pseudo-Random Coatings" and the work presented in it are my own. I confirm that:

- This work was done wholly or mainly while in candidature for a research degree at this University.
- Where any part of this thesis has previously been submitted for a degree or any other qualification at this University or any other institution, this has been clearly stated.
- Where I have consulted the published work of others, this is always clearly attributed.
- Where I have quoted from the work of others, the source is always given. With the exception of such quotations, this thesis is entirely my own work.
- I have acknowledged all main sources of help.
- Where the thesis is based on work done by myself jointly with others, I have made clear exactly what was done by others and what I have contributed myself.
- This research is supported by an Australian Government Research Training Program.

Signed: Production Note: Signature removed prior to publication.

Date: 6th February 2019

"All truths are easy to understand once they are discovered; the point is to discover them. "

Galileo Galilei

UNIVERSITY OF TECHNOLOGY SYDNEY

Abstract

Science
School of Mathematical and Physical Sciences

Doctor of Philosophy

Optical Transport of Pseudo-Random Coatings

by Marc A. GALÍ LABARIAS

Coatings are widely used to improve the optical performance of surfaces exposed in the built environment, technological devices, and consumer goods. In the last decades the improvement of techniques to create structured coatings has hugely increased the range of properties that can be achieved by such systems. Unfortunately, the theoretical techniques to model the complex and often pseudo-random nature of structured coatings are not yet fully adequate. In this thesis I will address this problem. Specifically, I will develop improved techniques that can be used on different kinds of coatings: mesoporous metals, random two-phase structures, heterogeneous matrices and rough surfaces.

First, I will consider silver mesoporous sponges. These are both random and isotropic, and are readily synthesized in the laboratory in various physical densities. Therefore they provide a useful platform on which to begin developing computational strategies. I will analyse these structures using an *effective medium approximation* based on their far-field response. Mesoporous metals offer a very distinct optical response compared to their constitutive bulk metal. In particular, the topology of such structures creates metal systems with low plasmon response but with high conductivity thanks to their percolated metal *filaments*. These characteristics make them suitable for many applications, for example as highly absorptive optical coatings.

Next, I will introduce the concept of anisotropy into the coating structure by analysing columnar morphologies obtained using physical vapour deposition. These kind of coatings offer some degree of order caused by shadowing effects, and a degree of randomness due to the statistical roughening present when depositing such structures. The most important structural dependence is the plane perpendicular to the growth direction, hence in this work I will analyse them as two-dimensional structures. I will obtain the effective permittivity and optimal bounds (which I will call *leaf bounds*) by expanding the averaged polarization field in a power series on the susceptibility. To

do this we developed a method that relies on a Monte Carlo algorithm to efficiently obtain higher orders of this series expansion. Therefore, this new methodology permits the study of higher order micro-structural parameters. In this thesis I will analyse up to fourth order effects. For anisotropic coatings, the depolarization of the Gaussian random fields studied is related to the depolarization factors of an ellipsoid with the same anisotropy. This fact will make it relatively easy to design simple anisotropic structures that are optically equivalent to experimentally measured ones. Coatings of this type are useful for angular, spectral or polarization selectivity.

Thirdly, having explored single-material structures that are either random isotropic (sponges) or pseudo-random anisotropic (columnar), I turn to the problem of heterogeneous systems. The prototypical example is a paint-like coating in which some phases are randomly distributed inside a light-absorbing matrix. I will present a *generalized four-flux method* which is capable of analysing the optical response of realistic heterogeneous matrices. My new methodology is capable of dealing with factors including different size distribution of components, heterogeneous mix of materials, and weak absorption by the matrix (binder). A matrix formalism is developed to extend this method to multi-layer systems. The methodology is applied to the optimization of paints for achieving solar efficiency and I find that multi-layer paints with larger particles in the outer layer offer better performance in the IR.

Finally, I use a variation of the *C-method* to examine the effect of surface roughness on optical properties. Surface roughness is present in any kind of coating, including any of those described above, and, depending on its scale size, the optical response can vary significantly as a function of angle and wavelength. I analyse the angular effects caused by changing the correlation length of a surface profile with a fixed groove depth, i.e. increasing the noise of the surface and the effective slope of the profile to determine the angular dispersion. The effect of roughness on the optical properties is exemplified by showing how it can control the perceived colour of a gold surface. I show that some tuning of optical properties is possible by this means. My findings include that a significant reduction on reflectance with short correlation length, and that angular colour dependence of rough gold profiles shows a blue-white colour for s-polarization and a yellow-reddish colour for p-polarization.

Acknowledgements

This thesis encompasses my three and a half years of research at the Institute for Nanoscale Technology in the University of Technology Sydney. I am very grateful to Prof. Geoff Smith, Prof. Matthew Arnold and Prof. Michael Cortie for giving me the opportunity to come to Sydney and to learn from their experience. The chance of doing my PhD in Australia has allowed me to live many new experiences and to grow not only as a researcher but as a person. I have greatly benefited from Angus Gentle for all his help providing experimental data, for valuable discussions particularly in the paints project and many proofreads; also for his sense of humour and to keep reminding me that "I should model something real". I would like to thank Michael Cortie and Geoff Smith for many things, but especially for their helpful advice; and for their many corrections and suggestions on different works. Michael Cortie's code for generating mesoporous sponge structures has been particularly very useful, also his valuable discussions on metal sponges and on the properties of rough gold.

My research would have been impossible without the aid of Matthew Arnold, thanks for the many discussions and explanations; and especially, for the patience in the many proofreads of my thesis, and the help and encouragement in the, quickly gone, last months of my candidature. Especially for trouble shooting the codes; and for helping to develop the column methodology; and providing advice on the rough surfaces study.

I am grateful to Chris Poulton and Christian Wolff for valuable discussions of the C-method.

I am very grateful to the scholarships that I received from the Australian Research Council (DP140102003) and the UTS Graduate Research School for awarding me with the International Research Scholarship, which allowed me to pursue this research. I would also like to express my gratitude for the scholarships that allowed me to attend international conferences: the HDR student conference fund from the Faculty of Science, and the Vice-Chancellor's postgraduate conference travel fund. I am also grateful to UTS:Insearch for the PD grant that facilitated my attendance to the SPIE conference in San Diego, USA.

In my candidature I have been able to attend at the AMSI summer school on 2016 and 2017 thanks to the financial support of the student project funding of the Faculty of Science, and to the AMSI travel grant.

I would like to thank my fellow doctoral students for all the support, the jokes and the shared laughs even in the most stressful times. For introducing me to the craft beer and sharing all together too much cheese. To the *Device & Development* (D&D) group for the great nights of imagination where we lived many "pseudo-random" experiences, I think that I am rolling quite high on *wisdom* now.

Finally, last but by no means least, I want to thank my family and friends back in Catalonia for their constant support, and their understanding that to fulfil my dreams I could not be around all these years. You have taught me to never give up in order to finish what I decided to start. My sincere thanks to Alba for her patience with my stressed moods and her constant encouragement.

Moltes gràcies.

Author's Contributions

Publications

- M. A. Gali and M. D. Arnold (Nov. 2018). "Recurrent approach to effective material properties with application to anisotropic binarized random fields". In: *(submitted to Physical Review B)*. arXiv: 1811.06163. URL: http://arxiv.org/abs/1811.06163

- Marc A. Gali et al. (2017). "Extending the applicability of the four-flux radiative transfer method". In: *Applied Optics* 56.31, pp. 8699–8709. ISSN: 21553165. DOI: 10.1364/AO.56.008699

- M.A. Gali et al. (2017). "Super-cool paints: Optimizing composition with a modified four-flux model". In: *Proceedings of SPIE - The International Society for Optical Engineering* 10369. ISSN: 1996756X. DOI: 10.1117/12.2273548

- Marc A. Galí et al. (2015). "Plasmonic response in nanoporous metal: dependence on network topology". In: *Proc. SPIE 9668, Micro+Nano Materials, Devices, and Systems, 96683S*. DOI: 10.1117/12.2202278;

Oral Presentations

- M. A. Galí , M. C. Tai, M. D. Arnold, M. B. Cortie, A. R. Gentle, G. B. Smith,
  Plasmonic response in nanoporous metal: dependence on network topology,
  Micro+ Nano Materials, Devices, and Systems,
  SPIE 2015 (2015, Sydney, Australia).

- (Invited Speaker) M. A. Galí , M. D. Arnold,
  Optical properties of nanomaterials: Curvature approach,
  Metamaterials, nanophotonics and plasmonics,
  Photon 16 (2016, Leeds, UK).

- M. A. Galí , M. D. Arnold, A. R. Gentle, G. B. Smith,
  Super-cool paints: optimizing composition with a modified four-flux model,
  Thermal Radiation Management for Energy Applications,
  SPIE 2017 (2017, San Diego, US).

Contents

List of Figures

List of Abbreviations

EMF	**E**lectro**M**agnetic **F**ield
EMA	**E**ffective **M**edium **A**pproximations
UV	**U**ltra**V**iolet
VIS	**VIS**ible
IR	**I**nfra**R**ed
NIR	**N**ear-**I**nfra**R**ed
MSP	**M**icro-**S**tructural **P**arameters
GRF	**G**aussian **R**andom **F**ield
LCGRF	**L**evel-**C**ut **G**aussian **R**andom **F**ield
BRDF	**B**idirectional **R**eflectance **D**istribution **F**unction

List of Symbols

$\vec{E}$	electric field	$\mathrm{V\,m^{-1}}$
$\vec{D}$	electric displacement field	$\mathrm{C\,m^{-2}}$
$\vec{B}$	magnetic inductance field	T
$\vec{H}$	magnetic field	$\mathrm{A\,m^{-1}}$
$\vec{P}$	polarization field	$\mathrm{C\,m^{-2}}$
$\vec{F}$	electric cavity field	$\mathrm{V\,m^{-1}}$
$\hat{\epsilon}$	permittivity tensor	$\mathrm{F\,m^{-1}}$
$\hat{\mu}$	permeability tensor	$\mathrm{H\,m^{-1}}$
$\hat{\alpha}$	polarizability tensor	$\mathrm{C\,m^{2}\,V^{-1}}$
χ	susceptibility	
$m = n + ik$	complex refractive index	
ω	angular frequency	$\mathrm{rad\,s^{-1}}$
c	speed of light	$\mathrm{m\,s^{-1}}$
λ	wavelength	m
Q_{ext}	extinction efficiency	
Q_{sca}	scattering efficiency	
Q_{abs}	absorption efficiency	
Q_{pha}	phase efficiency	
C_{ext}	extinction cross-section	$\mathrm{m^2}$
C_{sca}	scattering cross-section	$\mathrm{m^2}$
C_{abs}	absorption cross-section	$\mathrm{m^2}$
C_{pha}	phase cross-section	$\mathrm{m^2}$
$\hat{g}$	metric tensor	
η	number density	$\mathrm{m^{-3}}$
σ	standard deviation	

Chapter 3:

k	wavenumber	$\mathrm{m^{-1}}$
x	scale parameter	
a	effective radius	m

Chapter 4:

p_n	n-point probability function	
$K(\vec{r})$	kernel function	
β_{ji}	polarizability	$\mathrm{C\,m^2\,V^{-1}}$
ϕ	fill-factor	
d	system dimension	
k	wavenumber	$\mathrm{m^{-1}}$
$\mathcal{I}_i(\vec{r})$	indicator or occupancy function	
$\mathbb{G}$	Dyadic Green Tensor	
$\tilde{\mathbb{G}}$	Reduced Dyadic Green Tensor	
$\hat{a}_n$	system geometry tensor (permittivity series expansion)	
$\hat{\alpha}_n$	system geometry tensor (inverse permittivity series expansion)	
$\hat{A}_n$	Torquato's system geometry tensor (polarizability series expansion)	
$\mathbb{A}_n$	Monte Carlo system geometry tensor (polarizability series expansion)	
$\lfloor\cdot\rfloor_n$	$\mathrm{n^{th}}$ order lower bounds	
$\lceil\cdot\rceil_n$	$\mathrm{n^{th}}$ order upper bounds	
Υ_i	micro-structural parameters	

Chapter 5:

$n = n_1 + in_2$	complex refractive index	
k	absorption coefficient per unit length	$\mathrm{m^{-1}}$
s	scattering coefficient per unit length	$\mathrm{m^{-1}}$
ϵ	forward average path length	
β	backscattering ratio	
ζ	forward-scattering ratio	
K	total absorption coefficient per unit length	$\mathrm{m^{-1}}$
S	total scattering coefficient per unit length	$\mathrm{m^{-1}}$
$\tilde{\beta}$	average backscattering ratio	
$\tilde{\zeta}$	average forward-scattering ratio	
r	reflection coefficients	
R	total reflectance	
T	total transmittance	
ϕ	multi-layer transfer matrix	

μ_0	mean radius	m

Chapter 6:

$\vec{F}$	field parallel to the surface	$\mathrm{V\,m^{-1}}$ ($\mathrm{A\,m^{-1}}$)
$\vec{G}$	field parallel to the incidence plane	$\mathrm{A\,m^{-1}}$ ($\mathrm{V\,m^{-1}}$)
k	wavenumber	$\mathrm{m^{-1}}$
$\vec{S}$	Poynting vector	$\mathrm{W\,m^{-2}}$
ε	efficiency	
α_n	horizontal component of the wavenumber	$\mathrm{m^{-1}}$
β_n	vertical component of the wavenumber	$\mathrm{m^{-1}}$
K	grating number	
d	super-period	m
l_c	correlation length	m

To my family

Chapter 1

Introduction

1.1 Introduction

The interaction of light with materials has intrigued humans for centuries, for example Egyptians and Mesopotamians developed quartz lenses and the Greek philosophers developed the first theories on geometrical optics (Lloyd, 1970; Lloyd, 1973). This marked the beginning of optics and motivated continuing research in understanding the behaviour of light, so that it can be better controlled.

In this project, we are mainly interested in understanding and controlling optical transport for applications improving the energy efficiency of several devices, like building roofs and windows (for example by M. Gali et al. (2017), Marc A. Gali et al. (2017), A. R. Gentle and G. B. Smith (2007), and Mbise et al. (1989)). In this line of research, good results in controlling the *spectral* response have been obtained using simple flat coatings: for instance, A. R. Gentle and G. B. Smith (2008) and A. R. Gentle, Yambem, et al. (2015) designed optimized stacks that performed well with a wide angular response due to the resonant cavity. However, when the angular response is considered, it has been demonstrated that this sometimes only works for a small angular range Chou et al. (2014), Lee et al. (2012), and Shen et al. (2014), and also the developed materials do not work for all polarizations.

Pioneering work by Tamm (1924) offered hints of a general strategy to completely harness the flow of light through the theory of *transformation optics*, however his theoretical achievements were not pursued experimentally for many years due to technology limitations. One of the limitations in earlier work is the limited range of optical properties of available materials, which can be overcome by constructing composite structures out of individual materials. However, the breakthrough of metamaterials, which allow us full control over the local refractive indices, revived interest in the topic (Nicorovici, McPhedran, and G. W. Milton (1994), Leonhardt (2006), Graeme W. Milton, Briane, and John R. Willis (2006), and Schurig et al. (2006)). As an example, Pendry et al. (2012) found mathematically what profile of local refractive indices is required to control the flow of light to allow cloaking, and examples of structures that can achieve

this. These are difficult to produce over large (building scale) areas, but techniques to obtain coatings present a new plethora of structures that can facilitate our control over optical transport, however these complex systems are not easy to understand. Example of these structured materials are complex thin film stacks Shen et al. (2014) and G. B. Smith (2002) or nano-structured coatings Jahan and G. Smith (1998), Mbise et al. (1989), and G. B. Smith, Ben-David, and Swift (2001); these systems are designed to create an effective graded refractive index to achieve better performance. One of the main methods to create such graded coatings is the vapour deposition technique, which produces structures such as: metal island films, metal-in-insulator composites, obliquely deposited anisotropic thin films, sponge from alloy dissolution, and stacks of such films. The problem is that the obtained structures are at least quasi-random, a property that makes their response more difficult to design.

In general, given enough computational resources, it is possible to simulate any kind of structure, however, the structure has to be known completely (which is generally not possible); moreover, non-periodic structures require very significant computational resources. In order to have a reasonable understanding of these complex structures, and progress towards using this knowledge in design, several theories/approximations have been developed, all of which have compromises:

(1) Differential/integral methods to solve the complete Maxwell equations. Several models have been developed in order to solve using differential or integral equations Maxwell equations. Usually these methods are very accurate but they are very restricted by the geometry of the system (J. Chandezon, Maystre, and Raoult, 1980; Maystre, 1978), and become computationally expensive for complex systems.

(2) Ray tracing. This framework relies on geometrical optics where it is assumed that the structure scale is much bigger than the incident wavelength. This is typically not valid for the structures of interest in this thesis.

(3) *Effective medium theories/approximations (EMT or EMA)*. The classical models are *Maxwell-Garnett*, *Bruggeman* and *Drude-Lorentz* approximations. These define simple homogenized media to represent the actual complex structure, but generally these models fail to capture important aspects of the optical response, and so there is a need to develop some new models that can address these short-comings.

(4) Energy balance equations. These models rely only on the energy transfer, thus instead of solving the full electromagnetic problem the scenario is simplified considering only energy conservation. Examples of this kind of framework can be found in flux-theories based in Kubelka (1948) and Chandrasekhar (1960) equations, which include scattering. These simple models have so far been limited

in application, so there is a need to develop implementations that broaden their applicability to more realistic systems.

1.2 Aims and Overview

The main aim of this thesis is to develop models that can explain and optimize complex structured optical coatings [1]. The main difficulty to study these coatings arises from their almost fully random structure. Thus we use the term *pseudo-random* to indicate that our generated structures are not fully random, since they are obtained using uniform randomly generated numbers (quasi-random numbers) and then filtered using certain kernel functions.

In particular, our research group is interested in coatings that increase energy efficiency, from solar cell coatings through to highly reflective coatings to decrease thermal absorptance. As mentioned before one of the main techniques to create green energy coatings is vapour deposition; this method can create structures with a large variety of morphologies: mesoporous metals (Galí et al., 2015; Galinski et al., 2011; Supansomboon et al., 2014; M. C. Tai, A. Gentle, Arnold, et al., 2016), column-like structures with certain angle of growth (Arnold, 2005; M. C. Tai, Arnold, et al., 2017), or more exotic configurations (M C Tai et al., 2018).

In this project our broad aim is to develop and test models that describe the optical transport of different kinds of heterogeneous matrices or systems created via vapour deposition techniques, such as foam-like structures or columns systems. Here we outline three specific investigations of this thesis:

[1] We use the word coating to indicate that every structure studied here can be used as an optical coating. In other words, these systems can be put as a layer spread over the surface of certain material in order to alter its optical properties

Randomly structured two-phase anisotropic systems: Here the aim is to develop a model that is capable of predicting the effective permittivity of pseudo-random anisotropic systems which modify the polarization of light. Thus in chapter 4 we will extend the method introduced by Brown (1955) and later extended by Sen and S. Torquato (1989), which will allow us to study the optical properties of these kind of coatings in detail. In particular we will focus on column-like structures, which are characterised by their degree of randomness and anisotropy.

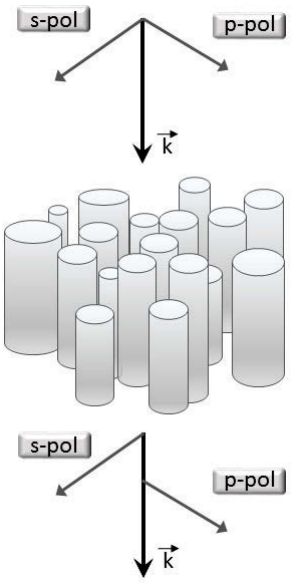

FIGURE 1.1: Diagram showing the polarization delay produced by the effective response of a column-like structure.

Heterogeneous matrices: We aim to develop a model that can predict the scattering and absorption of multi-layered stacks of heterogeneous materials, or in particular white paint coatings. Paints are the most used coatings since they are easy to make, cheap and easy to apply too. Hence, in chapter 5 we will present an extended version of the *four-flux method* that allows us to model multi-layered stacks made of different compositions, where each stack can contain several materials where the particles of the composite can have different size probability distributions and where the binder (matrix) is allowed to be absorbing. Therefore this method enables us to study and optimize realistic paints.

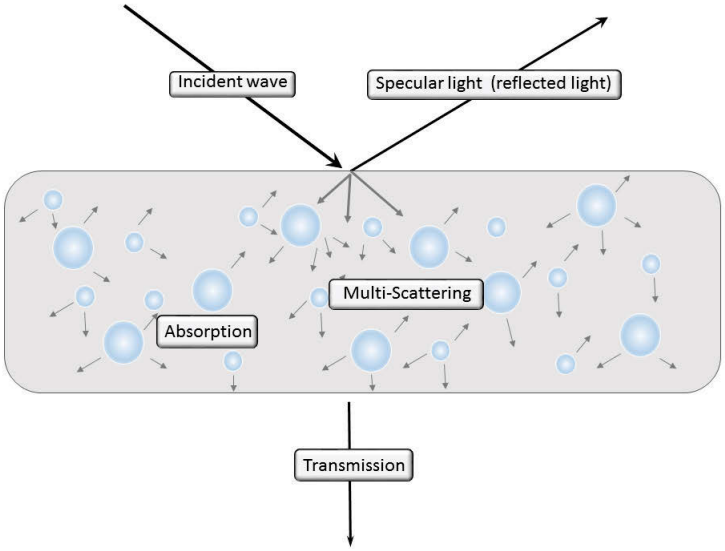

FIGURE 1.2: Diagram of light interaction events on a paint system with flat interfaces.

Random rough surfaces: Finally, in chapter 6 we will analyse the effect of surface roughness and the influence of its randomness on spectral (and angular) scattering and absorption of metals. Roughness is an important variable to take into account when modelling optical transport, since it has a great influence on the behaviour of polarized light and on the optical transport at high incident angles on any kind of surface. Even small amounts of roughness can have a significant effect on the scattering of metal surfaces (A. A. Maradudin, 2007), but we are particularly interested in the effect on the spectral properties of light scattered from dispersive materials and the associated near-glancing exitance.

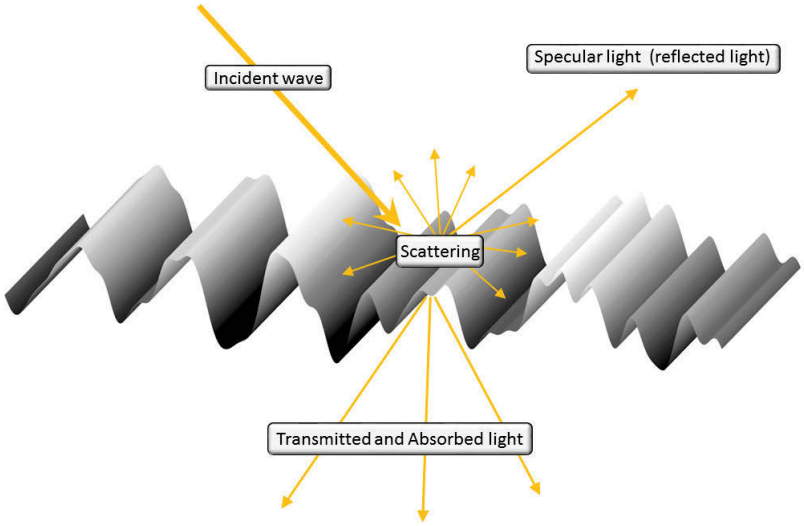

FIGURE 1.3: Diagram of the light interactions on a cylindrical (1D grating) rough surface.

Chapter 2

Background Theory

In this chapter I will introduce the basic concepts that are involved in my thesis. To study the optical transport of coatings we need to understand the following fundamental concepts on electromagnetism and statistics [1]:

- Maxwell's equations.
- Constitutive relations and intrinsic anisotropic optical quantities.
- Polarization.
- Scattering.
- Effective medium approximations.
- Monte Carlo modelling.

2.1 Maxwell's Equations

Predicting the transport of light in complex systems requires a consistent theory of electromagnetic radiation. In the 19$^{\text{th}}$ century J. C. Maxwell united many observations to form a theoretical framework to describe the electromagnetic field propagation. But it was later on when those relations where re-expressed in the vectorial form that we now use,

$$\nabla \cdot \vec{D} = \rho_f, \tag{2.1a}$$

$$\nabla \cdot \vec{B} = 0, \tag{2.1b}$$

$$\nabla \times \vec{E} = -\frac{\partial \vec{B}}{\partial t}, \tag{2.1c}$$

$$\nabla \times \vec{H} = \vec{J}_f + \frac{\partial \vec{D}}{\partial t}, \tag{2.1d}$$

[1] In this introductory chapter we will not go into much detail, but when more detail is required it will be contained in the appropriate chapter.

where $\vec{D} = \hat{\epsilon}\vec{E}$ is the *electric displacement* vector, $\vec{H} = \hat{\mu}^{-1}\vec{B}$ is the *magnetizing field*, ρ_f are the free charges, and $\vec{J}_f = \hat{\sigma}\vec{E}$ is the *current density of free charges* where $\hat{\sigma}$ is the conductivity.

Maxwell's equations describes the interaction and propagation of light with matter: this framework is called *classical regime* in which light behaves like a wave. In this thesis we work in the *classical regime*, hence we will use Maxwell's equations to develop our models, but we will ignore source charges and currents, leaving only induced currents implicit in the complex electric displacement ($\vec{D}$), i.e. $\rho_f = 0$ and $\vec{J}_f = 0$.

In general further derivation is required to make useful predictions, e.g. to find model solutions such as plane waves and how they interact at flat surfaces. For heterogeneous media, there are many numerical approaches and the selection of these is situation-dependent. We will consider some of these in specific chapters, but in the remainder of this chapter we will examine some of the general phenomena that can be observed.

2.2 Scattering

When light interacts with a structured medium it can react in different ways depending on the scale between the structure scale and the wavelength of the incoming light: if the wavelength is much shorter than the characteristics of the structure the light can be thought of as a ray which will go through a series of reflections and transmissions in the structure, this regime is called *geometric optics* and techniques such as *ray tracing* can be applied. On the other extreme, where the wavelength is much larger than the structure characteristics, is the *homogenization regime* where *effective medium approximations* can be used, which we will discuss in the next section. Finally, in the "in-between" regime, where the wavelength of the incoming light is of the same order as the characteristic size of the structure there are many complicated interactions and a full wave model is required.

Therefore to understand the behaviour of the EMF when it interacts with a medium we have to analyse Maxwell's equations (eq. 2.1). Suppose that we have an isotropic flat surface, solving the equations with appropriate boundary conditions at the interface we can find the reflected and transmitted light and their angle of propagation. The reflected and transmitted light is coherent light since the difference in phase between the initial EM wave and the later two would be constant. Now let's imagine the same scenario but for a rough surface. Thus when the light interacts with the medium diffraction will occur, and refracted and reflected light will return to the initial medium and transmitted light will propagate in the material. As before, part of the transmitted and the reflected light will be coherent with respect to the initial light, on

the other hand the rest of the diffracted light will possess some degree of incoherence caused by the random superposition of diffracted waves. The concept of coherence is very important since it tells us the degree of information kept after a certain event. Thus if we look at our reflection on a polished surface we see a "sharp" image (the information is well preserved), but if the surface is irregular the reflection looks "blurry" (information is not well preserved).

Multi-scattering effects is a recurring topic in this thesis since many systems studied here produce multi-scattering. Multi-scattering occurs when multiple scattering events happen iteratively. If these are randomly distributed the result is incoherent scattering. In chapter 4 to model randomly-structured two-phase media we rely on effective medium approximation, nevertheless the interaction series can be thought of as multi-scattering events. In chapter 5 we solve a set of energy balance equations relying on the fact that on average multi-scattering effects are equivalent to diffuse radiation. Thus in later chapters, depending on the system studied, different solutions will be outlined as needed.

As we mentioned before scattering effects are tightly connected to the scale relation between the light wavelength and the material structure size. In our daily life we are constantly seeing scattering effects. For example change in the sky colour is due to different scattering interactions: the blue color of the day sky is due to *Rayleigh scattering*[2] caused when the Sun light scatters with the atmosphere molecules. In equation 2.8a we can see that in the small size regime scattering has a strong dependence on the wavelength ($\sim \lambda^{-4}$), thus blue light scatters a lot more than red light, since it has shorter wavelength. By the same argument at sunrise or sunset more blue light is scattered while propagating in the atmosphere, but in these cases because of the asymmetry of the relative position of the observer and the Sun a great part of the scattered light is deviated from the direct path Sun-observer, thus we see the sky reddish since it is the light that has deviated less. On the other hand, in the sky we see the opposite effect too. The blue light from the sky becomes white again after propagating through a cloud, in these cases the light gets scattered by the larger and denser water molecules in the clouds producing multi-scattering. As a result the light that emanates from a cloud is fully incoherent (due to multi-scattering) and therefore depolarized.

We have just explained the scattering events that happens in the sky, which determine the colour that we see. Hence we can assume that the atmosphere behaves as a some kind of filter for the Sun light. This brings us to our next topic the *polarization* of light. Sun light is depolarized (white) but the atmosphere partially polarizes the Sun light, due to single scattering. These are just some examples that we are used to seeing

[2] *Rayleigh scattering* is a scattering approximation applicable to small structure sizes compared to the wavelength, i.e. $x << \lambda$ where x is the size parameter and λ the incident wavelength.

every day but many other materials polarize light to some extent, either because of their composition (refractive index) or by their structure (scattering).

2.3 Polarization and Power Transport

Maxwell equations (eq. 2.1) show that electromagnetic waves are transverse waves, in other words the electric and magnetic field oscillate in a perpendicular plane to the propagation direction, thus by construction the propagation vector ($\vec{k}$), the electric field ($\vec{E}$) and the magnetic field ($\vec{B}$) define an orthogonal triad in free space (see figure 2.1).

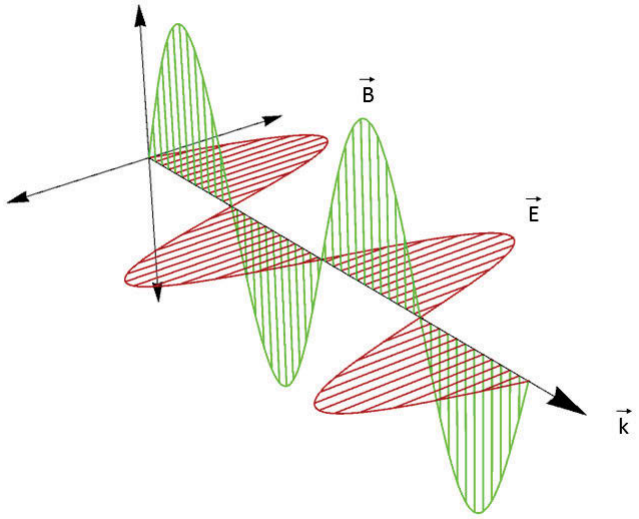

FIGURE 2.1: Picture showing the propagation of a plane wave. It can be seen the spatial relationship between the electric field, magnetic field and propagation vector.

Transverse waves have a property called polarization: the polarization determines how the oscillating field of the transversal wave behaves. Hence, as EM waves are transverse waves they exhibit polarization. By convention we refer to the behaviour of the electric field to determine the polarization.

For the specific case of incident plane waves with linear polarization, two polarizations can be defined depending on the oscillation direction of the electric field respect to the interface. Thus we will call *s-polarization* or *transversal electric polarization* (TE) when the electric field oscillates in the perpendicular direction of the plane of propagation; and we will call *p-polarized* light or *transversal magnetic field* when the magnetic field oscillates perpendicularly to the plane of propagation. Figure 2.2 represents graphically these two polarizations.

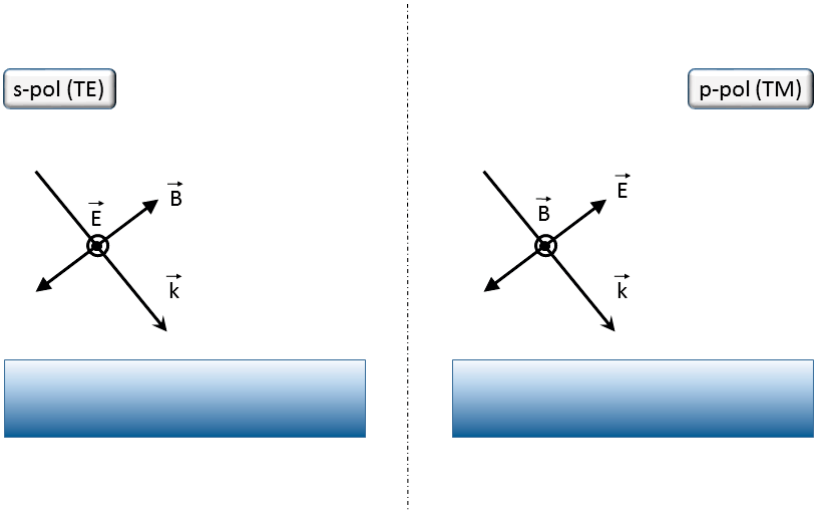

FIGURE 2.2: This picture shows the orientation of the electromagnetic field for s-polarized light (left) and p-polarized light (right).

At a planar interface a superposition of *p-pol* and *s-pol* waves is sufficient to predict the optical response, but more generally we need the *Stokes vector* to fully determine the resultant scattering profile. In this thesis we will mostly consider *p-pol* and *s-pol* to be sufficient, because for most structures we impose some symmetry to simplify investigation. In chapter 6 we will study the dependence between polarization and surface structure.

Several authors have studied the polarization of the EMF (see e.g. Chandrasekhar (1960) and Stokes (1851)), one of the ways to describe the polarization of an electromagnetic wave is using *Stokes vector* or *Stokes parameters* which rely on the fact that an arbitrary monochromatic wave can be expressed as a superposition of two orthogonal components. The notation to describe the Stokes parameters is very diverse, in this work we follow the notation favoured by Bohren and Huffman (2007),

$$I =< E_{\parallel}E_{\parallel}^{*} > + < E_{\perp}E_{\perp}^{*} >, \tag{2.2a}$$

$$Q =< E_{\parallel}E_{\parallel}^{*} > - < E_{\perp}E_{\perp}^{*} >, \tag{2.2b}$$

$$U =< E_{\parallel}E_{\perp}^{*} + E_{\perp}E_{\parallel}^{*} >, \tag{2.2c}$$

$$V = i < E_{\parallel}E_{\perp}^{*} - E_{\perp}E_{\parallel}^{*} >, \tag{2.2d}$$

where $E_{\parallel}$ and $E_{\perp}$ are the transmitted waves through horizontal and vertical polarizers, respectively; I is (incoherent) intensity of the electric fields, whereas Q and U are linearly polarized indicating some degree of coherence. This method is specially useful to determine the polarization of scattered light, since as mention before scattering events increases the amount of incoherent light. And in these cases to find the

Stokes parameters of the resultant light we can add the Stokes parameters of the scattered light that propagates in the same direction, that is superposed scattered light (i.e. incoherently).

2.4 Constitutive Relations and Intrinsic Anisotropic Optical Quantities

In previous section we introduced Maxwell's equations (eq. 2.1) and presented the *electric displacement field* and the *magnetizing field*. These two quantities describe the behaviour of the electric and magnetic field inside a material, and are related to the incident EMF through the permittivity (ϵ) and permeability (μ). Isotropic media are not sensitive to orientation, thus the permeability and permittivity of such media can be fully represented by scalars. However, anisotropic media are orientation dependent and therefore their permittivity and permeability must be expressed as tensors to express the anisotropy of the media. Hence the constitutive equations of the electromagnetic field can be described for a general case as follows,

$$\begin{pmatrix} D_x \\ D_y \\ D_z \end{pmatrix} = \underbrace{\begin{pmatrix} \epsilon_{xx} & \epsilon_{xy} & \epsilon_{xz} \\ \epsilon_{yx} & \epsilon_{yy} & \epsilon_{yz} \\ \epsilon_{zx} & \epsilon_{zy} & \epsilon_{zz} \end{pmatrix}}_{\hat{\epsilon}} \begin{pmatrix} E_x \\ E_y \\ E_z \end{pmatrix} \tag{2.3a}$$

$$\begin{pmatrix} H_x \\ H_y \\ H_z \end{pmatrix} = \underbrace{\begin{pmatrix} \mu_{xx} & \mu_{xy} & \mu_{xz} \\ \mu_{yx} & \mu_{yy} & \mu_{yz} \\ \mu_{zx} & \mu_{zy} & \mu_{zz} \end{pmatrix}^{-1}}_{\hat{\mu}^{-1}} \begin{pmatrix} B_x \\ B_y \\ B_z \end{pmatrix}, \tag{2.3b}$$

It is important to note that the permittivity and permeability tensors can be diagonalized when the structure presents enough symmetries and the appropriate coordinate system can be chosen, or when the optical axis and the material axis are aligned. In the systems studied here we assume the latter, hence our permittivity and permeability tensors are diagonal tensors; note that the elements of the diagonal will be distinct for anisotropic media and equal for isotropic.

A somewhat more intuitive quantity that describes the intrinsic optical properties of a medium is the *refractive index* (m). The refractive index is a dimensionless quantity that expresses how much light is delayed inside a medium compared to the speed of light in vacuum, and it can also be determined through the permittivity and permeability of such medium. Thus the refractive index encompasses all the intrinsic optical

properties of a medium.

$$m = \frac{c}{v} = \sqrt{\epsilon\mu}, \tag{2.4}$$

where c is the speed of light in vacuum, v is the speed of light inside the medium, and ϵ and μ are respectively the relative permittivity and permeability of the system. The *complex refractive index* can be expressed explicitly through its real and imaginary parts as $m = n + ik$ where n is also called refractive index and k is called the *extinction coefficient*. The real refractive index gives information on the how the path of the light is bent inside the medium, e.g. *Snell's law*; and the extinction coefficient gives information on how much light is absorbed by such medium. Note that from equation 2.4, the refractive index is a tensor and it can only be treated as a one-dimensional complex number for isotropic systems.

In this thesis we will assume isotropic bulk properties but it is possible for structural anisotropy to appear, e.g. in chapter 6.

2.5 Effective Medium Approximations

Effective medium models have been developed since J.C. Maxwell and Lord Rayleigh in the late 19th century. These models consider a distribution of different homogeneous mediums as one effective homogeneous medium, for sufficient large scale observations. To begin our discussion of effective medium models, we consider the electromagnetic response of a finite system, in terms of the *polarizability* α, which gives the *induced dipole moment* $\vec{P}$ in response to an external field $\vec{E}$,

$$\vec{P} = \hat{\alpha}\vec{E}, \tag{2.5}$$

which is the polarization produced by a singe dipole with polarizability α. Thus if we have a system of dipoles we can find the average polarization created by them using the effective polarizability of the system (α_{eff}),

$$< \vec{P} >= \hat{\alpha}_{eff} < \vec{E} >, \tag{2.6}$$

where $< \cdot >$ denotes volume average.

For a small sphere the polarizability is defined as follows [3],

$$\alpha = \frac{3V}{N}\frac{\epsilon - 1}{\epsilon + 2}, \tag{2.7}$$

[3]Equivalent formulae were found independently by different authors: *Claussius-Mossoti*, *Maxwell* or *Lorentz-Lorenz*.

where α is the *polarizability*, N is the number of particles in the volume V and $\epsilon = \chi_e + 1$ is the relative permittivity. Using the polarization of a small sphere ($x << 1$ and $|m|x << 1$ with m the complex refractive index) Bohren and Huffman (2007) showed that the absorption and scattering cross sections can be written as,

$$C_{sca} = \pi a^2 \frac{8}{3} x^4 \left| \frac{\epsilon - 1}{\epsilon + 2} \right|^2, \tag{2.8a}$$

$$C_{abs} = \pi a^2 4x \text{Im} \left[\frac{\epsilon - 1}{\epsilon + 2} \right], \tag{2.8b}$$

where $x = ka$ is the size parameter with k begin the wavenumber and a the radius of the sphere and ϵ the relative permittivity. We can see that scattering rapidly diminishes as size goes towards zero ($x \to 0$), which is required for EMA.

These equations are the basis for the derivation of the well known *Maxwell-Garnett approximation (MG)*, which considers a two composite medium as a distribution of spheres of one material, with a low concentration, inside an homogeneous matrix. To get the desired expression, he surmised that the polarizability of the entire system has to be equivalent to the polarizability of the effective media, i.e. $\sum_i \alpha_i = \alpha_{eff}$. Then using the previous formula 2.7 the relation between the distribution electric parameters and the effective one is given by:

$$f \frac{\epsilon - \epsilon_{env}}{\epsilon + 2\epsilon_{env}} = \frac{\epsilon_{eff} - \epsilon_{env}}{\epsilon_{eff} + 2\epsilon_{env}}, \tag{2.9}$$

where f is *the fill factor*, ϵ_{env} and ϵ are respectively the permittivities of the main constituent of the matrix and spheres particles.

It is important to note that the MG model is very useful approximation in many situations, but generally it is not a good approach when the concentration of either of two phases becomes bigger, specially near the percolation threshold. Bruggeman tried to resolve this in his model, the *Bruggeman Approximation (BA)*, also known as *Effective Medium Theory approximation (EMT)*:

$$f_1 \frac{\epsilon_1 - \epsilon_{eff}}{\epsilon_1 + (d-1)\epsilon_{eff}} = f_2 \frac{\epsilon_2 - \epsilon_{eff}}{\epsilon_2 + (d-1)\epsilon_{eff}}, \tag{2.10}$$

where d is the system dimensionality. The Bruggeman model can also be expressed in terms of the *depolarization factors*, which give a direct relation between the electrical properties and the geometry of these phases.

$$f_1 \frac{\epsilon_1 - \epsilon^i_{eff}}{\epsilon_{eff} + L_i(\epsilon_1 - \epsilon^i_{eff})} + f_2 \frac{\epsilon_2 - \epsilon^i_{eff}}{\epsilon_{eff} + L_i(\epsilon_2 - \epsilon^i_{eff})} = 0, \tag{2.11}$$

for $i = x, y, z$. The depolarization factors of ellipsoids are well known, so is convenient to consider an effective ellipse of more complex systems.

The same generalizations on dimensionality and shape can be applied to the *MG model*, however the *Bruggeman model* is thought to be more appropriate for high volume fractions. Several authors compared and studied both models, particularly Bergman (1978), and usually the *Bruggeman approx.* is consider to be better than MG, nevertheless the MG model predicts *Surface Plasmon Resonances* of ϵ_{eff} for a certain ratio ϵ/ϵ_{env}, that have been seen experimentally, but the Bruggeman model does not.

Another interesting aspect of these two models is how they differ in predicting percolation. Several scientists studied the influence of the *percolation threshold* on optical and electromagnetic properties, and how the *EMT* differ in determining this *critical fill factor* (f_c) Brouers (2000), Earp and G. B. Smith (2011), Granovsky, Kuzmichov, and Clerc (1999), Sen and S. Torquato (1988), and G. B. Smith, A. I. Maaroof, and Cortie (2008). Thus, using *MG* one finds that the *critical fill factor* is constant $f_c = 1$ (or $f_c = 0$), i.e. there is no percolation in the fill factor transition. Instead, *Bruggeman* predict $f_c = L_i$, that means that there could be more than one *critical fill factors* (e.g. $L_1 \neq L_2$). Both approximations predict different percolation points that differ from the experimental data and from the *percolation theory* (Stauffer and Aharony, 1992).

2.6 Monte Carlo Modelling

To deal with statistical systems the simplest and more powerful approach is to use the Monte Carlo method (MC) (Allen and Tildesley, 2017; J. E. Gentle, 2009). This technique relies on generating an ensemble of structures and averaging the response. For some well-known statistical distributions it is possible to expand the average response as a power series, but generally this is significantly more difficult as the order increases. We will see examples of this in various chapters, but in general it is sufficient to use the direct ensemble approach, understanding that the uncertainty will decline with the sample size N as $1/\sqrt{N}$ since we focus on incoherent processes (coherent processes converge as $1/N$).

To implement the Monte Carlo method it is important to first determine the sample size. To estimate the number of iterations needed we can analyse the standard deviation of the ensemble in terms of the sampling number. With this study one can infer the accuracy of the Monte Carlo method for a fix sample size [4]. Once the number of iterations has been determined, we can proceed to use the MC method; to do so, we will calculate the results over and over till we have a number of calculations equal to

[4]The results presented in this thesis have been obtained using sample sizes that were previously determined using validation tests.

the sample size, then we will average the results to obtain a representative solution of our calculations.

Although we use the Monte Carlo method to analyse random systems, and therefore each system has a distinct configuration and characteristics, the results obtained using this method will show the common pattern present over the whole ensemble. Thus we will be able to infer the intrinsic properties that are relevant to given distributions.

2.7 Concluding Remarks

Here we have outlined some general interactions and frameworks. In the following chapters we give concrete examples, starting with small spheres of metal sponges, which illustrate some of the issues that will arise in later chapters.

Chapter 3

Metal Sponges

This chapter is based on my conference paper Galí et al. (2015): here we will demonstrate the use of Monte Carlo modelling and dipole scattering in an attempt to find the effective response of metal sponges.

Nanoporous metals are of interest because they can be used in a wide range of applications, including as capacitive sensors, actuators, chemical catalysts, electrodes for supercapacitors of Li-ion cells, or as surface coatings with controlled optical properties (Cortie et al., 2007; Earp and G. B. Smith, 2011; Galinski et al., 2011; Garoli et al., 2015; G. B. Smith, A. Maaroof, et al., 2006). It is this latter application that is relevant here: in the present work we investigate the correlation between the morphology and the optical properties of sponges. To do so, we will study a silver (Ag) sponge-like metamaterial of the form typically produced by de-alloying Ag-Al precursor alloys.

The interaction of light with materials is influenced by their dielectric function (an intrinsic property) and their morphology structure (extrinsic property). For a nanoscaled structure illuminated by visible light the dielectric function and its geometry become intertwined and the resulting properties are often expressed as an 'effective medium' which takes geometry into account (G. B. Smith, A. I. Maaroof, Allan, et al., 2004). The transition from a network with weak metal connectivity and more localized optical response to one with macroscopic percolation and delocalized response involves a sequence of morphologies. Signature topological features emerge near the percolation threshold, but there is usually a broad admix of local void topologies within any sponge, making analysis complex. The fine detail of geometry is thus lost in the formulation of the effective medium. Explicit consideration of the geometry of the material would give an extra order of precision in these models but the problem is intractable from an analytical viewpoint.

Here we generate model versions of these sponges by a numerical process that simulates de-alloying and atomic rearrangement. It has been shown elsewhere that the model successfully reproduces the classic bicontinuous vermicular sponges that are frequently observed in noble metals (M. C. Tai, A. Gentle, de Silva, et al., 2015). The sponges are then used as targets for the calculation of the optical properties using

the discrete dipole approximation (DDA) and the resulting optical properties used, in turn, to construct an 'effective medium approximation' (EMA) for the material. We then explore how these EMAs are related to the morphology of each type of sponge.

3.1 Methodology

3.1.1 Simulation of Sponge Geometry

In this work we generated a series of nanoporous sponges using a code that simulates the dealloying of an alloy between a noble metal and an active metal (this code developed by Michael Cortie is detailed in Supansomboon et al., 2014; M. C. Tai, A. Gentle, de Silva, et al., 2015). In our case the noble element was silver (Ag) and the active, sacrificial, element was aluminum (Al). Elapsed time in the simulations is measured in 'sweeps', with one sweep defined as the completion of the same number of Monte Carlo iterations as there are atoms in the simulation. Therefore, on average, each atom has been visited once after one sweep has been completed. The dealloying part of the simulation finishes when all Al is gone from the sponge, and at this point we reset the sweep counter to 0 and anneal the target for 15,000 sweeps. During this annealing phase thermally-activated atomic movements driven by a Metropolis Monte Carlo[1] algorithm operating with a Lennard-Jones interatomic potential reshape the sponge. The process leads to coarsening of the ligaments and is effectively being driven by the intrinsic surface tension of the Lennard-Jones solid. Finally, we machine a spherical shape from each cuboid of sponge, for use in the optical property calculations. As we will show, use of a spherical target brings the distinct advantage that the analytical Mie solutions (Mie, 1908)[2] can be applied within the analysis. The sponges are labeled according to their initial Al content, and the number of sweeps to which they had been coarsened.

The spherical cutout is performed on structures recorded at selected sweep numbers chosen so that the intervals are approximately evenly spaced on a logarithmic time axis. Consequently, the amount of Ag inside the ball of sponge after additional sweeps can vary slightly, since although we cut it in the same region every time the silver atoms can move a little between sweeps. Therefore, there is a small flux of Ag atoms passing in or out of the spherical template used to machine the ball of sponge. The second implication of our method is related to how we cut the cube; in order to be more realistic, the method that we are using to simulate the dealloying and coarsening process works in real space ($\mathbb{R}^3$), i.e. it is a so-called 'off-lattice' algorithm and

[1] Metropolis Monte Carlo algorithms are used when the configuration or normalization of a system is not known. To find this optimal state, at each iteration we allow the system particles to move under a certain potential function. Thus for each iteration the system converges to a more energy stable state.

[2] A detailed explanation of Mie theory can be found in Bohren and Huffman (2007).

the position of each atom is expressed using a floating point number. In contrast, the computer code we used to calculate the optical properties (see section 3.2.1), needs a target where the dipoles have integer coordinate positions, i.e. are in $\mathbb{Z}^3$. There are small computational discrepancies when a $\mathbb{R}^3$ sponge is converted to an array of dipoles in $\mathbb{Z}^3$, and further small errors when we fix a radius and proceed with cutting the sphere shape out of the block of sponge (in the latter case, dipoles near the sphere surface have to fall completely inside or outside the cut-out and there will be some stochastic variation). Consequently, the actual radii of the resulting spheres vary slightly from the nominal value of 30nm. These small errors will of course propagate through to the effective medium approximation (EMA) that we will be deriving.

3.1.2 Discrete Dipole Approximation

While there are different numerical techniques for calculating the required electromagnetic response Zhao et al. (2008), the most practical for our purposes seems to be the *Discrete Dipole Approximation (DDA)* in which the voxels are assumed to interact as small dipoles. Thus the total polarization field can be expressed as the sum of the polarization fields created by each dipole to every dipole,

$$\sum_{k=1}^{N} \vec{A}_{jk}\vec{P}_k = \vec{E}_{inc,j}, \tag{3.1}$$

where $-\vec{A}_{jk}\vec{P}_k$ is the contribution of the electric field at position j due to the dipole at position k,

$$\vec{A}_{jj}\vec{P}_j = \alpha_j^{-1}\vec{P}_j, \tag{3.2}$$

$$\vec{A}_{jk}\vec{P}_k = \frac{\exp(ikr_{jk})}{r_{jk}^3}\left[k^2\vec{r}_{jk}\times(\vec{r}_{jk}\times\vec{P}_k) + \frac{1-ikr_{jk}}{r_{jk}^2}\left(r_{jk}^2\vec{P}_k - 3\vec{r}_{jk}(\vec{r}_{jk}\cdot\vec{P}_k\right)\right], \tag{3.3}$$

with $\vec{r}_{jk} \equiv \vec{r}_j - \vec{r}_k$.

Several authors have studied and developed this technique DeVoe (1964), DeVoe (1965), and Purcell and Pennypacker (1973). For instance, Draine and Flatau (1994) and Draine and Flatau (2008) developed the free software called *DDSCAT*, which applies the *Complex-Conjugate Gradient (CCG)* and *Fast Fourier Transformations (FFT)* methods for numerically efficiency. Additionally, the *Amsterdam DDA (aDDA)* is a fully parallel code that was developed for very finely sampled problems. These codes are mainly aimed at determining the extinction and absorption factors of a finite particle at a particular incident wavelength, but they can also be used to determine field

distributions which are required for a full understanding of material response. However, as we explain later, we are able to determine effective properties using a few key far-field measurements.

A key reason to use a numerical solution is that we only know the analytical solution of a few shapes, but using a *DDA* we are able to get data for any kind of shape and for any kind of incident wave. In *DDA* we are practically restricted in terms of the size of structures that can be simulated: $\frac{2\pi a}{\lambda} < 1$, where a is the effective radius of our sample ($a = (\frac{3V}{4\pi})^{1/3}$). However, a similar restriction applied to the validity of the effective medium concept, since very large structures exhibit size-dependent scattering.

3.1.3 Effective Medium Approach

There are several models that aim to provide a quantitative understanding of the optical properties of mesoporous materials (Bergman, 1980; Jalas et al., 2014; A. I. Maaroof, Cortie, A. Gentle, et al., 2007), but in our opinion none of them is fully satisfactory yet. Here we will exploit a new approach to develop an effective medium approximation (EMA) of the sponges. Essentially, our aim is to define a homogeneous virtual material that has the same extinction cross section and same phase delay cross section as the complex sponges under study. To achieve this, we will use the extinction and phase efficiency calculated by DDSCAT to derive the complex dielectric function (or, equivalently, the refractive index) of the effective medium. We are using this method instead of finding the effective response through field averaging because the fields generated by DDSCAT are not smooth enough due to high dependence on sampling (both in the filaments and in the ball surface); also with our alternative method we analyse far field quantities that, in theory, can be obtained experimentally.

The desired extinction and phase cross sections are defined by Bohren and Huffman (2007) and Draine (1988) as:

$$C_{ext} = \frac{4\pi k}{|E_{inc}|^2} \sum_{i=1}^{n} \mathrm{Im}\left[E^*_{inc,i} \cdot P_i\right], \tag{3.4}$$

$$C_{pha} = \frac{2\pi k}{|E_{inc}|^2} \sum_{i=1}^{n} \mathrm{Re}\left[E^*_{inc,i} \cdot P_i\right]. \tag{3.5}$$

C_{ext} gives the energy loss caused by the combination of scattering and absorption. On the other hand, $Q_{pha} = \frac{dC_{pha}}{d\Omega}$ is a factor that is related to the phase lag due to the effective medium, and consequently is directly related to the real part of the polarizability, α. In principle this quantity can also be measured directly by interferometry or indirectly by ellipsometry. Note that in the literature there is a difference of a factor 2 in the definition of this parameter, however, as we are using the simulated data

from DDSCAT, to be internally consistent, we will use the definition given by Draine (Draine, 1988) (eq. 3.5).

First of all, we will work with the expressions of C_{ext} and C_{pha} (eq. 3.4 and 3.5) in order to define the effective polarizability. Therefore, as we are assuming that our effective medium is homogeneous, previous relations, equations 3.4 and 3.5 simplify since the polarizability tensor becomes diagonal (assuming either isotropy or alignment of optical and material axes), i.e. $\alpha_{i,j} = 0$ if $i \neq j$, and $\alpha_{i,i} = \alpha$. Then, using the relationship $P = \alpha E_{inc}$, the previous equations become:

$$\begin{aligned} C_{ext} &= 4\pi k \mathrm{Im}\left[\alpha\right], \\ C_{pha} &= 2\pi k \mathrm{Re}\left[\alpha\right], \end{aligned} \tag{3.6}$$

where $k \equiv 2\pi/\lambda$ is the wave number. Let be C^S and C^{eff} the sponge and effective medium cross section factors, then imposing our EMA, i.e. $C^S \equiv C^{eff}$, the efficiencies are related as follows:

$$Q^{eff} \equiv \left(\frac{a_{eff}}{R}\right)^2 Q^S, \tag{3.7}$$

where Q^S and Q^{eff} are the sponge and the effective medium efficiencies, respectively. Then, we can define the effective polarizability in terms of the efficiencies of our sponge.

$$\alpha^{eff} = \frac{Q^{eff}_{pha}}{2x} + \frac{Q^{eff}_{ext}}{4x} i \tag{3.8}$$

$$\equiv \left(\frac{a_{eff}}{R}\right)^2 \left(\frac{Q^{S}_{pha}}{2x} + \frac{Q^{S}_{ext}}{4x} i\right), \tag{3.9}$$

where $x = 2\pi R \epsilon_0^{1/2}/\lambda$ is the scale parameter.

Finally, we can use *Claussius-Mossotti* approximation to relate the polarizability to the permittivity. Thus, we obtain the following expression:

$$\epsilon^{eff} = \epsilon_0 \frac{2\alpha^{eff} + 1}{1 - \alpha^{eff}}. \tag{3.10}$$

3.2 Results

3.2.1 Optical Properties

Six different model precursors with starting Al concentrations of 60%, 65%, 70%, 75%, 80% and 85% (atomic percentages) were dealloyed, and each then subjected to 15000 sweeps of coarsening under the action of the model. Intermediate structures were recorded at 0, 100, 200, 500, 2000, 5000 and 15000 sweeps. Thus, we study 6×7 different Ag [3] sponges. Representative examples are shown in Figure 3.1. It can be seen that increasing the Al content of the precursor results in a loss of percolation of the silver phase and decrease in density of the resulting Ag sponge. In addition, prolonged application of the Monte Carlo simulation results in the growth and thickening of the ligaments of the sponge.

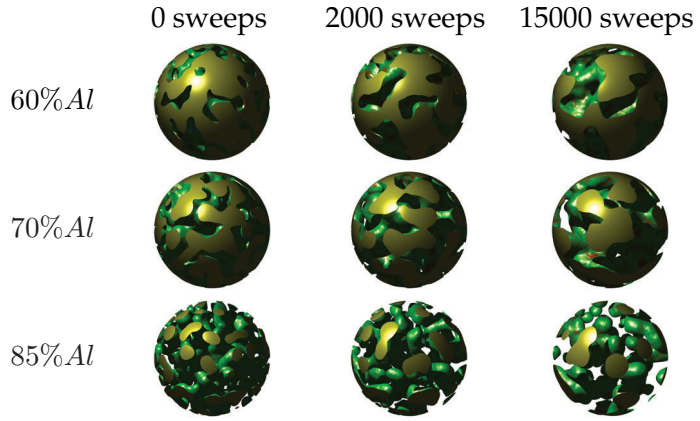

FIGURE 3.1: Simulated metallic ball sponges classified by initial aluminium content and number of sweeps. These simulations were generated by Michael Cortie.

The calculated optical properties are shown in Figure 3.2 in which it can be seen that the sponges do not scatter significantly, i.e. the extinction is mainly dominated by the absorption ($Q_{ext} \sim Q_{abs}$) - thus the sponges meet a necessary condition for application of any EMA. Also, as the concentration of Al in the precursor alloy increases the resulting sponges become less absorbent, which is expected since the sponges are less dense.

[3] Johnson and Christy (1972) source of Silver data.

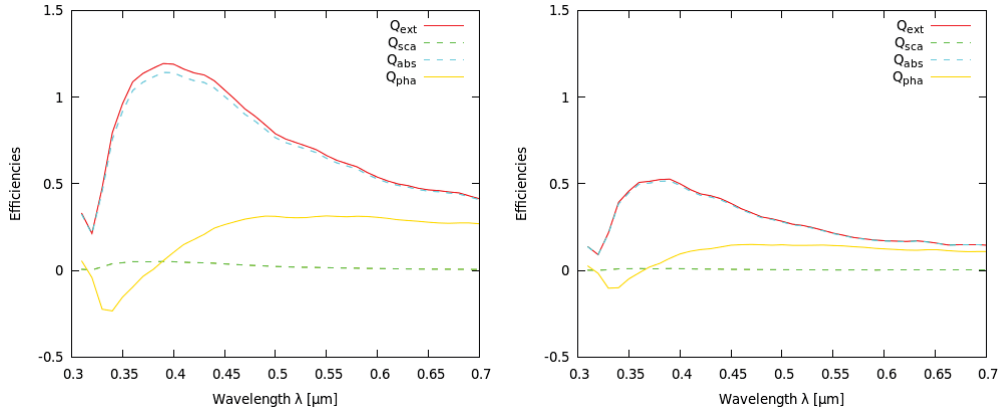

FIGURE 3.2: Normalized efficiencies (cross section equals to $\pi 30^2 nm^2$) at 0 sweeps for sponges with an initial Al fill factor of 60% (left) and 85% (right).

The distinct extinction peak due to a dipolar plasmon resonance in the sphere is lost as the density of the sponge decreases and this is more clearly shown in the color map of Figure 3.3.

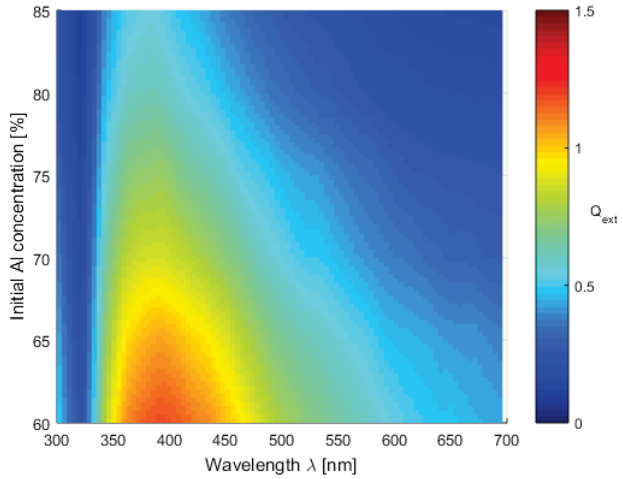

FIGURE 3.3: Extinction efficiency of a spherical sponge at 0 sweeps in terms of the initial concentration of aluminium in the precursor alloy. To a first order approximation the latter quantity can be taken as the void fraction.

As we explained in the previous section (sec. 3.1.3), Q_{pha} is related to the phase lag, where positive phase efficiency means that the phase velocity (v_p) is smaller than c, and negative Q_{pha} means $v_p > c$, it is worth noting that $v_p > c$ only means the the phase is travelling faster than the light, but not the wavefront.

Phase velocity is defined as $v_p \equiv c/n$, i.e. $v_p > c$ if the refractive index is smaller than 1. As our sponges are dispersive media ($n(\lambda)$), the phase velocity will vary with the incident wavelength and thus, the Q_{pha} will do too. It can be seen in Figure 3.2, that Q_{pha} achieves negative values at smaller wavelengths ($< 400nm$) and, as expected, that happens in the same wavelength range where bulk $n < 1$ (see figure 3.4).

3.2.2 Effective Media

Effective medium models can only be applied when the size of the original medium is much smaller than the incident wavelength. Thus, the applicability of EMA usually is determined by the wavelength (λ) and the scale parameter (x) through the inequality $2\pi x << \lambda$. Our simulated samples have a radius $\sim 30nm$ and we are analysing them for incident wavelength in the visible range $300 - 700nm$, so we are well inside the limit. Therefore, it is reasonable to apply an EMA.

It is important to note that the generation of the spherical sponges implies another problem: as we cut the sphere our samples have a very rough surface (especially the sponges with low concentration of silver) and in these samples the outermost regions of the ball are almost unpercolated. This means that the grade of connectivity of the outermost part ('shell') of the sphere is not the same than the core, i.e. the 'shell' of the sphere lacks the representative topology of the porous sphere. This may cause another issue (that we will not study further in the present work): if the skin depth is smaller than the thickness of the sphere shell, we will only be analysing the optical response of the shell, which is not the topological representative part of the sample.

Using the approximation explained before (section 3.1.3), and the data that we calculated for our sponges we found a spherical effective medium, figure 3.4. It is important to emphasise two points; our effective media model is useful for directly analysing the equivalent refractive index or dielectric permittivity of each sponge, and so, provide insights into fundamental trends of the sponge spectra. Nevertheless, specific information about localized electric fields or plasmon resonances of the porous samples cannot be found from the EMA. Indeed, as demonstrated in the literature Bosman et al. (2012), Earp and G. B. Smith (2011), Lang et al. (2011), and A. I. Maaroof, A. Gentle, et al. (2007), the localized plasmon resonances are very sensitive to structural irregularities and may be present at a size scale of the order of several nanometres. One implication of this is that plasmon resonances of the original cubic sponge will not be the same as the resonances of the spherical sponge. The original sponge has been generated with periodic boundaries in the horizontal plane, i.e. the structure is topologically equivalent to an infinite plane, and a structure such this generates a surface polariton current (Berini, 2000; Burke, Stegeman, and Tamir, 1986). Nonetheless, after the cutting we obtained a small sphere (compared to the incident

wavelength) and this structure is more likely to create a localized surface plasmon (LSP). Thus, with this method the localized plasmon resonance of the sphere surface dominates the optical response.

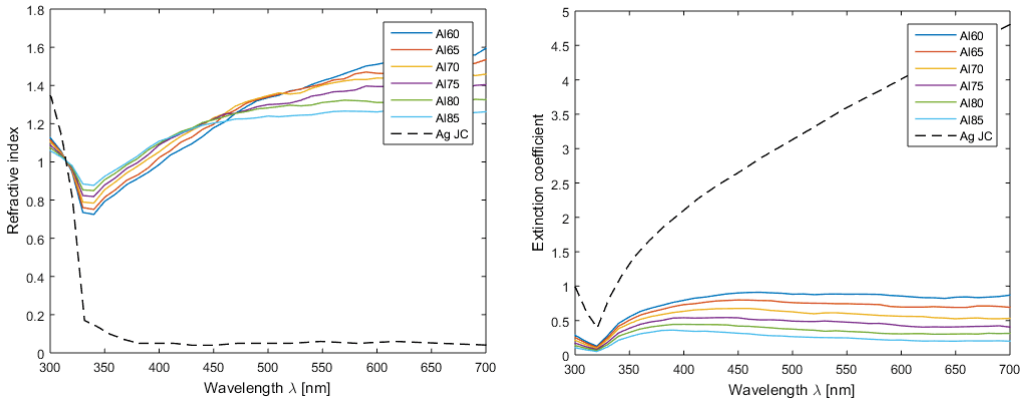

FIGURE 3.4: Comparison between the real part of the refractive index (left) and the extinction coefficient (right) of the effective medium of a sponge at 0 sweeps, and the refractive index of bulk silver (Johnson and Christy, 1972).

A. I. Maaroof, Cortie, and G. B. Smith (2005) measured experimentally the optical response of mesoporous gold films, and fitted the data to find the effective refractive index of such structures. They found a very weak plasmon response similar to the results that we obtained with silver mesoporous structures. Even though they analysed gold structures and we studied silver ones, these two materials have negative permittivity in the visible range, with silver having a sharper plasmon peak than gold. In this figure it can be seen that, as expected, the extinction coefficient decreases as the metal fill factor decreases as well. This is because the sponge becomes less absorbent and scattering. Nonetheless, the behavior of its refractive index (n) is more interesting because at the shorter wavelengths ($\sim 300 - 350$ nm) the response of each sponge is closer to bulk silver, Figure 3.4. However, for greater wavelengths (> 350 nm) the topology of the sponge starts to play a dominating role. Due to the low amount of Ag, instead of having a solid sphere with voids inside (concave metal structure), we have a spherical network of silver filaments (convex metal structure). In this situation, the phase that has a higher grade of connectivity is the void-phase, i.e. the incident wave will mainly travel through vacuum. This implies that our sample would have a higher transmittance and a low energy loss ($k \sim 0$), figure 3.4. Figure 3.4 shows another interesting aspect of the sponges, the real part of the refractive index and the extinction coefficient acquire an almost constant value at longer wavelengths, i.e. at these wavelengths the trend is similar to the refractive index of vacuum.

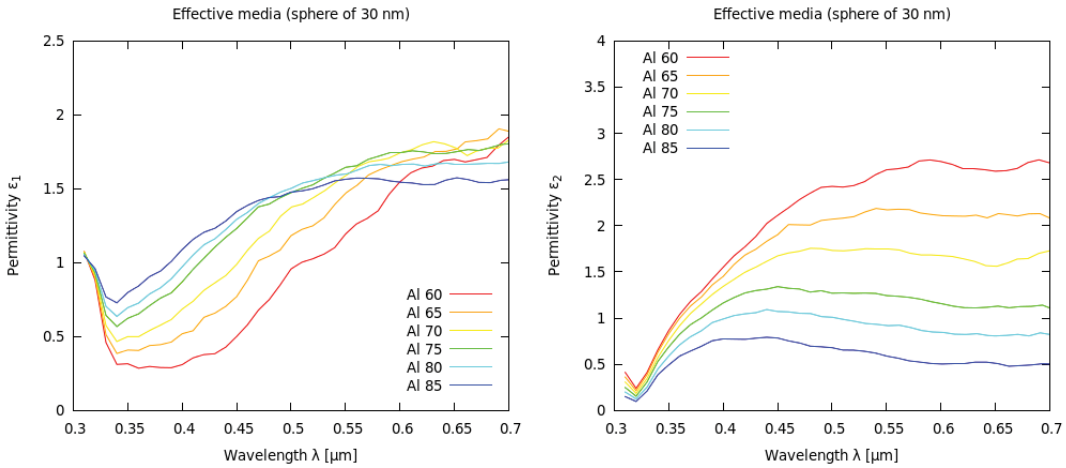

FIGURE 3.5: Real (left) and imaginary (right) parts of the effective permittivity of a ball sponge at 0 sweeps and at different concentrations of silver.

Arnold and Blaber (2009) showed that plasmonic response can be identified by analysing the complex dielectric function. In our samples, overall, the optical responses of the sponges are not strongly plasmonic due to the positive values of the effective ϵ_1 (see figure 3.5). This can also be seen in the fact that, in general, the effective refractive index n is larger than the effective extinction coefficient, k, i.e. $k/n < 1$, so they do not behave as metallic systems. This intuitively surprising result was previously reported by G. B. Smith, A. R. Gentle, and A. I. Maaroof (2007). We believe that the random morphology and low density of the sponges smooth the plasmonic response of the silver filaments.

3.3 Conclusion

In this chapter we used numerical methods to study the optical properties of model spherical targets made of nanoporous silver sponges. A range of simulated sponges of different densities and morphologies was investigated. A decrease in overall density of the silver reduced the absorption, but the spectral position of the absorption peaks was scarcely changed due to the dominance of the spherical shape of the sponge over the internal morphology.

The spherical shape of the targets was exploited to build an effective medium model for each type of sponge by solving the extinction and phase cross-sections equations (3.6) in reverse to extract an ϵ_1 and ϵ_2 for each wavelength. This model provided an effective refractive index of each sponge which incorporated the effects of void fraction and shape into an effective medium.

Analysis of the trends of the data indicates that, while fill fraction is the dominant factor controlling optical properties, the morphology of the sponge also has an important influence. Nonetheless in our results the optical effects of the internal morphology were slightly obscured by the strong dependence on the spherical shape. This result shows the importance of the surface finish to be considered in a later chapter.

This work motivated our investigation in randomly structured materials (chapter 4) and on the optical dependence due to surface structure which we will present on chapter 6. We retain the Monte Carlo framework, but will need specialised techniques for solving Maxwell's equations efficiently in those geometries.

Chapter 4

Effective Permittivity of Random Two-Phase Anisotropic Composites

As mentioned in the motivation chapter (ch. 1), of particular interest to us are anisotropic structures grown by physical vapour deposition (Arnold, 2005; M. C. Tai, Arnold, et al., 2017; Walsby et al., 2005). These kind of structured materials are extended along the growth direction, so their phase distribution in the plane perpendicular to the growth direction can be adequately described by a two-dimensional (2D) system. As it can be seen in figure 4.1, these structures are partially ordered in one direction and disordered otherwise. This particular characteristic will influence the appropriate distribution method to use when modelling these systems, and this anisotropic behaviour can be visualized using the autocorrelation function of the structure, as will be explained in section 4.1. Several authors have focused much of their research on developing theories that can explain the physical properties of these heterogeneous materials from their statistical characteristics (G. W. Milton, 2002; S. Torquato, 2002). We will extend these to gain new insights into the anisotropy of pseudo-random 2D composites.

FIGURE 4.1: Top view of a silicon column-like structure, the Si was deposited by serial bideposition at oblique incidence. This structure was deposited by Matthew Arnold and the SEM picture was taken by Ed Walsby and edited by Matthew Tai.

The overview of this chapter can be summarized as follows:

(i) Review of several models to obtain pseudo-random distributed systems (sec. 4.1).

(ii) Generation of structures statistically similar to the column-like structures shown in figure 4.1 (sec. 4.2).

(iii) Extending the work done previously by several authors, e.g. (Brown, 1955; Sen and S. Torquato, 1989; Torquato, 1985; S. Torquato, 2002), on electrical properties of composites by introducing a unified notation and a detailed explanation of the series manipulations used in this work, allowing extension to any order (sec. 4.3).

(iv) Presentation of a Monte Carlo based methodology that will allow us to easily implement the method to arbitrary order (sec. 4.3.5),

(v) New insights on bounds of the dielectric function (sec. 4.5) and the nature of micro-structural parameters of high order (sec. 4.6).

(vi) Discussion on the micro-structural parameters and permittivity of different kinds of structures (sec. 4.7).

4.1 System Generation

In this section we consider some different methods to generate a pseudo-random two dimensional system similar to the column-like structure that we are interested in (see figure 4.1). These structures have the following structure characteristics:

(i) Long range disorder due to statistical roughening.

(ii) Short range damping due to diffusion.

(iii) Short range order due to shadowing.

To choose the appropriate kernels we will compare the autocorrelation functions of the generated systems with the autocorrelation of the SEM picture of the column-like structure.

4.1.1 Autocorrelation Functions

As its name suggests an autocorrelation function gives information on the correlation between a function and a displaced copy of the same function. We can define the autocorrelation function as follows:

$$C_{ff}(\tau) = \int_{-\infty}^{\infty} f(t)f^*(t-\tau)dt, \tag{4.1}$$

where $f(t)$ is an arbitrary function (in this case represents the occupancy of the structure) and $f^*(t)$ is the complex conjugate of $f(t)$.

Hence, autocorrelation functions are useful to find repeated patterns hidden in a given function. In our case we are using the autocorrelation of the structures to see which spatial patterns characterise our structures.

To interpret the autocorrelation function we have to analyse the amplitude and position of its peaks: the central peak tells us the correlation of the function under zero displacement (it will always be the point with maximum amplitude and is equal to the fill factor). The height of the peaks away from the central peak give information of the correlation under that displacement, thus if high amplitude peaks appear at long displacement means that the structure presents long range correlation. On the other hand, no oscillations implies randomised structures which do not offer any positional preference: the value should decay to the square of the fill factor (ϕ^2) as the spatial displacement goes to infinity $\tau \to \infty$.

Specifically, in figure 4.2, we can see an example of the autocorrelation function of a relevant experimental system, from it we can discern two main behaviours in the vertical (growth) and horizontal axis:

(i) the "black spots" next to the main peak indicate that the structure is anti-correlated with itself at short range, thus the dips in that direction reflect a pattern at short order, consistent with the spacing between the arrays of columns that can be seen in the SEM image (left side of figure 4.1);

(ii) on the other hand, in the opposite direction the correlation decreases exponentially without any oscillations and therefore showing no particular pattern, i.e it presents a disordered system.

This information tell us of higher connectivity in the horizontal direction, which agrees with the strap-like structures that can be seen in the SEM image (fig. 4.1). In figure 4.2 the white lines on the autocorrelation image show us the cross-section at the centre point of the function, we can see that in one direction the autocorrelation behaves like a decaying oscillating function, e.g. sine cardinal function (sinc); and in the other direction it presents an exponential decay, e.g. exponential. Therefore, this gives us a concrete insight on which kind of generating functions we are interested in.

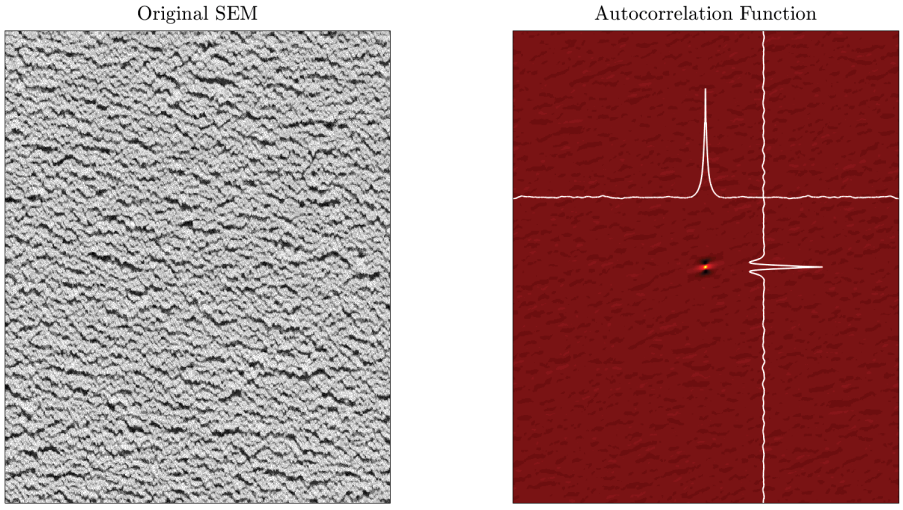

FIGURE 4.2: On the left, we can see a heat-map in gray scale of the SEM image of the column-like structure shown in figure 4.1. Right picture shows the autocorrelation function of the left image, the white lines are the scaled cross-sections of the autocorrelation function.

Before deciding on an implementation of structure generation, I considered three generation methods:

(a) *Probability Well Method*[1]: this method allows for the creation of pseudo-randomly

[1] *Probability Well Method* is an extension of the *random sequential addition* method detailed in S. Torquato, 2002

distributed particles in a probabilistic way. It has the advantages that it can be applied to different fixed shapes or to random morphologies (similar to the *Level-Cut Gaussian Random Fields Method*) and each particle can create a well on the probability space using a different probability distribution. The main disadvantages are that it puts new particles iteratively and therefore its randomness is more limited to the iteration process and to the fixed probability wells chosen, also being an iterative method for large systems it can become computationally very expensive.

(b) Molecular potential based methods (Alder and Wainwright, 1959; Rahman, 1964; Rapaport, 1996), this classical method relies on potential functions to describe a given system. It is very useful to describe a system where the interaction potential is known, nevertheless this is not always the case and to reach a minimal energy state can be again very computational expensive if the system is very large.

(c) *Level-Cut Gaussian Random Fields Method* (sec. 4.1.2), this method filters a Gaussian random field using a chosen function, thus it has a strong correlation dependence on the chosen filtering function (similar effect as that of the *Probability Well Method* with the well probability). On the other hand, it is very computational efficient and its implementation is very simple. Also, using the *level-cut* method, for a given signal we can obtain structures with different fill factor and pseudo-random morphology. These characteristics make this method very useful to simulate structures with a randomized internal morphology but that offer some structural pattern.

Several other system generator methods are outlined in Isichenko (1992) and S. Torquato (2002) (e.g. cell methods), but we will not discuss these here.

4.1.2 Level-Cut Gaussian Random Fields

In this section we present a particularly efficient method to generate random two-phase media; this method is based on filtering a two-dimensional Gaussian random noise using a chosen kernel, in doing so the resultant structure has a characteristic length determined by the kernel. Therefore, this property allows us to create systems with smoother morphologies similar to the structures found experimentally in a very simple and efficient way. Other authors have worked in developing similar methods to filter Gaussian random noise to obtain realistic structures (Cahn, 1965; J. A. Quintanilla et al., 2007; Teubner, 1991; S. Torquato, 2002). Another important advantage of using this methodology is that in principle we could extract the autocorrelation function of a real structure, and use it to find a kernel that generates a probabilistic equivalent composite.

All these characteristics make this method the most suitable, among the methods that we considered, to analyse the column-like structures mentioned in the motivation. This is because it is an efficient and easy procedure to design structures with a given anisotropy and disorder. Here, we will focus on this method in the analysis of anisotropic 2D structures (a detailed explanation can be found in J. E. Gentle (2009) and S. Torquato (2002)).

A summarized explanation of the methodology to apply this method is the following:

(i) generate a 2D pseudo-random signal, *Gaussian Random Fields* (GRF),

(ii) filter the noise using a specific kernel[2],

(iii) cut the filtered signal at the amplitude that gives the required fill factor [3].

GRF have been applied in many areas where it was necessary to generate systems with a certain degree of simplicity. This method allows control over the correlation length, mean and standard deviation of the heterogeneities distribution through the chosen kernel (filter function). For instance Rice (1958) used this method to analyse the attenuation of radio signals, and Hegge et al. (2017), Letnes et al. (2012), A. A. Maradudin (2007), A. A. Maradudin and Mills (1975), Nordam, Letnes, and Simonsen (2013), and Simonsen et al. (2011) used it to analyse the electromagnetic properties of random rough surfaces. We use this method in chapter 6 for the same purpose, to study the optical response on rough coatings characterised by a Gaussian kernel.

Step (iii) determines the final structure cutting the GRF. Thus to obtain the level-cut structure we need to cut the filtered Gaussian random field at certain level. Let's consider α the level where to cut the signal, then the i-phase particles are in the space coordinates that satisfy $y(\vec{r}) > \alpha$, where $y(\vec{r})$ is the filtered GRF. Then the n-probability function will be given by the volume average of n Heaviside functions,

$$p_n(\vec{r}_1, \vec{r}_2, \ldots, \vec{r}_n) =< H(y_1 - \alpha) \ldots H(y_n - \alpha) >, \tag{4.2}$$

where $y_i = y(\vec{r}_i)$.

Orthant Probabilities

This last step, cutting the filtered spectra, creates a new problem in the generated structure; to obtain the *n-point probability functions* (p_n), required for full description of the system, we have to integrate over multidimensional probability space, but now

[2] In this context a kernel is the function that characterises a certain probability density function.

[3] Note that using the same filtered signal we can obtain different structures cutting the signal at a different amplitude (different fill factor).

these integrals are also constrained by the level where we are cutting (α). For instance, Berk (1991) and Teubner (1991) found the one point probability function (fill factor) is defined as follows:

$$p_1 = \frac{1}{\sqrt{2\pi}} \int_{\alpha}^{\infty} \exp(-\frac{t^2}{2}) dt. \tag{4.3}$$

These kind of multi-dimensional integrals restrained to a region of the space have been widely studied in statistics in the field of *orthant probabilities*, which are the probabilities in a subdivision of the integration space. Miwa, Hayter, and Kuriki (2003) and Miwa, Hayter, and Liu (2000) studied non-centred orthant probabilities and found an iteration method to calculate the multidimensional integrals that arise in these problems, nevertheless his methodology only applies directly to tridiagonal correlation matrices. They show an algorithm to transform arbitrary matrices to tridiagonal, but this is quite tedious to implement. The results given by Miwa, Hayter, and Liu and also by Roberts and Teubner; Teubner are based on earlier research by Abrahamson (1964), Genz and Bretz (2009), Rogers (1961), van der Vaart (1953), and van der Vaart (1995). They found analytic expressions for the two-point, three-point and four-point probability functions in terms of the field-to-field correlation functions (g_{ij}), but with the significant restriction that the volume fraction is a half ($\phi = 1/2$).

$$\begin{aligned} p_2 &= \frac{1}{4} + \frac{1}{2\pi} \arcsin(g_{12}), \\ p_3 &= \frac{1}{8} + \frac{1}{4\pi} \left(\arcsin(g_{12}) + \arcsin(g_{13}) + \arcsin(g_{23}) \right), \end{aligned}$$

with higher dimensions become increasingly more difficult.

Kernels

As mentioned before, GRF methods have been used in different research areas, but was first applied to effective media by Berk (1987) and Berk (1991) as the *Leveled-Wave Model of Random Morphologies* as a model to analyse bi-continuous morphologies. This methodology was later expanded by Blumenfeld and Salvatore Torquato (1993), Roberts and Teubner (1995), and Roberts and S. Torquato (1999). In these works other probability densities and field to field correlation functions where used. In particular, Roberts and S. Torquato used *chord-length distributions* obtaining basic smoothness structures that are useful to represent 3D foam-like structures (porous materials) where the p_1 probability function can be determined.

From the previous explanation, we can see that the system behaviour will depend on the kernel that we use as a filter. To do so a field-to-field correlation function (g) (kernel) must be determined. From the isotropic models that Roberts and Teubner (1995) analysed we are interested in the following:

Model I:

$$g(\vec{r}) = \exp(-r)\,\frac{\sin(\nu r)}{\nu r}, \tag{4.4}$$

where $r = |\vec{r}|$, $\nu = 2\pi l_1/l_2$ with l_1 the decay length of the field and l_2 the characteristic size structure.

Model II:

$$g(\vec{r}) = \exp(-\vec{r}\cdot\vec{r}), \tag{4.5}$$

They used these models to analyse the third order MSP (η) finding that $\zeta = 1/2$ at $\phi = 1/2$ for isotropic systems and that ζ is nearly linear with the fill factor (ϕ), giving different slopes for each model.

4.2 Anisotropic Random Structures

As mentioned above, in this section we will use the *Level-Cut Gaussian Random Field Method* to generate the systems under study. In figures 4.3, 4.4 and 4.5 we show the dependence of the structure morphology on the kernel function used for an isotropic and an anisotropic case. The level of anisotropy can be expressed using the ratio of the *decay lengths* in each axis: e_x for the horizontal and e_y for the vertical. Thus isotropic structures generated with isotropic kernels satisfy $e_y/e_x = 1$, while for anisotropic structures $e_y/e_x \neq 1$.

As can be seen in these figures (fig. 4.3, 4.4 and 4.5) the selection of the kernel affects the structure morphology: using the autocorrelation function we can see how the exponential kernels are less correlated at long range, while for sinc kernels the structures offer a high degree of correlation at long range. These are key characteristics to consider when deciding which structure we want to represent. For instance, if we compare the autocorrelation function of these three kernel structures with the autocorrelation function of our column-like structure (see figure 4.2), we can see that the autocorrelation images of both the sinc kernel and the experimental data have long range interactions, but due to its symmetry it offers a high degree of order at long range which is not apparent on the column-like structure. On the other hand, the exponential and Gaussian kernels offer a quicker decay on the long range correlations which smooths the order dependence of the structure. This analysis suggests that the combination effects of these kernels achieve a similar structure to figure 4.1. This conclusion is what we expected from the cross-sections on the autocorrelation function in figure 4.2, since we need several functions to account for the structure qualities.

Another intrinsic difference between the structures generated with different kernels is their fractal behaviour. From the isotropic structures with 50% fill-factor we can easily see that the morphology of the sinc system is very homogeneous in shape

and size; the Gaussian structures offer more variation on the shape and size, but these variations are not very prominent. On the other hand, the exponential structures offer a wide range of shapes and sizes, going from similar morphologies of larger size to tinny ones. This fractal behaviour of structures generated with certain kernels have been studied by several authors (Bale and Schmidt, 1984; Roberts and Knackstedt, 1996).

- Exponential kernel:

$$K(\vec{r}) = \exp\left(-|\vec{r}|\right). \tag{4.6}$$

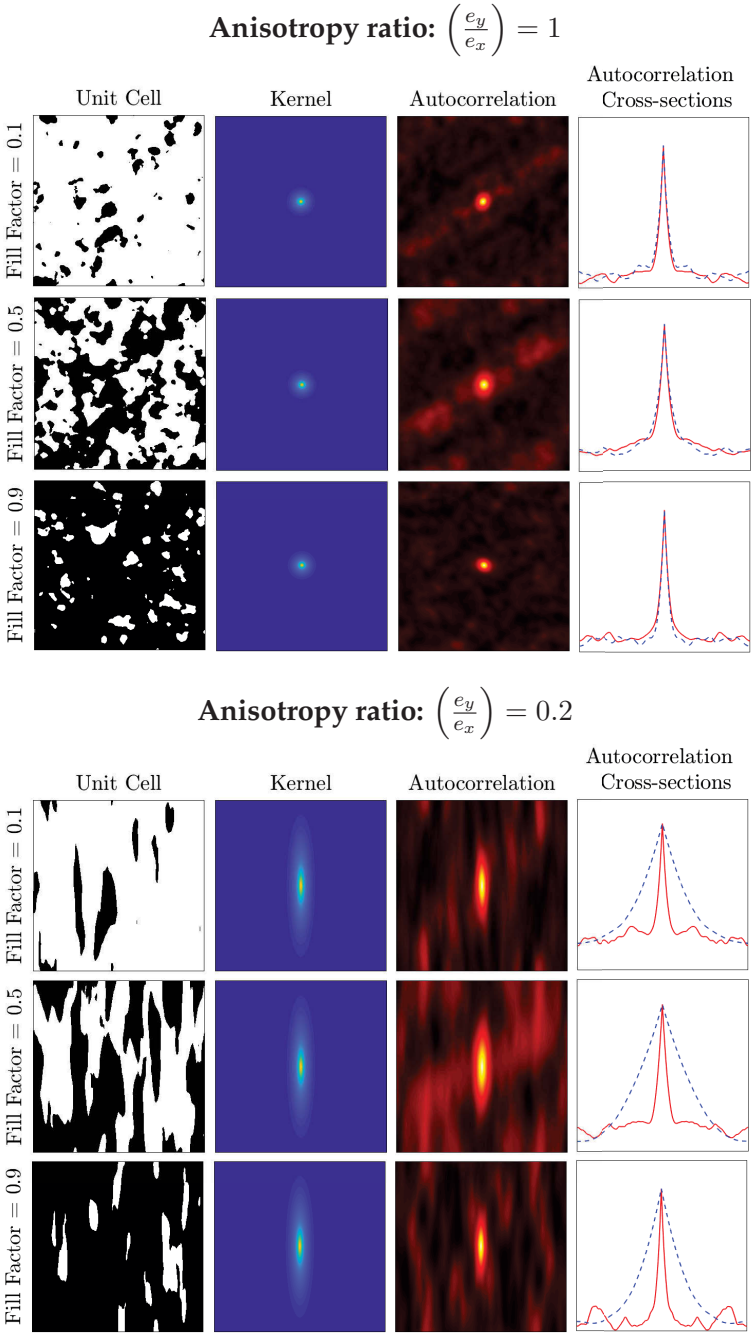

FIGURE 4.3: In this figure we can see the unit cell, kernel and autocorrelation functions for systems generated with an exponential kernel. The fill factors analysed represent 10%, 50% and 90% of occupancy and anisotropy ratios defined as the ratio of the edges of the unit cell, hence $e_y/e_x = 1$ is the isotropic case.

- Gaussian kernel:

$$K(\vec{r}) = \exp\left(-\vec{r}\cdot\vec{r}\right). \tag{4.7}$$

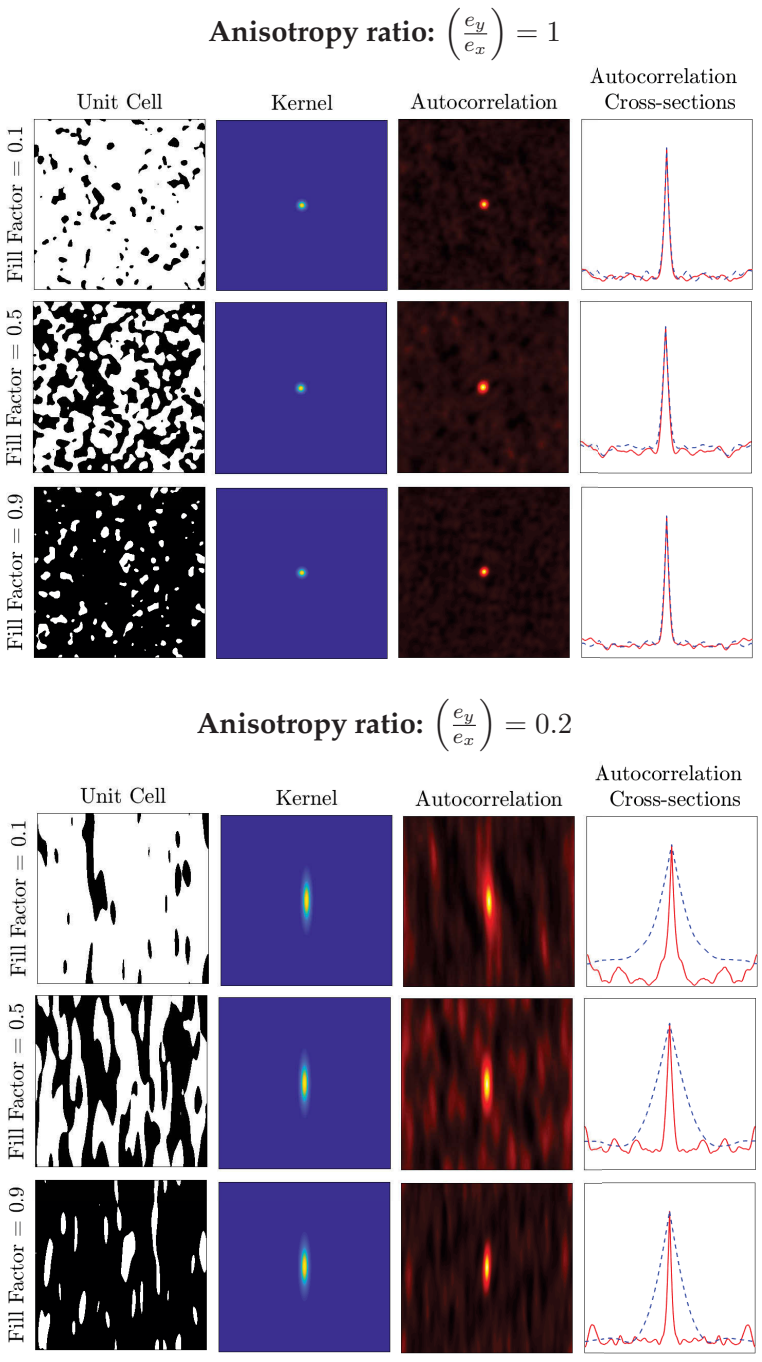

FIGURE 4.4: In this figure we can see the unit cell, kernel and autocorrelation functions for systems generated with a Gaussian kernel. The fill factors analysed represent 10%, 50% and 90% of occupancy and anisotropy ratios defined as the ratio of the edges of the unit cell, hence $e_y/e_x = 1$ is the isotropic case.

- Sinc kernel:

$$K(\vec{r}) = \frac{\sin(|\vec{r}|)}{|\vec{r}|}. \tag{4.8}$$

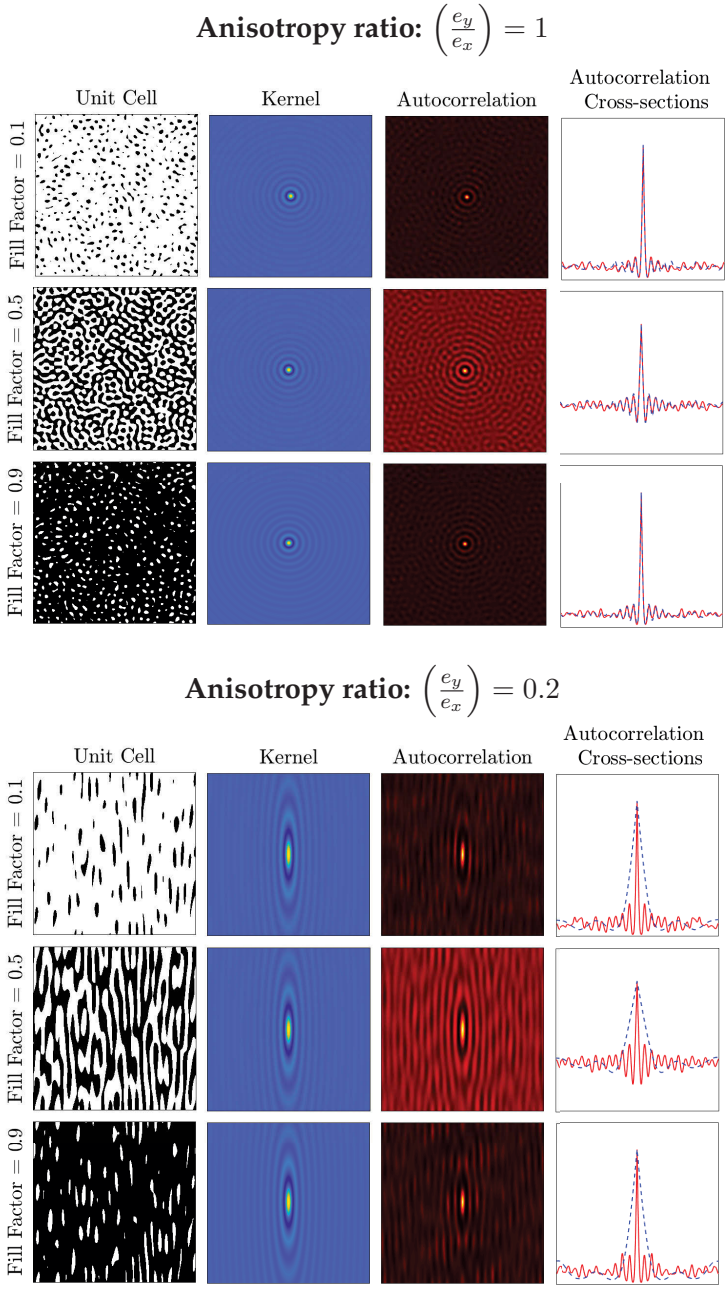

FIGURE 4.5: In this figure we can see the unit cell, kernel and autocorrelation functions for systems generated with a sinc kernel. The fill factors analysed represent 10%, 50% and 90% of occupancy and anisotropy ratios defined as the ratio of the edges of the unit cell, hence $e_y/e_x = 1$ is the isotropic case.

Notice that the position vector includes the decay length in each direction, $\vec{r} = (e_x \cdot x, e_y \cdot y)$.

4.2.1 Column-like Structure Generation

Using the *Level-Cut Gaussian Random Field Method* (LCGRF-method) we will find a kernel that creates structures that are statistically similar to the column-like structures that we are interested in. To do so we will use the information extracted from the autocorrelation function of the SEM image (figure 4.2); in order to be able to find a kernel similar to the anisotropy of these structures we will compare the SEM image correlation function cross-sections with the ones of systems created with known kernels. Thus, we will be able to decide which functions are better suited to define the kernel of our structures. In figure 4.6 is shown the autocorrelation function cross sections of the SEM image in the main directions of anisotropy, and these are compared with the equivalent cross-sections of structures generated using the LCGRF-method for different kernels. The left plot shows the "delta"-like autocorrelation function and the kernels that resemble it are the sinc function times the first or second derivative of a Gaussian. On the other side, right plot shows an autocorrelation function with a dip in the short range interactions; it can be seen that the sinc kernel is a reasonable approximation.

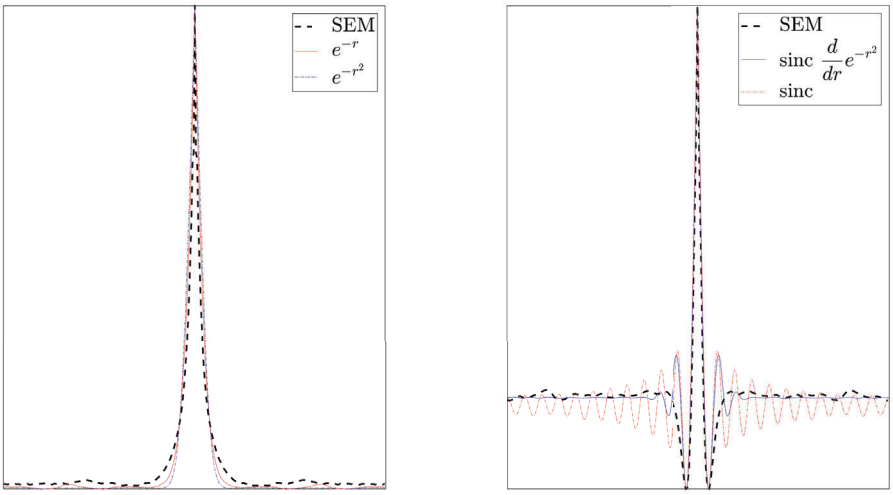

FIGURE 4.6: Autocorrelation cross-sections in the horizontal direction (left) and vertical direction (right) of the SEM image (fig. 4.2) compared with structures generated using different kernels. These autocorrelations are the result of an ensemble average of 100 realizations.

Looking at left image of figure 4.2, we can see how the exponential is better than the Gaussian in matching the curvature of the main peak of the cross-section, but the curvature at the base of the central peak can be the result of the behaviours in the two perpendicular directions, hence it is not clear that we can use it to discern between the Gaussian and exponential kernels. On the other hand, the cross-section that represents the ordered structure is better described by a combination of a sinc and the first derivative of a Gaussian. Hence, it seems natural to choose the combination of the sinc and the first derivative of a Gaussian, since this kernel includes the Gaussian trend appearing in the horizontal direction. Thus in this section we will define the following kernel to use in the *Level-Cut Gaussian Random Field Method* in order to obtain structures statistically similar to the column-like structure represented in figure 4.1.

$$K(\vec{r}) = \left(-2r_g \cdot e^{-r_g^2}\right) \cdot \frac{\sin(r_s)}{|r_s|}, \tag{4.9}$$

$$r_s = \sqrt{(x \cdot e_x)^2 + (y)^2}, \tag{4.10}$$

$$r_g = \sqrt{(x)^2 + (y \cdot e_y)^2}, \tag{4.11}$$

where $e_x = 1/3$ is the decay length of the *x-axis* for the sinc function, and $e_y = e_x/2 = 1/6$ the decay length of the derivative of the Gaussian in the *y-axis* that best match figure 4.2. The ratio between the anisotropies must be a half in order that the Gaussian aligns with the sinc function to create the big dip that it is present in the autocorrelation cross-section of the SEM image. In the horizontal cross-sections of figure 4.7 we can see that in the main peaks there is a bump that changes the decay of the peak, this characteristic can also be seen in horizontal cross-section of the SEM correlation function in figure 4.6.

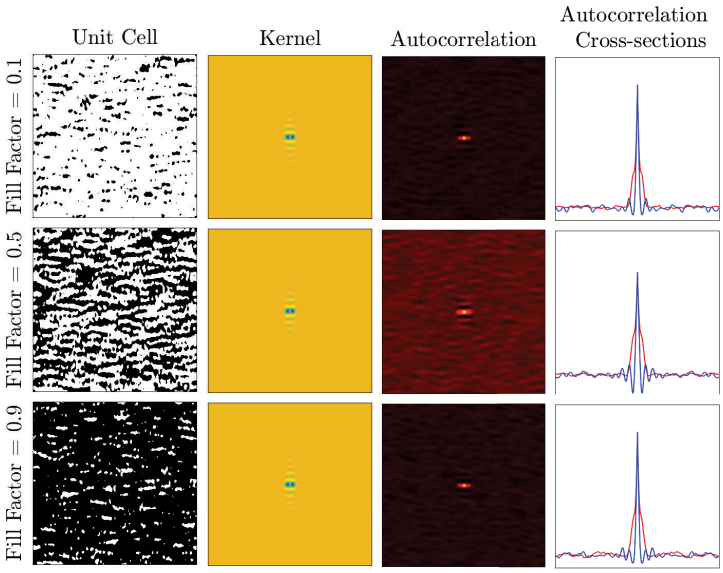

FIGURE 4.7: From right to left: Unit cell of a structure generated with the mixed kernel defined in equation 4.11, mixed kernel used, the autocorrelation function of the unit cell and the cross-sections of each autocorrelation function.

In figure 4.7 we can see the unit cell, kernel, and autocorrelation functions of structures generated using the kernel defined in 4.11 for fill factors equivalent to 10%, 50% and 90% filling. In particular we can see that using this kernel for structures with 0.5 fill factor the cross-sections of the autocorrelation function resembles the autocorrelation function of our experimental sample (fig. 4.2). Therefore, structures generated with this kernel can give us some insight on the column-like structures which have similar phase statistical distributions.

4.3 Fundamental Electrostatic Theory of Composites

To analyse the electrostatic properties of these structures we need to develop a theoretical framework that connects the dielectric function of the phases with the morphology of the macroscopic system. Hence, in this section, I will introduce a summarized version of the method that was first developed by Brown (1955) and later by Sen and S. Torquato (1989) and S. Torquato (1985) which provide a method to analyse the physical properties of two-phase media. Other relevant works include Hori and Yonezawa (1975a), Hori and Yonezawa (1975b), Rechtsman and S. Torquato (2008), Sen and S. Torquato (1988), S. Torquato (2009), and S. Torquato and Sen (1990) which attempted to give more insights on this method. Here I will also present an alternative method

to calculate the interaction dependence that we developed, which will allow us to obtain arbitrary orders of the series expansion of the anisotropic effective permittivity, micro-structural parameters and optimal bounds.

Throughout this chapter we are assuming two-phase composites in which the phases can be arranged in several ways. Thus we will use a generalised notation that does not assume any particular distribution or geometry, and separates permittivity and geometry. It is important to note that although we will focus on permittivity analysis, there are exact analogies with conductivity since mathematically the electrical and thermal equations are equivalent. There also exist similarities of this method to elastic and fluid transport, but these are more complicated and will not be discussed here (S. Torquato, 2002).

4.3.1 Implementation Outline

In this section we give the necessary steps to implement the series methodology that we have developed in detail in this chapter. The overall strategy is to use a sequence of series inversions on the iterated interaction equation to derive a series in permittivity contrast, where the coefficients are entirely determined by the geometry. These steps, will be followed:

(1) Generate the system structure (sec. 4.1 in particular we are using the method outlined in section 4.1.2).

(2) Create the occupancy function (eq. 4.12) and the interaction tensor (eq. 4.22).

(3) Obtain the equivalent tensors to $\hat{A}_n$ using the Monte Carlo approach (sec. 4.3.5).

  (3.1) Obtain the q_n coefficients (eq. 4.44).

  (3.2) Obtain the equivalent tensors $\mathbb{A}_n$ (eq. 4.53).

(4) Use the $\hat{A}_n$ ($\mathbb{A}_n$) tensors to find the $\hat{\xi}_n$ tensors (eq. 4.57).

(5) Use the $\hat{\xi}_n$ to find the $\hat{q}_n$ and $\hat{p}_n$ of the Padé approximant (eq. 4.60).

(6) Find the tensor coefficients of the permittivity series expansion $\hat{a}_n$ using $\hat{q}_n$ and $\hat{p}_n$ in equation 4.61.

Once the $\hat{a}_n$ tensor coefficients are found, the macroscopic permittivity is determined by the series expansion on the susceptibility in equation 4.54.

Bounds on $\hat{\epsilon}$ can be easily obtained using the $\hat{a}_n$ and following the directions of section 4.4; to obtain the leaf bounds an explanation is given in section 4.5, and the explicit algorithm is given in equation 4.75. The algorithm to obtain the micro-structural parameters of different order is given in equation 4.76, note that the extremal points of the leaf bounds are necessary for the normalization (eq. 4.71 and 4.73).

4.3.2 Geometry Specification

From the point of view of optics, these two-phase systems are characterized by the particle distribution of the phases with permittivity ϵ_1 and ϵ_2. Thus to generalize this problem is convenient to separate $\epsilon(\vec{r})$ into the permittivity of the phases and the geometry using an *indicator or occupancy function*. Therefore, first we will introduce the *indicator or occupancy function*, $\mathcal{I}_i(\vec{r})$, which selects particular phases depending on their position (eq. 4.12). Secondly, using $\mathcal{I}_i(\vec{r})$ we can define the position dependent dielectric function, $\epsilon(\vec{r})$ (eq. 4.13).

$$\mathcal{I}^{(i)}(\vec{r}) = \begin{cases} 1, & \vec{r} \in \Omega_i, \\ 0, & \vec{r} \notin \Omega_i, \end{cases} \tag{4.12}$$

where Ω_i define the regions of the structure with phase i.

$$\epsilon(\vec{r}) = \epsilon_j + (\epsilon_i - \epsilon_j)\mathcal{I}^{(i)}(\vec{r}), \quad i \neq j. \tag{4.13}$$

With these definitions in hand we can start solving the electrodynamic problem; using the reduced form of Maxwell's equations in terms of the electric field:

$$\nabla \times \nabla \times \vec{E}(\vec{r}) - \epsilon(\vec{r})\mu(\vec{r}) \left(\frac{\omega}{c}\right)^2 \vec{E}(\vec{r}) = 0, \tag{4.14}$$

where ω is the frequency of the incoming light and c is the speed of light. Also, we will assume non magnetic materials, i.e. the permeability will be a constant equal to one ($\mu(\vec{r}) \equiv 1$), and to simplify notation we will write equation 4.14 in terms of the wavenumber,

$$\begin{aligned} k(\vec{r}) &= k_0\sqrt{\epsilon(\vec{r})\mu} = k_0\sqrt{\epsilon(\vec{r})}, \\ k_i &= k_0\sqrt{\epsilon_i\mu} = k_0\sqrt{\epsilon_i}, \end{aligned} \tag{4.15}$$

In order to solve this differential equation we will use *Green's Functions*; to do so, we need to express eq. 4.14 as a non-homogeneous differential equation in the form of $\Delta g(x) = f(x)$, where $g(x)$ and $f(x)$ are two functions and Δ is an operator. Thus, we will add and subtract the term $k_i^2\vec{E}(\vec{r})$ in equation 4.14, where subscript i refers to a material with permittivity ϵ_i, i.e. one of the phases inside the composite,

$$\begin{aligned} \nabla \times \nabla \times \vec{E}(\vec{r}) - k(\vec{r})^2\vec{E}(\vec{r}) &= k_i^2\vec{E}(\vec{r}) - k_i^2\vec{E}(\vec{r}), \\ \nabla \times \nabla \times \vec{E}(\vec{r}) - k_i^2\vec{E}(\vec{r}) &= \left[k(\vec{r})^2 - k_i^2\right]\vec{E}(\vec{r}), \end{aligned} \tag{4.16}$$

The *Dyadic Green's function*, $\mathbb{G}(\vec{r},\vec{s})$, satisfies,

$$\nabla \times \nabla \times \mathbb{G}(\vec{r},\vec{s}) - k_i^2 \mathbb{G}(\vec{r},\vec{s}) = \delta(\vec{r}-\vec{s})\mathbb{I}, \tag{4.17}$$

where $\mathbb{I}$ is the identity matrix. Thus, the previous relation implies that the solution of equation 4.16 can be expressed in terms of $\mathbb{G}(\vec{r},\vec{s})$ as follows:

$$\vec{E}(\vec{r}) = \vec{E_0}(\vec{r}) + \int \mathbb{G}(\vec{r},\vec{s}) \left[k(\vec{r})^2 - k_i^2\right] \vec{E}(\vec{s}) d\vec{s}. \tag{4.18}$$

In order to simplify the problem we will apply the electrostatic approximation, i.e. we are assuming that the temporal dependence of the electric and magnetic field is small enough. This hypothesis holds if we work in a regime where the scale of the heterogeneities is very small compared to the wavelength, and where the material decay length is bigger than the structure scale allowing us to ignore the dynamic effects (Arnold, 2017; Chen et al., 2004; Lapine, Jelinek, and Marqués, 2012). Therefore, to take into account the interaction dependence between the phases we will use the steady Green function in spherical coordinates (static result) (Coilin, 1986; Rechtsman and S. Torquato, 2008; S. Torquato, 2002) which has a delta dependence term giving information on the cavity field, and the interaction tensor term which expresses the induced field:

$$\mathbb{G}(\vec{r},\vec{s}) = -\frac{\mathbb{I}}{dk_i^2}\delta(\vec{r}-\vec{s}) + \frac{e^{ik\rho}}{2\pi(d-1)k_i^2\rho^d}\left(d\cdot\hat{\rho}\hat{\rho}-\mathbb{I}\right), \tag{4.19}$$

where d is the dimension, $\rho \equiv |\vec{r}-\vec{s}|$, $\hat{\rho} \equiv \frac{\vec{r}-\vec{s}}{|\vec{r}-\vec{s}|}$, i is the imaginary number, and $\mathbb{I}$ is the unit tensor.

4.3.3 Iterative Series of the Polarization Field

In equation 4.18 we can split the dyadic Green's function in the delta term and the rest. Then, subtracting the delta term from the total electric field we can obtain the *Cavity Intensity Field*, also known as *Lorentz Field*, $\vec{F}$. Therefore using the definition of the delta function we find the Lorentz field in terms of the electric field,

$$\begin{aligned}\vec{F}(\vec{r}) &= \left[\frac{k(\vec{r})^2 - k_i^2}{k_i^2 d} + 1\right]\vec{E}(\vec{r}),\\ \vec{F}(\vec{r}) &= \left[\frac{\epsilon(\vec{r}) - \epsilon_i}{\epsilon_i d} + 1\right]\vec{E}(\vec{r}),\end{aligned} \tag{4.20}$$

so we can write equation 4.18 in terms of $\vec{F}$,

$$\vec{F}(\vec{r}) = \vec{E}_0(\vec{r}) + \int \tilde{\mathbb{G}}(\vec{r},\vec{s}) \left[k(\vec{r})^2 - k_i^2\right] \vec{E}(\vec{s}) d\vec{s}, \tag{4.21}$$

where $\tilde{\mathbb{G}}(\vec{r},\vec{s})$ is the Green's function without the delta term. In the electrostatic regime[4] $\tilde{\mathbb{G}}$ simplifies to,

$$\tilde{\mathbb{G}}(\vec{r},\vec{s}) = \frac{d\cdot\hat{\rho}\hat{\rho} - \mathbb{I}}{2\pi(d-1)k_i^2\rho^d}. \tag{4.22}$$

The *Green's Integral Equation* can be solved numerically, e.g. DDSCAT uses the *Discrete Dipole Approximation* (DDA) to solve this integral equation (Draine and Flatau, 1994; Draine and Flatau, 2008). On the other hand, with this method we also want to find the general effect that the micro-structure has on the optical transport. In order to obtain this connection we will obtain the effective permittivity by solving this equation iteratively as used by Brown and others.

In equation 4.18, the electric field at $\vec{r}$ is expressed in terms of the electric field in an arbitrary position $\vec{s}$. Thus, our goal is to iteratively use equation 4.18 in order to solve the integral equation. To have a more compact notation it is convenient to work in terms of the polarization field, defined as follows:

$$\vec{P}(\vec{r}) = \left[k(\vec{r})^2 - k_i^2\right] \vec{E}(\vec{r}), \tag{4.23}$$

thus we can combine equations 4.20 and 4.23 in order to express the Lorentz field in terms of the polarization field,

$$\vec{P}(\vec{r}) = k_i^2 d\cdot\beta_i(\vec{r})\cdot\vec{F}(\vec{r}), \tag{4.24}$$

$$\beta_i(\vec{r}) = \frac{k(\vec{r})^2 - k_i^2}{k(\vec{r})^2 + (d-1)k_i^2}. \tag{4.25}$$

In this chapter we are considering two-phase media, thus using the definition of the indicator phase function $\mathcal{I}^{(j)}(\vec{r})$ (eq. 4.12), we can write $\beta(\vec{r}) = \beta_{ji}\mathcal{I}^{(j)}(\vec{r})$ where we have defined

$$\beta_{ji} = \frac{k_j^2 - k_i^2}{k_j^2 + (d-1)k_i^2}, \tag{4.26}$$

using the definition of the wavenumber in equation 4.15, β_{ji} can be expressed in terms of the permittivity,

$$\beta_{ji} = \frac{\epsilon_j - \epsilon_i}{\epsilon_j + (d-1)\epsilon_i}, \tag{4.27}$$

[4]Further, we find convenient to work in a periodic system, with the lattice sum given by Abramowitz, Stegun, and McQuarrie (1966) and Arnold (2017).

and using this definition of β (eq. 4.27) we can express the mathematical relationship between the Lorentz field and the polarization field:

$$\vec{P}(\vec{r}) = \epsilon_i k_0^2 d \cdot \beta(\vec{r}) \cdot \vec{F}(\vec{r}), \tag{4.28}$$

Then, using equations 4.18 and 4.20 with the definition of the static polarization field (eq. 4.28) we can obtain a more compact integral equation,

$$\vec{P}(\vec{r}) = \epsilon_i k_0^2 d \beta_{ji} \mathcal{I}^{(j)}(\vec{r}) \cdot \left(\vec{E_0}(\vec{r}) + \int \tilde{\mathbb{G}}(\vec{r}, \vec{s}) \vec{P}(\vec{s}) d\vec{s} \right), \tag{4.29}$$

where as before, $\tilde{\mathbb{G}}(\vec{r}, \vec{s})$ is the Green's function without the delta term. Now, we can consider the polarization field at the position give by $\vec{s}$ due to a particle of the same phase at a position determined by $\vec{q}$,

$$\vec{P}(\vec{s}) = \epsilon_i k_0^2 d \beta_{ji} \mathcal{I}^{(j)}(\vec{s}) \cdot \left(\vec{E_0}(\vec{s}) + \int \tilde{\mathbb{G}}(\vec{s}, \vec{q}) \vec{P}(\vec{q}) d\vec{q} \right), \tag{4.30}$$

to simplify notation let's call $\kappa = \epsilon_i k_0^2 d$. Thus, inserting equation 4.30 into eq. 4.29 we can easily see how the expansion over all the specimens with the same phase will be,

$$\begin{aligned}
\vec{P}(\vec{r_1}) =& \kappa \beta_{ji} \mathcal{I}^{(j)}(\vec{r_1}) \cdot \left(\vec{E_0} + \int d\vec{r_2} \tilde{\mathbb{G}}(\vec{r_1}, \vec{r_2}) \left(\kappa \beta_{ji} \mathcal{I}^{(j)}(\vec{r_2}) \cdot \left(\vec{E_0} + \int d\vec{r_3} \tilde{\mathbb{G}}(\vec{r_2}, \vec{r_3})(\dots) \right) \right) \right), \\
=& \kappa \beta_{ji} \mathcal{I}_1^{(j)} \vec{E_0} + (\kappa \beta_{ji})^2 \int \mathcal{I}_1^{(j)} \mathcal{I}_2^{(j)} \tilde{\mathbb{G}}_{12} \cdot \vec{E_0} d\vec{r_2} \\
&+ (\kappa \beta_{ji})^3 \int d\vec{r_2} \int \mathcal{I}_1^{(j)} \mathcal{I}_2^{(j)} \mathcal{I}_3^{(j)} \tilde{\mathbb{G}}_{12} \cdot \tilde{\mathbb{G}}_{23} \cdot \vec{E_0} d\vec{r_3} + \dots,
\end{aligned} \tag{4.31}$$

where to simplify notation we have defined $\tilde{\mathbb{G}}_{ij} \equiv \tilde{\mathbb{G}}(\vec{r_i}, \vec{r_j})$ and $\mathcal{I}_n^{(j)} \equiv \mathcal{I}^{(j)}(\vec{r_n})$.

4.3.4 Effective Permittivity Series Expansion: β Powers

Averaging over the whole volume the indicator functions $\mathcal{I}_n^{(j)}$ become the *n-point probability function* introduced first by Brown (1955) as $p_{12\dots n}^{(n)}$ and later by S. Torquato (1986) as $S_n^{(i)}(\vec{r}_{12}, \vec{r}_{23}, \dots)$. In this thesis we will use a similar notation to the classical papers (Brown, 1955; Roberts and Teubner, 1995):

$$p_n^{(j)}(\vec{r}_1, \vec{r}_2, \dots \vec{r}_n) = < \prod_{k=1}^{n} \mathcal{I}^{(j)}(\vec{r}_k) >, \tag{4.32}$$

where the angular brackets denotes volume average.

Thus, using the *n-point probability functions*, we will average over the whole volume to use the averaged polarization field, $< \vec{P} >$, so equation 4.31 becomes:

$$< \vec{P} >=\kappa\beta_{ji}p_1^{(j)}\vec{E_0} + (\kappa\beta_{ji})^2 \int p_2^{(j)}(\vec{r}_1,\vec{r}_2)\tilde{\mathbb{G}}_{12}\cdot\vec{E_0}d\vec{r_2} + (\kappa\beta_{ji})^3 \int d\vec{r_2}\int p_3^{(j)}(\vec{r}_1,\vec{r}_2,\vec{r}_3)\tilde{\mathbb{G}}_{12}\cdot\tilde{\mathbb{G}}_{23}\cdot\vec{E_0}d\vec{r_3}+\dots. \tag{4.33}$$

As our goal is to find an operator acting on the averaged polarization field, the next step is to eliminate $\vec{E_0}(\vec{r})$ from previous equation. To do so, we will use iteratively the averaged version of eq. 4.29 so we can substitute $\vec{E_0}(\vec{r})$ for a term depending on $< \vec{P} >$.

$$\vec{E_0} =\frac{< \vec{P} >}{\kappa\beta_{ji}\phi_j} - \int \frac{p_2^{(j)}(\vec{r}_1,\vec{r}_2)}{\phi_j^2}\tilde{\mathbb{G}}_{12}\cdot < \vec{P} > d\vec{r_2} - (\kappa\beta_{ji})\int d\vec{r_2}\int\left[\frac{p_3^{(j)}(\vec{r}_1,\vec{r}_2,\vec{r}_3)}{\phi_j^2} - \frac{p_2^{(j)}(\vec{r}_1,\vec{r}_2)p_2^{(j)}(\vec{r}_2,\vec{r}_3)}{\phi_j^3}\right]\tilde{\mathbb{G}}_{12}\cdot\tilde{\mathbb{G}}_{23}\cdot < \vec{P} > d\vec{r_3}+\dots, \tag{4.34}$$

where ϕ_j is the volume fraction of phase j in the entire volume, which is by construction $p_1^{(j)}$. From previous equation (4.34), we can see that for isotropic systems the only term that has full geometry dependence is the second term in the RHS of equation 4.34, since the rest of integral terms vanish when their respective positions cluster, i.e $\vec{r_{ij}} \to 0$; or when they are farther apart, i.e $\vec{r_{ij}} \to \infty$, which means that all these terms vanish at the boundaries. Brown (1955) used this property to obtain a fully non localized equation. In this work we want to study the anisotropic effect (as was done in Sen and S. Torquato, 1989), thus, for reasons that will be clear in the next pages, we are interested in keeping the dependence on the two-point probability function as well. Hence, we will use the averaged value over the total volume of equation 4.21 to obtain the averaged Lorentz field in the left hand side of the equation,

$$< \vec{F} >=\frac{< \vec{P} >}{\kappa\beta_{ji}\phi_j} - \int\left[\frac{p_2^{(j)}(\vec{r}_1,\vec{r}_2)}{\phi_j^2} - \mathbb{I}\right]\tilde{\mathbb{G}}_{12}\cdot < \vec{P} > d\vec{r_2} - (\kappa\beta_{ji})\int d\vec{r_2}\int\left[\frac{p_3^{(j)}(\vec{r}_1,\vec{r}_2,\vec{r}_3)}{\phi_j^2} - \frac{p_2^{(j)}(\vec{r}_1,\vec{r}_2)p_2^{(j)}(\vec{r}_2,\vec{r}_3)}{\phi_j^3}\right] \times\tilde{\mathbb{G}}_{12}\cdot\tilde{\mathbb{G}}_{23}\cdot < \vec{P} > d\vec{r_3}+\dots, \tag{4.35}$$

where we have used the uncorrelated macroscopic behaviour on the *n-probability function* $\frac{p_2^{(j)}(\vec{r}_1,\vec{r}_2)}{\phi_j^2} \to 1$. Finally, to obtain an expression for the operator that applies on

$< \vec{P} >$, we will average equation 4.24 over the whole volume also averaging $\epsilon(\vec{r})$:

$$< \vec{P} > = \kappa < \beta_i >< \vec{F} >, \tag{4.36}$$

$$< \beta_i > = \left(\hat{\epsilon}_{\text{eff}} + (d-1)\epsilon_i \mathbb{I}\right)^{-1} \left(\hat{\epsilon}_{\text{eff}} - \epsilon_i \mathbb{I}\right). \tag{4.37}$$

Thus, combining equation 4.35 and 4.36 we can obtain a relation between the effective response of the whole volume depending on the physical and statistical properties of the phase that compose the whole.

$$(\beta_{ji}\phi_j)^2 < \beta_i >^{-1} = \phi_j \beta_{ji} - \sum_{n=2}^{\infty} \hat{A}_n^{(j)} \beta_{ji}^n, \tag{4.38}$$

where the tensor coefficients $\hat{A}_n^{(j)}$ were introduced by S. Torquato (1985) (see also Sen and S. Torquato, 1989; S. Torquato and Sen, 1990) which are equivalent to the tensors introduced by Brown (1955).

$$\hat{A}_2^{(j)} = \kappa \int \left[p_2^{(j)}(\vec{r}_1, \vec{r}_2) - \phi_j^2 \cdot \mathbb{I} \right] \tilde{\mathbb{G}}_{12} d\vec{r}_2 \tag{4.39}$$

$$\hat{A}_n^{(j)} = (-1)^n \phi_j^{2-n} (\kappa)^{n-1} \int \cdots \int d\vec{r}_2 d\vec{r}_3 \ldots d\vec{r}_n \tilde{\mathbb{G}}_{12} \cdot \tilde{\mathbb{G}}_{23} \cdots \tilde{\mathbb{G}}_{n-1n} \cdot C_n^{(j)}, \tag{4.40}$$

where $C_n^{(j)}$ is the determinant of the *n-probability function matrix* of phase j:

$$C_n^{(j)} = \begin{vmatrix} p_2^{(j)}(\vec{r}_1, \vec{r}_2) & p_1^{(j)}(\vec{r}_2) & 0 & \ldots & 0 \\ p_3^{(j)}(\vec{r}_1, \vec{r}_2, \vec{r}_3) & p_2^{(j)}(\vec{r}_2, \vec{r}_3) & p_1^{(j)}(\vec{r}_3) & \ldots & 0 \\ \vdots & \vdots & \vdots & \ldots & \vdots \\ p_{n-1}^{(j)}(\vec{r}_1, \vec{r}_2, \ldots, \vec{r}_{n-1}) & p_{n-2}^{(j)}(\vec{r}_2, \ldots, \vec{r}_{n-1}) & p_{n-3}^{(j)}(\vec{r}_3, \ldots, \vec{r}_{n-1}) & \ldots & p_1^{(j)}(\vec{r}_{n-1}) \\ p_n^{(j)}(\vec{r}_1, \vec{r}_2, \ldots, \vec{r}_n) & p_{n-1}^{(j)}(\vec{r}_2, \ldots, \vec{r}_n) & p_{n-2}^{(j)}(\vec{r}_3, \ldots, \vec{r}_n) & \ldots & p_2^{(j)}(\vec{r}_{n-1}, \vec{r}_n) \end{vmatrix}.$$

4.3.5 Monte Carlo Based Method to obtain the $\hat{A}_n$ Tensors

The multipoint probability functions (p_n) are the probabilistic functions that determine the morphology of a system. Nevertheless, high orders of these functions are very expensive to calculate directly. Some work has been done to calculate these functions for particular cases of systems made of fully penetrable spheres S. Torquato and Stell (1983) and fully impenetrable spheres J. Quintanilla (1999). However, to calculate orders higher than four of the multipoint probability functions p_n for arbitrary geometries is a problem that becomes significantly more difficult due to the increase on the integration dimension.

As presented in the previous section these functions are precisely what we need to determine the $\hat{A}_n$ tensors, which describe the power expansion of the dielectric function. Thus, for the reasons mentioned before, it is impractical to use the multipoint probability functions to define arbitrary systems. On the other hand, for a given structure we can express the $\hat{A}_n$ tensors as a successive application of the interaction tensor $\tilde{\mathbb{G}}$. In doing so we are able to extend the method beyond order 4^{th} which was the maximum order derived by Sen and S. Torquato (1989).

In this section we present a method to obtain the $\hat{A}_n$ relying on Monte Carlo average procedures. To implement this methodology we will start from the expression in equation 4.31, then instead of working with the general probability-point functions in terms of the volume integrals we will use Monte Carlo method to average the indicator functions. Thus averaging equation 4.31,

$$< \vec{P} >= \vec{E}_0 \kappa \beta_{ji} < \mathcal{I}^{(j)} > + \vec{E}_0 \left(\kappa \beta_{ji}\right)^2 < \mathcal{I}^{(j)} \cdot \tilde{\mathbb{G}} \cdot \mathcal{I}^{(j)} > \tag{4.41}$$

$$+ \vec{E}_0 \left(\kappa \beta_{ji}\right)^3 < \mathcal{I}^{(j)} \cdot \tilde{\mathbb{G}} \cdot \mathcal{I}^{(j)} \cdot \tilde{\mathbb{G}} \cdot \mathcal{I}^{(j)} > + \ldots, \tag{4.42}$$

this expression can be written as a series expansion on $(\kappa \beta_{ji})$,

$$< \vec{P} >= \vec{E}_0 \sum_{n=1}^{\infty} \underbrace{< \mathcal{I}^{(j)} \prod_{i=2}^{n} \left(\tilde{\mathbb{G}} \cdot \mathcal{I}^{(j)} \right) >}_{q_n} \left(\kappa \beta_{ji}\right)^n, \tag{4.43}$$

$$q_n = < \mathcal{I}^{(j)} \prod_{i=2}^{n} \left(\tilde{\mathbb{G}} \cdot \mathcal{I}^{(j)} \right) > . \tag{4.44}$$

As we did in previous section, to obtain an equivalent expression of equation 4.34, we need to invert the series expansion 4.43,

$$\vec{E}_0 = < \vec{P} > \left[\sum_{n=1}^{\infty} q_n \left(\kappa \beta_{ji}\right)^n \right]^{-1},$$

$$\vec{E}_0 = < \vec{P} > \sum_{n=-1}^{\infty} r_n \Omega^n, \tag{4.45}$$

where $\Omega \equiv \kappa \beta_{ji}$, and the r_n coefficients are determined by q_n. Note that the series on r_n must start at the order $n = -1$ otherwise the system is incompatible. Hence, the

algorithm to determine r_n is as follows:

$$\sum_{n=-1}^{\infty} r_n \Omega^n = \left[\sum_{m=1}^{\infty} q_m \Omega^m \right]^{-1},$$
$$\sum_{n=-1}^{\infty} r_n \Omega^n \cdot \sum_{m=1}^{\infty} q_m \Omega^m = \mathbb{I}, \tag{4.46}$$

equating powers of Ω the r_n coefficients are determined. For instance, the first three terms are defined as follows:

$$r_{-1} q_1 = \mathbb{I} \quad \Rightarrow \quad r_{-1} = q_1^{-1}, \tag{4.47}$$
$$r_0 q_1 + r_{-1} q_2 = \hat{0} \quad \Rightarrow \quad r_0 = -r_{-1} q_2 q_1^{-1}, \tag{4.48}$$
$$r_1 q_1 + r_0 q_2 + r_{-1} q_3 = \hat{0} \quad \Rightarrow \quad r_1 = -\left(r_0 q_2 + r_{-1} q_3 \right) q_1^{-1}. \tag{4.49}$$

Now we can write explicitly equation 4.45,

$$\vec{E}_0 = < \vec{P} > \frac{1}{\kappa \beta_{ji}} \underbrace{\hat{\phi}_j^{-1}}_{r_{-1}} - < \vec{P} > \underbrace{\phi_j^{-2} < \mathcal{I}^{(j)} \cdot \tilde{\mathbb{G}} \cdot \mathcal{I}^{(j)} >}_{r_0} - < \vec{P} > (\kappa \beta_{ji})$$
$$\times \underbrace{\phi_j^{-3} \left[\phi_j < \mathcal{I}^{(j)} \cdot \tilde{\mathbb{G}} \cdot \mathcal{I}^{(j)} \tilde{\mathbb{G}} \cdot \mathcal{I}^{(j)} > - < \mathcal{I}^{(j)} \cdot \tilde{\mathbb{G}} \cdot \mathcal{I}^{(j)} >< \mathcal{I}^{(j)} \cdot \tilde{\mathbb{G}} \cdot \mathcal{I}^{(j)} > \right]}_{r_1} - \ldots, \tag{4.50}$$

where $< \mathcal{I}^{(j)} > \equiv \phi_j \mathbb{I} \equiv \hat{\phi}_j$. By inspection it can be easily seen that previous equation (eq. 4.50) is the equivalent of equation 4.34. Therefore as we did before to eliminate the incident field dependence, we will use equation 4.21 using Monte Carlo average.

$$< \vec{F} > = < \vec{P} > \frac{1}{\kappa \beta_{ji}} \hat{\phi}_j^{-1} - < \vec{P} > \left[\phi_j^{-2} < \mathcal{I}^{(j)} \cdot \tilde{\mathbb{G}} \cdot \mathcal{I}^{(j)} > - < \tilde{\mathbb{G}} > \right] - < \vec{P} > (\kappa \beta_{ji})$$
$$\times \phi_j^{-3} \left[\phi_j < \mathcal{I}^{(j)} \cdot \tilde{\mathbb{G}} \cdot \mathcal{I}^{(j)} \tilde{\mathbb{G}} \cdot \mathcal{I}^{(j)} > - < \mathcal{I}^{(j)} \cdot \tilde{\mathbb{G}} \cdot \mathcal{I}^{(j)} >< \mathcal{I}^{(j)} \cdot \tilde{\mathbb{G}} \cdot \mathcal{I}^{(j)} > \right] - \ldots. \tag{4.51}$$

Finally, equation 4.51 is equivalent to equation 4.35, which leads to the same relationship for the macroscopic permittivity (eq. 4.38):

$$(\beta_{ji} \phi_j)^2 < \beta_i >^{-1} = \phi_j \beta_{ji} - \sum_{n=2}^{\infty} \mathbb{A}_n^{(j)} \beta_{ji}^n, \tag{4.52}$$

where the tensors $\mathbb{A}_n$ are the equivalent $\hat{A}_n$ tensors obtained using Monte Carlo ensemble averaging to account for probabilistic effects (instead of using S_n).

$$\mathbb{A}_2^{(j)} = \kappa \left(< \mathcal{I}^{(j)} \cdot \tilde{\mathbb{G}} \cdot \mathcal{I}^{(j)} > - \phi_j^2 < \tilde{\mathbb{G}} > \right) \tag{4.53a}$$

$$\mathbb{A}_n^{(j)} = (-1)^n \phi_j^{2-n} (\kappa)^{n-1} r_n^{(j)}, \tag{4.53b}$$

where $r_n^{(j)}$ can be expressed as a determinant of the q_n coefficients:

$$r_n^{(j)} = \begin{vmatrix} q_2 & q_1^{-1} & 0 & \dots & 0 \\ q_3 & q_2 & q_1^{-1} & \dots & 0 \\ \vdots & \vdots & \vdots & \dots & \vdots \\ q_{n-1} & q_{n-2} & q_{n-3} & \dots & q_1^{-1} \\ q_n & q_{n-1} & q_{n-2} & \dots & q_2^{-1} \end{vmatrix} ,$$

where to simplify notation we have omitted the phase dependence on $q_n^{(j)}$ (implicit on the definition of q_n in equation 4.43).

With this method we obtain an expression that it is very easy to implement numerically; nevertheless since we are using Monte Carlo, the trade off is that we need a very fine sampling to converge to the analytic results. As far as we know this methodology shown above (eq. 4.53) has not been used before. This framework also allows us to study high order bounds without much difficulty, thus we can obtain bounds never presented before for different 2D structured composites.

4.3.6 Effective Permittivity Series Expansion: Susceptibility Powers

In order to obtain a more suitable expression to analyse the effective permittivity, we will expand $\frac{\hat{\epsilon}_{\text{eff}}}{\epsilon_i}$ in a series expansion in powers of the susceptibility $\chi_{ij} = \frac{\epsilon_i - \epsilon_j}{\epsilon_j}$.

$$\frac{\hat{\epsilon}_{\text{eff}}}{\epsilon_i} = \sum_{n=0}^{\infty} \hat{a}_n \chi_{ji}^n, \tag{4.54}$$

We chose to denote the contrast χ for its similarity to the electric susceptibility (note that S. Torquato defines it as δ_{ij}; and in the work done by Engström (2005) the contrast is defined as z). In order to obtain the series expansion defined in equation 4.54 the tensors $\hat{a}_n$ must be determined. Thus equation 4.38 can be expanded in powers of the

susceptibility χ using $\beta_{ji} = \left(1 + \frac{d}{\chi_{ji}}\right)^{-1}$:

$$\frac{\phi_j^2}{d} < \beta_i >^{-1} = d^{-1}\beta_{ji}^{-2}\left[\phi_j\beta_{ji} - \sum_{n=2}^{\infty}\hat{A}_n^{(j)}\beta_{ji}^n\right]$$
$$\frac{\phi_j^2}{d} < \beta_i >^{-1} = d^{-1}\left(1+\frac{d}{\chi_{ji}}\right)^2\left[\phi_j\left(1+\frac{d}{\chi_{ji}}\right)^{-1} - \sum_{n=2}^{\infty}\hat{A}_n^{(j)}\left(1+\frac{d}{\chi_{ji}}\right)^{-n}\right], \quad (4.55)$$

thus expanding the RHS of equation 4.55 in powers of χ we obtain the following expression:

$$\frac{\phi_j^2}{d} < \beta_i >^{-1} = \underbrace{\chi_{ji}^{-2}\sum_{n=0}^{\infty}\hat{\xi}_n\chi_{ji}^n}_{\Xi}, \quad (4.56)$$

where

$$\hat{\xi}_0 = 0, \quad (4.57a)$$
$$\hat{\xi}_1 = \phi_j\mathbb{I}, \quad (4.57b)$$
$$\hat{\xi}_2 = d^{-1}\left(\phi_j\mathbb{I} - \hat{A}_2^{(j)}\right), \quad (4.57c)$$
$$\hat{\xi}_n = d^{1-n}\sum_{k=3}^{n}\binom{n-3}{k-3}(-1)^{n+k+1}\hat{A}_k^{(j)}, \qquad (\forall n > 2)\,. \quad (4.57d)$$

Finally, rearranging equation 4.56 and using the definition of $< \beta_i >^{-1}$ (eq. 4.37), we can obtain a series expansions of $\frac{\epsilon_{\text{eff}}}{\epsilon_j}$ with powers of χ,

$$\frac{\phi_j^2}{d}\left(\hat{\epsilon}_{\text{eff}} - \epsilon_i\mathbb{I}\right)^{-1}\left(\hat{\epsilon}_{\text{eff}} + (d-1)\epsilon_i\mathbb{I}\right) = \Xi \quad (4.58a)$$
$$\frac{\phi_j^2}{d}\left(\hat{\epsilon}_{\text{eff}} + (d-1)\epsilon_i\mathbb{I}\right) = \left(\hat{\epsilon}_{\text{eff}} - \epsilon_i\mathbb{I}\right)\Xi \quad (4.58b)$$
$$\frac{\hat{\epsilon}_{\text{eff}}}{\epsilon_i}\left(\Xi - \frac{\phi_j^2}{d}\mathbb{I}\right) = \frac{\phi_j^2}{d}(d-1)\mathbb{I} + \Xi. \quad (4.58c)$$

Finally, using equation 4.58c we can express the relation between the power series expansions in equations 4.54 and 4.56,

$$\sum_{n=0}\hat{a}_n\chi_{ji}^n \cdot \sum_{k=0}\hat{q}_k\chi_{ji}^k = \sum_{m=0}\hat{p}_m\chi_{ji}^m, \quad (4.59)$$

where,

$$\hat{q}_n = \hat{p}_n = \hat{\xi}_n, \qquad (\forall n \neq 2)\,, \tag{4.60a}$$

$$\hat{q}_2 = \hat{\xi}_2 - \frac{\phi_j^2}{d}\mathbb{I}, \tag{4.60b}$$

$$\hat{p}_2 = \hat{\xi}_2 + \frac{\phi_j^2}{d}(d-1)\mathbb{I}. \tag{4.60c}$$

Then, after truncation we can determine the tensors $\hat{a}_n$ that determine the series power expansion of $\hat{\epsilon}_{\text{eff}}/\epsilon_i$. Equating by powers of χ the tensors $\hat{a}_n$ are determined by $\hat{q}_n$ and $\hat{p}_n$ as follows:

$$\hat{a}_n = \sum_{m=n}^{N} \hat{p}_m \cdot \hat{q}_{m-n}^{-1}, \tag{4.61}$$

where N is the truncation order. From this point, in order to simplify notation we will define $\chi = \frac{\epsilon_1}{\epsilon_2} - 1$ with $\epsilon_2 > \epsilon_1$. Then with these definitions of $\hat{a}_n$ and Ξ we can express the relative effective permittivity as the following power series expansion:

$$\frac{\hat{\epsilon}_{\text{eff}}}{\epsilon_i} = \sum_{n=0}^{\infty} \hat{a}_n \chi^n. \tag{4.62}$$

4.4 Effective Permittivity Bounds and Padé Approximants

As has been shown in equation 4.38, it is possible to find a series expansion for the effective permittivity of the composite ϵ_{eff}. Nonetheless, the convergence of this series towards the analytic solution depends in great measure on the contrast between permittivities, thus for high contrast scenarios this series expansion can fail to determine the effective permittivity. On the other hand, Padé Approximant of the effective permittivity typically converges faster than the Taylor series expansion, and using numerical techniques we can obtain higher orders to achieve more accurate results. However, obtaining high orders of the analytical n-probability function for an arbitrary surface can be impractical. Being able to generate bounds on some effective physical properties (e.g. permittivity) is an interesting method to understand the physical limitations of the effective structure given certain statistical data of the composite.

In order to achieve those bounds first Hashin and Shtrikman (1962) and Wiener (1912) and then Hashin (1965) used the variational principle technique to obtain first order bounds of the effective magnetic permeability of a macroscopically homogeneous and isotropic multiphase material; later on Bergman (1976), Bergman (1978), Bergman (1979), and Bergman (1980) used Hashin and Shtrikman methodology to analyse particular cases of two-phase composites finding more optimal bounds. Golden

and Papanicolaou (1983), G. W. Milton (1981), G. W. Milton (1982), G. W. Milton (1987a), G. W. Milton (1987b), and G. W. Milton and Phan-Thien (1982) using the results presented by previous authors analysed the effective permittivity bounds of two-phase composites with complex dielectric function, in particular showing which structures lie on the extreme of the first order bounds.

S. Torquato (1985) (see also Sen and S. Torquato, 1989; S. Torquato, 1986; S. Torquato and Sen, 1990) used the *Padé Approximant Technique* on the power series expansion of χ_{ji} [5], with this methodology S. Torquato realised that upper and lower bounds of the effective conductivity tensor can be found using the Padé approximation on the series expansion in equation 4.54, expanding in powers of χ_{21} and χ_{12} respectively. Engström (2005) relied on Padé approximants to derive a more systematic methodology to obtain high order bounds using two distinct power series expansions, in this work he also presented a novel technique to obtain the extremal bounds on the $\hat{a}_n$ parameters: he gave explicit expressions till fourth order and obtained bound diagrams similar to the ones found by G. W. Milton (1981) and G. W. Milton (2002).

In this chapter we will give an explicit methodology to implement Engström technique in order to generate new optimal bounds which we call *Optimal "Leaf" Bounds* (sec. 4.5).

In this chapter we will denote the n order lower bounds as $\lfloor\cdot\rfloor_n$, and the n order upper bounds as $\lceil\cdot\rceil_n$. Using this notation the effective bounds used by Sen and S. Torquato (1989) are:

$$\text{Upper bounds}: \quad \begin{cases} \lceil\hat{\epsilon}\rceil_{2M} = \hat{\epsilon}(\chi_{21})_{[M,M]} \\ \lceil\hat{\epsilon}\rceil_{2M+1} = \hat{\epsilon}(\chi_{21})_{[M+1,M]} \end{cases} \tag{4.63a}$$

$$\text{Lower bounds}: \quad \begin{cases} \lfloor\hat{\epsilon}\rfloor_{2M} = \hat{\epsilon}(\chi_{12})_{[M,M]} \\ \lfloor\hat{\epsilon}\rfloor_{2M+1} = \hat{\epsilon}(\chi_{12})_{[M,M+1]} \end{cases} \tag{4.63b}$$

where we assume $\epsilon_2 > \epsilon_1$, and to simplify notation $\hat{\epsilon} \equiv \hat{\epsilon}_{\text{eff}}$.

Nonetheless, we find it more convenient to implement the methodology introduced by Engström (2005). In order to find the lower and upper bounds of $\hat{\epsilon}_{\text{eff}}$, Engström uses two series expansions: one for $\hat{\epsilon}_{\text{eff}}/\epsilon_2$, and one for $(\hat{\epsilon}_{\text{eff}}/\epsilon_1)^{-1}$, but in contrast to Sen and S. Torquato paper, both series are expanded in powers of $\chi = \epsilon_1/\epsilon_2 - 1$ (Engström denotes the contrast as z instead of χ). Then, using Padé approximation to each series expansion the bounds of the effective permittivity are found: Padé approximation of $\hat{f}(\chi)$ provides the upper bounds; lower bounds are obtained approximating $\hat{\zeta}(\chi)$.

[5] The Padé approximants are derived by expanding a power series expansion in a fraction of two distinct power series expansions, as this method uses a rational polynomial functions the resultant series offers better convergence than a simple Taylor series (or the original power series expansion).

$$\frac{\hat{\epsilon}_{\text{eff}}}{\epsilon_2} = \hat{f}(\chi), \qquad \text{where} \quad \hat{f}(\chi) = \sum_{n=0} \hat{a}_n \chi^n, \tag{4.64a}$$

$$\left(\frac{\hat{\epsilon}_{\text{eff}}}{\epsilon_1}\right)^{-1} = \hat{\zeta}(\chi), \qquad \text{where} \quad \hat{\zeta}(\chi) = \sum_{n=0} \hat{\alpha}_n \chi^n, \tag{4.64b}$$

where the tensors $\hat{a}_n$ have been defined previously in equation 4.61, and tensors $\hat{\alpha}_n$ can be determined relating the series expansions of $\hat{\epsilon}_{\text{eff}}/\epsilon_2$ and $(\hat{\epsilon}_{\text{eff}}/\epsilon_1)^{-1}$ (eq. 4.64) as follows:

$$\hat{\zeta}(\chi) = \left(\frac{\hat{\epsilon}_{\text{eff}}}{\epsilon_1}\right)^{-1} \cdot \frac{\epsilon_2}{\epsilon_2} = \left(\frac{\hat{\epsilon}_{\text{eff}}}{\epsilon_2}\right)^{-1} \cdot \frac{\epsilon_1}{\epsilon_2} = \hat{f}(\chi)^{-1} \cdot (\chi + 1) \tag{4.65a}$$

$$\hat{f}(\chi) \cdot \hat{\zeta}(\chi) = \hat{\zeta}(\chi) \cdot \hat{f}(\chi) = (\chi + 1)\,\mathbb{I}, \tag{4.65b}$$

note that as by construction $\hat{f}(\chi) \propto \hat{\zeta}(\chi)^{-1}$ thus $\hat{f}(\chi)$ and $\hat{\zeta}(\chi)$ commute. Using series expansion we can obtain a relation between the tensors $\hat{a}_n$ and $\hat{\alpha}_n$,

$$\sum_{k=0}^{N} \hat{a}_k \chi^k \cdot \sum_{n=0}^{N} \hat{\alpha}_n \chi^n = (\chi + 1)\,\mathbb{I} \tag{4.66a}$$

$$\sum_{k=0}^{N} \hat{a}_k \chi^k \cdot \left(\sum_{n=0}^{N-1} \hat{\alpha}_n \chi^n + \hat{\alpha}_N \chi^N\right) = (\chi + 1)\,\mathbb{I} \tag{4.66b}$$

$$\sum_{k=0}^{N} \hat{a}_k \chi^k \cdot \hat{\alpha}_N \chi^N = (\chi + 1)\,\mathbb{I} - \sum_{k=0}^{N} \hat{a}_k \chi^k \cdot \sum_{n=0}^{N-1} \hat{\alpha}_n \chi^n \tag{4.66c}$$

$$\sum_{k=0}^{N} \hat{a}_k \cdot \hat{\alpha}_N \chi^{N+k} = (\chi + 1)\,\mathbb{I} - \left[\sum_{k=0}^{N-1} \sum_{n=0}^{k} \hat{a}_{k-n} \cdot \hat{\alpha}_n \chi^k + \sum_{n=0}^{N-1} \hat{a}_{N-n} \cdot \hat{\alpha}_n \chi^N + \mathcal{O}(\chi^{N+1})\right]. \tag{4.66d}$$

Comparing by powers of χ the series expansion of the LHS and RHS of equation 4.66d we can establish relations between tensors $\hat{a}_n$ and $\hat{\alpha}_n$,

$$\mathbb{I} = \hat{a}_0 \cdot \hat{\alpha}_0, \tag{4.67a}$$

$$\mathbb{I} = \hat{a}_0 \cdot \hat{\alpha}_1 + \hat{a}_1 \cdot \hat{\alpha}_0, \tag{4.67b}$$

$$\hat{0} = \sum_{k=2}^{N-1} \sum_{n=0}^{k} \hat{a}_{k-n} \cdot \hat{\alpha}_n \chi^k, \tag{4.67c}$$

$$\hat{a}_0 \cdot \hat{\alpha}_N = -\sum_{n=0}^{N-1} \hat{a}_{N-n} \cdot \hat{\alpha}_n, \tag{4.67d}$$

using $\hat{a}_0 = \mathbb{I}$ and $\hat{a}_1 = \phi_1\mathbb{I}$ in equations 4.67, we can retrieve the relation introduced by Engström (2005):

$$\hat{\alpha}_0 = \mathbb{I}, \tag{4.68a}$$

$$\hat{\alpha}_1 = \phi_2\mathbb{I}, \tag{4.68b}$$

$$\hat{\alpha}_n = -\sum_{k=0}^{n-1} \hat{\alpha}_k \cdot \hat{a}_{n-k}, \qquad \forall n \geq 2, \tag{4.68c}$$

note that $\hat{f}(\chi)$ and $\hat{\zeta}(\chi)$ commute so $\hat{a}_n$ and $\hat{\alpha}_n$ commute as well. Therefore with both series determined the lower and upper bounds for $\hat{\epsilon}_{\text{eff}}$ can be summarized as follows,

$$\text{Upper bounds}: \quad \begin{cases} \lceil\hat{\epsilon}\rceil_{2M} = \hat{f}(\chi)_{[M,M]} \\ \lceil\hat{\epsilon}\rceil_{2M+1} = \hat{f}(\chi)_{[M+1,M]} \end{cases} \tag{4.69a}$$

$$\text{Lower bounds}: \quad \begin{cases} \lfloor\hat{\epsilon}\rfloor_{2M} = \hat{\zeta}(\chi)_{[M,M]} \\ \lfloor\hat{\epsilon}\rfloor_{2M+1} = \hat{\zeta}(\chi)_{[M+1,M]} \end{cases} \tag{4.69b}$$

The bounds derived by Sen and S. Torquato and Engström are equivalent in the limit of perfect sampling. However, these methods differ numerically which can be analysed by the *phase interchange identity* presented by Keller (1964); this identity which is also known as Keller theorem states that the macroscopic conductivity in a principal axis is inversely proportional to the macroscopic conductivity in the second principal axis (orthogonal to the first) in the reciprocal system (swapping the phases conductivities of the first system).

In the last century several authors analysed bounds of the optical properties. For instance, second-order lower bounds were derived by Hashin and Shtrikman (1962) for the three dimensional case, or equal to the bounds derived by Hashin (1965) for the two-dimensional case ($d = 2$) which is also equal to *Maxwell's effective media formula* (eq. 2.9). J. R. Willis (1977) explicitly derived the second order bounds for the anisotropic three dimensional case following the variational principal used by Hashin and Shtrikman (1962). He studied the particular case of orientated ellipsoids in a matrix and defined a tensor P that implicitly includes the *Depolarization Factor*. Sen and S. Torquato (1989) pointed out the relation between J. R. Willis P tensor and their A_2 tensor (eq. 4.70b), and also, they presented the relation between the depolarization

factor and the A_n (eq. 4.70c).

$$\hat{L} = \frac{1}{d}\left[\mathbb{I} - \frac{1}{\phi_1\phi_2}\hat{A}_2\right], \tag{4.70a}$$

$$\hat{P} = \frac{1}{\sigma_1}\hat{L}, \tag{4.70b}$$

$$\hat{L}_{ii} = \frac{a_1 a_2 a_3}{2}\int_0^\infty \frac{ds}{(s+a_i)\sqrt{(s+a_1^2)(s+a_2^2)(s+a_3^2)}}, \tag{4.70c}$$

where $\hat{A}_2$ has been defined previously in equation 4.40. Also, it is straight forward to see that equation 4.70c corresponds to the well known *depolarization factor tensor* (see eq. A.1)[6].

Also, S. Torquato (1985) pointed out that the fourth-order bounds obtained using Padé approximation are equivalent to the fourth-order bounds presented by G. W. Milton (1981) and G. W. Milton (1982).

In the next section we present a methodology to obtain optimal bounds on the permittivity at arbitrary order.

4.5 Optimal Leaf Bounds

Here we use Engström's observation that $\hat{a}_n$ are bounded to find tight leaf-shaped bounds on ϵ. These optimal bounds are achieved starting with the upper and lower bounds defined in equations 4.69. For instance, if we want to obtain the n$^{\text{th}}$ order *leaf bounds* we will use the definition of the (n+1)$^{\text{th}}$ order 'square' bounds considering the coefficients of the tensors $\hat{\alpha}_{n+1}$ and $\hat{a}_{n+1}$ parameters (to be able to use this approach these tensors must be diagonal, i.e. the optical and material axis must be aligned), hence to not get confused between the parametrized tensors and the tensors obtained by Padé approximants we will denote the parametrized $\hat{\alpha}_{n+1}$ and $\hat{a}_{n+1}$ as $\{\hat{\alpha}_{n+1}\}$ and $\{\hat{a}_{n+1}\}$. Thus we determine the bounds of $\hat{\alpha}_{n+1}$ and $\hat{a}_{n+1}$ imposing that the extreme of these bounds must coincide with the n$^{\text{th}}$ order bounds. This was proposed by Engström (2005) who found explicit expressions up to order four, we instead use simple numerical procedures to determine the bounds at any order. To do so, we find which values of $\{\hat{\alpha}_{n+1}\}$ and $\{\hat{a}_{n+1}\}$ satisfy:

$$\begin{cases} \lceil\hat{\epsilon}\rceil_n &= \lceil\hat{\epsilon}\rceil_{n+1}(\{\hat{a}_{n+1}\}), \\ \lfloor\hat{\epsilon}\rfloor_n &= \lceil\hat{\epsilon}\rceil_{n+1}(\{\hat{a}_{n+1}\}). \end{cases} \tag{4.71}$$

[6]Note Sen and S. Torquato use A_2^* instead of $\hat{L}$.

Thus, the values that satisfy equations 4.71 ($\lfloor \hat{a}_{n+1} \rfloor$ and $\lceil \hat{a}_{n+1} \rceil$) are the extreme values of the leaf bounds (the vertices of the leaf):

$$\lfloor \hat{a}_{n+1} \rfloor \leq \{\hat{a}_{n+1}\} \leq \lceil \hat{a}_{n+1} \rceil, \tag{4.72}$$

The limit values of $\hat{\alpha}_{n+1}$ can be found using equation 4.68 which defines $\hat{\alpha}$ in terms of $\hat{a}$; or by solving for the lower bounds the equivalent constraints defined before for the upper bounds,

$$\begin{cases} \lceil \hat{\epsilon} \rceil_n & = \lfloor \hat{\epsilon} \rfloor_{n+1}(\{\hat{\alpha}_{n+1}\}), \\ \lfloor \hat{\epsilon} \rfloor_n & = \lfloor \hat{\epsilon} \rfloor_{n+1}(\{\hat{\alpha}_{n+1}\}). \end{cases} \tag{4.73}$$

$$\lfloor \hat{\alpha}_{n+1} \rfloor \leq \{\hat{\alpha}_{n+1}\} \leq \lceil \hat{\alpha}_{n+1} \rceil. \tag{4.74}$$

The extremal points on equation 4.72, $\lfloor \hat{a}_n \rfloor$ and $\lceil \hat{a}_n \rceil$, satisfy equation 4.71; and equivalently the extremes on equation 4.74, $\lfloor \hat{\alpha}_n \rfloor$ and $\lceil \hat{\alpha}_n \rceil$, satisfy equations 4.73; it is important to note that these extreme values do not depend on the permittivity of the phases, they are completely determined by the structure. It is important to note that to obtain the two extreme parameters, in equations 4.72 and 4.74, we have to pay attention to which bounds are equated to each other, if not only one of the extreme values would be obtained. A useful extension of this idea is that both the upper and lower leaf bounds are bounded by a sequence of the previous order 'square' bounds.

4.5.1 Leaf Bounds Algorithm

In equations 4.72 and 4.74 we have the bounds that determine the possible values of the parameters $\{\hat{a}_{n+1}\}$ and $\{\hat{\alpha}_{n+1}\}$, this range of parameters will allow us to parametrize the edges of the leaf bounds. Hence, to obtain the leaf bounds of n$^{\text{th}}$ order, we need to obtain the extremal values of the effective permittivity, to do so we will use the series expansion defined in equation 4.64a till the $n+1$ term, where the value of the tensor coefficient of $n+1$ order will be determined by the parametrised tensors $\{\hat{a}_{n+1}\}$ for the upper bound and $\{\hat{\alpha}_{n+1}\}$ for the lower bound. Thus, we can obtain the edges of the leaf bounds of n$^{\text{th}}$ order using the following algorithm:

$$\lceil \hat{\epsilon} \rceil_n^{LB} = \epsilon_2 \left(\sum_{k=0}^{n} \hat{a}_k \chi^k + \{\hat{a}_{n+1}\} \chi^{n+1} \right), \tag{4.75a}$$

$$\left(\lfloor \hat{\epsilon} \rfloor_n^{LB} \right)^{-1} = \frac{1}{\epsilon_1} \left(\sum_{k=0}^{n} \hat{\alpha}_k \chi^k + \{\hat{\alpha}_{n+1}\} \chi^{n+1} \right), \tag{4.75b}$$

where to trace the bounds we need to sweep $\{\hat{a}_{n+1}\}$ and $\{\hat{\alpha}_{n+1}\}$ through the range defined in equations 4.72 and 4.74 respectively.

4.5.2 Bounds Analysis

In the following lines we will analyse the *optimal leaf bounds* and connect them with the literature. As our main aim is to analyse the effect on the anisotropy we express the bounds in the effective permittivity space. In figure 4.8 several order bounds are presented, starting from the less restrictive bounds (0^{th} order), we have the trivial box and well known bound called the *G-closure* by A. Cherkaev (2000); on the 1^{st} order bounds we have the *Wiener box* (Wiener, 1912) and the optimal bounds described by Lurie and A V Cherkaev (1984) and Murat and Tartar (1994); finally, on the 2^{nd} order bounds we have the Hashin and Shtrikman bounds (Hashin and Shtrikman, 1962): in their work they found the second order isotropic bounds which are the extremes of the second order leaf. In this section we will demonstrate bounds beyond these.

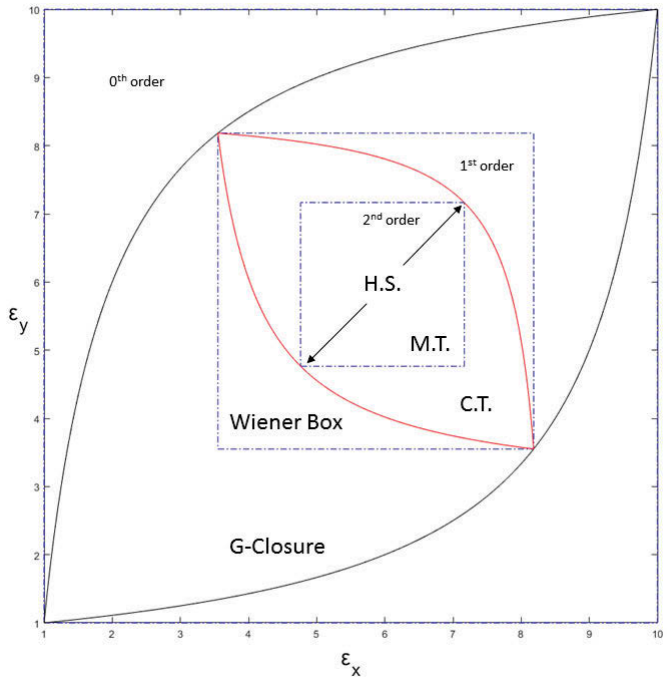

FIGURE 4.8: In this figure several known bounds in the literature can be seen (*C.T.* stands for Cherkaev and Tartar, *H.S.* for Hashin and Shtrikman, *M.T.* for Milton and Torquato). These bounds have been obtained for a two-phase 2D material described by a square unit cell with a circle, where the occupancy phase has $\epsilon_1 = 10$ and fill factor of 80%, and the background phase has $\epsilon_2 = 1$ and fill factor of 20%.

These bounds determine the possible values of the effective permittivity tensor given certain amount of information about the structure. Thus, zero order bounds assume no information, so they barely restrict the possible values of ϵ_{eff}. First order bounds only have information on the fill factor, thus the region bounded by them does

not have any information on the morphology of the structure, in figure 4.9 this can be appreciated.

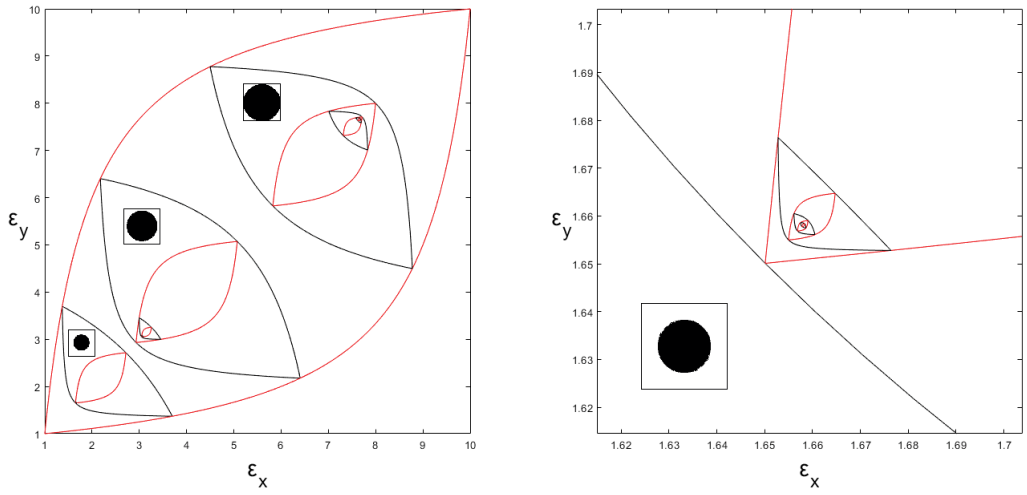

FIGURE 4.9: This leaf bounds plot shows the effect of increasing the fill factor in a two-phase system with $\epsilon_1 = 10$ and $\epsilon_2 = 1$. Left hand side picture shows three different fill factors of a sphere in a square unit cell, with fill factors of 30%, 60% and 90% moving from the left corner to the right corner of the big leaf (0^{th} order bounds) respectively. The right hand side picture is a zoom of the left corner of the leaf bound with 30% fill factor.

Second order bounds offer information on the anisotropy, which means that structures with different morphology but same fill factor and anisotropy will be bounded by the same 2^{nd} order bound. For instance, figure 4.10 show several orders of leaf bounds for two opposite ellipse and a circle unit cell for a fixed fill factor of 77%, thus as the three structures have the same fill factor they are bounded by the same 1^{st} order bound. Higher order bounds offer tighter closures since they are constrained by more information on a particular system. By the geometry of the leaf bounds it can easily be seen how in non-percolating or anisotropic situations high order bounds are less important, since the region of possible permittivity values that they enclose becomes very small. For instance, in figure 4.9 we have three isotropic unit cells with different fill factors, and on the cases further away from percolation higher order bounds get tighter very quickly; for example the fourth-fifth orders in the 60% and 90% fill factors, or even more extreme is the 30% fill factor case, where the third order bounds constrain under $\approx 5\%$ of the bulk permittivity. The quick tightening of high order bounds caused by the anisotropy can be seen in figure 4.10; it is obvious how the enclosure region of the fourth order bounds in the isotropic (middle case in the figure) is much bigger than the equivalent region of the anisotropic structures.

In these examples we are using a relative permittivity between the occupied and non-occupied cells of 10, i.e. $\epsilon_1 = 10$, $\epsilon_2 = 1$. Also, in the unit cell images the color refers to phase with higher permittivity (ϵ_1) and white refers to the phase with lower permittivity (ϵ_2).

In this work we have focused on structures with real permittivity values and high contrast (χ). The aim of this section is to present a methodology to obtain and analyse high order bounds, to do so, we have chosen structures that offer clear bounds and therefore they are nicer to analyse. We chose real values to focus on the anisotropy effects, i.e. the difference between the diagonal elements (ϵ_x, and ϵ_y) of the effective permittivity tensor ($\hat{\epsilon}$). Other authors have studied the bounds of structures with complex permittivity values (Engström, 2005; G. W. Milton, 2002), in those cases we would obtain two set of bounds like the one shown in figure 4.8: one in the real space, bounding the real part of the macroscopic permittivity; and another one in the imaginary space, bounding the imaginary part of $\hat{\epsilon}$.

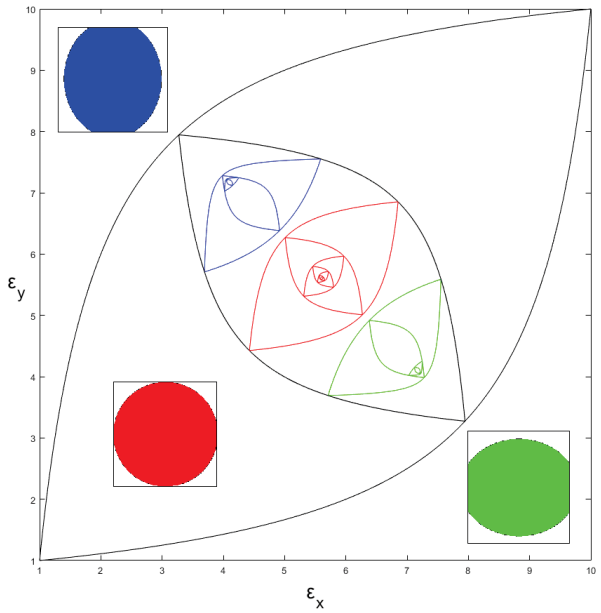

FIGURE 4.10: This figure show the relation between second order bounds and anisotropy for three different structures with fixed fill factor of 77%. In this figure, next to each leaf bound there is the unit cell that characterise each system (semi-axis ratio of the ellipses is 1.2).

4.5.3 Extremal Structures

The optimal leaf bounds specify the achievable values of the effective permittivity (macroscopic permittivity) that structures with the specified information can achieve, therefore it is interesting to know which kind of morphologies are the extremal ones,

in other words, which structures sit on the bounds. It is known that parallel plates can achieve extremal anisotropy, these structures "sit" on the vertices of the second order leaf bounds. Vigdergauz (1994) gave explicit smooth shapes that achieve lower H.S. bounds (isotropic structure) at any fill factor. Later on A. Cherkaev (2000) and A. V. Cherkaev and Gibiansky (1996) theorised that second order tensor plates can achieve the values on the bounds in between the extreme points (along the edge of the leaf), and Albin (2006) and Albin, A. Cherkaev, and Nesi (2007) showed that these extreme points are attainable. Zhou and Q. Li (2008) showed a methodology to obtain the structures that sit along the edge of these bounds for two and three phase composites, obtaining results in agreement with previous work done by Albin. In figure 4.11 we show which plate-like structures sit in each edge of the second order leaf bounds: The extremes of the leaf are achieved by parallel plates, where the orientation gives the anisotropy of the composite; on the other hand to achieve macroscopic permittivity values on the edges of the leaf second rank tensor structures must be used, in other word the equivalent structure to a parallel plate but with one extra dimension. Zhou and Q. Li studied in a detail manner this kind of structures and 'where they sit' in the bounds. From the results in the literature it can be theorised that the edge of higher order bounds can be achieved by parallel plate-like structures of high order. Nonetheless the characteristic length scale of the subdivisions in the parallel plate-like structures is constrained by the incident wavelength, so there is a scale limit on how many subdivisions we can make in order that these structures can keep their extremal behaviour.

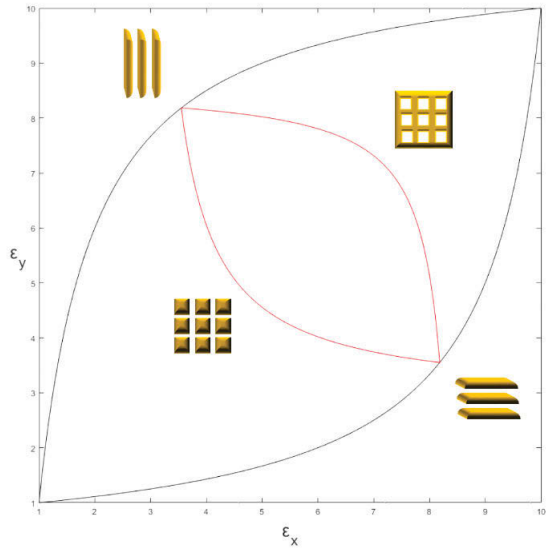

FIGURE 4.11: Diagram showing which kind of plate-like structures achieve the edge of the second order bounds.

4.6 Micro-Structural Parameters

These micro-structural parameters are values that, as their name suggests, give information of the physical distribution of the matter in the unit cell. The first and second order micro-structural parameters are the fill factor and depolarization factors respectively. Higher orders of these parameters have been studied for different structures by several authors: first, Brown (1955) expressed analytically the micro-structural parameter of third order for an heterogeneous isotropic composite in the 2D. Berryman and G. W. Milton (1988), G. W. Milton (1982), and G. W. Milton and Phan-Thien (1982) analysed the same micro-geometry parameter under the same hypothesis but for the three dimensional case, defining this parameter as ζ_1. Sen and S. Torquato (1989) and S. Torquato (1985) developed expressions for the micro-structural parameters of third and fourth order (ζ and γ respectively) for isotropic materials in an arbitrary dimension d, in terms of the micro-structural tensors $\hat{A}_n$, and an analytic expression for ζ for anisotropic cases.

Thus, as shown by S. Torquato, the micro-structural parameters can be determined for each phase normalizing the $\hat{A}_n$ tensors presented (eq. 4.40). Here we define these parameters for the anisotropic case and for arbitrary dimension using the extremal values of the *leaf bounds* presented in the previous section (4.5) to normalize the micro-structural tensors $\hat{A}_n$,

$$\hat{\Upsilon}_n^{(j)} = \frac{\hat{a}_n - \lfloor \hat{a}_n \rfloor}{\lceil \hat{a}_n \rceil - \lfloor \hat{a}_n \rfloor}, \tag{4.76}$$

where $\hat{\Upsilon}_n^{(j)}$ is the micro-structural tensor of n-order for phase j, $\hat{a}_n$ is the tensor of the series power expansion of order n (eq. 4.64a), and $\lceil \hat{a}_n \rceil$, $\lfloor \hat{a}_n \rfloor$ are the maximum and minimum values that $\hat{a}_n$ can achieve on the leaf bounds of n-order (see equations 4.71 and 4.72).

Some general characteristics of the micro-structural tensors in **2D** (Sen and S. Torquato, 1989) are:

(i) They are normalized,

$$0 \leq \hat{\Upsilon}_n^{(j)} \leq 1.$$

(ii) Odd orders:

- They give information on the structural relationship between the phases of the composite.
- The diagonal elements of the tensor are equal,

$$\left(\hat{\Upsilon}_n^{(j)}\right)_{ii} = \frac{Tr\left(\hat{\Upsilon}_n^{(j)}\right)}{d}, \quad i = 1, \ldots, d = 2.$$

(iii) Even orders:

- They give information on the structural anisotropy.
- The trace of the tensor is equal to one,

$$Tr\left(\hat{\Upsilon}_n^{(j)}\right) \equiv \sum_i^d \left(\hat{\Upsilon}_n^{(j)}\right)_{ii} = 1.$$

where $d = 2$ is the dimension. In the literature different notations have been used to describe each micro-structural parameter, the most common notation is:

$\hat{\Upsilon}_1^{(j)} \sim \hat{\phi}_j$ is the fill factor.

$\hat{\Upsilon}_2^{(j)} \sim \hat{L}$ is the depolarization tensor.

$\hat{\Upsilon}_3^{(j)} \sim \hat{\zeta}$ is associated with non-smoothness, e.g. sharp edges or percolation.

$\hat{\Upsilon}_4^{(j)} \sim \hat{\gamma}$ gives high order information on anisotropy. In the literature, with isotropy, $\hat{\gamma} \to 0$, but our micro-structural parameter $\hat{\Upsilon}_4 \to 1/2$

to simplify notation in this work we have chosen $\hat{\Upsilon}_n^{(j)}$ to define the micro-structural parameters of any order. Extending our earlier discussion of constraints, to maximise anisotropy the following relations are necessary:

$$\begin{cases} \hat{\Upsilon}_{odd} \sim \frac{1}{2}, \\ \left|\hat{\Upsilon}_{even} - \frac{1}{2}\right| \sim \frac{1}{2}, \end{cases} \tag{4.77}$$

with low order relations being more important, and the relative signs of the even terms are also significant.

Now that we have a general framework for classifying structures and determining their effective properties, we will parametrically generate interesting structures, particularly with an arbitrary degree of disorder and anisotropy.

4.7 Discussion

In this section we will analyse isotropic and anisotropic systems generated with the *Level-Cut Gaussian Random Field Method* explained in previous section (sec. 4.1.2); the bounds, micro-structural parameters and effective permittivity are calculated using the Monte Carlo framework introduced before with averaged results for 50 realizations. First, we will study the micro-structural parameters up to fourth order. Secondly, we will study the dependence of the macroscopic permittivity on the fill factor

for isotropic and anisotropic systems, also showing the convergence of the leaf bounds towards the effective permittivity at any fill factor.

4.7.1 Micro-Structural Parameters

The *micro-structural parameters* (MSP) give information on the system structure, it is known that the first order MSP is the fill factor, and the second order is the *depolarization tensor*. Nevertheless higher orders have not been discussed as much, since they are more difficult to calculate. Therefore we will present results for the third and fourth order MSP for structures generated with three different kernel functions: exponential, Gaussian and sinc functions. We will start on isotropic systems and then we will move to anisotropic structures.

As mentioned in section 4.6, micro-structural parameters of odd order give information related to the filling of the system, on the other hand even orders give information on the anisotropy. Another characteristic is that the diagonal elements of the odd orders are equal, and the diagonal elements on the even orders must add up to one (Sen and S. Torquato, 1989). Hence, as we are working in dimension two, we find it convenient to represent the odd orders with the mean of the diagonal elements; on the other hand, to plot even orders we will use the difference between the diagonal elements,

$$< \hat{\Upsilon}_{2n+1} > = \frac{\left(\hat{\Upsilon}_{2n+1}\right)_{11} + \left(\hat{\Upsilon}_{2n+1}\right)_{22}}{2}, \tag{4.78}$$

$$\Delta\hat{\Upsilon}_{2n} = \left(\hat{\Upsilon}_{2n}\right)_{22} - \left(\hat{\Upsilon}_{2n}\right)_{11}. \tag{4.79}$$

Isotropic Systems

Roberts and Teubner (1995) studied the third order MSP (ζ) for isotropic 3D GRF generated systems, in the following lines we study the different behaviour of $\hat{\Upsilon}_3$ (directly related to γ) and $\hat{\Upsilon}_4$ in isotropic systems changing the fill factor. In figures 4.12, 4.13 and 4.14 we can see the kind of structures that each kernel creates: it can be seen how exponential kernels create more agglomerated structures, on the other extreme sinc kernels create very dispersive systems, while Gaussian kernels have intermediate behaviour. From these pictures it can be deduced that, depending on which kind of composite is of interest, a particular kind of kernel would be more suitable than others to represent it. On the micro-structural parameters we can see that, as expected, for isotropic systems $\Delta\hat{\Upsilon}_4$ is close to zero and $< \hat{\Upsilon}_3 >$ is almost linear with the fill factor. Despite the similar results between the different kernel systems we can see some subtle differences:

- Exponential kernel:

$$K(\vec{r}) = \exp\left(-|\vec{r}|\right).$$

Among the kernels studied in this chapter, the exponentials have the smaller curvature in the decaying section of the main peak. This property affects the size distribution of the particles allowing a range of sizes to appear. Consequently phases tend to agglomerate in a rough manner (edgy clusters appear) and also make the phase-clusters more heterogeneously distributed. In figure 4.12 it can be seen how the trend line of $< \hat{\Upsilon}_3 >$ has a gradient smaller than one, which is the gradient of the trending line of $< \hat{\Upsilon}_1 >$. We hypothesise that third and fourth order give similar information to first and second order respectively, but constrained by some extra degree of connectivity of the phases. Thus, more homogeneous distributions will have similar $< \hat{\Upsilon}_1 >$ and $< \hat{\Upsilon}_3 >$. In 4.12 oscillations of $\Delta\hat{\Upsilon}_4$ around the zero can be seen. For an isotropic system we would expect it to be constant at zero, nevertheless because of noise around percolation it is possible that in one direction it percolates while it does not happen in the other, and hence oscillations appear around the zero. This is a numerical artefact which tells us that for exponential kernels the size of our unit cell was not big enough compared to the longer decay length of exponential. We can see that this effect is greatly reduced for the Gaussian (fig. 4.13) and sinc (fig. 4.14) kernel structures where their unit cell dimensions are the same as the exponential kernel structures presented here (fig. 4.12).

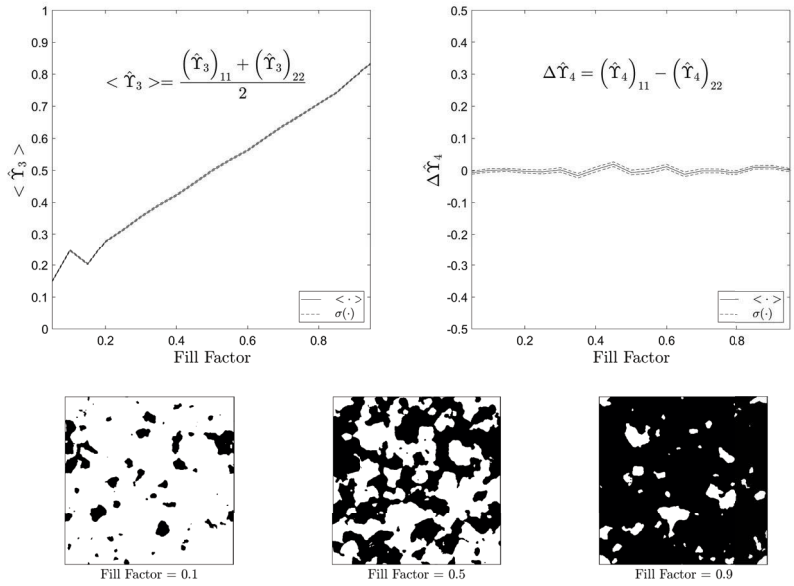

FIGURE 4.12: Study of isotropic systems generated with exponential kernels. On the left picture it is shown how the micro-structural parameter of third order ($\hat{\Upsilon}_3$) depends on the fill factor. On the right, it is shown the difference between the diagonal elements of the micro-structural parameter of fourth order ($\hat{\Upsilon}_4$) and its dependence on the fill factor. These results have been obtained averaging over 500 realizations.

- Gaussian kernel:

$$K(\vec{r}) = \exp\left(-\vec{r}\cdot\vec{r}\right).$$

Figure 4.13 shows $< \hat{\Upsilon}_3 >$ and $\Delta\hat{\Upsilon}_4$ of systems generated using Gaussian kernels, it can be seen that the slope of the trending line of the third order MSP is closer to one, since these structures are more dispersed than the exponentials. Also, $\Delta\hat{\Upsilon}_4 \sim 0$ at any fill factor which tells us that the relation between Gaussian decay length and unit cell size is adequate.

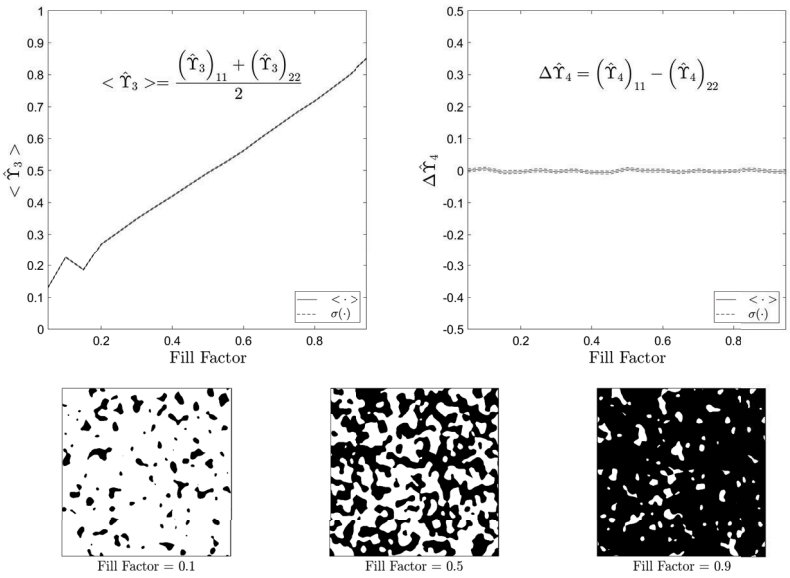

FIGURE 4.13: Study of isotropic systems generated with Gaussian kernels. On the left picture it is shown how the micro-structural parameter of third order ($\hat{\Upsilon}_3$) depends on the fill factor. On the right, it is shown the difference between the diagonal elements of the micro-structural parameter of fourth order ($\hat{\Upsilon}_4$) and its dependence on the fill factor. These results have been obtained averaging over 500 realizations.

- Sinc kernel:

$$K(\vec{r}) = \frac{\sin\left(|\vec{r}|\right)}{|\vec{r}|}.$$

Figure 4.14 shows $< \hat{\Upsilon}_3 >$ and $\Delta\hat{\Upsilon}_4$ of systems generated using sinc kernels, in this image it can be seen that the slope is very close to one, which agrees with the homogeneously dispersed structures that this kernel generates. The difference on the diagonal elements of the fourth order MSP of sinc kernel structure offer even less oscillations around zero than the Gaussian kernels, $\Delta\hat{\Upsilon}_4 \sim 0$ at any fill factor; which as before tells us that the relation between sinc decay length and unit cell size is adequate.

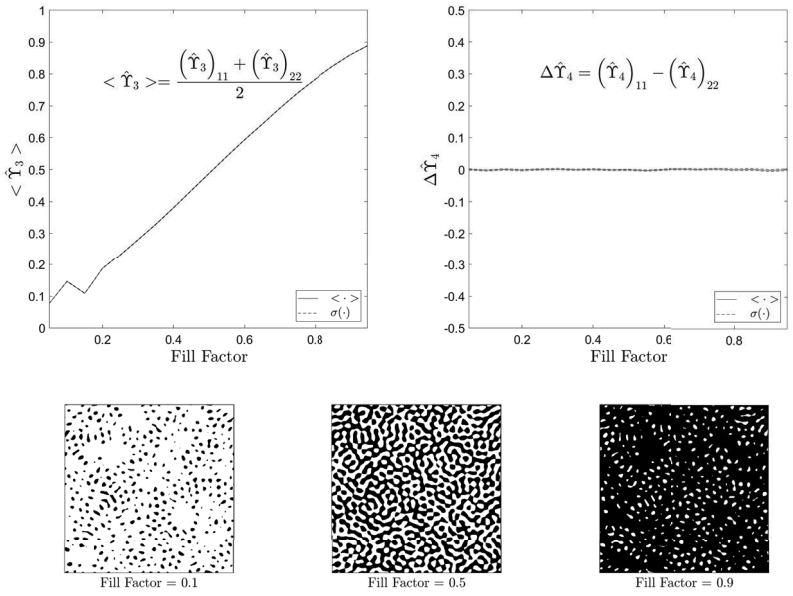

FIGURE 4.14: Study of isotropic systems generated with sinc kernels. On the left picture it is shown how the micro-structural parameter of third order ($\hat{\Upsilon}_3$) depends on the fill factor. On the right, it is shown the difference between the diagonal elements of the micro-structural parameter of fourth order ($\hat{\Upsilon}_4$) and its dependence on the fill factor. These results have been obtained averaging over 500 realizations.

At low fill factors, in figures 4.12, 4.13 and 4.14 we can see a sampling issue causing an odd "spike" on the micro-structural parameter of third order.

Anisotropic Systems

Results on MSP have been found for isotropic systems (Berryman and G. W. Milton, 1988; Brown, 1955; Roberts and Teubner, 1995; Sen and S. Torquato, 1989), but not as far as we know for anisotropic structures. The structures that we well present here are generated by the same kernel functions as before: exponential, Gaussian and sinc. To study only the anisotropic behaviour we will fix the fill factor at 0.5, and modify the ratio between the unit cell axis from 0.2 till 1. With this set up, doing the Monte Carlo ensemble average of enough realizations, the third order MSP should remain constant at $1/2$. To study the anisotropy we will analyse the second and fourth order MSP. In each case we will compare the 2^{nd} order to that of an ellipse with the same stretch factor.

- Exponential kernel:

  Figure 4.15 shows $\Delta\hat{\Upsilon}_2$ (difference on the diagonal elements of the depolarization factors) and $\Delta\hat{\Upsilon}_4$ depending on the anisotropy ratio. On the left, we see similarity by $\Delta\hat{\Upsilon}_2$ to the equivalent ellipsoid, some deviation probably due to insufficient sampling. On the other hand, the right picture shows the difference between the first and second diagonal elements of the fourth order MSP tensor; we can see a steep increase of $\Delta\hat{\Upsilon}_4$ for high anisotropy. This result tells us that for this kind of structure there exist many more connections through one direction than the other, this agrees with the unit cell for high anisotropy ratio ($e_y/e_x = 0.2$) where we can see strap like structures where in one main direction we have percolation, but not in the other.

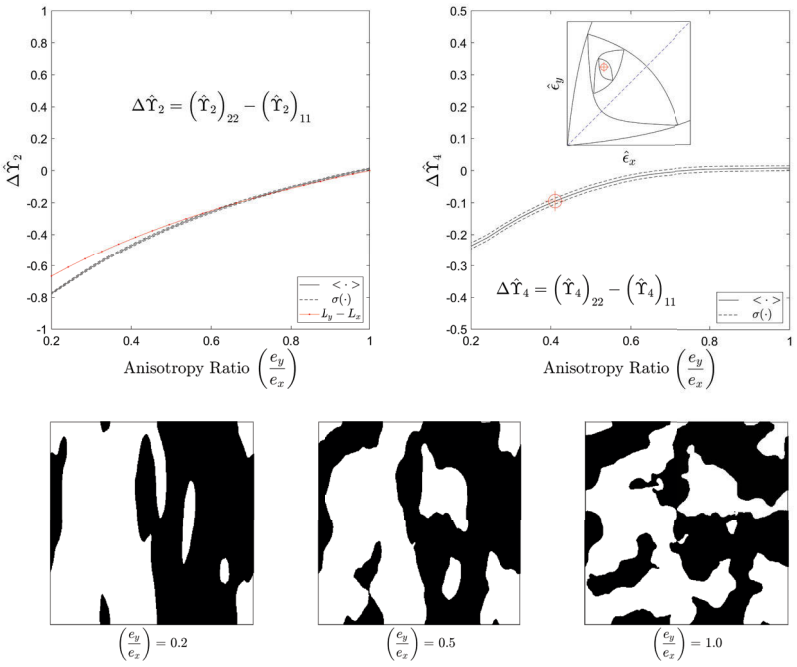

FIGURE 4.15: Study of anisotropic systems generated with exponential kernels. On the left picture the anisotropy dependence of the difference of the diagonal elements of the micro-structural parameter of second order ($\Delta\hat{\Upsilon}_2$) and the depolarization factors of an ellipsoid with same degree of anisotropy (red line with dots) are shown. On the right, we show the difference between the diagonal elements of the micro-structural parameter of fourth order ($\Delta\hat{\Upsilon}_4$) in terms of the anisotropy ratio; we put an inset image with the leaf bounds up to fourth order of a solution at certain anisotropy (marked by the red circle with a cross). These results have been obtained averaging over 500 realizations.

- Gaussian kernel:

  Figure 4.16 shows $\Delta\hat{\Upsilon}_2$ and $\Delta\hat{\Upsilon}_4$ depending on the anisotropy ratio (e_y/e_x). In the left image the depolarization factors difference in the horizontal and vertical directions are shown, it can be seen that unit cell structures with high anisotropy show strap-like clusters which are described by high difference of the depolarization factors. On the right side, the difference between the diagonal elements of the fourth order MSP tensor is shown; we can see an increase of $\Delta\hat{\Upsilon}_4$ smaller than for the exponential case. This fact is evidence that the difference in connectivity between the main directions of these structures is smaller than for the exponential ones. Comparing the exponential and Gaussian unit cells it can easily be seen how the exponential unit cell forms wider strap-like structures while the Gaussian ones creates systems where the strap-like structure is not as clearly defined. From the $\Delta\hat{\Upsilon}_4$ behaviour we can state that for the same degree of

anisotropy, Gaussian systems do not offer a big preference on connectivity along one or other main direction. $\Delta\hat{\Upsilon}_4$ is weakly positive for moderate anisotropy, and the sign appears to change at high anisotropy but it is possible that this is caused by a sampling issue.

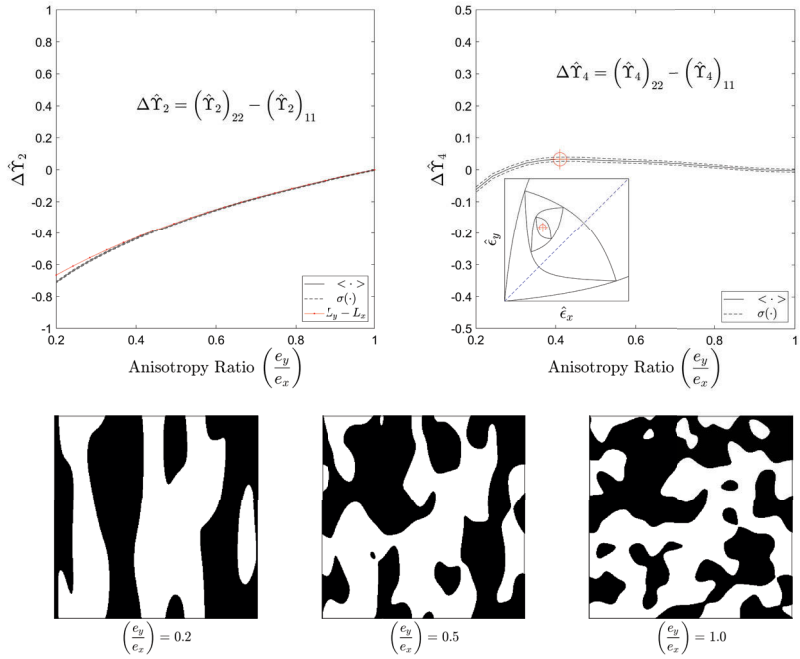

FIGURE 4.16: Study of anisotropic systems generated with Gaussian kernels. On the left picture we show the anisotropy dependence of the difference of the diagonal elements of the micro-structural parameter of second order ($\Delta\hat{\Upsilon}_2$) and the depolarization factors of an ellipsoid with same degree of anisotropy (red line with dots). On the right, the difference between the diagonal elements of the micro-structural parameter of fourth order ($\Delta\hat{\Upsilon}_4$) in terms of the anisotropy ratio is shown; we put an inset image with the leaf bounds up to fourth order of a solution at certain anisotropy (marked by the red circle with a cross). These results have been obtained averaging over 500 realizations.

- Sinc kernel:

  Finally in figure 4.17 we can see, as before, $\Delta\hat{\Upsilon}_2$ and $\Delta\hat{\Upsilon}_4$ depending on the anisotropy ratio (e_y/e_x). On the right side, the difference between the first and second diagonal element of the fourth order MSP tensor is shown. This is the most interesting case, because by the combination of its almost linear depolarization and its homogeneous dispersion (characteristic of sinc structures); $\Delta\hat{\Upsilon}_4$ provides more anisotropy than other kernels as seen in figure 4.17. Also note that

deviation of second order from the equivalent ellipsoid hints that the sampling is not completely sufficient in this case.

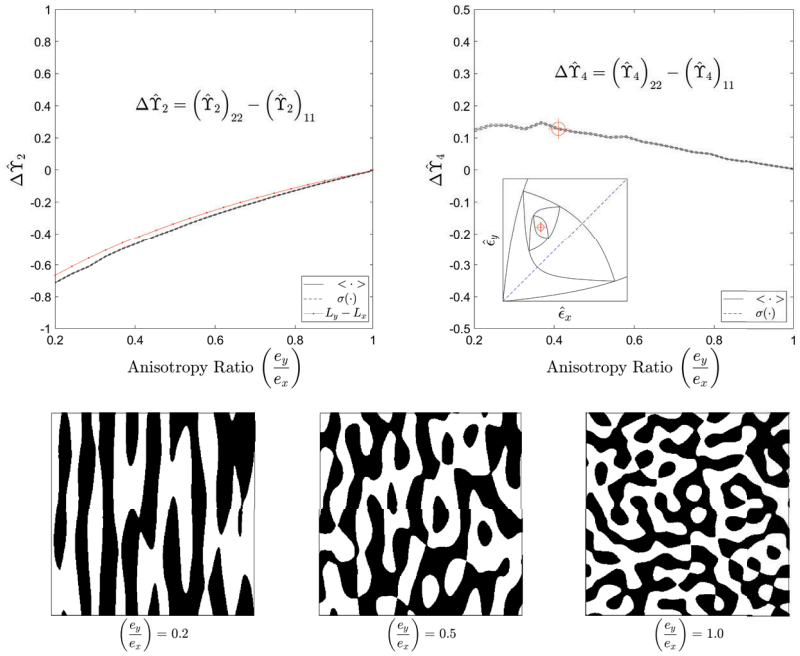

FIGURE 4.17: Study of anisotropic systems generated with sinc kernels. On the left picture we show the anisotropy dependence of the difference of the diagonal elements of the micro-structural parameter of second order ($\Delta\hat{\Upsilon}_2$) and the depolarization factors of an ellipsoid with same degree of anisotropy (red line with dots). On the right, the difference between the diagonal elements of the micro-structural parameter of fourth order ($\Delta\hat{\Upsilon}_4$) in terms of the anisotropy ratio is shown; we put an inset image with the leaf bounds up to fourth order of a solution at certain anisotropy (marked by the red circle with a cross). These results have been obtained averaging over 500 realizations.

In the three anisotropic studies, figures 4.15, 4.16 and 4.17 we have seen some similar behaviours: (i) The standard deviation was very small for every study, hence we can conclude that 500 realizations was enough to account for the Monte Carlo ensemble averaging working properly. (ii) The three studies on the depolarization factors ($\hat{\Upsilon}_2$) show that the depolarization factors of such structures are very similar to the depolarization of ellipsoids with same degree of anisotropy. We think that the small difference is caused by our choice of the unit cell size with respect to the decay length of each kernel, for a bigger unit cell we hypothesis that the depolarization factors should converge to the equivalent ones of an ellipsoid, at least for single kernels. (iii)

In general $\Delta\hat{\Upsilon}_2$ and $\Delta\hat{\Upsilon}_4$ have different signs which is consistent with the fact that depolarization factors are inversely related to the structure anisotropy[7].

Mixed Kernels

In this section we will study structures generated with a mixed kernel of Gaussian and sinc functions where each function can impart anisotropy to the structure,

$$\begin{aligned} K(\vec{r}) &= \frac{\sin(r_s)}{r_s} \cdot e^{-r_g^2}, \\ r_s &= \sqrt{(x)^2 + (y \cdot e_s)^2}, \\ r_g &= \sqrt{(x)^2 + (y \cdot e_g)^2}. \end{aligned} \tag{4.80}$$

To follow the same sequence that we used for single function kernels, we will analyse isotropic structures generated with the kernel defined in eq. 4.80 with $e_s = e_g = 1$. In figure 4.18 we can see the mean of the diagonal elements of the third order MSP and the difference in the diagonal elements of the fourth order MSP, we can see that the structure generated by this isotropic mixed kernel is very similar to the *sinc kernel* and therefore their MSP are also very similar.

[7] Appendix A presents a study on depolarization factors.

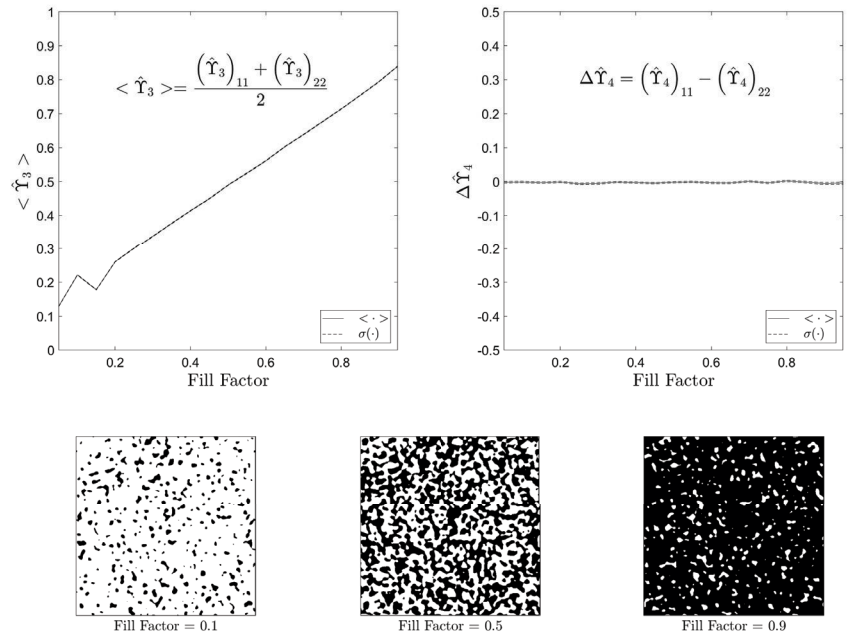

FIGURE 4.18: Third order (left) and fourth order (right) microstructural parameters of mixed kernel structures at different volume fill factors. Different unit cells that represent these structures for different fill factor values on the bottom of the figure. These results have been obtained averaging over 500 realizations.

To study the anisotropy of this mixed kernel we have to split the anisotropy contributions of each kernel function. In this work we will study structures generated by eq. 4.80 varying e_s and fixing $e_g = 1$. Figure 4.19 shows the MSP of structures generated by mixed kernels of a sinc and a Gaussian, where the anisotropy is created by the sinc part. We can see that $\hat{\Upsilon}_4$ has a very similar behaviour to the sinc kernel, but it acquires larger anisotropy, we can also see that the depolarization of such kernels strongly agrees with the depolarization of ellipsoids with the same anisotropy.

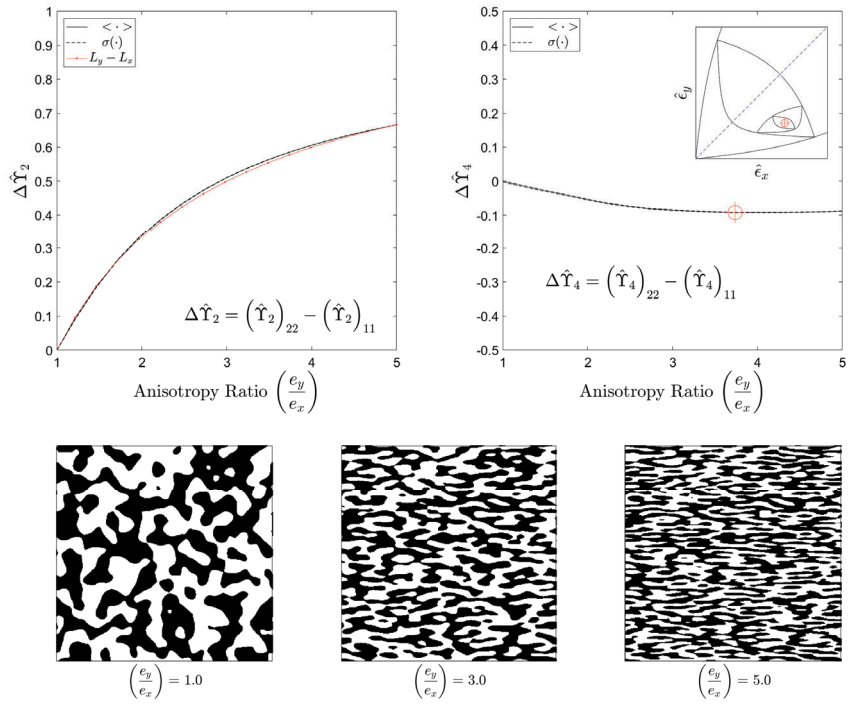

FIGURE 4.19: Simulated anisotropic parameters of a mixed kernel with the anisotropy in the sinc term. In the left plot we show the MSP of second order (black lines) and we compared it to the depolarization factors of an ellipsoid with same anisotropy ratios (red lines with dots). In the right image we show the MSP of fourth order and its dependence to the anisotropy, we put an inset plot to analyse the degree of anisotropy. Leaf bounds up to fourth order of a solution at certain anisotropy (marked by the red circle with a cross) are also shown. These results have been obtained averaging over 500 realizations.

The common results on the study of mixed kernel structures show: (i) As for single kernels, the standard deviation was very small for every study, hence we can conclude that 500 realizations was enough to account for Monte Carlo ensemble averaging working properly. (ii) The depolarization factors of these structures are very similar to the depolarization of ellipsoids with same degree of anisotropy.

4.7.2 Macroscopic Permittivity

In this section we will study the macroscopic permittivity of isotropic and anisotropic systems generated with different kernels, the constituent phases have permittivities of $\epsilon_1 = 10$ and $\epsilon_2 = 1$.

The optical properties of the single kernel structures with the same fill factor and anisotropy parameter have a very similar effective optical response (see figure 4.20),

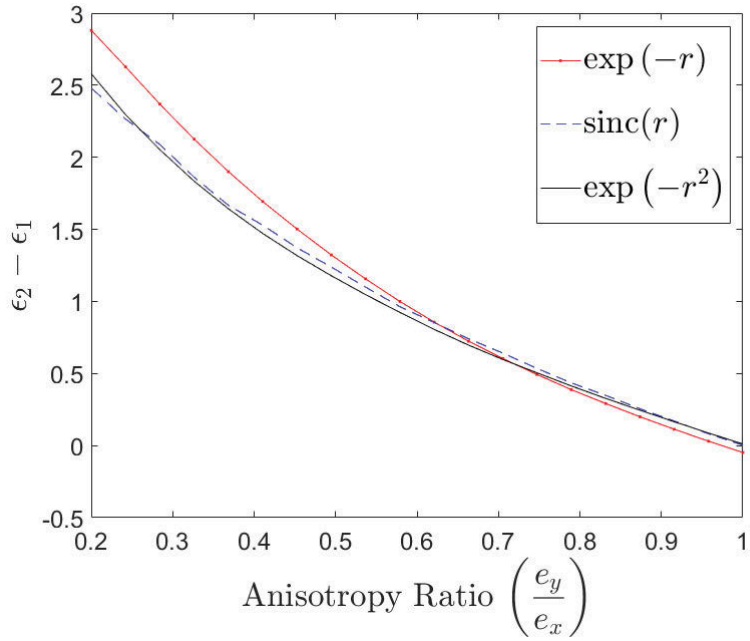

FIGURE 4.20: Comparison between the macroscopic permittivity anisotropy of structures generated with different kernels (sinc results are possibly inaccurate due to insufficient sampling).

Hence in this section we will use, as representative results, the effective permittivity of Gaussian kernel structures.

The results for the isotropic Gaussian (4.21) kernel show, as expected, that higher orders bounds tighten the solutions more, on the left images it can be appreciated that the difference between the diagonal elements on the effective permittivity is zero, i.e. they are isotropic structures. On the right images we can see that the numerical solution, $(\hat{\epsilon}_x, \hat{\epsilon}_y)$, moves linearly in the isotropic line, going from the minimum point of the first order bounds (0% fill factor) till the maximum value of the first order bounds (100% fill factor). These results are not very interesting, but they give sensible results which reinforces the validity of the model.

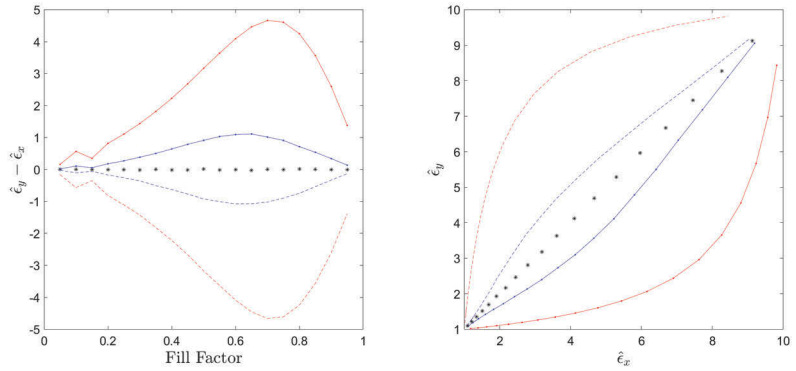

FIGURE 4.21: (Left) Difference between the diagonal terms of the effective permittivity depending on the fill factor bounded by the difference on the *leaf bounds*, $\lfloor\epsilon\rfloor - \lceil\epsilon\rceil$ and $\lceil\epsilon\rceil - \lfloor\epsilon\rfloor$. (Right) Numerical macroscopic permittivity values and their first and third order leaf bounds. Red represents first order leaf bounds, blue lines are third orders, and in black $*$ the numerical solutions for each value, (left) $\hat{\epsilon}_y - \hat{\epsilon}_x$, and (right) $(\hat{\epsilon}_x, \hat{\epsilon}_y)$.

Figure 4.22 shows that the bounds enclose the numerical solution as expected. On the right images I decided to plot the leaf bounds for each anisotropic structure to clarify the trend on the anisotropic direction (parallel to the "line of maximum anisotropy" $y = -x + \epsilon_1$).

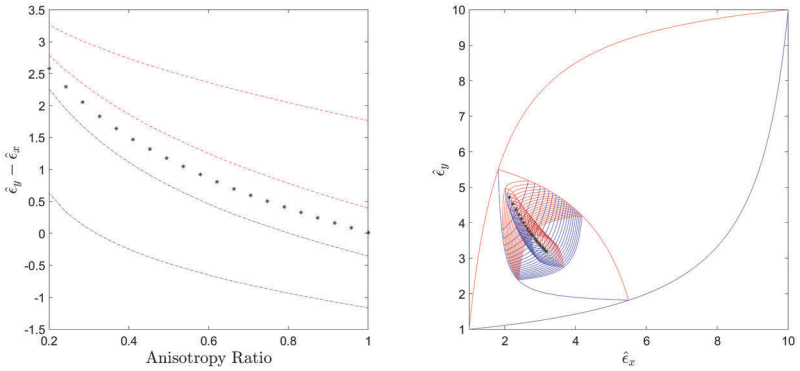

FIGURE 4.22: (Left) Difference between the diagonal terms of the effective permittivity depending on the anisotropy ratio at 50 % fill factor bounded by the difference on the *leaf bounds*, $\lfloor\epsilon\rfloor - \lceil\epsilon\rceil$ and $\lceil\epsilon\rceil - \lfloor\epsilon\rfloor$. (Right) Numerical macroscopic permittivity values and their first till fourth order leaf bounds. Red represents top leaf bounds $\lceil\epsilon\rceil$, while blue lines represents bottom leaf bounds $\lfloor\epsilon\rfloor$; and in black $*$ the numerical solutions for each value, (left) $\hat{\epsilon}_y - \hat{\epsilon}_x$, and (right) $(\hat{\epsilon}_x, \hat{\epsilon}_y)$.

Mixed Kernels

In figure 4.23 we show the isotropic effective permittivity of a mixed kernel, it can be seen that the results are identical to the macroscopic permittivity of a Gaussian single kernel (fig. 4.21) for the same reasons mentioned before.

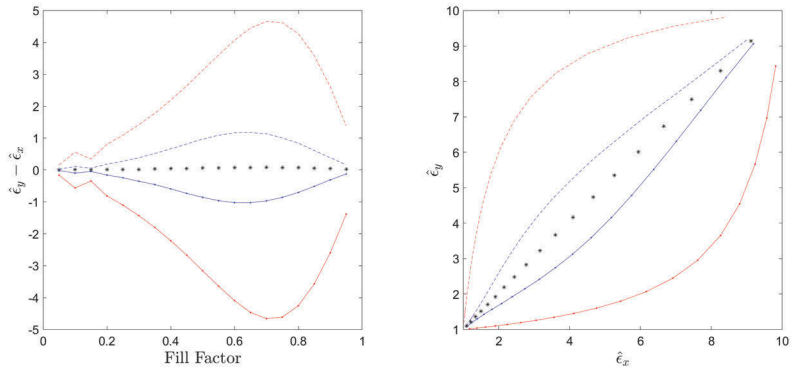

FIGURE 4.23: (Left) Difference between the diagonal terms of the effective permittivity depending on the fill factor bounded by the difference on the *leaf bounds*, $\lfloor\epsilon\rfloor - \lceil\epsilon\rceil$ and $\lceil\epsilon\rceil - \lfloor\epsilon\rfloor$. (Right) Numerical macroscopic permittivity values and their first and third order leaf bounds. Red represents first order leaf bounds, blue lines are third orders, and in black $*$ the numerical solutions for each value, (left) $\hat{\epsilon}_y - \hat{\epsilon}_x$, and (right) $(\hat{\epsilon}_x, \hat{\epsilon}_y)$.

To explicitly analyse the optical anisotropy created by mixed kernel structures, we will follow the same procedure that we used when we analysed the MSP of mixed kernels. We will study the anisotropy of the sinc part while the Gaussian remains isotropic. In figure 4.24 we can see the optical response of this kind of structures. As expected by the MSP results, the anisotropy of the macroscopic permittivity is weaker than the results seen for the sinc structures; this result is caused by the effect of the isotropic Gaussian term. This can be seen comparing the structures shown in figure 4.17 and 4.19, we see that single sinc kernels create structures that are more anisotropic than the mixed sinc-Gaussian kernels.

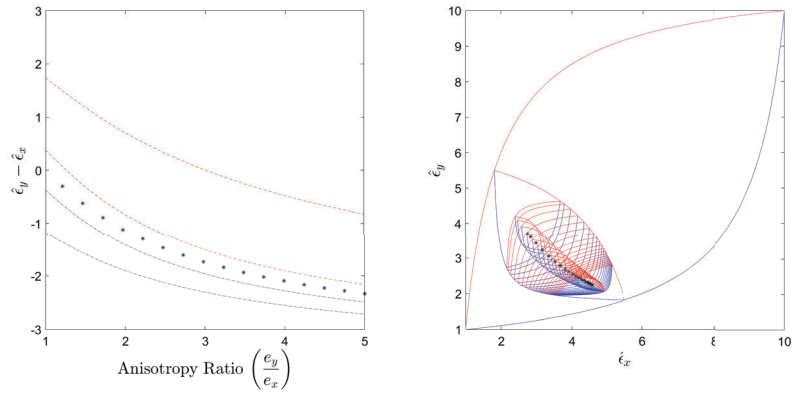

FIGURE 4.24: (Left) Difference between the diagonal terms of the effective permittivity depending on the anisotropy ratio at 50 % fill factor bounded by the difference on the *leaf bounds*, $\lfloor\epsilon\rfloor - \lceil\epsilon\rceil$ and $\lceil\epsilon\rceil - \lfloor\epsilon\rfloor$. (Right) Numerical macroscopic permittivity values and their first till fourth order leaf bounds. Red represents top leaf bounds $\lceil\epsilon\rceil$, while blue lines represents bottom leaf bounds $\lfloor\epsilon\rfloor$; and in black $*$ the numerical solutions for each value, (left) $\hat{\epsilon}_y - \hat{\epsilon}_x$, and (right) $(\hat{\epsilon}_x, \hat{\epsilon}_y)$.

4.8 Conclusion

In this chapter we, firstly, presented a method to generate structures similar to the experimental column-like systems obtained using physical vapour deposition techniques. To create such systems we obtained the autocorrelation cross-sections of the SEM image of our sample, and used them to create a mixed kernel function to filter a Gaussian random field, then this filtered signal was cut to obtain a structure with the desired fill factor.

Then, to analyse the optical response, we have presented a framework that starts with the work done by Brown (1955), Engström (2005), S. Torquato (1985), and S. Torquato and Sen (1990). Then, using this framework we presented a Monte Carlo based algorithm to calculate arbitrary high orders of the effective permittivity series expansion; also allowing us to study higher order micro-structural parameters and bounds. We have shown a methodology to obtain the *optimal leaf bounds* where their zeroth order coincides with the *G-closure*, and the first order coincides with the Cherkaev and Tartar bound (A. Cherkaev, 2000; Murat and Tartar, 1994).

We have studied structures with different degree of anisotropy which we generated using the *Level-Cut Gaussian Random Field Method* (sec. 4.1.2) for different kernels as noise filters. For these structures we have studied the micro-structural parameters of third and fourth order giving an explanation of the information that they give. Also, we have shown the convergence of the optimal leaf bounds to the numerical solution of the macroscopic permittivity at any fill factor and for any anisotropy level.

The micro-structural parameters of second order were compared with the depolarization factors of an ellipse with the same anisotropy stretching ratio. We have seen that they are very similar and that the small deviation present it is probably caused by an insufficient sampling, which will be addressed in future work. The comparison between the anisotropic MSP, even orders, showed that the difference between their diagonal terms have opposite signs, these results reinforces our hypothesis that the fourth order MSP describe the structural anisotropy ($\hat{\Upsilon}_4$) which is inversely related to the anisotropy on the depolarization ($\hat{\Upsilon}_2$).

We analyse the MSP and macroscopic permittivity of structures generated using a GRF method with a mixed kernel of a sinc and a Gaussian function (equation 4.80). We showed that the single kernels have similar optical response, while mixed kernels give a somewhat lower optical anisotropy. An interesting results is that the depolarization factors of any of the structures can be predicted by the depolarization factors of an ellipsoid with equivalent degree of anisotropy.

In this chapter we discussed 2D structures, nevertheless the methodology to obtain the series expansion of the effective permittivity can be used for 3D structures as well. On the other hand, the method to obtain the *leaf bounds* and the MSP would need to be generalized, since it is not straight forward which kind of surface would bound optimally the macroscopic permittivity, and how to normalize the micro-structural parameters for the three-dimensional case.

We can conclude that the new methodology presented here allows the study of high order parameters, improving the accuracy that previous methods provided in the literature. The main limitation of this method is that it requires large number of realizations to allow Monte Carlo ensemble averaging to be accurate. With this framework we can obtain the effective optical response of pseudo-random structures that are statistically equivalent to experimental samples.

Chapter 5

Heterogeneous Matrices

Heterogeneous media have been a topic of great interest in human history, since these kind of materials offer an interesting response when interacting with light. We can see examples of this in the colourful glasses of ancient buildings such as churches and palaces. From a scientific point of view, the understanding of these kind of effects in light stimulated the realisation of other useful properties of heterogeneous media. Therefore, because of their optical properties and the fact that these materials are ubiquitous in nature (e.g. clouds), there arose the need and the interest to study these scenarios in a more detailed manner. For instance, modelling the reflectance and transmittance of scattering media, such as natural particle suspensions which can be utilized for practical effect in artificial materials like coatings and paints has been an active area of research in the last decade (Baneshi et al., 2012; Chai et al., 2017; Gonome et al., 2014; G. B. Smith and Granqvist, 2010). The random distribution of the scattering elements makes it impossible to solve these systems analytically; instead Monte Carlo methods are often used requiring a long computational time to obtain accurate results. Also, the radiative transfer problem for diffused light has been presented in the framework of Chandrasekhar's equation (Chandrasekhar, 1960) solving the problem for different incident angles which give accurate solutions for diffused light (Barman, 2000; M. Elias and G. Elias, 2002; Mady Elias and Georges Elias, 2004; Siewert, 2000). On the other hand, methods based on flux balance equations usually present a much faster way to obtain results (Dombrovsky, Randrianalisoa, and Baillis, 2006; Hébert and Becker, 2008; Maheu, Letoulouzan, and Gouesbet, 1984); two-flux models assume fully diffused fluxes propagating in opposite directions, among those there is the well known work developed by Kubelka (1948) and Kubelka (1954), which has been intensively used and researched by different authors, e.g. Fukshansky and Kazarinova (1980), Molenaar, Bosch, and Zijp (1999), and W. E. Vargas and G. A. Niklasson (1997a). In particular, the four-flux method has been used broadly for its easy applicability and the good balance that it offers between complexity and accuracy (Laaksonen et al., 2014; Maheu, Letoulouzan, and Gouesbet, 1984; W. Vargas and G. Niklasson, 1997; W. E. Vargas, 2000), consequently several developments have

been made in its formulation and applicability (Rozé, Girasole, Grehan, et al., 2001; Rozé, Girasole, and Tafforin, 2001; W. E. Vargas, 1998), nevertheless implementations presented to this point still have a number of limitations.

In the last decade, due to the consequences of pollution and climate change, today's society has increased its interest in improving energy efficiency and in developing green technologies. This scenario is also motivation of this chapter, since as discussed in the introduction (ch. 1): scattering composites such as paints are an important technology for mitigating the overheating effects on building roofs in moderate and hot climates. Improving the reflectance of those paints can reduce considerably the temperature of those buildings and surroundings, saving the energy that would be used to cool down these structures. Moreover, some aspects are not well understood, due to the fact that classical models do not consider absorbing matrices (binder in paints), despite common binders having strong absorption bands in the NIR region. Thus, overlooking this fact usually results in obtaining misleading results when simulating and analysing paints.

In this chapter, most of which is based on my publication (Marc A. Gali et al., 2017), we will:

- Explain the *Classical Four-Flux method*.
- Present the *Generalized Four-Flux method*, which can deal with the following improvements:
  - Absorbing matrices.
  - Different kind of scatterers, considering different size and composition.
  - A systematic way to implement particle size distributions.
  - A clear and specific methodology to determine model parameters
  - A convenient matrix formalism to implement multilayer matrices in our model.
- Present the final results, which show the agreement between experimental and simulated data.

5.0.1 Classical Four-Flux Method

The keystone of the four-flux method is solving a system of four energy balance equations. These equations depend on several parameters that define how the light is scattered, absorbed and therefore propagated through the medium. In the following pages the classical method will be presented.

The method used in this chapter belongs to the family of N-flux methods, where the N represents the number of balance equations that define the problem: basically

at larger N more accurate results are obtained, but at same time, the problem becomes more complex and more computational time is needed in order to solve it. In the literature (Beasley, Atkins, and Billmeyer, 1967; Mudgett and Richards, 1971) it has been shown that for N = 4 accurate results are obtained more efficiently than higher N. As sketched in figure 5.1, in the four-flux method four differential equations are presented which represent two collimated and two diffused incoming fluxes, one of each for each side of the 'slab' or matrix.

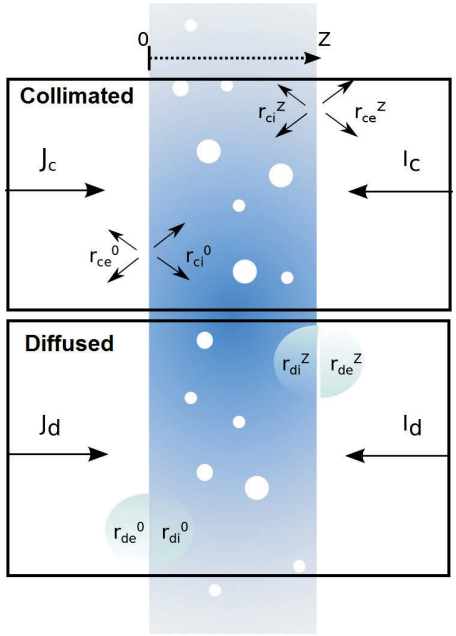

FIGURE 5.1: Diagram of the four-fluxes and interface parameters used in the four-flux model. $J_{c,d}$, $I_{c,d}$ are the incident collimated and diffused fluxes at each side of the slab; Z is the slab thickness; r_i^j are the reflection coefficients at the interfaces; superscript 0 refers to the side where J fluxes enter the slab, while Z refers to the side where I fluxes are incident; subscript d refers to diffused light, c for collimated; while subscript i refers to the interior edge and e to the exterior edge.

Throughout this chapter we will consider the problem represented schematically in figure 5.1. A matrix of thickness Z that separates two media has incident and exit fluxes on each side made up of two collimated and two diffuse fluxes. In our model we will assume the same hypotheses as the classical papers written by Maheu, Letoulouzan, and Gouesbet (1984) and W. E. Vargas (1998):

(a) Collimated light can become diffused, but not the other way around;

(b) Assuming an infinite slab in the x,y-axis, and consequently reflectance and transmittance on these directions are omitted.

The justification of these assumptions is: (a) since the probability that diffused light becomes collimated due to scattering of random distributed particles is negligible, this is not a very restrictive assumption when considering real samples; hypothesis (b) should be taken into account depending on which scenario is modelled, since the edge effect sometimes has great importance. In particular, the ultimate goal of developing this model is to apply it to model paints. In this scenario, the difference in magnitude between the incident direction (z-axis) length scale of microns; and the paint plane dimensions (x,y-axis), scale of centimetres or meters, does not break the four-flux hypothesis, and therefore the four-flux method can be applied.

Having this system (fig. 5.1) in mind, our method depends on:

(i) the difference of the refractive index at each interface,

(ii) the scattering appearing inside the composite due to the added particles, and

(iii) any absorption caused by the particles and the matrix itself.

The diffuse scattering profile depends on a parameter called *forward average path length* (ϵ), which weights the amount of scattered light entering a solid angle. The value of ϵ is a measure of the impact of particle spatial distribution on average path length. If distributed isotropically, hence fully randomly, the particles will lead to an isotropic optical response. If distributed anisotropically, with greater linear density along some directions than others, anisotropic scattering results. W. E. Vargas and G. A. Niklasson (1997b) discussed this parameter and analytical ways to define it. In this work we assume isotropic diffuse scattering, which yields a value of $\epsilon = 2$.

Moreover it is assumed that collimated light can become diffused inside the matrix (slab), but not the other way around. Under these assumptions, Maheu, Letoulouzan, and Gouesbet (1984) showed that our energy balance system can be reduced to:

$$\frac{dI_c}{dz} = (k+s)I_c, \tag{5.1}$$

$$\frac{dJ_c}{dz} = -(k+s)J_c, \tag{5.2}$$

$$\frac{dI_d}{dz} = -\zeta s I_c - \beta s J_c + \epsilon(k+\beta s)I_d - \epsilon\beta s J_d, \tag{5.3}$$

$$\frac{dJ_d}{dz} = \beta s I_c + \zeta s J_c + \epsilon\beta s I_d - \epsilon(k+\beta s)J_d, \tag{5.4}$$

where k is the absorption coefficient, s the scattering coefficient, ϵ is the forward average path length, ζ the forward scattering ratio and β the backscattering ratio, which satisfy $\zeta + \beta = 1$.

These equations can be solved by imposing the initial conditions (Maheu, Letoulouzan, and Gouesbet, 1984; Tonon et al., 2001)

$$I_{0_c} = I_c(z = Z), \tag{5.5}$$
$$I_{0_d} = I_d(z = Z), \tag{5.6}$$
$$J_{0_c} = J_c(z = 0), \tag{5.7}$$
$$J_{0_d} = J_d(z = 0), \tag{5.8}$$

where $I_{0_c}, I_{0_d}, J_{0_c}, J_{0_d}$ are the incident fluxes on both interfaces of the slab.

Once these ordinary differential equations are solved, i.e. we have obtained the expressions for $I_c(z), I_d(z), J_c(z), J_d(z)$, we can obtain the total reflectance and transmission on both sides of the slab simply by comparing initial incoming light to the obtained results. We can express this as follows:

$$R_Z = \frac{J_c(Z) + J_d(Z)}{I_{0_c} + I_{0_d}}, \tag{5.9}$$
$$R_0 = \frac{I_c(Z) + I_d(Z)}{J_{0_c} + J_{0_d}}, \tag{5.10}$$
$$T_Z = \frac{J_c(Z) + J_d(Z)}{J_{0_c} + J_{0_d}}, \tag{5.11}$$
$$T_0 = \frac{I_c(Z) + I_d(Z)}{I_{0_c} + I_{0_d}}. \tag{5.12}$$

As shown in equations 5.1-5.4, the four-flux method depends on the scattering and absorption coefficients, and on the forward average path length, which can be obtained experimentally or theoretically. In later sections of this chapter we will give more detail about those, and we will present an alternative definition of them in order to generalize the method.

5.1 Generalized Four-Flux Method

In this section we will introduce a generalized four-flux method which is capable of modelling and tuning the spectral reflectance of a diverse range of complex composite coatings. Also, this extended model is further enhanced by an explicit matrix algorithm which allows analysis of diverse multilayer stacks. This work is published (Marc A. Gali et al., 2017).

In order to check the accuracy of this model, simulated results are compared to experimental data on dried single layer paint profiles using imaged cross sections. The model input covering actual pigment and binder properties used are: material, shape, size, and size distributions, mass added, and the measured optical constants from 400

nm to 2500 nm of the un-doped binder resin layer. One interesting novel result is the comparison of a two-layered stack with bigger particles in the first layer and smaller in the second to one with the opposite depth profile. Also, it is important to note that in this work diluted dispersions are considered. As a consequence the four-flux method is better suited to study them than two-flux methods, due to the importance of both collimated and diffused light. The four-flux method offers versatility in modelling the dependence between collimated and diffused fluxes as the coating thickness changes.

After introducing the theory and mathematics of this model, in the following sections, we will be able to study a more specific situation where the main aim will be exploring and maximising the visible (VIS) and near infra-red (NIR) spectral reflectance considering the diverse structures arising from combinations of the many practical paint ingredients, which are available or can be made when applied to different substrates. This requires consideration of scatterers which can differ in composition, particle size, size distribution, fill factor, and are held in place by a variety of organic binders (which typically partially absorb in the near IR). Moreover, the study of a multilayer structure will be considered, where the main goal will be again to maximise the reflectance in the VIS and NIR optimising pigment fill factor as a function of depth within a layer.

A novel feature is the way the scattering impacts on matrix absorptance. The model includes contributions to total absorptance from the scattering pigments and from paint binder (which can arise in different bands or simultaneously at the same wavelengths).

Thus, the main innovations presented in this work are:

1. the capability to analyse the impact of absorbing matrices,
2. an implementation with an ad-mix of different kinds of scatterers including different particle sizes and particle compositions,
3. a systematic way to implement particle size distributions,
4. a clear and specific methodology to determine model parameters,
5. a convenient matrix formalism to apply the generalized four-flux method developed in this paper in a multilayer system.

5.1.1 Generalized Balance Equations

The differential equations in the normal direction z are written in terms of the forward (J) and backward (I) fluxes, divided into collimated (subscript c) and diffuse (subscript

d) components:

$$\frac{dI_c}{dz} = (K_c + S)I_c, \tag{5.13}$$

$$\frac{dJ_c}{dz} = -(K_c + S)J_c, \tag{5.14}$$

$$\frac{dI_d}{dz} = -\tilde{\zeta}I_c - \tilde{\beta}J_c + \epsilon(K_d + \tilde{\beta})I_d - \epsilon\tilde{\beta}J_d, \tag{5.15}$$

$$\frac{dJ_d}{dz} = \tilde{\beta}I_c + \tilde{\zeta}J_c + \epsilon\tilde{\beta}I_d - \epsilon(K_d + \tilde{\beta})J_d, \tag{5.16}$$

where $\tilde{\zeta}, \tilde{\beta}$ are the averaged forward and back scattered light per unit length, $K_{c,d}$ is the total absorption per unit of length of collimated (c) or diffused (d) light, and S the total scattered light per unit of length. In the classical four-flux models, those parameters are defined as the scattering and absorption rates. In most studies to date the particles were embedded in a non-absorbing matrix, however in the model presented here these coefficients will include the absorption caused by an absorbing matrix. In following sections a detailed explanation of these coefficients will be given.

5.1.2 Reflectance and Transmittance Coefficients

The solution of a position-dependent differential equation is usually given by the expression that defines the variable (here each J or I) in terms of its position within the slab e.g. $J(z)$ for any z between 0 and Z. In most cases the main interest is in knowing the light irradiated after travelling inside the matrix. Therefore the resultant fluxes irradiated by the matrix can be expressed in terms of reflection and transmission coefficients at each side of the matrix and these total R and T values at $z = 0$ and $z = Z$ can be broken down into collimated or diffused radiation if desired. In order to distinguish each R and T, three subscripts are used: (cc) incident collimated to exit collimated; (cd) incident collimated to exit diffuse; and (dd) incident diffuse to exit diffuse. Superscripts 0 ($z = 0$) and Z ($z = Z$) denote the different boundaries. In this work it is assumed that light is incident at the 0 interface, thus the main coefficients to find would be: R^0, the total reflectance at the incident interface ($z = 0$); and T^Z, the total transmittance at the other end of the matrix ($z = Z$), since some transmittance data has been obtained on free-standing composites.

The expressions derived here are equivalent to those introduced by Tonon et al. (2001), but it is important to notice the expressions presented here are simplified in order to avoid non-physical numerical singularities that previous expressions could present. This enables a more robust framework to accurately study the extreme cases where the thickness of the slab becomes large or tends to zero, or the cases where the extinction coefficient becomes very large. For example, these expressions allow

computation results of composites with both small size parameter and thick matrices. The R and T coefficients for collimated, diffused, and diffused from collimated light at both ends of the slab ($z = 0$ and $z = Z$) are:

$$R^0_{cc} = r^0_c + \frac{r^Z_c(1 - r^0_c)^2}{\varphi \tilde{D}_1}, \tag{5.17}$$

$$R^0_{cd} = \frac{(1 - r^0_{di})(1 - r^0_c)}{\tilde{D}_1 \tilde{D}_2} \left[\tilde{C}_1 + \tilde{C}_2 + \tilde{C}_3\right], \tag{5.18}$$

$$R^0_{dd} = r^0_{de} + \frac{(1 - r^0_{d1})(1 - r^0_{de})}{\tilde{D}_2} \tilde{C}_4, \tag{5.19}$$

$$T_{cc} = \frac{(1 - r^0_c)(1 - r^Z_c)}{D_1}, \tag{5.20}$$

$$T^0_{cd} = \frac{(1 - r^Z_{di})(1 - r^0_c)}{\tilde{D}_1 \tilde{D}_2} (\tilde{B}_1 + \tilde{B}_2 + \tilde{B}_3), \tag{5.21}$$

$$T^0_{dd} = \frac{(1 - r^Z_{di})(1 - r^0_{de})}{D_2} (1 - \alpha^2_3), \tag{5.22}$$

C_i, B_i, D_i coefficients are defined in the appendix (sec.B.1), the $r^0_c, r^0_{di}, r^0_{de}$ are the reflection coefficients at the $z = 0$ interface of collimated light, diffused light inside the matrix and diffused light outside the matrix, respectively; equivalently the coefficients r^Z_i are the respective reflection coefficients at the interface $z = Z$. The collimated reflection coefficients are obtained using Fresnel equations. On the other hand, in order to obtain the diffused reflection coefficient we integrate the normal projection of Fresnel equations over the half-hemisphere, since in the four-flux method it is considered the flux propagating perpendicular to the matrix interfaces. Thus, r_c and r_d can be obtained as follows:

$$\text{s-pol} : \begin{cases} r_c &= \left| \frac{Z_2 \cos\theta_1 - Z_1 \cos\theta_2}{Z_2 \cos\theta_1 + Z_1 \cos\theta_2} \right|^2, \\ r_d &= \frac{1}{\pi} \int_0^{2\pi} \int_0^{\pi/2} r_c \sin\theta \cos\theta d\theta d\varphi \\ &= \int_0^{\pi/2} r_c \sin(2\theta) d\theta, \end{cases} \tag{5.23}$$

$$\text{p-pol} : \begin{cases} r_c &= \left| \frac{Z_2 \cos\theta_2 - Z_1 \cos\theta_1}{Z_1 \cos\theta_1 + Z_2 \cos\theta_2} \right|^2, \\ r_d &= \int_0^{\pi/2} r_c \sin(2\theta) d\theta, \end{cases} \tag{5.24}$$

where we have used the trigonometric relation $\sin(2\theta) = 2 \sin\theta \cos\theta$.

Finally, the problem is solved using the previous equations (5.17-5.22) to express the total reflectance and transmittance at both ends of the slab.

$$R^0 = \frac{(R^0_{cc} + R^0_{cd})J_c + R^0_{dd}J_d}{J_c + J_d}, \tag{5.25}$$

$$T^Z = \frac{(T^0_{cc} + T^0_{cd})J_c + T^0_{dd}J_d}{J_c + J_d}, \tag{5.26}$$

$$R^Z = \frac{(R^Z_{cc} + R^Z_{cd})I_c + R^Z_{dd}I_d}{I_c + I_d}, \tag{5.27}$$

$$T^0 = \frac{(T^Z_{cc} + T^Z_{cd})I_c + T^Z_{dd}I_d}{I_c + I_d}. \tag{5.28}$$

5.1.3 Effective Volume Coefficients

In this section we will introduce the effective volume coefficients, which allow the inclusion of the effects of different kind of particle compositions, same particles but with different sizes, or the absorption done by the matrix. These effects are crucial to model real paints, as will be shown in the discussion section.

The balance equations define the change of flux per unit of length, i.e. $dI \propto Idz$, which means that to use a coefficient to express loss or gain of this flux, it has to have units of [length]$^{-1}$: this is one of the main things that has to be considered when defining the effective volume coefficients.

In the classical four-flux method (Maheu, Letoulouzan, and Gouesbet, 1984), they obtained those parameters theoretically using Mie theory. To do so, they define the scattering and absorption albedos multiplying the energy cross sections for the density number of the scatterer. Thus, they have a coefficient that gives information on the amount of energy absorbed or scattered per unit of length.

$$k = \eta \cdot C_{abs}, \tag{5.29}$$

$$s = \eta \cdot C_{sca}, \tag{5.30}$$

where η is the number density, and C_{abs}, C_{scat} are the absorption and scattering cross sections, respectively.

In order to generalize the four-flux method, the absorption and scattering coefficients will be approached in a different way. Instead of defining them as the energy scattered or absorbed by the scatters, they will be defined as the energy scattered or absorbed *per unit of volume*. This change in the approach implies significant differences; first, inhomogeneity of scatterers, secondly, the particles on the medium are only one of the factors that play a crucial role in the energy extinction, i.e. the effects of the matrix can be considered as well.

In order to implement this approach, the absorption coefficient (K) and the scattering coefficient (S) will be obtained considering the effect of each element (matrix and scatterers). In order to encapsulate this information in an effective coefficient, the scattering and absorption will be averaged, weighting each component by its relative volume, i.e. volume occupied by the component over the total volume (fill factor), or by its number density (number of scatterers per unit volume).

For instance, the effective absorption coefficient due to all different kind of particles in the matrix is defined as the sum of the absorption coefficients of each of them. Thus, using the definition given by equation 5.29, the following expression for the effective absorption coefficient of the particles is obtained:

$$k^p = \sum_{i}^{N} k_i, \tag{5.31}$$

where k^p is the absorbed light due to the particles and N is the number of different types of particles. We will consider two particles different if they have different energy cross-sections, for instance, two particles of different size but made of the same material will be considered different.

On the other hand, if the absorption due to the matrix is to be considered, first we should obtain the absorption coefficient of the medium for collimated and diffused light, i.e. to find how much light is absorbed only by the matrix when the collimated and diffused light are travelling in the considered system. Thus, as the travel distance of the diffused light depends on the average path-length, ϵ, it should be considered when studying the effective decay of diffused light in the system. To do so, an equivalent diffusive medium (diffused light has same *average path-length* as the original system) is considered, only composed of the particular matrix, therefore in this scenario the balance equations 5.13-5.16 can be reduced to the following:

$$\frac{dJ_c}{dz} = -K_c J_c, \tag{5.32}$$

$$\frac{dJ_d}{dz} = -\epsilon K_d J_d. \tag{5.33}$$

These differential equations are straightforward to solve and have as a solution a decaying exponential:

$$J_i = J_{0,i} \cdot \exp[-\alpha_i z], \tag{5.34}$$

where $i = c, d$ and $\alpha_c = K_c$, $\alpha_d = \epsilon K_d$. Thus, using previous expressions, the skin depth (δ_s) in terms of the decaying constant (α_i) can be obtained, which allows the following relation (Kreibig and Vollmer, 1995):

$$\alpha_i = \frac{2}{\delta_s} = \frac{4\pi n_2}{\lambda}, \tag{5.35}$$

where $n = n_1 + in_2$, is the refractive index, n_2 being the extinction coefficient, and λ is the incident wavelength. Then, the collimated and diffused absorption coefficients due to the matrix can be defined by,

$$k_c = \frac{4\pi n_2}{\lambda}, \tag{5.36}$$

$$k_d = \frac{4\pi n_2}{\lambda \cdot \epsilon}. \tag{5.37}$$

Therefore, it is possible to define a characteristic coefficient of the composite that expresses the total energy loss due to absorption per unit of length. These effective coefficients ($K_{c(d)}$) will be the result of doing a volume average of the absorption coefficients of each element (k_i). Thus, using previous definitions, a discrete expression for the effective coefficient, considering the volume occupied for each element, can be written as follows:

$$K_{c(d)} = \sum_{i}^{N} k^i + k_{c(d)} \cdot \left(1 - \sum_{i}^{N} f_i\right), \tag{5.38}$$

where f_i is the fill factor of particles of type i of N different types.

Similarly, the same approach can be applied with the scattered energy per unit of volume, unlike the absorbed light the background medium does not scatter light, so it is only necessary to consider how much light is scattered due to the particles in a certain volume. Thus, as it has been done in equation 5.31 the effective scattering coefficient can be expressed as follows:

$$S = \sum_{i}^{N} s_i. \tag{5.39}$$

5.1.4 Forward and Back Scattering Ratios

In the four-flux model, an additional two coefficients called the forward and back scattering coefficients are required. They are not to be confused with the forward and back scattering of the particles, instead these coefficients are a ratio that indicates how much of the scattered light from a particle goes towards the forward or back hemisphere. Thus, as in this work we are assuming spherical particles, these coefficients can be defined using Mie theory. Using notation of Bohren-Huffman (Bohren and Huffman, 2007), the scattered light on the two main polarizations depends on the coefficients S_1, S_2, is defined as follows:

$$S_1 = \sum_n \frac{2n+1}{n(n+1)}(a_n\pi_n + b_n\tau_n), \tag{5.40}$$

$$S_2 = \sum_n \frac{2n+1}{n(n+1)}(a_n\tau_n + b_n\pi_n), \tag{5.41}$$

where τ_n and π_n are the angular dependent functions. As can be seen in figures 5.2 & 5.3 the angular scattering profile is highly dependent on the size parameter (x), wavenumber (k) and refractive index of the particle and surrounding medium. This fact makes it important to know not only the total amount of scattered light, but also how much energy is scattered in the forward or back direction for every particle inside the matrix.

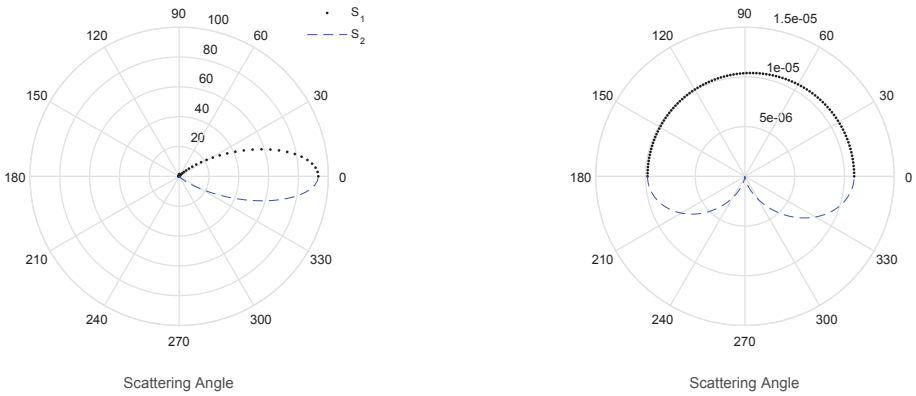

FIGURE 5.2: Angular scattering profile of a TiO_2 sphere of radius 80nm in acrylic: (Left) incident wavelength of 200nm; (Right) incident wavelength of 2000nm.

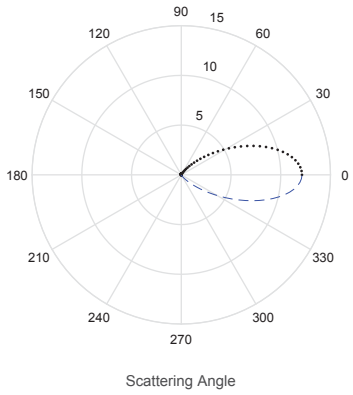

FIGURE 5.3: Angular scattering profile of a TiO_2 sphere of radius 1 μm in acrylic with incident wavelength of 2.5 μm.

Therefore, if we want to know the ratio of scattered light in the forward or back hemisphere we have to integrate over the respective angles and then average the polarizations.

$$\zeta_{1,2} = \frac{\int_0^{2\pi}\int_0^{\pi/2} |S_{1,2}|^2 |\cos\theta|\, d\Omega}{\int_0^{2\pi}\int_0^{\pi} |S_{1,2}|^2 |\cos\theta|\, d\Omega}, \tag{5.42}$$

$$\beta_{1,2} = \frac{\int_0^{2\pi}\int_{\pi/2}^{\pi} |S_{1,2}|^2 |\cos\theta|\, d\Omega}{\int_0^{2\pi}\int_0^{\pi} |S_{1,2}|^2 |\cos\theta|\, d\Omega}, \tag{5.43}$$

where $d\Omega = \sin\theta d\theta d\phi$ is the solid angle, $|S_{1,2}|^2$ are the scattered irradiance per unit incident irradiance given that the incident polarization is perpendicular ($|S_1|^2$) or parallel ($|S_2|^2$) to the scattering plane given by θ. Note that the cosine term is necessary, because ζ and β are the ratios of scattered light in the forward and backward directions, so the projection on that direction is what should be considered. The reason to use the absolute value of the cosine is that these ratios consider the amount of energy scattered in each projection and to do so the sign of the cosine should be omitted, since the direction information is implicit on ζ and β.

Finally averaging over the two polarizations,

$$\zeta = \frac{1}{2}(\zeta_1 + \zeta_2), \tag{5.44}$$

$$\beta = \frac{1}{2}(\beta_1 + \beta_2), \tag{5.45}$$

and by definition they satisfy the relation $\zeta + \beta = 1$.

Therefore, we can define the amount of light scattered into the forward or backward hemisphere for each kind of scatterer in order to obtain the final forward and back scattering ratios used in the balance equations 5.13-5.16. Finally in order to obtain the average scattered light in the forward and back hemisphere, we will use the ratios that we just defined (eq.5.44-5.45), and use them to average the scattered light.

$$\tilde{\zeta} = \sum_i^N \zeta^i \cdot s^i, \tag{5.46}$$

$$\tilde{\beta} = \sum_i^N \beta^i \cdot s^i, \tag{5.47}$$

where β^i, ζ^i are the coefficients of the ith scatterer, and s^i its total scattered light.

5.1.5 Size Distribution Function of Scatterers

Real heterogeneous materials offer a distribution of sizes and shapes on their components (see figure 5.5). Thus, in order to model the optical response of these kind of matrices, it is important to include the overall statistical effect of the components' heterogeneities. In this section we define a method to include the effect of distinct sizes of the matrix phases (components).

As has been shown in previous section, characteristic parameters can be used to define the effect of several scatters. In this section, the same principle will be applied, but for scatterers of same composition, but different size. Thus, the parameters of a particular kind of particle will be defined by using the distribution function of their radius to weight the total fill factor of that kind of particles. In particular, the number density of all particles made of the same material can be defined as follows:

$$\eta(i) = \int_{-\infty}^{+\infty} \rho(r)dr = \int_{-\infty}^{\rho_0-\Delta} \rho(r)dr + \int_{\rho_0-\Delta}^{\rho_0+\Delta} \rho(r)dr + \int_{\rho_0+\Delta}^{+\infty} \rho(r)dr,$$

assuming $\rho(r)$ symmetric then $\delta \equiv \int_{-\infty}^{\rho_0-\Delta} \rho(r)dr = \int_{\rho_0+\Delta}^{+\infty} \rho(r)dr$, and we can write

$$\begin{aligned} \eta(i) &= \int_{\rho_0-\Delta}^{\rho_0+\Delta} \rho(r)dr + 2\delta, \\ &\sim \int_{\rho_0-\Delta}^{\rho_0+\Delta} \rho(r)dr, \end{aligned} \tag{5.48}$$

where $\eta(i)$ is the total number density of inclusions made of the material i, and Δ is the cut-off value of the size distribution function.

Using this relation and taking in account equations 5.29 and 5.30, we can define the absorption or scattering coefficient of same phase particles by the following relation:

$$\begin{aligned} k &= \int_{\rho_0-\Delta}^{\rho_0+\Delta} \rho(r)C_{abs}(r)dr, \\ s &= \int_{\rho_0-\Delta}^{\rho_0+\Delta} \rho(r)C_{sca}(r)dr, \end{aligned} \tag{5.49}$$

where $\rho(r)$ is the distribution function of the radius and $C_{abs}(r)$, $C_{sca}(r)$ are the energy cross sections of the particle.

To implement it in a numerical algorithm, the discrete version of equation 5.49 is used,

$$k = \sum_{i=0}^{N} \eta(r_i) C_{abs}(r_i), \tag{5.50}$$

$$s = \sum_{i=0}^{N} \eta(r_i) C_{sca}(r_i), \tag{5.51}$$

$$r_i = (\rho_0 - \Delta) + i\frac{2\Delta}{N}, \tag{5.52}$$

with N the sampling number.

5.1.6 Forward Average Path Length

As has been said previously, four-flux equations consider the propagation of light per unit length in the direction perpendicular to the interfaces. Thus, for the collimated light is straightforward to define how it propagates, since it propagates in a given direction; on the other hand, diffused light irradiates the whole hemisphere, therefore it is necessary to define a coefficient that weights how much of this diffused light is propagating in the direction under study. The coefficient that incorporates this information is the average path length (ϵ) which has been studied extensively. As has been defined by W. E. Vargas and G. A. Niklasson (1997b), ϵ can be defined as the average ratio between Δz over ΔL $\Delta z = \mu \Delta L$ where ΔL is the length that the diffused light travelled by a given angle θ with $\mu = \cos\theta$. Then, integrating this relation over the forward hemisphere, considering the light irradiated over a solid angle divided by the total light. The definition for ϵ introduced by W. E. Vargas and G. A. Niklasson (1997b) is the following:

$$\epsilon = \frac{\int_0^1 I(z,\mu) d\mu}{\int_0^1 I(z,\mu) \mu d\mu}, \tag{5.53}$$

5.1.7 Multilayer Formalism

In this section an iterative matrix algorithm is presented to solve a multilayer problem using the four-flux method in each slab (layer). A four-flux multilayer method has been studied before (Tonon et al., 2001), nevertheless in that article the propagation phase matrix was not explicitly addressed; only continuous equations were presented. Therefore the aim of this section is to explicitly present the matrix formalism for an arbitrary number of layers (a similar approach was used by Simonot et al. (2016), also at the time of writing another multilayer four-flux approach was published by Slovick et al. (2017)).

Assuming a system of slabs as presented in diagram figure 5.4, where the number of layers increases in the z-axis direction, interfaces are labelled as follows: increasing

along the z direction, the first interface of each layer is labelled with 0 and the ending interface with Z. In order to find the propagation matrix from one layer to another, the incoming and outgoing fluxes of any slab should be determined.

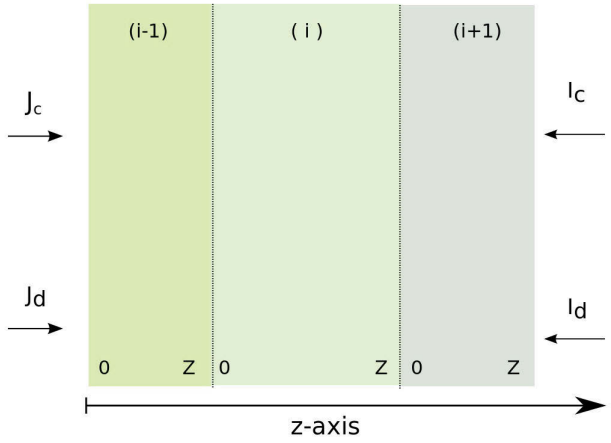

FIGURE 5.4: Diagram of the multilayer structure and notation.

$$I_c^Z(i-1) = I_c^0(i+1)T_{cc}(i) + J_c^Z(i-1)R_{cc}^0(i), \tag{5.54}$$

$$\begin{aligned} I_d^Z(i-1) = {} & I_c^0(i+1)T_{cd}^Z(i) + I_d^0(i+1)T_{dd}^Z(i) \\ & + J_c^Z(i-1)R_{cd}^0(i) + J_d^Z(i-1)R_{dd}^0(i), \end{aligned} \tag{5.55}$$

$$J_c^0(i+1) = J_c^Z(i-1)T_{cc}^0(i) + I_c^0(i+1)R_{cc}^Z(i), \tag{5.56}$$

$$\begin{aligned} J_d^0(i+1) = {} & J_c^Z(i-1)T_{cd}^0(i) + J_d^Z(i-1)T_{dd}^0(i) \\ & + I_c^0(i+1)R_{cd}^Z(i) + I_d^0(i+1)R_{dd}^Z(i), \end{aligned} \tag{5.57}$$

where the brackets with the i arguments denote the layer.

$$\begin{cases} I_c^0(i+1) = I_c^Z(i), & J_c^0(i+1) = J_c^Z(i), \\ I_d^0(i+1) = I_d^Z(i), & J_d^0(i+1) = J_d^Z(i). \end{cases} \tag{5.58}$$

Using equations (5.54-5.57) and imposing the conservation of the flux between interfaces eq.(5.58), we can obtain a linear system that relates two adjacent slabs, which can be expressed in matrix form eq.(5.59). In order to explicitly obtain the flux-propagation matrix, it is more suitable to write a matrix equation relating the fluxes at both interfaces of a particular layer.

$$\begin{pmatrix} T_c c & 0 & 0 & 0 \\ T_c d^0 & T_d d^0 & 0 & 0 \\ -R_c c^0 & 0 & 1 & 0 \\ R_c d^0 & R_d d^0 & 0 & -1 \end{pmatrix} \begin{pmatrix} J_c(i-1) \\ J_d(i-1) \\ I_c(i-1) \\ I_d(i-1) \end{pmatrix} = \begin{pmatrix} 1 & 0 & -R_c c^Z & 0 \\ 0 & 1 & -R_c d^Z & -R_d d^Z \\ 0 & 0 & T_c c^Z & 0 \\ 0 & 0 & -T_c d^Z & -T_d d^Z \end{pmatrix} \begin{pmatrix} J_c(i) \\ J_d(i) \\ I_c(i) \\ I_d(i)) \end{pmatrix} \tag{5.59}$$

where all reflectance and transmittance coefficients are the coefficients of the ith layer. Expressing the previous equation in matrix form we can generalize the flux transfer for an arbitrary number of layers:

$$A \cdot F_{(i-1)} = B \cdot F_{(i)}, \tag{5.60}$$

with $F_i = (J_c(i), J_d(i), I_c(i), I_d(i))^T$, thus we can easily express the transfer matrix from eq.5.60.

$$F_{(i-1)} = A_i^{-1} B_i F_{(i)}, \tag{5.61}$$

$$F_{(i-1)} = M_i F_{(i)}. \tag{5.62}$$

By induction it is easy to see that we can write the flux F at the first interface of the stack in terms of the flux at the final interface of it.

$$F_0 = \phi \cdot F_\tau, \tag{5.63}$$

$$\phi = \prod_{i=1}^{L} M_i, \tag{5.64}$$

where $\prod_{i=1}^{L} M_i = M_1 \cdot M_2 \cdot M_3 \cdot \cdots \cdot M_L$. Finally, the last step to do is to relate the incident flux (initial condition) with the outgoing flux of the whole stack. The incident fluxes are $X_0 = (J_c(0), J_d(0), I_c(\tau), I_d(\tau))^T$, and the outgoing fluxes are $X = (J_c(\tau), J_d(\tau), I_c(0), I_d(0))^T$, with τ the total stack thickness.

5.2 Validating Results with Experimental Data

Finally, our model is tested by its ability to model experimental data using structural information obtained from two samples whose spectral hemispherical reflectance and transmittance had been measured. Including binder absorption and particle (e.g.

paint pigment) size distributions significantly improved the agreement obtained between experimental and model data. The experimental hemispherical reflectance data was collected using a Perkin Elmer Lambda 950 with 150 mm integrating sphere. The refractive index of the binder was determined via preparation of a binder-only sample on a silicon wafer measured via ellipsometry, using a JA Woollam V-VASE ellipsometer, combined with spectroscopic transmittance of the same free-standing film after peeling it off the silicon wafer substrate. The TiO_2 refractive index data was modelled using a Tauc-Lorentz oscillator model matching the band-gap to the experimental data.

5.2.1 Sample preparation

Two samples were made following the same process [1]: mixing the compounds and leaving the samples to dry for one week, after which the weights of the composites were estimated. Paint used in figure 5.6 was made mixing water (0.53 g), acrylic (2.25 g) and TiO_2 (0.74 g of *ALTIRIS 550* and 0.1 g of *ALTIRIS 800*, which we will refer to as small and big sizes respectively); after drying the volatile component loss leaves weights of: 1.24 g acrylic, small size TiO_2 0.41 g and big size TiO_2 0.06 g; and a final thickness of 380 μm. Using the final weight of the compounds the fill factors of TiO_2 particles were found to be 7.72% for the small size, and 1.79% for the big size. Paint represented by figure 5.7 was made mixing water (0.67 g), acrylic (1.46 g) and TiO_2 (0.40 g); after the drying process the compound weights got reduced to: acrylic (0.5 g) and TiO_2 (0.34 g). The estimated fill factor for the TiO_2 was 15%.

[1] These samples were made with the assistance of Dr. Angus R. Gentle.

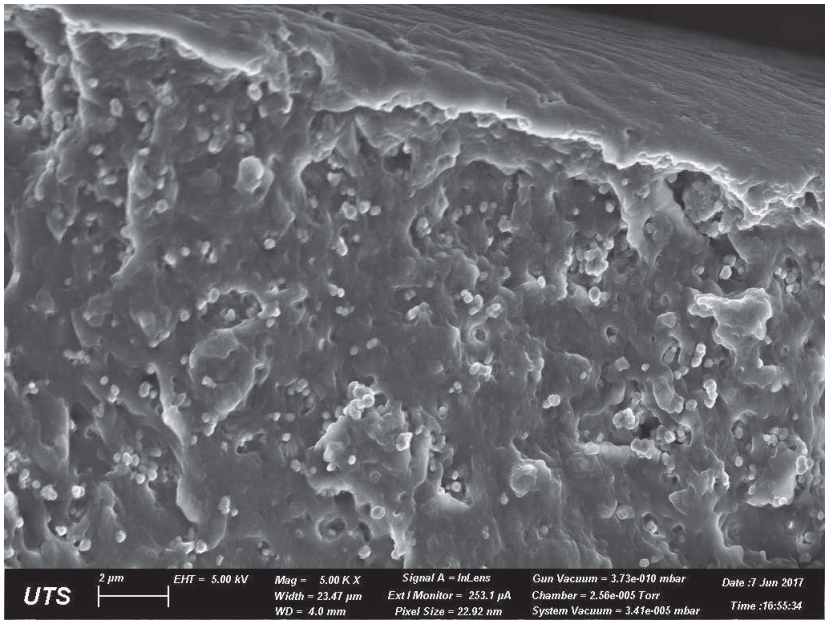

FIGURE 5.5: SEM picture taken by Matthew C. Tai of a paint sample made of TiO_2 in acrylic binder.

5.2.2 Models of Experimental Data

In order to fit simulation with experimental results, the scatterers' size and fill factor have been used as a fitting parameter, thus the best fitting result gives a close estimate of the average size of the pigments and their fill factor.

Figure 5.6 compares the experimental and simulated data. The position of the absorption bands of the binder allows a good match to the experimental optical result over most of the solar spectral range. Reflectance agrees with some minor quantitative differences in the depths of the absorption bands. In order to obtain this result we used two distribution sizes, one with mean radius of 10 nm and the other with mean radius 180 nm. In both cases the distributions follow a Gaussian with standard deviation set at 10% of the mean diameter value. Thus, combining different distributions allowed us to match the experimental behaviour in both the visible and IR. However, it is important to test the response of other distributions to determine if this result is unique. This is because, as shown in the previous sections, the reflectance of a composite is very sensitive to the size and volume fraction of the scatterers inside, therefore different combinations of them could give a similar result. This is why we cannot use only the reflectance to fit optical data. Some of the variables must be constrained to avoid any ambiguity on structural impacts. For instance, the total volume fraction of scatterers can be measured, or the size distribution of the composites can be found using microscopy. In addition, pigment supplies often come with information on mean pigment diameters and their distribution which can also be used. Figures

5.6 and 5.7 show that the simulated results agree with the experimental data at all wavelengths apart from details in some NIR absorption bands. Differences between simulation and experiment could be attributable to differences between the refractive index data of the acrylic used in the simulation which was separately characterized for index, and its actual refractive index in the measured material after formulation and drying, for example some voids might be present.

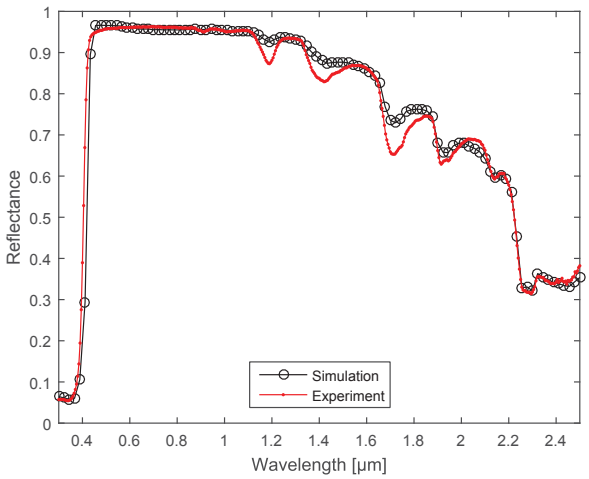

FIGURE 5.6: Comparison between the reflectance of experimental and simulated data of an acrylic paint with 6% TiO_2 scatterers where their size follows a normal distribution with mean radius μ_0 =90 nm and standard deviation σ =18 nm, and a 1% TiO_2 with a size distribution characterized by a mean radius μ_0 =500 nm and standard deviation of σ =100 nm.

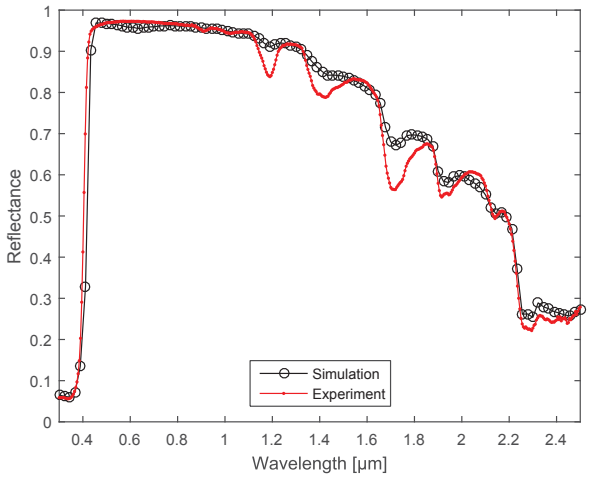

FIGURE 5.7: Comparison between the reflectance of experimental and simulated data of an acrylic paint with 14% TiO_2 scatterers where their size follows a normal distribution with mean radius μ_0 =80 nm and standard deviation σ =16 nm.

Overlaying fig. 5.6-5.7 shows that adding large particles uniformly reduces the NIR absorptance. We found that the fitted size distributions agree with the SEM (fig. 5.5).

5.3 Results and Discussion

One of the main innovations of the work presented in this chapter is the overall effect caused by different kind of scatterers: different in composition, size and size dispersion. It is important to know the extent to which exploiting these differences will allow for wider degrees of spectral tuning of the optical response. Therefore, in order to analyse the optical response of these variables, a fixed matrix of thickness 380 μm is considered. The reader should note that if other effects were under consideration the matrix thickness would be a crucial parameter; for instance, if the objective was to analyse or improve a particular system the thickness of the composite should also be considered, especially if the matrix is absorbing. Also, if not stated otherwise we are considering size distributions with standard deviation of 20% of the mean radius.

The code used has been simulated with MATLAB; some of the Mie scattering routines for spherical particles were based on Bohren and Huffman (2007) and Mätzler (2002) codes [2].

[2]We used Mie scattering theory to obtain the scattering and absorption cross sections of the embedded particles.

The aim of this subsection is to convince the reader of the effectiveness and value of the modifications presented in this work. With this goal in mind, systematic simulations are presented showing: first, the effect of these effective coefficients, and second, the improvement of the accuracy that they bring. Thus, the improvement in the agreement with experimental data due to the incorporation of the binder absorption will be demonstrated by comparing results obtained with and without binder absorption, but all other model parameters retained.

5.3.1 Binder Absorption

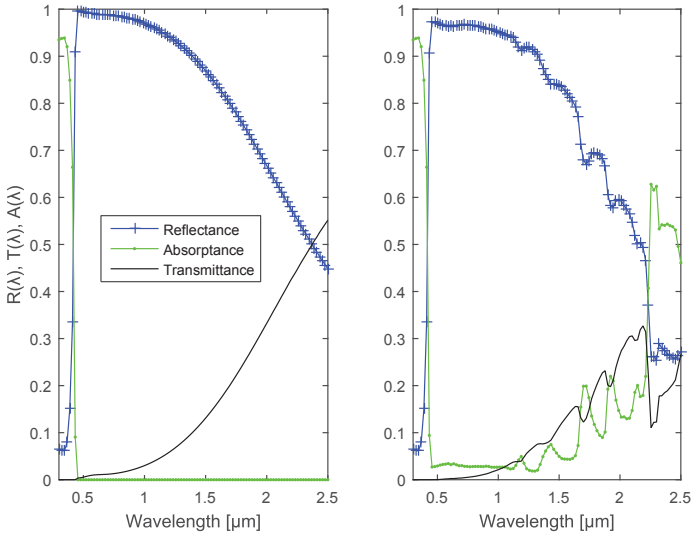

FIGURE 5.8: Simulations of the spectra of acrylic paint with a normal distribution of TiO_2 particles of mean radius 0.08 μm and fill factor 10%; (left) without binder absorption; and (right) with absorption of the actual acrylic resin used included.

Figure 5.8 shows that the effect of simulating the binder absorption is obvious, with strong absorption bands evident in the infrared region. From figure 5.9 it can be easily seen that the difference in reflectance in the IR is due to added acrylic polymer related absorption (green lines). It can also be appreciated that in the visible-NIR the binder adds significant absorptance and therefore the reflectance profile in this region also changes considerably. For instance, if the goal was to improve the reflectance in the visible, smaller particles should be included in the mixture in order to add backscattered light in this particular region. Also, it is interesting to see the high absorption in the ultraviolet region. In figure 5.9 this band appears in both simulations, the one with and without binder absorption. This fact tells us that this absorption comes from the

embedded particles, indeed this absorption region matches closely with the inter-band absorption edge of rutile TiO_2.

The study of the NIR absorption bands resulting from the binder is a crucial matter in coatings used for cooling. Therefore, being able to model this effect accurately can help to improve coatings, in order to achieve less absorption in the IR regime.

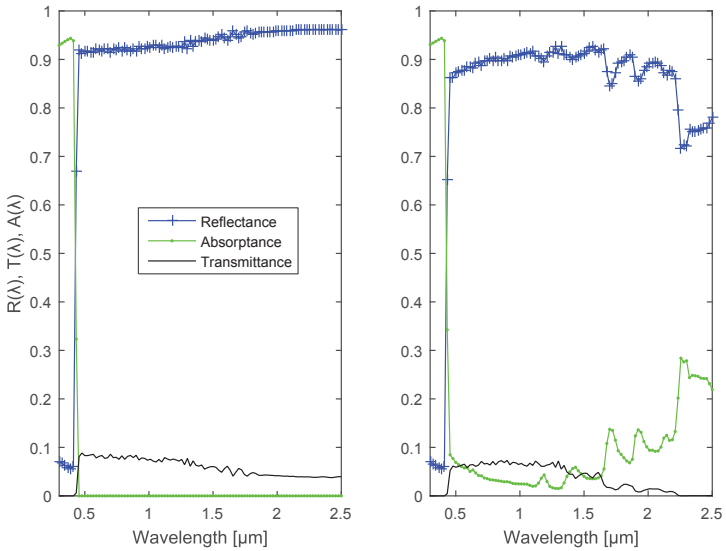

FIGURE 5.9: On the left side it can be seen a non-absorbing acrylic paint with a normal distribution of TiO_2 particles of mean radius $1\mu m$ and fill factor 10%. Right graph shows acrylic paint with a normal distribution of TiO_2 particles of mean radius $1\mu m$ and fill factor 10%.

5.3.2 Distribution of Sizes

A convenient way to study the effect of different size particles over the solar energy wavelengths is to plot the optical response as a 3D surface. Figure 5.10 shows the reflectance, absorption and transmittance of acrylic paint for different size of scatterers and incident wavelengths. It can be seen that particles with radius between 0.3-0.4 μm yield the highest average reflectance over the whole wavelength spectrum, while these smaller particles are also the ones that yield reflectance values of nearly 100% across the visible range. This is because they backscatter more in this wavelength region. On the other hand bigger particles reflect and backscatter more strongly in the NIR. It is interesting to note the size dependence that can be seen in the transmittance spectra, with clear predominance of backscattered light in the NIR regime caused by the small particles in comparison with larger ones.

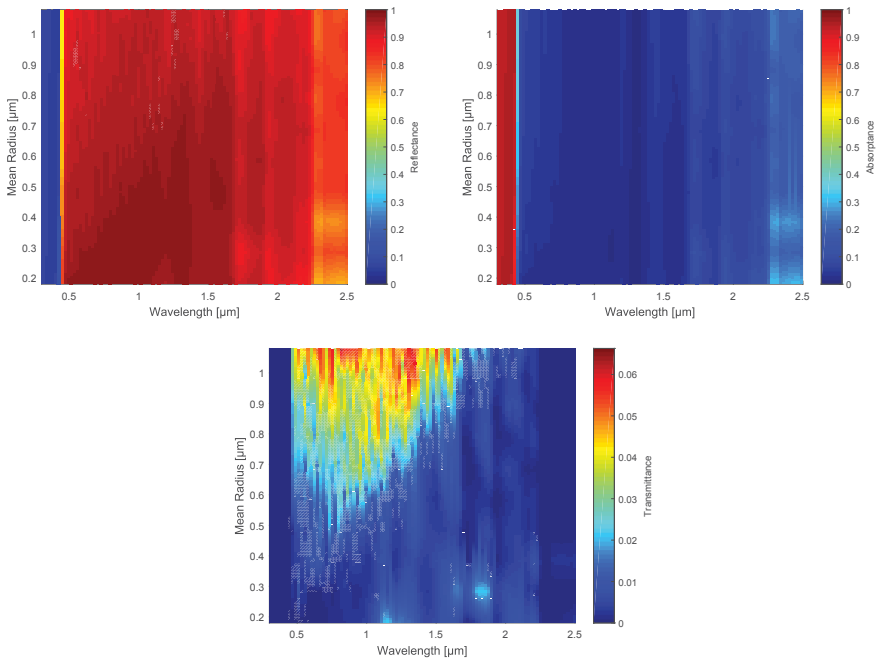

FIGURE 5.10: These images show the optical response ((top-left) reflectance, (top-right) absorptance and (bottom) transmittance) of an acrylic matrix with TiO_2 sphere particles depending on the radius of those and on the incident wavelength.

By comparing different composites in which mean particle radius (r) changes in large steps over a wide range , with its standard deviation σ a fixed fraction of r, and particle volume fraction fixed, different optical responses can be systematically studied in particular wavelength bands. As an example, the case of a white acrylic based paint with TiO_2 pigments as scatterers is considered. In figure 5.11 can be seen the reflectance of four different paint compositions, where the volume fraction of scatterers is fixed, while their mean radius (r) is changed (note that the standard deviations of these distributions is $0.2r$). It is interesting to see that the back-scattering ratio, which in this work is defined as the fraction of light scattered into the half-hemisphere projected into the backward direction (see Section 5.1.4), is strongly dependent on the size as can be seen in the bottom-left image on figure 5.11. In this picture it can be seen that small particles are more efficient at backscattering overall, but this advantage diminishes at NIR wavelengths as their scattering there is less than at visible wavelengths. In contrast, big particles become much more efficient at backscattering at these longer wavelengths. Nevertheless, what matters is the product of backscattered ratio to total scattered light, in other words, how much scattered *intensity* goes into the backward hemisphere. Thus, even though for wavelengths around 2 μm the

small particles ($r \sim 0.5$ μm) scatter more than bigger ones, the total energy backscattered by bigger particles is larger. In particular, can be seen that for wavelengths in the range of 2 μm - 3 μm, particles with diameter of the same order as the incident wavelength ($1 < r < 1.5$ μ m) are more efficient backscattering light than smaller particles. Integrated solar reflectance clearly decreases as size increases since the solar intensity falls beyond wavelengths of 1 μm. This analysis links the total spectral reflectance presented on the top-left image in figure 5.11 to the directional composition of internal scattering.

If spectral adjustment of backscattering to total scattering ratio is of interest, a response that combines those of small and big particles can help. In order to achieve that there are two main options: the first would be choosing a dominant size, the mean size, and to increase the standard deviation of the size distribution for a single fix r value, which will yield a broader spectral response. On the other hand, two or more considerably different mean r values can provide a different spectral response, so then including two or more different distributions of radius r which may be separate or partially overlap as a function of r. Figure 5.12 follows the first idea of one mean r value. There it can be seen that the wider the distribution is, the more the different spectral responses come together. As the Gaussian approaches a delta function, the spectral response approaches that for a composite with mono-disperse, single size particles.

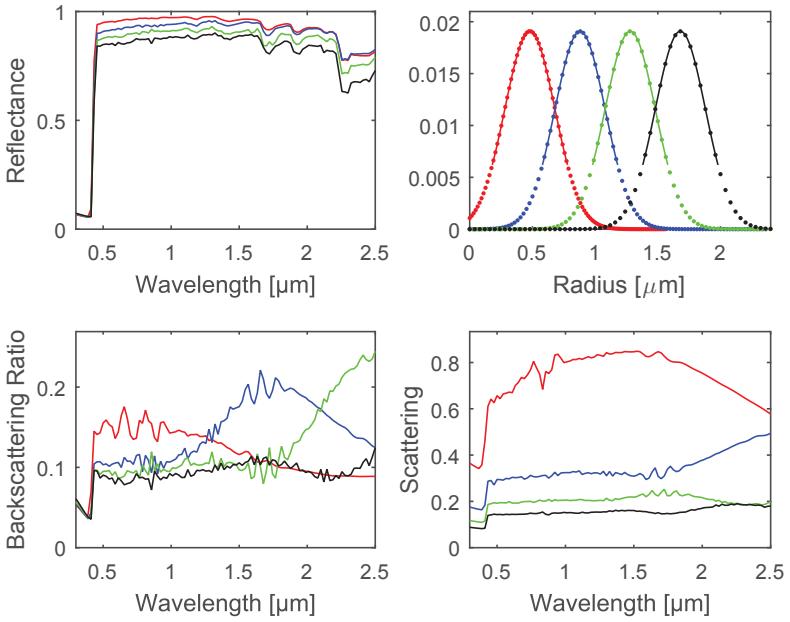

FIGURE 5.11: (Top-left) Reflectance of acrylic paint for different size particle distributions. (Top-right) Gaussian distribution of particle radius for each paint. (Bottom-left) Back-scattering ratio of each distribution. (Bottom-right) Total scattering of each distribution.

On the other hand, sometimes two clearly distinct sizes are present, then to model this response two distinct distributions should be considered as well (second approach). To exemplify this effect in figure 5.13. We compare three types of composites: two of them are characterized by a single size distribution of scatterers with well separated mean radius values of 0.1 μm and 1.5 μm, whereas the third example is a result of the weighted combination of the two separate spreads. It can be clearly seen that in doing so a composite is achieved that maintains the very high visible reflectance of the small particles, and the high NIR reflectance achievable with big particles. In the bottom images of figure 5.13 it can be appreciated that the mixed composite has backscattering and total scattering spectral responses in between the values arising with either a small or large mean radius. Thus it seems intuitive to think that by mixing two particle supplies with very different mean diameters an improvement of overall solar reflectance will occur in the final composite.

These examples shown that mixing different size particles with tailored size distributions can be used to adjust spectral diffuse response over a wide range. This revised four-flux model is an excellent and flexible composite layer design tool as demonstrated by its ability to optimize the hemispherical reflectance spectrum of heterogeneous matrices, by taking advantage of the spectral variations in their radiative-transfer profiles which are very sensitive to particle size.

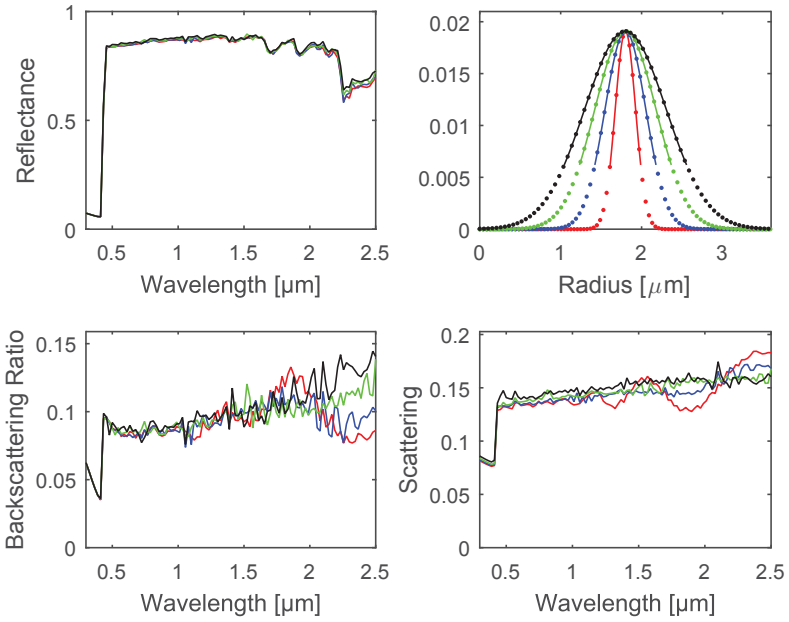

FIGURE 5.12: Shows the effect of varying the standard deviation of the composite size distribution. This system represents an acrylic based paint with 14% of TiO_2 particles with fixed mean radius of 1.8 μm.

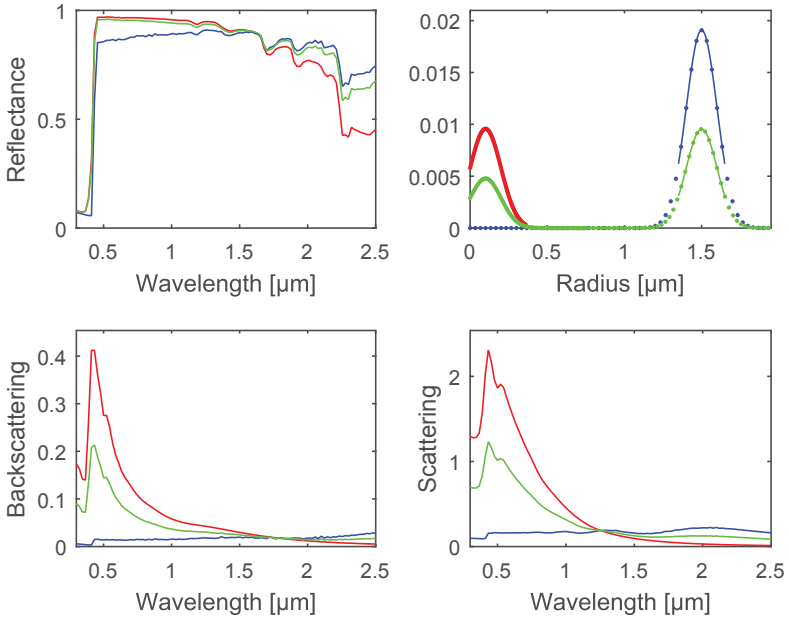

FIGURE 5.13: Top-left figure shows the reflectance of 3 different paints. Top-right graph shows the size distribution of each paint. Bottom-left shows the backscattering ratio of each paint. Bottom-right shows the total scattering of each composition.

5.3.3 Analysis of a Two-Layer Stack

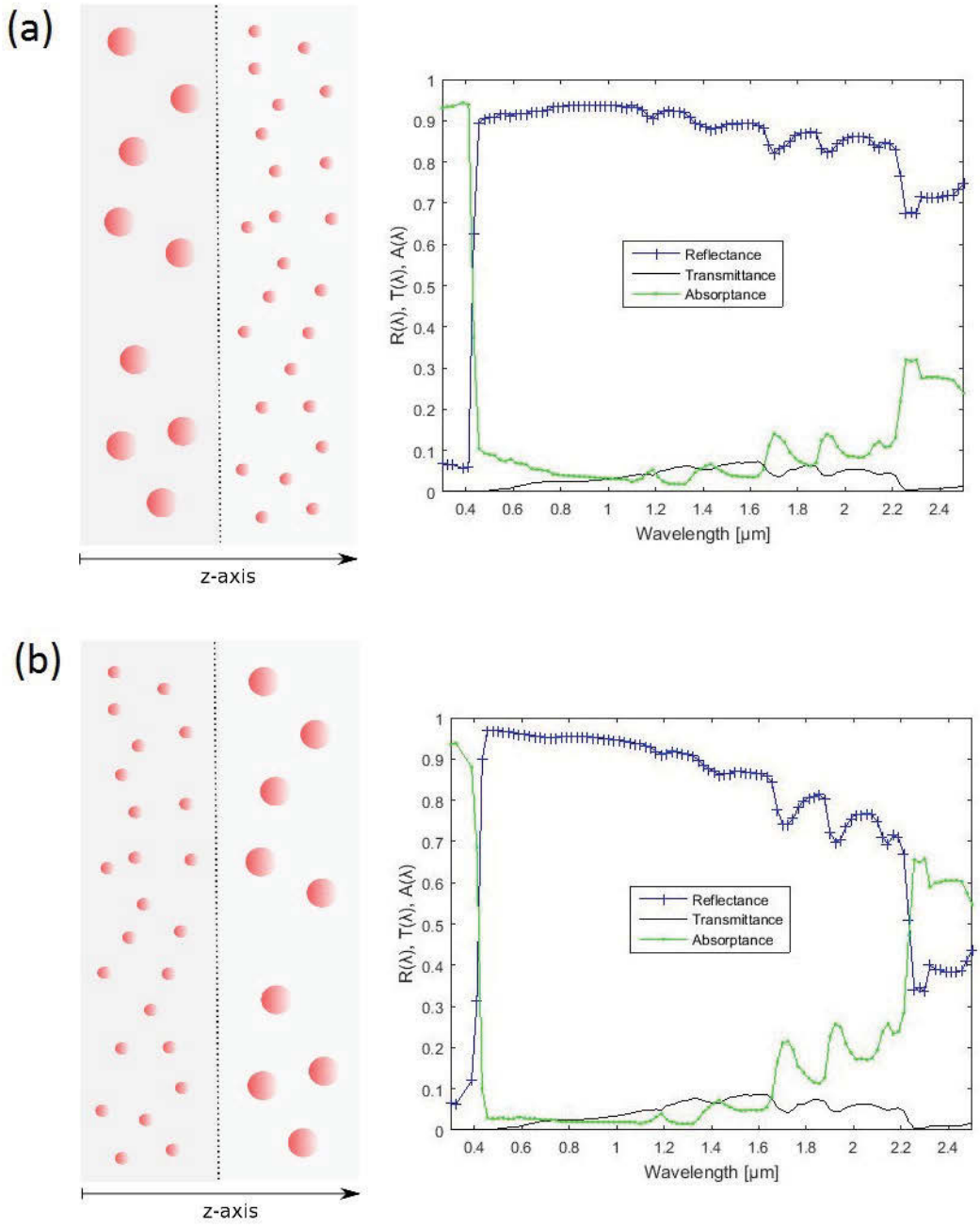

FIGURE 5.14: (a) Left image is a cartoon of the system modelled in the right image. The system is a two-layered stack with acrylic matrix and 7% of TiO_2 scatterers for both layers; first layer, particles with mean radius 1 μm and standard distribution 200 nm; second layer, particles with mean radius 100 nm and standard distribution of 20 nm. Reflectance, transmittance and absorptance are calculated for incidence fluxes from the left. (b) Left image is a cartoon of the system modelled in the right image. The system is a two-layered stack with acrylic matrix and a 7% of TiO_2 scatterers for both layers; first layer, particles with mean radius 100 nm and standard distribution of 20 nm; second layer, particles with mean radius 1 μm and standard distribution 200 nm.

Very often natural or artificial composites present a grading in composition, which can be modelled as a multi-layered structure. For instance, some heterogeneous paint solutions dry into composites with a gradient in composition. This can change the overall optical response. The aim of this section is to show the capability of the formalism introduced in section 5.1.7, for different configurations. As a simple example, a two layer stack system will be studied, where both layers have same binder, same volume ratio of composites and same thickness, but different scatterer size.

Figures 5.14 shows that there is a significant difference in the optical response due to the arrangement of particles. In figure 5.14-(a), where the first layer contains the big particles ($r = 1$ μm), the reflectance spectra quite high over the spectra and it is relatively flat (stable). Also, it is important to note that the absorptance in the NIR is much lower than for the opposite configuration (fig 5.14-(b)), where the first layer has the small particles ($r = 0.2$ μm) and which reflectance is much more light dependent, since it decreases with increasing wavelength much quicker than in configuration (a). This result can be explained considering previous results presented in this chapter; bigger particles backscatter more at long wavelengths corresponding to the bigger absorption bands. Thus, reflecting those wavelengths as soon as they get inside the matrix is an easy way to prevent absorption.

5.4 Conclusion

In this chapter we introduced an extended version of the classical four-flux method, explained how to obtain all the model coefficients needed and then how to analyse heterogeneous media with different composites. Including any attenuation in the matrix is important. Using this method we can easily analyse the extreme cases where material thickness becomes very large, or when extinction governs the flux transfer. However it is important to note that in our formalism we are assuming non-dense media, i.e. that only single scattering events occur. For the study of a highly packed medium multi-scattering effects should be considered (Dlugach et al., 2011; G. A. Niklasson, 1987; W. E. Vargas, 2000). Although here we only analysed dielectric inclusions, this method can be applied to plasmonic materials, but special care should be taken when obtaining the scattering and absorption cross-sections if the scale parameters are large.

Finally, good agreement was obtained between experimental reflectance and reflectance obtained using our model with structural data obtained independently using a SEM.

With the present results our methodology can be used to optimize white paints in order to improve cooling of buildings exposed to solar radiation. As future research, this method can be extended in order to include: angular dependence, rough interfaces or generalize the geometry of the phases (inclusions).

Chapter 6

Rough Surfaces

Rough surfaces have been studied extensively for their scattering properties, e.g. Letnes (2012) investigated the polarization due to anisotropic surfaces at a fixed wavelength. Here we are particularly interested in the possibilities of rough metal surfaces for energy efficiency, which would benefit from spectral and angular selectivity. Thus we decided to investigate gold since it has the attractive experimental property of a reasonably strong plasmon resonance while being unaffected by surface oxidation; and also, in our investigations of gold we noted some interesting spectral scattering that became the focus of our analysis.

First we will review some methods and observations of scattering of rough metal surfaces, then we present our chosen methods: the *C-methods* and GRF generation; followed by our discussion on the surface random effects on the angular optical response of rough metals.

The influence of the surface roughness of a material over the behaviour of diffracted light has been widely studied in the literature. At first, understanding of the surface characterisation on the optical properties arose from the discovery made by Wood (1902). He discovered that when light interacts with metallic grid surfaces certain anomalies appear in the diffracted field, anomalies that only were present for p-polarized light, i.e. when the magnetic field is parallel to the grating grooves. Years later, Rayleigh presented an interpretation of those and gave a formula to predict for which incident angles the Wood anomalies appear (Rayleigh, 1907). This is the well-known grating formula:

$$\sin(\theta_n) = \sin(\theta) + n\frac{\lambda}{d}, \tag{6.1}$$

where d is the period of the grating, λ the wavelength and θ, θ_n the incident angle and the diffracted angle of order n, respectively.

But it was not until Fano (1941), that someone gave a qualitative answer to Wood's observations using Maxwell equations. Fano distinguished two kind of anomalies: sharp anomalies (predicted by Rayleigh formula), and diffused anomalies caused by

Surface Plasmon Polaritons (SPP). The roughness of a material not only affects the absorption, but it can also affect the anisotropy response or the polarization state. Thus there are many variables playing a role in the optical response: not only grating structures, but also the determined geometry and periodicity or the level of randomness of such grooves can produce very distinct optical outcomes.

In order to obtain a better understanding of these phenomena, several analytical and computational methods have been developed. A general classification of those methods can be made taking into account the scale ratio between the length parameters of the surface/structure, l, (e.g. average depth of the grooves or period, i.e. any characteristic structural length in any dimension) and the wavelength of the incident light in the material, λ, (refractive index and skin depth should be considered). Thus, three distinct region of study can be made:

(1) $l/\lambda << 1$, the roughness average lateral scale is much smaller than the incident wavelength: in this case *effective medium approximations* (EMA) can be applied;

(2) $l/\lambda \sim 1$, the scale order of roughness and wavelength is similar: in this cases no approximation can be made to simplify the problem, so differential or integration methods are used to solve Maxwell equations;

(3) $l/\lambda >> 1$, grooves much wider than the incident wavelength: in such cases geometric optics can be applies, thus techniques, such as *Ray Tracing*, offer good agreement.

In the first scale regime (scenario (1)), EMA can be used (Aspnes, Theeten, and Hottier, 1979), but this is quite restrictive, particularly for metals because of their small skin depth.

In the third scale regime (3), geometric optics approximations can be applied. *Ray Tracing* methods rely on considering each incoming light as a single ray that rebounds or trespasses the surfaces following Snell's law. Thus, each ray is either trapped inside the material after certain number of rebounds or reflected outwards. The ray-tracing approximation is unlikely to be accurate for our target geometries.

There are several methods that can solve scenario (2); among those there are integral methods (Letnes et al., 2012; A. A. Maradudin and Mills, 1975; Maystre, 1978; Mcgurn and A. Maradudin, 1996; J. Stratton and Chu, 1939; Tsang, Chan, and Pak, 1993) and differential methods (J. Chandezon, Maystre, and Raoult, 1980; Edee et al., 2008; Gotz et al., 2008; Lalanne and Morris, 1996; L. Li, 1993; L. Li, 1996b; L. Li and Jean Chandezon, 1996; Shcherbakov and Tishchenko, 2013), or somewhat more exotic methods that rely on statistical scattering (Tang and Buckius, 2001; Tsang, Chan, and Pak, 1994).

In particular, it is possible to expand the surface as a perturbation series (Letnes et al., 2012; Madrazo and A. A. Maradudin, 1997; Nordam, Letnes, and Simonsen, 2013), within the so-called *reduced Rayleigh equation*. This can be written explicitly as recurrent series (Bruno and Reitich, 1993a; Bruno and Reitich, 1993b; Bruno and Reitich, 1993c), and it was demonstrated that the Padé approximation improves convergence. The results of random surfaces obtained by GRF, in the Rayleigh approximation, can be predicted by integration: A. A. Maradudin and Mills (1975) analysed absorption and scattering of 2D Gaussian surfaces for different combinations of s and p polarizations; Marvin, Toigo, and Celli (1975) analysed the same type of surfaces and compared the validation of the results up to first order, they also discussed a discrepancy between their results for p-p polarized light and a mistake in a previous published article (A. A. Maradudin and Mills, 1975). A. A. Maradudin and Mendez (1993) expanded the perturbation expansion up to fourth order for p-pol, they found retro-reflection enhancement; and O'Donnell (2001) extended A. A. Maradudin and Mendez work up to 8^{th} order comparing his results with McGurn, A. A. Maradudin, and Celli (1985), showing agreement with the results obtained by A. A. Maradudin and Mendez on retro-reflection. These methods are computationally very efficient and the analytical terms of the perturbation theory expansion, found for Gaussian kernels avoid possible sampling problems. Nevertheless these methods are restricted by the Rayleigh approximation applicability (profiles with small slope $h/l_c << 1$), and the GRF integral methods have increasing difficulty due to multidimensional integrals. In this work we want to analyse the scattering effect of surfaces with larger rough heights, consequently we decided to use the C-method which is less restricted by the profile height, and rely on direct ensemble averaging.

Here we present the *C-Method* which has the following advantages and disadvantages:

- Advantages:
  - (i) Works for a wide range of scale sizes.
  - (ii) Allows any surface profile as long as it is differentiable.
  - (iii) The efficiency of the method does not depend on the incident angle, so it is very suitable to study angular dependence.
  - (iv) More accuracy can be obtained increasing the number of orders.
- Disadvantages:
  - (i) It is not very efficient for periods or profile height larger than the incident wavelength.
  - (ii) Limited to differentiable profiles.

(iii) Highly dependent on the eigenvalue problem solving routine.

In this chapter we will use the *C-method* to analyse 1D random profiles; we will present a numerical algorithm to assert good sampling depending on the eigenvalue efficiency. We will use an equivalent 1D method to the random generation method presented in chapter 4. In particular we are interested in the effect of the randomness on the angular optical response and the angular dependence of the colour of rough gold.

6.1 C-Method

The C-Method was first introduced by J. Chandezon, Maystre, and Raoult (1980) and later L. Li (1994) and L. Li (1996a) analysed more rigorously the mathematical considerations that should be considered when analysing non-smooth surfaces. Since its introduction, the C-method has been used and developed by several authors (Edee et al., 2008; Gérard Granet, 1998; L. Li, Jean Chandezon, et al., 1999). This is a differential method that relies on applying a change of coordinates that converts a rough surface into a plane, thus the boundary conditions become much simpler. The main idea is to express the electromagnetic field in an expansion of plane waves, then apply the required change of coordinates, which will modify the differential Maxwell equations. To solve the electromagnetic problem using the boundary conditions it is convenient to express the electric and magnetic fields and the surface characteristic functions in Fourier series; with this done the differential problem becomes a linear system.

One of the main issues of the C-method is identifying the eigenvalues and eigenvectors that represent propagating and evanescent modes. Usually the way to proceed is to order them in Bragg orders, but if a degeneracy appears in the eigenvalues, other methods can be more useful, for example the barycentre method introduced by (Edee et al., 2008). In this chapter we clarify and expand the derivation of J. Chandezon, Maystre, and Raoult (1980) incorporating advances made by L. Li (1994), L. Li (1996a), L. Li (1996b), and L. Li and Jean Chandezon (1996), and demonstrate a method to find the optimal number of orders required.

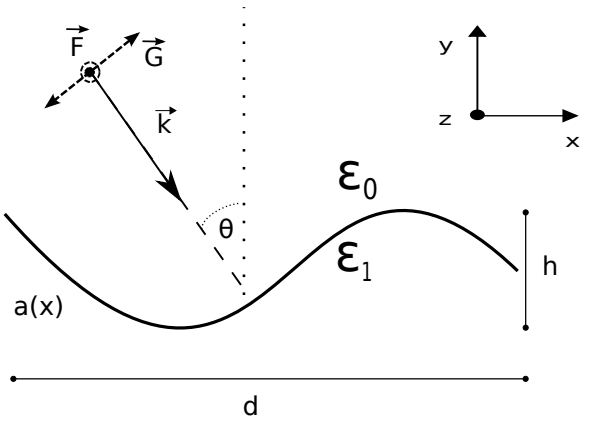

FIGURE 6.1: This diagram presents the scenario under study, which gives a qualitative idea of the main variables of the problem: grooves depth h, period d, electromagnetic fields $\vec{F}$, $\vec{G}$, wave vector $\vec{k}$, incident angle θ, and permittivities of the different layers ϵ_i.

6.1.1 Field Expansion

In this chapter we will focus on 1-dimensional gratings, in other words, structures invariant in one direction (in this chapter we will assume invariance in the z-axis), with all interesting behaviour occurring in a plane perpendicular to this. Thus, to study these systems it is appropriate to use two main polarizations: (s-pol) the electric field is perpendicular to the structural plane; (p-pol)the magnetic field is perpendicular to it. In the particular case of our coordinate system:

$$\vec{E} = E_0\vec{e_3} \quad \text{s-polarization}, \tag{6.2}$$

$$\vec{H} = H_0\vec{e_3} \quad \text{p-polarization}, \tag{6.3}$$

where $\vec{e_3}$ is the unit vector in the z-axis direction.

Throughout this chapter we will assume the configuration presented in figure 6.1. In this scenario, we define the incident electromagnetic field as a superposition of plane waves, defining $F(x, y)$ as the complex electric field (s-polarization) or magnetic field (p-polarization). In order to simplify notation, we will use Gaussian units and we will consider the time dependence factor of $\exp[-i\omega t]$. Also, we will normalize the incident field, i.e. $|F^i(x, y)| \equiv 1$, thus we can express it as a complex phase,

$$F^i = \exp\left[ik_0\left(x\sin\theta - y\cos\theta\right)\right], \tag{6.4}$$

where $\alpha_0 = k_0 \sin\theta$ and $\beta_0 = k_0 \cos\theta$, and with this notation we will define:

$$\alpha_n = \alpha_0 + nK, \tag{6.5}$$

$$\beta_n^2 = k^2 - \alpha_n^2, \tag{6.6}$$

where $k^2 = \epsilon\mu k_0^2$ and eq. 6.5 is the grating formula introduced before (eq. 6.1), with $K = 2\pi/d$ (d being the super-period of the structure) and $\alpha_n = k\sin\theta$. Hence, the whole diffracted field can be expressed as follows:

$$F(x,y,t) = F(x,y)\exp\left[-i\omega t\right], \tag{6.7}$$

$$F(x,y) = \sum_n^{\infty} F_n \exp\left[i(\alpha_n x + \beta_n y)\right]. \tag{6.8}$$

The main innovation of the C-method is using a smart change of coordinates that simplifies the boundary conditions. Thus, let be $a(x)$ the function that defines the surface profile, for the 1D problem we can define the change of coordinates, as follows:

$$(v,u,w) = (x, y - a(x), z), \tag{6.9}$$

in doing so the metric of the space changes and consequently, the differential operators gradient, divergence and curl ($\nabla, \vec{\nabla}\cdot, \vec{\nabla}\times$) are modified as well. Those operators depend on the metric of the space, thus the first step would be to write the metric of the new space. By definition the metric elements are defined as $g^{ij} \equiv < \frac{\partial}{\partial q^i}, \frac{\partial}{\partial q^j} >$ where q^i are the new coordinates, then for our particular case the metric will be as follows:

$$\hat{g} = \begin{pmatrix} 1+\dot{a}^2 & \dot{a} & 0 \\ \dot{a} & 1 & 0 \\ 0 & 0 & 1 \end{pmatrix}, \qquad \hat{g}^{-1} = \begin{pmatrix} 1 & -\dot{a} & 0 \\ -\dot{a} & 1+\dot{a}^2 & 0 \\ 0 & 0 & 1 \end{pmatrix}, \tag{6.10}$$

where we defined $\dot{a} \equiv \frac{d}{dx}a(x)$.

Therefore, under the framework of Riemannian geometry we can express those operators for an arbitrary set of coordinates B.2, thus we can express the Maxwell equations in the new set of coordinates as well.

$$\vec{\nabla}_q \times \vec{E} = -\hat{\mu}\frac{\partial \vec{H}}{\partial t}, \tag{6.11}$$

$$\vec{\nabla}_q \times \vec{H} = \hat{\epsilon}\frac{\partial \vec{E}}{\partial t}, \tag{6.12}$$

where the sub-index q in $\vec{\nabla}_q$ refers to the new coordinates system, and $\hat{\mu}, \hat{\epsilon}$ are the permeability and permittivity tensors. Thus, the equations 6.12 are mathematically equivalent to the Maxwell equations 2.1 if and only if μ and ϵ are defined as follows:

$$\hat{\mu} = \mu\hat{g}^{-1}\sqrt{det(\hat{g})}, \tag{6.13}$$

$$\hat{\epsilon} = \epsilon\hat{g}^{-1}\sqrt{det(\hat{g})}. \tag{6.14}$$

Lets consider first the s-pol. case, using equations 6.12 we will re-express the vectorial equations into scalar. In order to make the notation clearer, as this change of coordinates (6.9) leaves invariant the first and third axis, we will keep calling the first axis x and the third z.

$$\begin{pmatrix} \partial_u E_z \\ -\partial_x E_z \\ 0 \end{pmatrix} = ik_0\mu \begin{pmatrix} 1 & -\dot{a} & 0 \\ -\dot{a} & 1+\dot{a}^2 & 0 \\ 0 & 0 & 1 \end{pmatrix} \begin{pmatrix} H_x \\ H_u \\ 0 \end{pmatrix}, \tag{6.15}$$

where $\partial_k = \frac{\partial}{\partial k}$ is the partial derivative respect the variable $k \in \{x, u, z\}$.

$$\begin{pmatrix} 0 \\ 0 \\ \partial_x H_u - \partial_u H_x \end{pmatrix} = ik_0\epsilon \begin{pmatrix} 1 & -\dot{a} & 0 \\ -\dot{a} & 1+\dot{a}^2 & 0 \\ 0 & 0 & 1 \end{pmatrix} \begin{pmatrix} 0 \\ 0 \\ E_z \end{pmatrix}, \tag{6.16}$$

$$\partial_u H_x - \partial_x H_u = i\epsilon k_0 E_z, \tag{6.17}$$

$$\partial_u E_z = i\mu k_0 (H_x - \dot{a}H_u), \tag{6.18}$$

$$\partial_x E_z = i\mu k_0 (\dot{a}H_x - (1+\dot{a}^2)H_u). \tag{6.19}$$

From this point we will use the knowledge of the periodicity of our surface profile to express previous equations in a more suitable way. As we know that the profile, function $a(x)$, is periodic in the x direction, and we are interested in how the electromagnetic field (e.m.f.) propagates along the incident plane, u direction, we will use equations 6.17 - 6.19 to re-express the change of the e.m.f. in the vertical direction, $\partial_u F$, in terms of $\partial_x F$, with F either the electric or magnetic field. Therefore, using

equations 6.18 and 6.19:

$$\begin{aligned}
\partial_u E_z &= i\mu k_0 \left(H_x - \dot{a} \left[(1+\dot{a})^{-1} (\dot{a} H_x) - \frac{1}{i\mu k_0} \partial_x E_z \right] \right), \\
\partial_u E_z &= \left(\frac{\dot{a}}{1+\dot{a}^2} \right) \partial_x E_z + i\mu k_0 \left(H_x - \left(\frac{\dot{a}^2}{1+\dot{a}^2} \right) H_x \right), \\
\partial_u E_z &= \left(\frac{\dot{a}}{1+\dot{a}^2} \right) \partial_x E_z + i\mu k_0 \left(\frac{1}{1+\dot{a}^2} \right) H_x. \qquad (6.20)
\end{aligned}$$

In the following lines we will express the change of the magnetic field on the vertical direction using equations 6.17 and 6.18.

$$\begin{aligned}
\partial_u H_x &= i\epsilon k_0 E_z + \partial_x \left[\frac{\dot{a}}{1+\dot{a}^2} H_x \right] - \frac{1}{i\mu k_0} \partial_x \left[\frac{1}{1+\dot{a}^2} \partial_x E_z \right], \\
\partial_u H_x &= \frac{i}{\mu k_0} \left(k^2 E_z + \partial_x \left[\frac{1}{1+\dot{a}^2} \partial_x E_z \right] \right) + \partial_x \left[\frac{\dot{a}}{1+\dot{a}^2} H_x \right]. \qquad (6.21)
\end{aligned}$$

Similarly, we can solve Maxwell equations 6.12 in the new coordinate system for p-polarized light.

$$\begin{pmatrix} \partial_u H_z \\ -\partial_x H_z \\ 0 \end{pmatrix} = -ik_0\epsilon \begin{pmatrix} 1 & -\dot{a} & 0 \\ -\dot{a} & 1+\dot{a}^2 & 0 \\ 0 & 0 & 1 \end{pmatrix} \begin{pmatrix} E_x \\ E_u \\ 0 \end{pmatrix}, \qquad (6.22)$$

$$\begin{pmatrix} 0 \\ 0 \\ \partial_x E_u - \partial_u E_x \end{pmatrix} = ik_0\mu \begin{pmatrix} 1 & -\dot{a} & 0 \\ -\dot{a} & 1+\dot{a}^2 & 0 \\ 0 & 0 & 1 \end{pmatrix} \begin{pmatrix} 0 \\ 0 \\ H_z \end{pmatrix}, \qquad (6.23)$$

$$\partial_u E_x - \partial_x E_u = -i\mu k_0 H_z, \qquad (6.24)$$

$$\partial_u H_z = -i\epsilon k_0 (E_x - \dot{a} E_u), \qquad (6.25)$$

$$\partial_x H_z = -i\epsilon k_0 (\dot{a} E_x - (1+\dot{a}^2) E_u). \qquad (6.26)$$

By inspection is straight forward to see that equations 6.17-6.19 and equations 6.24-6.26, are identical under the change $H \leftrightarrow E$ and $\mu \leftrightarrow -\epsilon$. Thus, mathematically these systems are equivalent. Therefore using the result from equations 6.20 and 6.21, we will study the following generalized system.

$$\partial_u F = \left(\frac{\dot{a}}{1+\dot{a}^2}\right)\partial_x F + i\varphi k_0 \left(\frac{1}{1+\dot{a}^2}\right) G, \tag{6.27}$$

$$\partial_u G = \frac{i}{\varphi k_0}\left(k^2 F + \partial_x\left[\frac{1}{1+\dot{a}^2}\partial_x F\right]\right) + \partial_x\left[\frac{\dot{a}}{1+\dot{a}^2} G\right], \tag{6.28}$$

$$\text{s-pol} = \begin{cases} F = E_z \\ G = H_x \\ \varphi = \mu \end{cases}, \qquad \text{p-pol} = \begin{cases} F = H_z \\ G = E_x \\ \varphi = -\epsilon \end{cases}.$$

Finally, our problem has been reduced to solve equations 6.27 and 6.28 where the derivatives in the vertical direction are expressed in terms of the derivative in the x direction. Thus, we can use this to convert this differential system to a linear one. We will use that the profile function $a(x)$ and its derivatives have periodicity in the x direction, and as we are assuming them continuous we can express them as Fourier expansions. Also, by *Floquet-Bloch theorem* we can express the EMF as a Fourier expansion with the same periodic constant than the profile function.

$$F(x,u) = \sum_{m=-\infty}^{\infty} F_m(u) \exp\left[i\alpha_m x\right], \tag{6.29a}$$

$$G(x,u) = \sum_{m=-\infty}^{\infty} G_m(u) \exp\left[i\alpha_m x\right], \tag{6.29b}$$

$$\frac{1}{1+\dot{a}^2} = \sum_{s=-\infty}^{\infty} C_s \exp\left[iKsx\right], \tag{6.30a}$$

$$\frac{\dot{a}}{1+\dot{a}^2} = \sum_{s=-\infty}^{\infty} D_s \exp\left[iKsx\right]. \tag{6.30b}$$

Therefore using these infinity series expressions into equations 6.27-6.28, and taking into account the *Cauchy Product* $\sum_m X_m \sum_n Y_n = \sum_m \sum_n X_m Y_{n-m}$, it is easy to see that equations 6.27-6.28 get reduced to an infinite number of linear equations.

$$-i\partial_u F_m = D_{s-m}\alpha_m F_m + \varphi k_0 C_{s-m} G_m, \tag{6.31}$$

$$-i\partial_u G_m = \frac{1}{\varphi k_0}\left(k^2 - \alpha_s C_{s-m}\alpha_m\right) F_m + \alpha_s D_{s-m} G_m, \tag{6.32}$$

which can be expressed in matrix form as an eigenvalue problem:

$$-i\partial_u\psi = \begin{pmatrix} D_{s-m}\alpha_m & \varphi k_0 C_{s-m} \\ \frac{1}{\varphi k_0}\left(k^2 - \alpha_s C_{s-m}\alpha_m\right) & \alpha_s D_{s-m} \end{pmatrix}\psi, \tag{6.33}$$

with $\psi = (F_1, F_2, \ldots, G_1, G_2, \ldots)^T$. This formula is most similar to that used by J. Chandezon, Dupuis, et al. (1982) and J. Chandezon, Maystre, and Raoult (1980) where different eigenvalue problems are solved for each polarization, while in the framework used by L. Li (1994) both polarizations are included in the 4×4 eigenvalue matrix problem.

6.1.2 Boundary and Initial Conditions

Solving the eigenvalue problem (eq. 6.33) it is possible to obtain an expression of the electromagnetic field in terms of the eigenvectors and eigenvalues of the system matrix:

$$\psi(u) = \sum_{n=1}^{\infty} b_n \psi_n \exp[i r_n u], \tag{6.34}$$

where ψ_n are the eigenvectors and r_n the eigenvalues of the system, and b_n constants to be determined using boundary and initial conditions.

From Maxwell's equations it can be shown that the tangential component of the electric field ($\vec{E}$) and the induced magnetic field ($\vec{H}$) have to be continuous at every interface, which implies that ψ has to be continuous at the interfaces. Thus, using this condition the electromagnetic fields at different mediums can be related.

In order to solve the problem it is only left to impose the initial conditions, and thus, relate the energy in the incident medium with the energy at the bottom one. It is also at this step where the C-method mainly distinguishes itself from the Rayleigh approximation: in the initial medium it is assumed that the diffracted propagating field can be expanded as plane-waves, while the evanescent field has decayed completely: this approach greatly improves the numerical accuracy for deep gratings.

Therefore, we can relate the electromagnetic field at the bottom of the stack with the evanescent field at the top plus the incident and the asymptotic propagating field.

$$\psi_b = \psi_t^{ev} + \psi_0 + \psi_t^{pr}, \tag{6.35}$$

where ψ_b is the e.m. field at the bottom medium, ψ_t^{ev}, ψ_t^{pr} the evanescent and asymptotic propagating e.m. field at the top and ψ_0 the incident e.m. field. Note that all these fields are expressed in the new coordinate system.

6.1.3 Diffracted Field

Hence, in this section, we will express explicitly the electric and magnetic field and we will show their spatial representation, showing that the continuity of the tangential part of these fields is preserved on the interface, as we expect.

As the continuity of the electromagnetic field is independent of the coordinate system, for convenience, we will choose the coordinate system given by the transformation in equation 6.9, i.e. the *x,u-space* where the interface is flat. Thus, substituting equation 6.34 into equations 6.29a and 6.29b the parallel components to the interface of the electric $\vec{E}$ and magnetic $\vec{H}$ fields can be fully determined for any coordinate point (x, u).

$$F(x,u) = \sum_{m,n=-\infty}^{\infty} b_n^F \psi_n^F \exp\left[i(r_n u + \alpha_m x)\right], \tag{6.36}$$

$$G(x,u) = \sum_{m,n=-\infty}^{\infty} b_n^G \psi_n^G \exp\left[i(r_n u + \alpha_m x)\right], \tag{6.37}$$

where the superscripts F and G on the vectors b_n and ψ_n refer to the components related to the fields F and G respectively. Therefore using these definitions (eq. 6.36-6.37), we can represent the tangential components of the electromagnetic field.

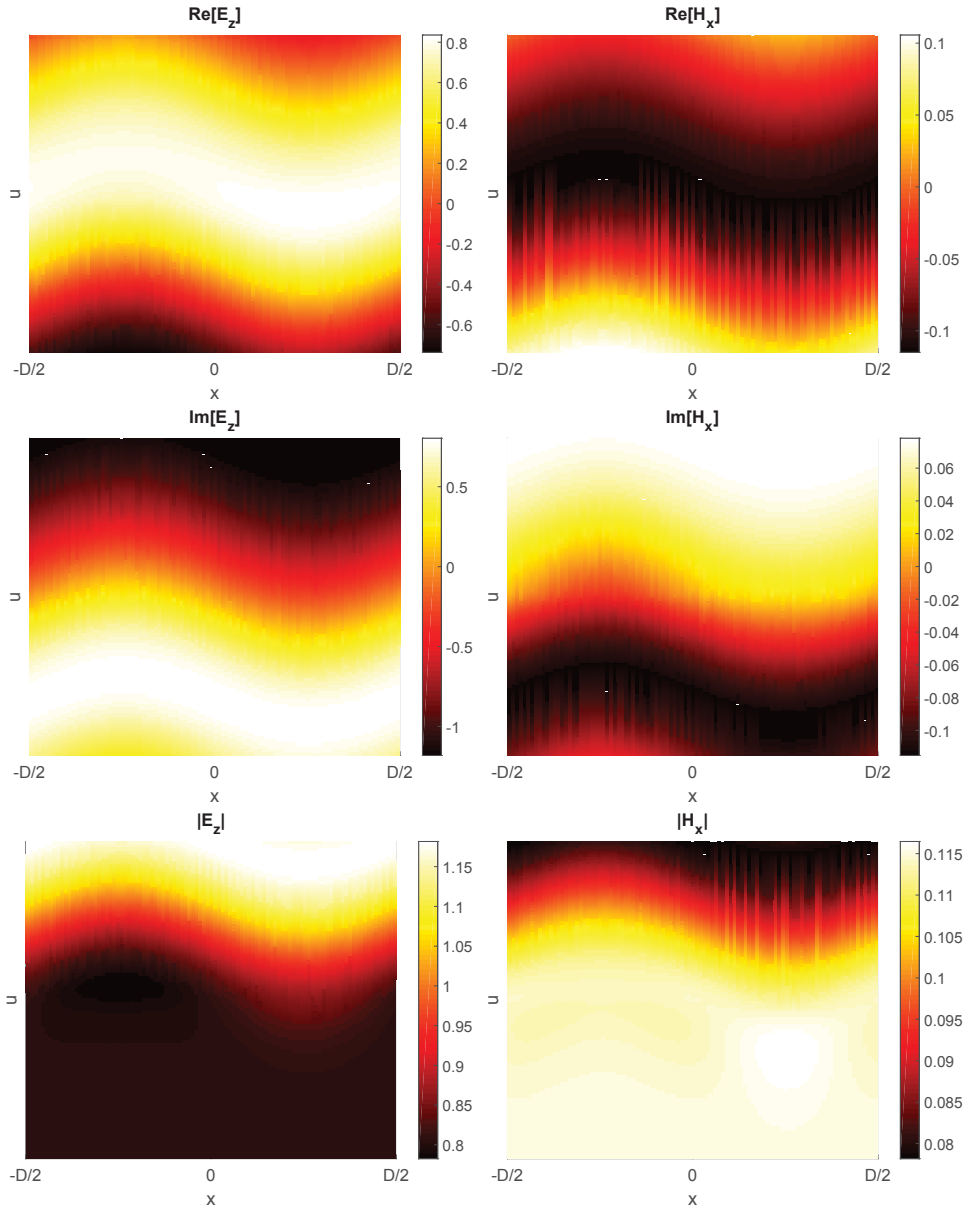

FIGURE 6.2: These colormaps show the parallel components of the electromagnetic field interacting with a sinusoidal profile made of glass (n=1.5), this response is the result of an incident s-polarized plane wave (electric field parallel to the plane of incidence) propagating at normal angle to the material surface.

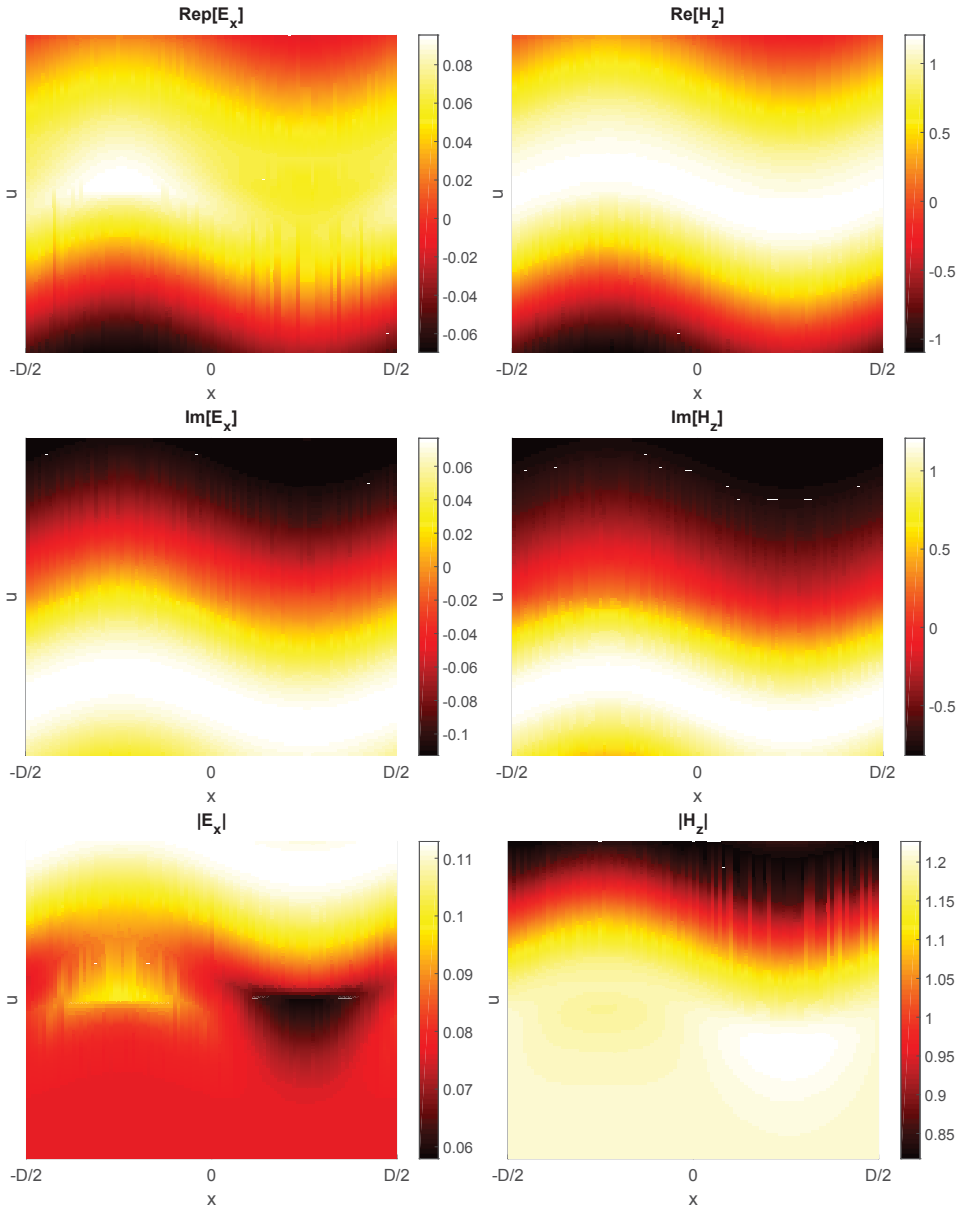

FIGURE 6.3: These colormaps show the parallel components of the electromagnetic field interacting with a sinusoidal profile made of glass (n=1.5), this response is the result of an incident p-polarized plane wave (magnetic field parallel to the plane of incidence) propagating at normal angle to the material surface.

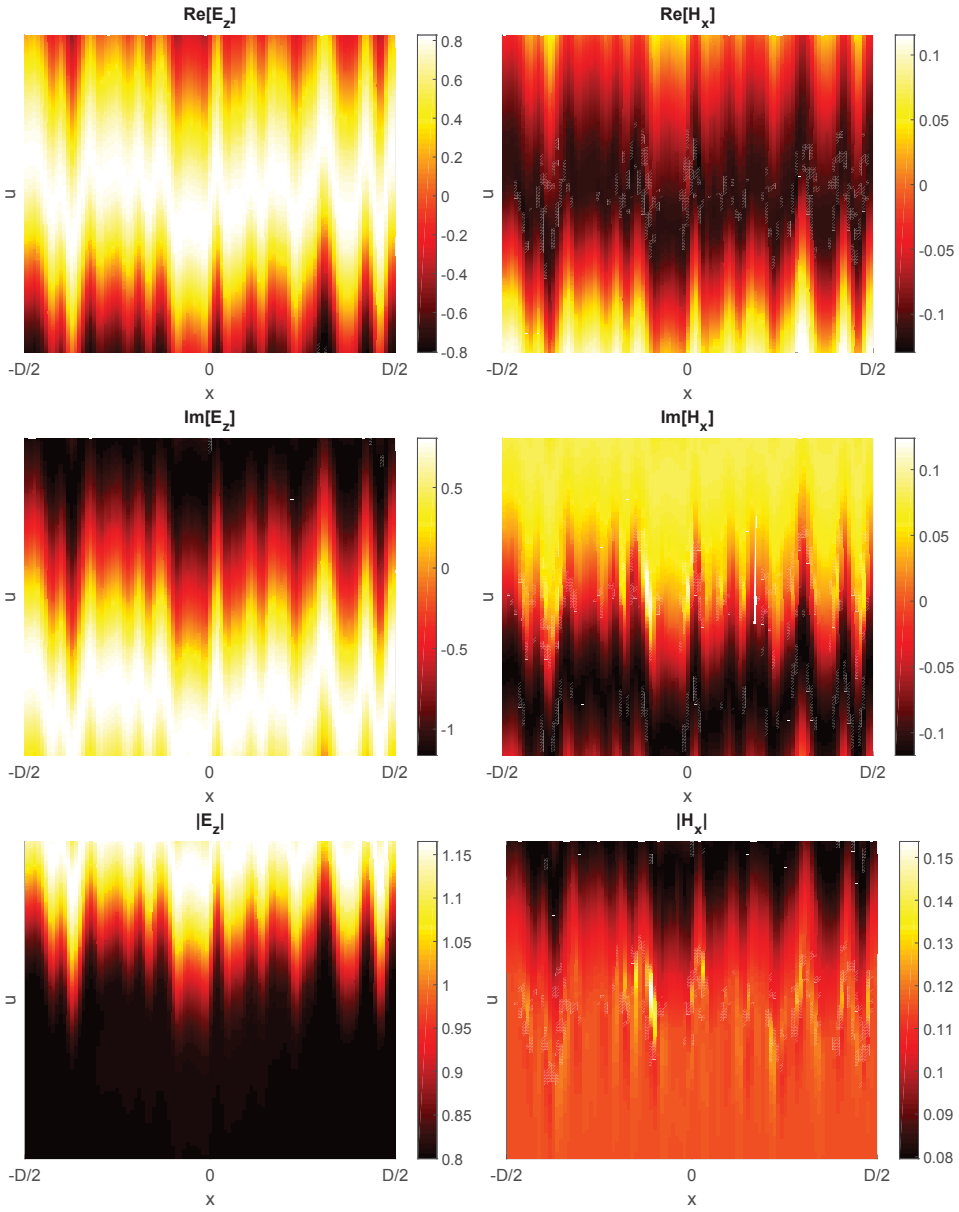

FIGURE 6.4: These colormaps show the parallel components of the electromagnetic field interacting with a random generated profile made of glass (n=1.5), this response is the result of an incident s-polarized plane wave (electric field parallel to the plane of incidence) propagating at normal angle to the material surface.

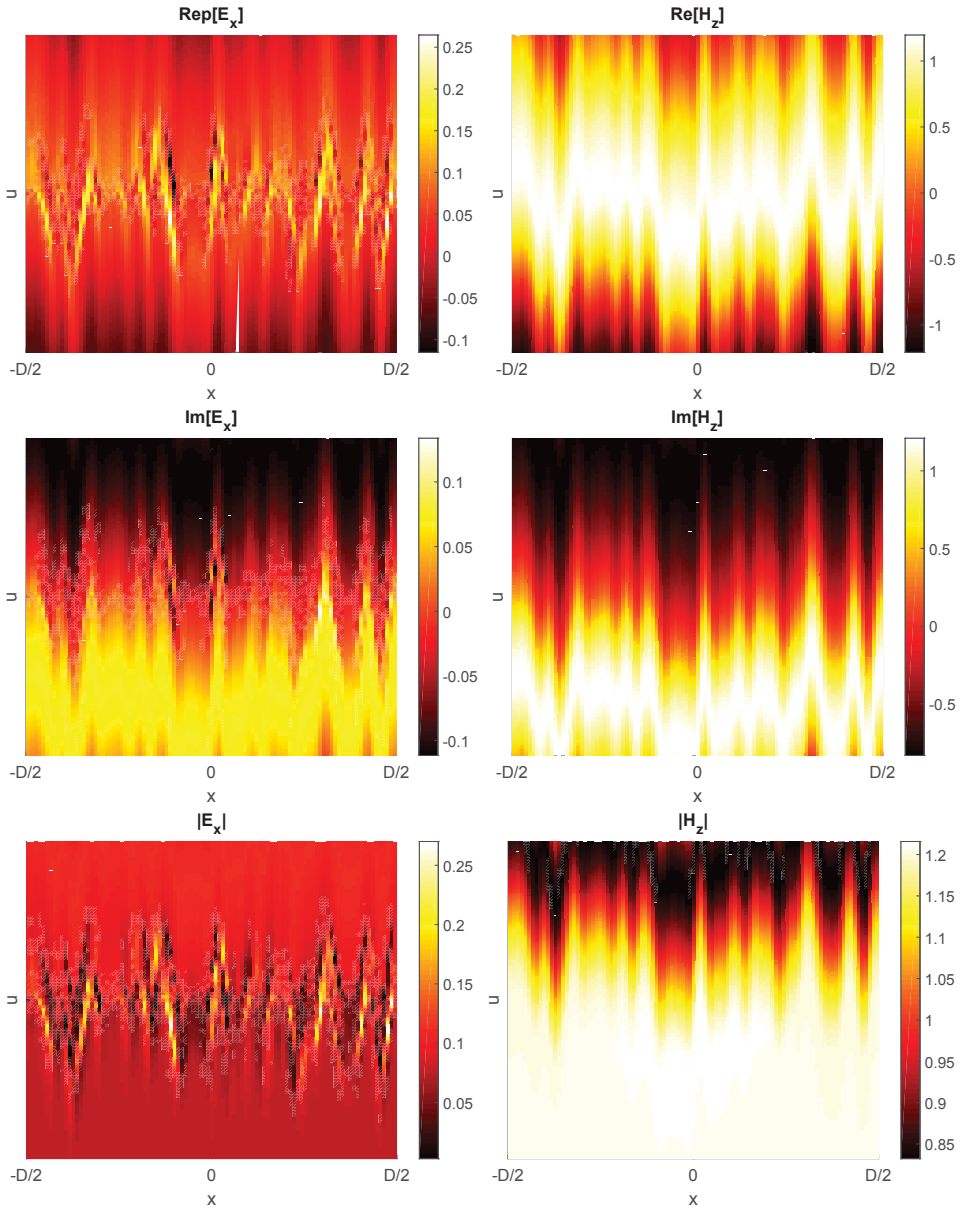

FIGURE 6.5: These colormaps show the parallel components of the electromagnetic field interacting with a random generated profile made of glass (n=1.5), this response is the result of an incident p-polarized plane wave (magnetic field parallel to the plane of incidence) propagating at normal angle to the material surface.

6.1.4 Energy Conservation

In this section we present a method, already introduced by J. Chandezon, Maystre, and Raoult (1980), that allows us to find the reflected and transmitted energy in an arbitrary interface. That paper gives an expression that only considers the propagating modes, since those are the only ones that carry energy. Nonetheless, here we give the

general mathematical solution that considers the evanescent modes as well (eq. 6.50). It is important to note that our expression coincides with the results introduced by Chandezon when only propagating modes are considered.

The reflectance and transmittance of each mode is calculated using *Poynting Theorem*, which states that the rate of energy transfer is equal to the total amount of energy getting in and out of a certain volume plus the work done by the flow of free charges:

$$\frac{\partial u}{\partial t} = \nabla \cdot \vec{S} + \vec{J} \cdot \vec{E}. \tag{6.38}$$

If we consider that there is no flux of energy and that there are not free charges ($\vec{J} = 0$), *Poynting Theorem* get reduced to the following expression:

$$0 = \int_V \vec{\nabla} \cdot \vec{S} dV. \tag{6.39}$$

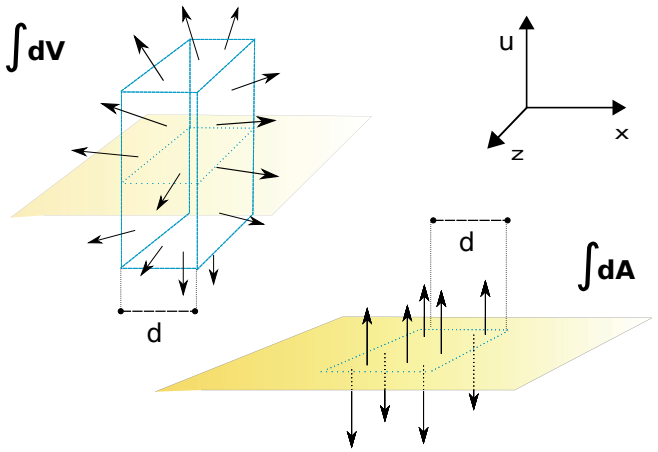

FIGURE 6.6: Diagram of the regions of integration using Poynting Theorem. Note that the volume of integration is in the new coordinate system (x, u, z), where the interface is flat.

Thus, using eq. 6.39 we can find the efficiency for each mode in terms of the eigenvectors of the system. As the Poynting Theorem is satisfied for any volume, to solve the integral equation, we will consider a cube with sides equal to the period of the grating (d) as a volume of integration.

Using the divergence theorem, the previous equation (eq.6.39) can be expressed as a surface integral:

$$0 = \oint_A \vec{S} \cdot \vec{n} dA, \tag{6.40}$$

$$0 = \oint_A \left(\vec{S}_{in} - \vec{S}_{out} \right) \cdot \vec{n} dA, \tag{6.41}$$

$$\oint_A \vec{S}_{in} \cdot \vec{n} dA = \oint_A \vec{S}_{out} \cdot \vec{n} dA, \tag{6.42}$$

$$1 = \frac{\oint_A \vec{S}_{out} \cdot \vec{n} dA}{\oint_A \vec{S}_{in} \cdot \vec{n} dA}. \tag{6.43}$$

As incident light with unit intensity is considered the denominator of equation 6.43 is equal to one, therefore the problem is reduced to solve the flux of outgoing energy.

$$\oint_A \vec{S}_{out} \cdot \vec{n} dA = \oint_A (F_z G_x^* \vec{e_2} - F_z G_u^* \vec{e_1}) \cdot \vec{n} dA \tag{6.44}$$

$$= \oint_A F_z G_x^* dA, \tag{6.45}$$

where we have used that $\vec{e_2}$ is parallel to the surface normal $\vec{n}$. From this point the notation $F = F_z$ and $G = G_x$ is considered again, and in order to solve the surface integral the Fourier expansion of the electromagnetic field defined in equations 6.29 is used. Thus, as *Poynting's Theorem* is satisfied for any arbitrary volume, for convenience we will integrate over a period.

$$\oint_A F \cdot G^* dA = \oint_A \sum_n F_n(u) e^{i\alpha_n x} \sum_m G_m^*(u) e^{-i\alpha_m x} dA \tag{6.46}$$

$$= \oint_A \sum_{n,m} F_n(u) G_m^*(u) \delta_{nm} dA \tag{6.47}$$

$$= \oint_A \sum_n \left(\sum_p F_{n,p} e^{ir_p u} \sum_q G_{n,q}^* e^{-ir_q^* u} \right) dA \tag{6.48}$$

$$= \oint_A \sum_n \sum_{p,q} F_{n,p} G_{n,q-p}^* e^{i(r_p - r_{q-p}^*)u} dA \tag{6.49}$$

$$= A \sum_n \sum_p F_{n,p} G_{n,k}^* \quad \text{with } p, k \text{ such as } r_p = r_k^*, \tag{6.50}$$

where the notation $\sum_{n,m}$ means $\sum_{n=0}^{\infty} \sum_{m=0}^{m=n}$. In the step from equation 6.46 to 6.47, we have used that we are integrating over the period of α_n, so functions $e^{i\alpha_m x}$ and

$e^{-i\alpha_n x}$ are orthonormal for any $n \neq m$:

$$\int_0^d e^{i\alpha_m x} \cdot e^{-i\alpha_m x} dx = \delta_{mn}. \tag{6.51}$$

From 6.48 to 6.49 we have used the *Cauchy Product*. Equation 6.50 has been obtained considering that K and u have the same period, and so, when integrating over a multiple of their period the only 'surviving' terms are those which zero the exponential powers, i.e. $r_p - r^*_{q-p} = 0$, which implies $r_p = r^*_{q-p}$.

Finally, from a physics point of view the only terms that will carry energy in the direction orthogonal to the surface are the propagating modes, which have real eigenvalues. Therefore from eq.6.50 if only real eigenvalues are considered the outgoing efficiency gets reduced to the following:

$$\oint_A \vec{S}_{in} \cdot \vec{n} dA = \oint_A \vec{S}_{out} \cdot \vec{n} dA \tag{6.52}$$

$$\varepsilon = \sum_n \sum_p F_{n,p} G^*_{n,p}, \tag{6.53}$$

$$\varepsilon = \sum_n \varepsilon_n, \tag{6.54}$$

in order to simplify the final result we have considered the incoming energy equal to one, i.e. LHS of equation 6.52 is equal to one. Thus, expressing it for each mode,

$$\varepsilon_n = \sum_p F_{n,p} G^*_{n,p}, \tag{6.55}$$

which is the result given in J. Chandezon, Maystre, and Raoult (1980).

6.2 Minimizing Propagation of Uncertainty

The method presented in previous sections solves the diffraction problem of rough surfaces. Nevertheless, the numerical results converge to the analytical solution depending on the number of modes used, i.e. how fine is the sampling, and on the numerical accuracy of the program used to solve the eigenvalue problem. Thus, one has to consider these two things before accepting a numerical result as good.

For simple surface functions a low number of modes achieves good accuracy; on the other hand, if the function defining the grooves is more complex (e.g. is rough) then choosing the right number of modes is crucial. We propose a method to determine this number:

1. Find the accuracy of the eigenvalues found (δ_{cc}).

2. Find the accuracy of the energy conservation principle introduced in previous section (sec. 6.1.4).

3. Compare both results, if the accuracy of (1) and (2) are of the same order we accept the results, otherwise we reject the results.

The scheme that we just presented follows a basic rule on propagation of uncertainty, which can be summarized as follows: *a numerical result can be as good as the accuracy that the computer or program can give*.

Thus, considering this, in (1) we calculate the accuracy of the pair of complex-conjugate eigenvalues, and consider the worst scenario, i.e. the pair that gives worst accuracy:

$$\delta_{cc} = \max_i |\mathrm{Im}[z_i] + \mathrm{Im}[z_i^*]|, \tag{6.56}$$

where z_i are non-pure real eigenvalues found numerically [1]. The reason to consider complex-conjugate pairs that have non-zero imaginary part, is that those pairs always exist in our framework; or more precisely, due to the symmetry of the profile and the plane wave incident angle, it can happen that propagating modes (real eigenvalues) are not exactly paired, and therefore we cannot rely on an algorithm that uses them to compare the complex-conjugate efficiency. It is important to remark that δ_{cc} is our best accuracy, therefore any accuracy that we can obtain through numerical and algebraic operations of the eigenvalues and eigenvectors must be equal or worse than δ_{cc}.

With this point in mind, in step (2), we will analyse the efficiency expression that we found in previous section. Let's consider a system without incoming light, under that condition equation 6.41 gets reduced to the following obvious equation:

$$0 = \oint_A \vec{S}_{out} \cdot \vec{n} dA, \tag{6.57}$$

this relation tells us that equation 6.50 must be equal to zero as well. In other words, it gives us an intrinsic accuracy that our eigenvectors must satisfy:

$$\delta_{pm} = \sum_n \sum_p F_{n,p} G^*_{n,k} \quad \text{with } p,k \text{ such as } r_p = r_k^*, \tag{6.58}$$

Thus, a good sampling number (N_0) is obtained minimizing $\delta_{pm} - \delta_{cc}$, i.e. $\delta_{pm} \sim \delta_{cc}$.

Finally, step (3) summarizes the information obtained in steps (1) and (2) in logical statements: (i) in our methodology a tolerance value is set as uncertainty limit that determines a maximum value of δ_{cc}, (ii) the next logical statement verifies that $\delta_{pm} \geq \delta_{cc}$. Figure 6.8 shows how profiles with same characteristics, but different levels

[1] Note that by the complex-conjugate definition, δ_{cc} should be exactly zero; nonetheless z_i and z_i^* are numerically found eigenvalues, i.e. they are complex-conjugate pairs to within a given tolerance.

of randomness need a different sampling number to achieve sensible results. From this figure it can be seen that the behaviour of δ_{cc} and δ_{pm} with N_0 are completely complementary; δ_{pm} decreases with increasing N_0 while δ_{cc} increases; consequently an optimal point is always achieved. Thus, if (i) is not satisfied the sampling number must be increased in order to achieve a better sampling; if (ii) is not verified there is an oversampling causing false efficiency results, so the sampling number has to be reduced. Figure 6.7 is a schematic of this process.

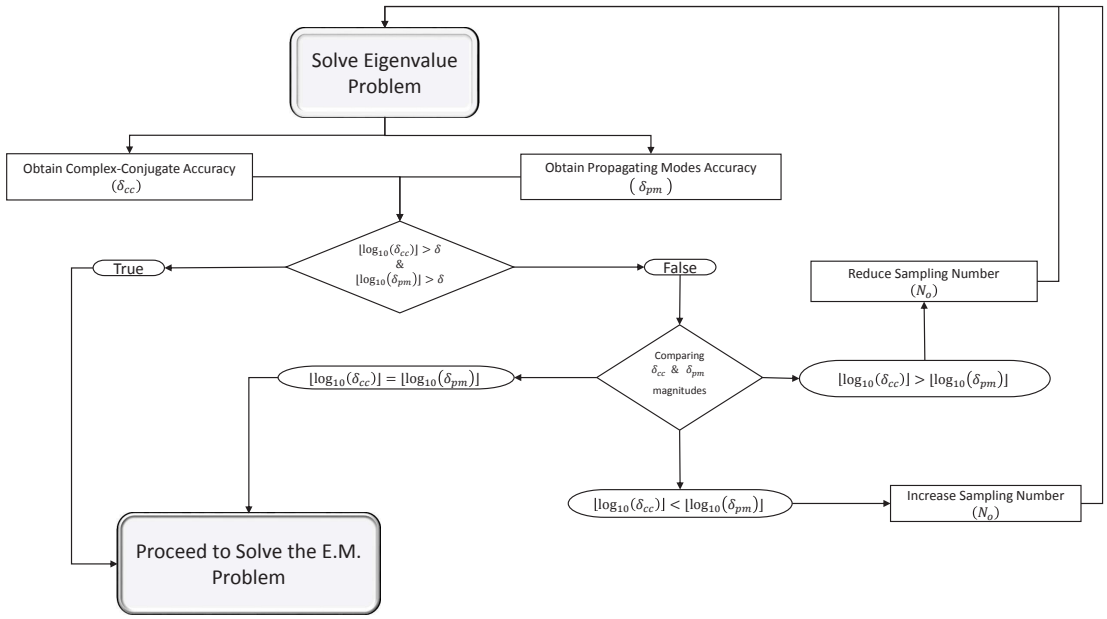

FIGURE 6.7: Logical diagram of the algorithm used to attain the required number of modes for a good accuracy. The parameter δ is the breaking point for symmetric and smooth profiles (e.g $\sin(x)$), in our code is set to be -8. This is needed because in these profiles the convergence of δ_{pm} is faster than δ_{cc} and thus, the optimization of N_0 is not needed.

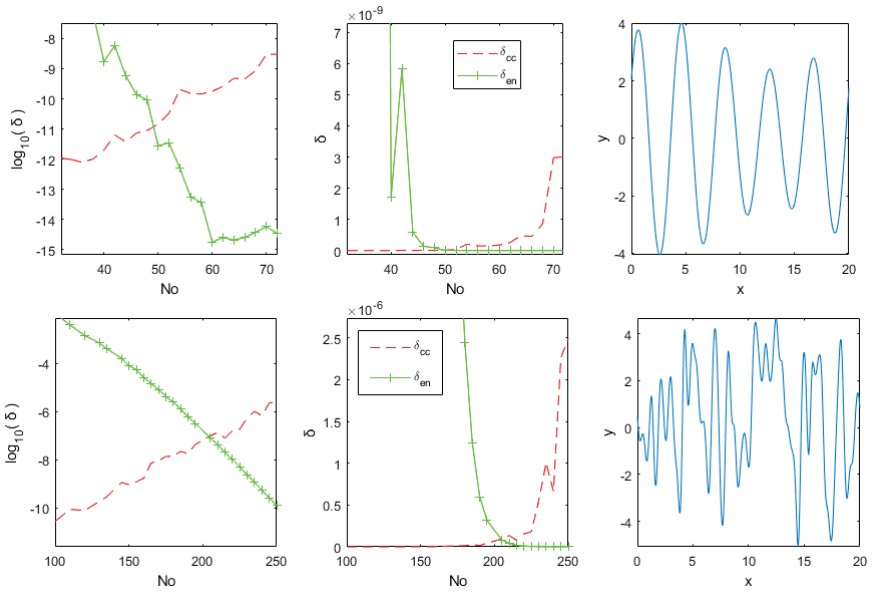

FIGURE 6.8: These images show the evolution of δ_{pm} and δ_{cc} in terms of the number of modes. (left column) Comparison of the logarithm accuracies; (centre column) comparison of the accuracies values; (right column) profile under which the comparisons have been made. These calculations where made assuming an aluminium material illuminated under normal incidence with a wavelength of $10\mu m$; the grooves have an averaged height of $2.3\mu m$ and the grating has a period of $20.1\mu m$.

6.3 Generating Random Surface Profiles

In a real-life scenario material surfaces present certain random configurations, and as has been noted in the introduction of this chapter the material termination produces significant variations on the optical response. Thus, to take into account this randomness it is necessary to create equivalent random profiles that are statistically equivalent, in doing so, the optical response can be obtained by averaging the results of a large ensemble of these similar random surfaces.

To obtain statistically similar functions, these have to have some degree of control, i.e. they cannot be fully random functions, otherwise averaging results would be meaningless. These pseudo-random functions will be created given some characteristic parameters: the period, the noise (randomness) and the number of sub-periods (oscillations).

The method that we use is a type of *random phase approximation* (RPA), the statistical characteristics of this probability density has been widely studied (Bardeen et al., 1986), and these kind of densities have been used in different disciplines to describe natural phenomena, as an example RPA has been used to describe energy density fluctuations in condensed matter and quantum physics (Beck, 1971; Olsen et al., 2011;

Pitarke and J. P. Perdew, 2003; X. Ren et al., 2011; Xinguo Ren, Rinke, and Scheffler, 2009; Yan, John P. Perdew, and Kurth, 2000). In a related work, Edee et al. (2008), A. A. Maradudin (2007), and Tsang, Kong, et al. (2000) used RPA to generate pseudo-random profiles using a similar methodology to the one presented here. This method is equivalent to the method that we use in chapter 4; here we are using 1D GRF filtered by a Gaussian kernel (but without cutting the filtered signal).

The pseudo-random profile generation that we use in this work can be simplified in the following points:

1. Create a probability distribution of frequencies with the given period and standard deviation (randomness parameter).
2. Apply a random phase at each frequency.
3. Use Fourier transformation to obtain the profile in real space.

Selecting the probability density to generate the random profiles is essential; in this work we will focus on Gaussian kernels to filter the random signal, since they seem to be representative of real roughness (A. A. Maradudin, 2007). Thus we will generate our surfaces by continuous stationary random processes distributed normally with a zero mean value $\mu = 0$,

$$\rho(k) = \frac{h^2}{\sigma\sqrt{2\pi}} \exp\left(-\frac{k^2}{2\sigma^2}\right), \tag{6.59}$$

where σ is the standard deviation of the distribution, and h the *root-mean square* (RMS) of the surface height. In the following sections we will analyse the effects of the surface correlation length, thus we can re-write equation 6.59 knowing that $l_c = \sqrt{\frac{2}{\sigma^2}}$,

$$\rho(k) = \frac{h^2 l_c}{2\sqrt{\pi}} \exp\left(-\frac{k^2 l_c^2}{4}\right). \tag{6.60}$$

Secondly, in order to obtain the random behaviour desired a random phase is applied to the probability density (eq.6.60):

$$\varrho(k) = \rho \cdot \exp(i2\pi\phi), \tag{6.61}$$

where ϕ is a uniform random number.

Finally, a Fourier transformation is applied to $\varrho(k)$ in order to obtain the profile function in real space:

$$f(x) = \hat{\varrho} = \int_{-\infty}^{+\infty} \varrho \cdot \exp\left(i2\pi kx\right) dk, \tag{6.62}$$

where $\hat{\varrho}$ indicated the Fourier transformed of ρ. With this methodology we can define random surfaces given their average RMS height and correlation length.

The size ratio between the period of the grating and the correlation length define the amount of "randomness" or noise on a surface for a given height.

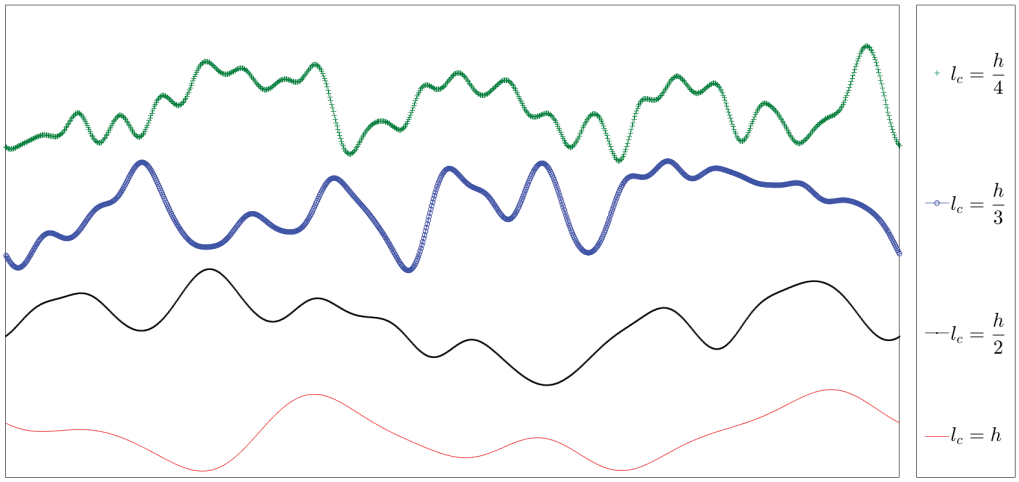

FIGURE 6.9: Four different random profiles using different correlation lengths. l_c is expressed as a fraction of a fixed RMS height h.

In figure 6.9 we can see that for smaller correlation lengths the apparent randomness increases. Thus in the next sections we will focus on the effect of l_c.

6.4 Discussion of the Optical Response of Random Rough Surfaces

In this section we will use the theoretical framework and methodology presented in previous sections to analyse different roughness scenarios.

The overview of this section is the following:

- Subsection 6.4.1: Validation of our methodology.
- Subsection 6.4.2: Analysis of randomness and groove depth of random surfaces and materials.
- Subsection 6.4.3: *Effective slope approach* to study the refractive angular spectra.
- Subsection 6.4.4: Discussion the roughness dependence of the colour of gold.

6.4.1 Method Validation

Before we start analysing the characteristics of random profiles, we will use results presented in one of the original papers on the *C-method* as a check of our methodology. To do so, we will replicate the results published in the classical *C-method* paper (J. Chandezon, Dupuis, et al., 1982). Thus in figures 6.10 and 6.11, we show the replication of figures (2) and (3-4) on the paper authored by J. Chandezon, Dupuis, et al. (1982) that we have obtained using our code, the reader can check that both plots are the same.

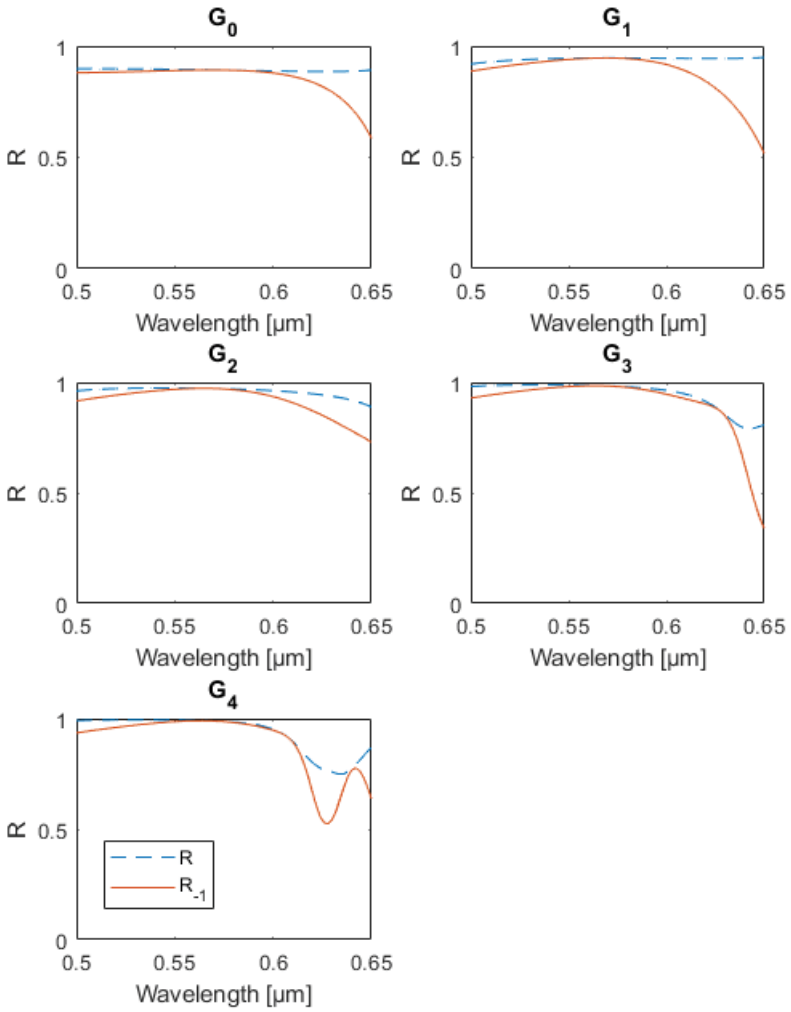

FIGURE 6.10: Replication of figure (2) in the work presented by J. Chandezon, Dupuis, et al. (1982). The parameters used are: groove depth 0.12 μm, period of $1/3$ μm under Littrow configuration. G_0 profile is uncoated Aluminium (Rakić, 1995), on the other hand $G_1 - G_4$ have respectively $1 - 4$ coatings of MgF_2 (0.106 μm) and TiO_2 (0.0602 μm).

In figure 6.10 several systems are simulated under Littrow configuration [2]. Those profiles are sinusoidal aluminium profiles coated with a coating of two layers; the bottom one made of MgF_2 with refractive index $n = 1.39$ and a thickness of 0.106 μm, and the top layer of this coating is made of TiO_2 ($n = 2.45$) with 0.0602 μm thickness. Thus, the G_0 plot is just the uncoated aluminium and the consecutive G_1, G_2, G_3 and G_4 are aluminium profiles coated with one, two, three or four coatings respectively.

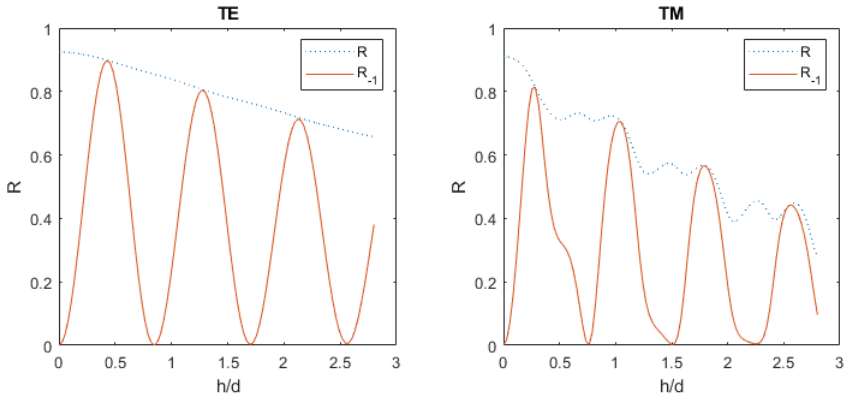

FIGURE 6.11: Replication of figure (3-4) in the work presented by J. Chandezon, Dupuis, et al. (1982). These plots show the total reflectance and -1 order refracted energy depending on the ratio groove depth/period (h/d) for an Aluminium profile. Left picture shows the results for s-polarization (TE) while on the right pictures the profile is illuminated under p-polarized light (TM). The parameters used are: period 0.737 μm, groove depth over period (h/d) from 0 to 2.8, and incident angle of 23.6°.

In figure 6.11, we show (for s-pol and p-pol) the reflectance dependence on the ratio height-period on an aluminium sinusoidal profile.

Thus after checking that our methodology and algorithms agrees with literature results, we continue to the study on the optical dependence on the structural parameters.

6.4.2 Randomness Effects on the Optical Response

The aim of this study is to understand better how the roughness and randomness affect the optical response of metals. We chose two high quality metals: Gold which is favoured in many experiments because it is chemically stable, and Aluminium which is relatively free of interbands which would complicate spectral analysis.

As we have a bivariate problem, to find the effect of each of the variables we will first fix the average groove depth and we will vary the randomness ratio and the incident wavelength. As we have seen in figure 6.9 the randomness increases when

[2] It is called Littrow configuration where the -1 order has the same direction than the incident wave.

the correlation length becomes small compared to the other structural scales. Here we will parametrise the randomness by the RMS height over the correlation length (h/l_c), where height and period are constants and l_c is the only structural variable.

Figure 6.12 shows the total reflectance for s-polarized and p-polarized light: we can see the s-pol is on average invariant in randomness, but it is affected by the incident wavelength. On the right side we can see that p-pol light offers much more dependence on these variables. In particular, at short wavelengths p-pol is strongly modulated by noise. On the wavelength axis its dependence is very similar to the response that we see for s-pol: this indicates that this variation comes from the different values of the refractive index of aluminium in this wavelength range.

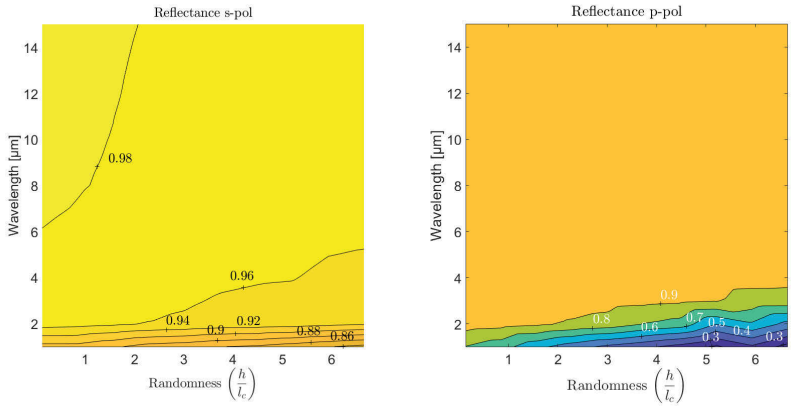

FIGURE 6.12: Average total reflectance for s-polarization and p-polarization at normal incidence depending on the incoming wavelength and the level of randomness h/l_c, where h is the average RMS height and l_c the correlation length . These are Aluminium (Rakić, 1995) profiles with an average RMS of 1.2 μm and super-period of 2 μm, and results were averaged over 10 realizations.

Thus from the analysis of figure 6.12 we can infer that randomness has more importance in the regime where the depth of the grooves and the incident wavelength are of comparable size. Also we see that s-pol light is not very affected by the change on the structure: this result is intuitive since we are studying 1D profiles where in the s-pol direction the structure is constant.

To obtain a clear view of the effect of the randomness, we will analyse the angular response when increasing the noise. Thus in figure 6.13 we fixed the groove depth at 1.2 μm (top row) and at 2.3 μm (bottom row), the super-period at 20 μm and the incident wavelength is constant at 10 μm. In this scenario we can clearly see the noise dependence of p-polarized light where for high noise level the reflectance decay

around 40 %, it is interesting to see that the randomness dependence is quite consistent with angle, until high incident angles are achieved (around 70-90 degrees) where the randomness dependence seems to disappear and the reflectance becomes similar to the s-pol reflectance.

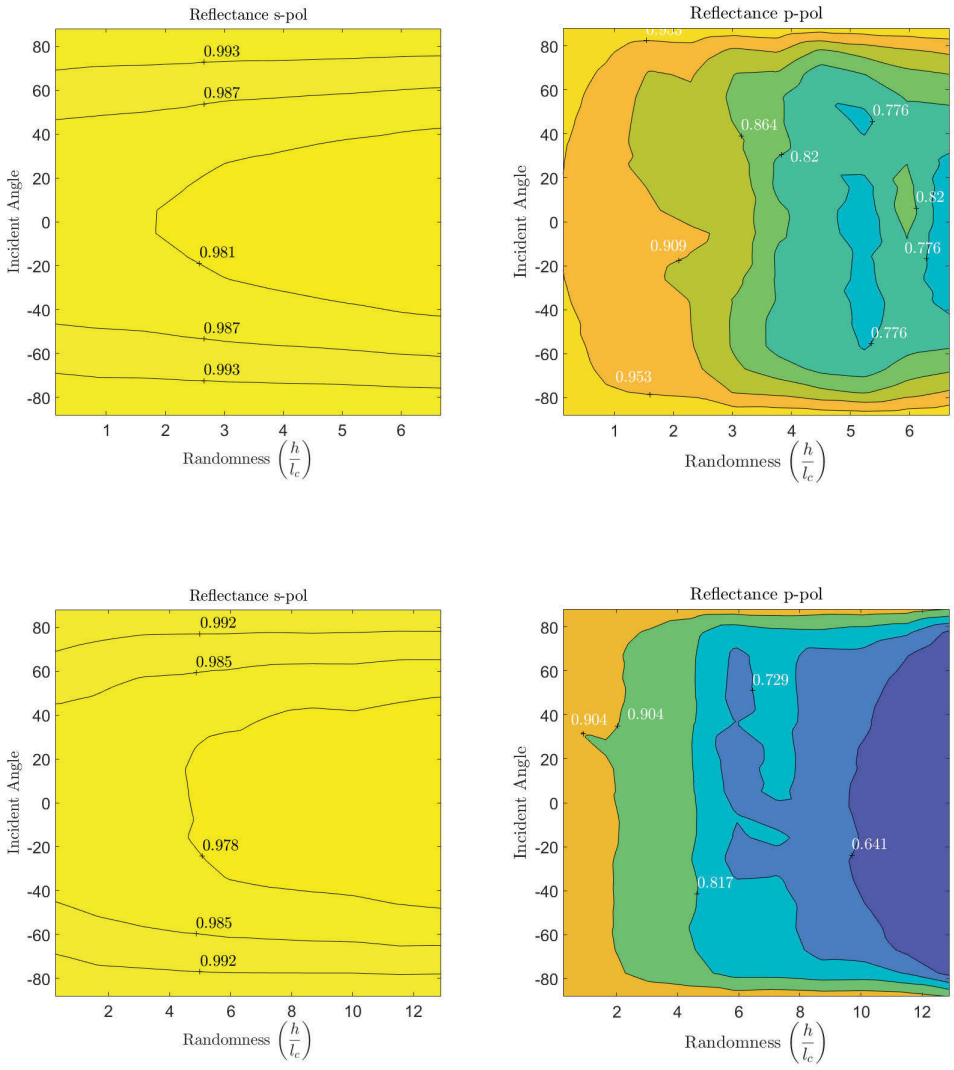

FIGURE 6.13: Angular analysis of the averaged total reflectance of rough profiles increasing the level of randomness h/l_c, where h is the average RMS height and l_c the correlation length. Top row images show the total reflectance of Al (Rakić, 1995) profiles with average RMS of 1.2 μm and bottom row images profiles with average RMS of 2.3 μm. In both cases the profiles studied have a super-period of 20 μm and the results were averaged over 10 realizations; the profiles were illuminated with a 10 μm wavelength.

In this figure (fig 6.13) we show two profiles statistically identical except for the groove RMS, thus we can infer the influence of the surface roughness. We can see that the optical response of the deeper profile (bottom row) is more sensitive to randomness. This is consistent with the similarity of the structure size to the incident wavelength leading to more sensitivity to the structure characterisation. Note that an average RMS of 2.3 μm means an average total depth (peak-to-peak) of 4.6 μm, which is of the order of half wavelength of the incident light.

After realizing that p-polarized light offers high randomness dependence, we decided to see if this effect is also dependent on the material. Then, to compare the effect of randomness between two different materials, in figure 6.14 we compare the percentage ratio between the p-pol and s-pol. This ratio gives us the relative effect of the randomness that we can use to compare different materials.

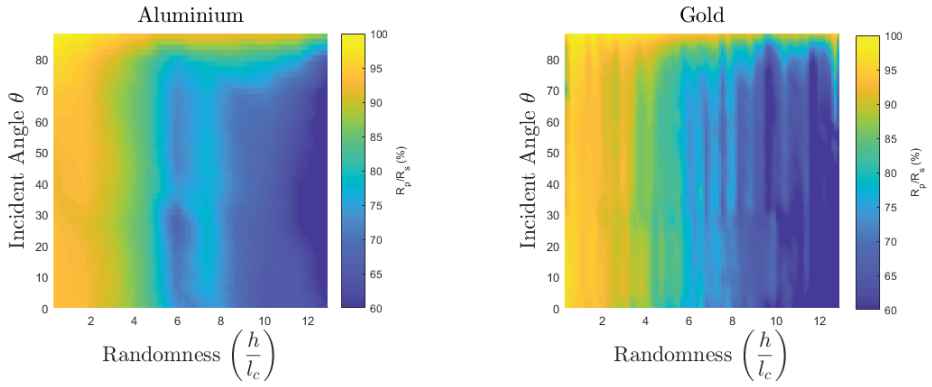

FIGURE 6.14: Comparison of the angular-randomness dependence between: (left) Aluminium (Rakić, 1995) profiles and (right) Gold (Olmon et al., 2012) profiles. The optical response is shown through the percentage polarization reflectance ratio ($R_p/R_s \times 100$) between identical statistical profiles. The level of randomness is parametrised by h/l_c, where h is the average RMS height and l_c the correlation length. These profiles have an average RMS height of 2.3 μm, period of 20 μm and incident wavelength of 10 μm, and the results have been obtained over an average of 10 realizations.

In figure 6.14 we can see that gold and aluminium offer a very similar angular optical response in terms of the level of noise; at this wavelength these materials are both highly reflective. Also, it is important to note that these are test cases that we are using to understand the overall behaviour of these structures, as such, for time-efficiency reasons, we are only averaging over ten realizations and consequently we can see some ripples on the gold spectra. If we intend to simulate an accurate result we need to increase the average number to be able to rely on Monte Carlo ensemble average; however these results are useful enough to understand the overall dependence on roughness depth and noise.

Our results show that increasing the randomness of the profile substantially decreases the reflectance of p-polarized light; this change is more subtle for s-pol since we are studying cylindrical gratings, and therefore s-polarized light is only affected by the roughness depth. This result is expected since intuitively we can imagine that the profile is becoming less "polished" when increasing the noise and therefore extra scattering events will take place increasing the probability to trap light inside the structure. Hence we can use surface noise to modulate the optical response of surfaces for any depth. It is well known that surface roughness increases the efficiency of solar absorbers. However, increasing R at long thermal λ can reduce thermal loss, so some degree of spectral selectivity is desirable. In this study we aim to determine the spectral and angular selectivity of specific rough surfaces.

6.4.3 Effective Slope to Determine Angular Dispersion

In this section we will study the effect of the *effective slope* to determine the reflectance angular dispersion. Given a profile we determine the effective slope as the maximum slope of the main oscillations of the profile, i.e. the maximum slope of the envelope of the profile. We choose the maximum slope in order to capture high angular dispersion. Note that every profile has two effective slopes: the maximum of the increasing slopes s_+, and the maximum of the decreasing slopes s_-. The idea is that we can infer the angular dispersion "substituting" the profile by a triangular profile of slopes s_+ and s_-: the specular reflectance of this profile gives us an estimate of the angular dispersion of the refracted energy of the actual profile. To find the angular bounds (γ_+, γ_-) we can apply geometric optics to the equivalent triangular profiles,

$$\gamma_+ = 2\varsigma_+ + \theta, \tag{6.63}$$

$$\gamma_- = 2\varsigma_- + \theta, \tag{6.64}$$

where θ is the incident angle, $\varsigma_+ \equiv \tan^{-1}(s_+)$ and $\varsigma_- \equiv \tan^{-1}(s_-)$ are the angles associated to the slopes of the triangular profiles.

Figure 6.15 and 6.16 show the BRDF of Gold (Babar and Weaver, 2015) sinusoidal profiles for different periods, and the effective bounding angles (red). We can see that this simple approach successfully defines the angular region where most of the energy is scattered for different configurations.

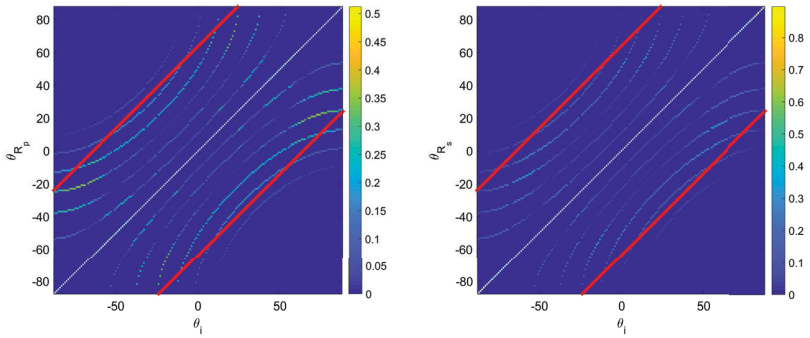

FIGURE 6.15: BRDF of a Gold sine profile with height 2 μm, period of 20.6 μm under an incident wavelength of 4 μm. Left image shows the BRDF under p-polarization and in the right plot the profile is under s-polarization. Red crosses show the effective bounding angles and white dots shows the line of specular reflectance.

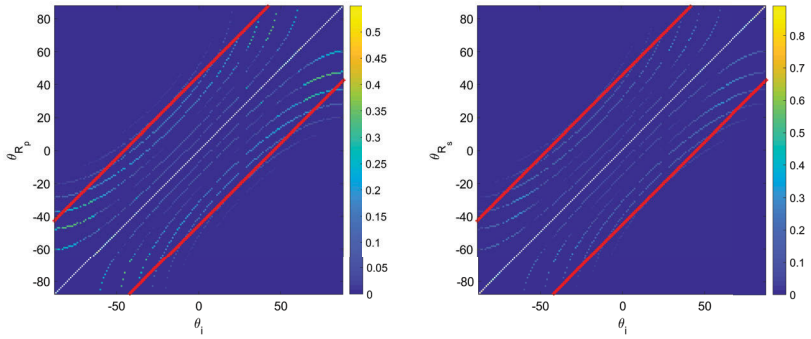

FIGURE 6.16: BRDF of a Gold sine profile with height 2 μm, period of 30.7 μm under an incident wavelength of 4 μm. Left image shows the BRDF under p-polarization and in the right plot the profile is under s-polarization. Red crosses show the effective bounding angles and white dots shows the line of specular reflectance.

Figure 6.17 and 6.18 show the BRDF of smooth sawtooth profiles [3] with different periods. We can see that due to the asymmetry of the profile the diffracted orders are asymmetrically distributed, the red lines show the angular bounds obtained using the effective slope, it can be seen that they bound the main energy diffracted for the different configurations.

[3] As C-method requires smooth profiles, we generated non-sharp sawtooth profiles using Fourier series up to tenth order.

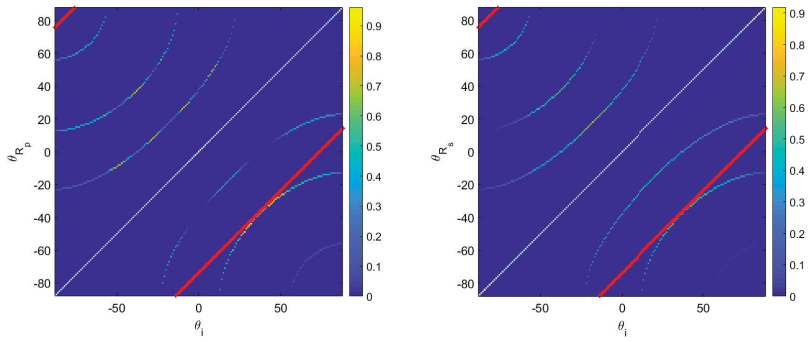

FIGURE 6.17: BRDF of a Gold sawtooth profile with height 2 μm, period of 6.6 μm under an incident wavelength of 4 μm. Left image shows the BRDF under p-polarization and in the right plot the profile is under s-polarization. Red crosses show the effective bounding angles and white dots shows the line of specular reflectance.

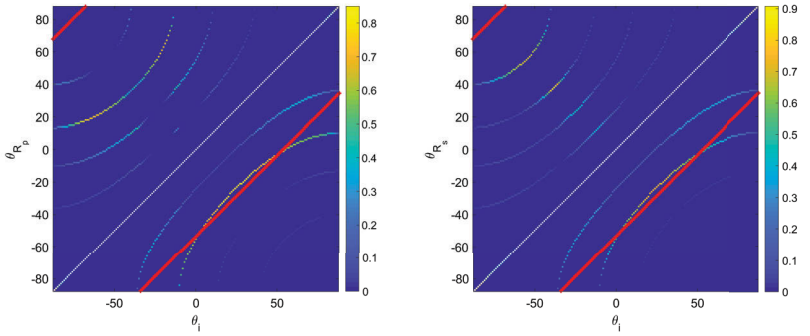

FIGURE 6.18: BRDF of a Gold sawtooth profile with height 2 μm, period of 9.8 μm under an incident wavelength of 4 μm. Left image shows the BRDF under p-polarization and in the right plot the profile is under s-polarization. Red crosses show the effective bounding angles and white dots shows the line of specular reflectance.

In this section we have shown a simple and easy method to infer the angular dispersion of symmetric and asymmetric profiles. This approximation can be useful for selecting profiles depending on the angular dispersion that is desired.

6.4.4 The Colour of Rough Gold

The dispersive response of gold in the visible range makes this material an interesting one to study. An important effect of the roughness is that it causes a structural anisotropy which makes the system sensitive to the polarization state. To analyse these effects we are using colour images since it is a good way to visualize three variable-dependent results (incoming and scattering angles, and incident wavelength). Thus in this study we expect a change in the colour of gold as we change the structural characteristics of the profile, and also a different response for each polarization.

The main energy reflected by a shallow profile is concentrated in the reflection at specular direction. Hence to visualize the change in colour caused only by scattering in shallow profiles we have to remove the coherent reflection (specular) from the incoherent reflectance (scattering),

$$\varepsilon_{sca} = \underbrace{< |r|^2 >}_{incoherent} - \underbrace{< r >^2}_{coherent}, \tag{6.65}$$

where ε_{sca} is the total scattered energy and r is the (complex) amplitude coefficient.

We found it easier to simply remove the specular order from the incoherent sum.

The next problem that we had to solve was to spectrally interpolate the diffracted orders, since we need an homogeneous angular dispersion to be able to obtain the resultant colour. We decided to interpolate the energy in α_n space since, as the C-method relies on the grating formula, the diffracted orders are equally spaced. Thus to disperse the energy of each mode, we converted each diffracted order into a Gaussian distribution with the same energy. With this methodology, instead of having discrete orders we have the energy distributed as a super-position of Gaussian distributions. Finally to convert the resultant energy from the k space to the angular space, we need to normalize it using the grating formula to connect α and θ_n. Thus the total refracted energy in both spaces can be related as follows,

$$\varepsilon = \int \varepsilon(\alpha) d\alpha \tag{6.66a}$$

$$\varepsilon = \int \varepsilon(\theta) k \cos\theta d\theta, \tag{6.66b}$$

sampling equations 6.66 as finite sums, and relating the interpolated efficiencies to the obtained diffracted efficiencies (eq. 6.54); we can obtain the following relation,

$$\varepsilon = \sum_n \varepsilon_n, \tag{6.67a}$$

$$\varepsilon = \sum_n \underbrace{\tilde{\varepsilon}_n \Delta\alpha}_{\varepsilon_n} = \sum_n \tilde{\varepsilon}_n k \cos\theta \cdot \Delta\theta \tag{6.67b}$$

$$\varepsilon = \sum_n \varepsilon_n \cos\theta \cdot \frac{k}{K}\Delta\theta = \sum_n \varepsilon_n \cos\theta \cdot \frac{d}{\lambda}\Delta\theta, \tag{6.67c}$$

where λ is the incident wavelength and d is the super-period. We have used that $\Delta\alpha = \alpha_{n+1} - \alpha_n = K$, which can be obtained from the grating equation (eq. 6.5).

To generate the colour plots we have transformed our spectral reflectance to CIE XYZ and then to sRGB. Thus to analyse the colour spectra, in figure 6.19, we showed the *bidirectional reflectance distribution function* (BRDF) averaged over the wavelength regions of blue (450 - 490 nm), green (520 - 560 nm) and red (635 - 700 nm). We can see that the BRDF of red light is very similar for p-pol and s-pol, but for green and blue light the BRDF of s-polarized light is more intense than for p-pol. This fact accounts for the whiter colour present for the s-polarization. Also, red is scattered more broadly than shorter wavelengths and this probably accounts for richer colour at wide scattering.

Using this formalism, we analyse the colour of gold for representative profiles: RMS $\sim$ 30 nm and a correlation length $\sim$ 50 nm. In figure 6.19 we show the colour of gold caused only by scattering, under p-polarization (top row) and s-polarization (bottom row).

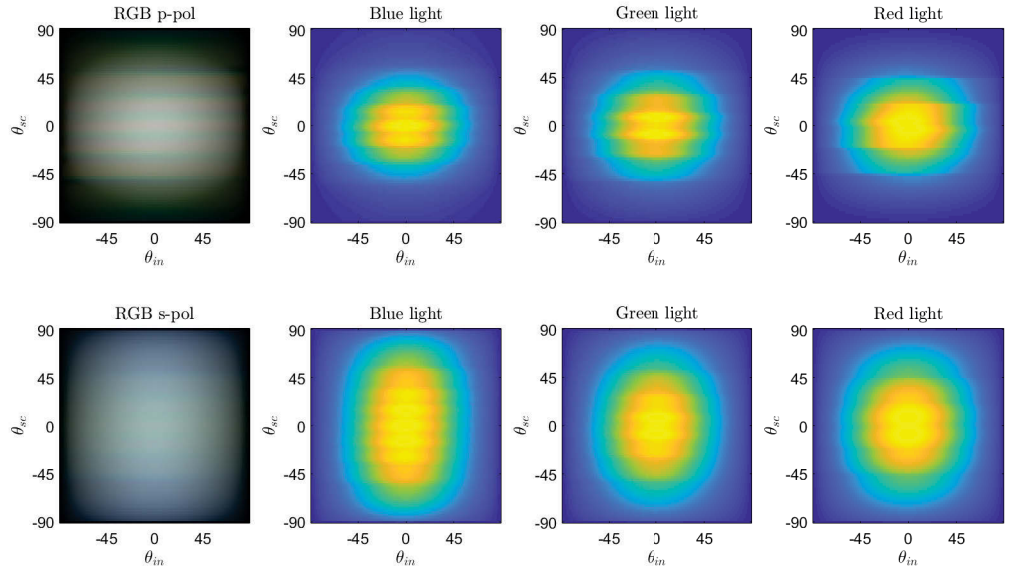

FIGURE 6.19: This figure shows the colour BRDF without specular reflectance of a gold surface with small roughness (RMS = 30 nm, correlation length = 50 nm and period 2 μm), and the BRDF for the different wavelength regimes associated to each colour: blue 450 - 490 nm; green 520 - 560 nm; and red 635 - 700 nm. In the first row we show the response for incident p-polarized light and second row shows the results under s-polarized light. These results have been obtain after averaging over 100 realizations.

The results shown in figure 6.19 show a whiter colour for s-pol, but this is obscured by diffracted orders: to solve this we would need to increase the ratio super-period wavelength, and increase the number of realizations, requiring very significant computational resources.

Alternatively, for very shallow profiles we can estimate the optical response using the Rayleigh approximation instead of the C-method. To implement it we used the lowest order perturbation integrated from the *reduced Rayleigh equations*; methodology that we mentioned before (A. A. Maradudin and Mendez, 1993; A. A. Maradudin and Mills, 1975; O'Donnell, 2001). The lowest order is mostly sensitive to l_c, with height only presenting a simple quadratic multiplier (does not affect the colour).

Thus, in figure 6.20 we show the angular colour dependence due to scattering caused by profiles with different correlation lengths. The top row shows the BRDF colour of a profile with l_c = 20 nm, we can see a surprising pink colouring at high retro-reflection angles for p-polarization, while for s-polarized light the resultant blueish colour. The middle row shows the colour reflectance of a profile with l_c = 200 nm; in this case we can see again a strong retro-reflection, but in this case the apparent colour is a red-gold while in the specular direction we have a whiter response; for s-polarized

light we have a weaker retro-reflection with an overall blue colour, a brownish colour only appears slightly in the retro-reflection direction. Finally, at the bottom row, we show the colour response of a profile with correlation length equal to 2 μm. We can see that for both polarizations the retro-reflection effects have disappeared, leaving reflectance only in the specular direction.

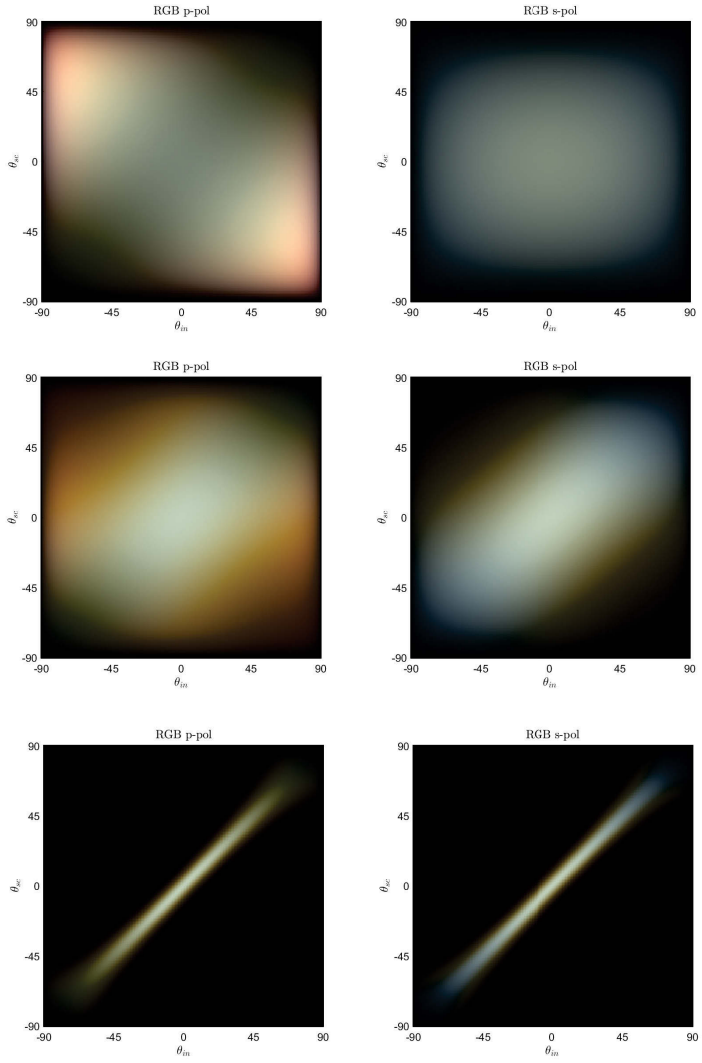

FIGURE 6.20: Colour of shallow gold profiles caused only by scattering. The profiles of each row have different correlation lengths: top row l_c = 20 nm, middle row l_c = 200 nm, and bottom row l_c = 2000 nm.

For comparison, in figure 6.21, we show aluminium profiles that are structurally equal to the profiles in figure 6.20. We can see that aluminium offers less colour variance than gold, with a blueish colour for all profiles and polarizations. Only the profiles in the middle row (l_c = 200 nm) present a distinct colour in the retro-reflection

direction, showing a brownish colouring. The Al profiles offer the same angular dispersion than the Au profiles. We can see that top (l_c = 20 nm) and middle row offer strong retro-reflection, while in the bottom row (l_c = 2 μm) the refracted light is focused in the specular direction.

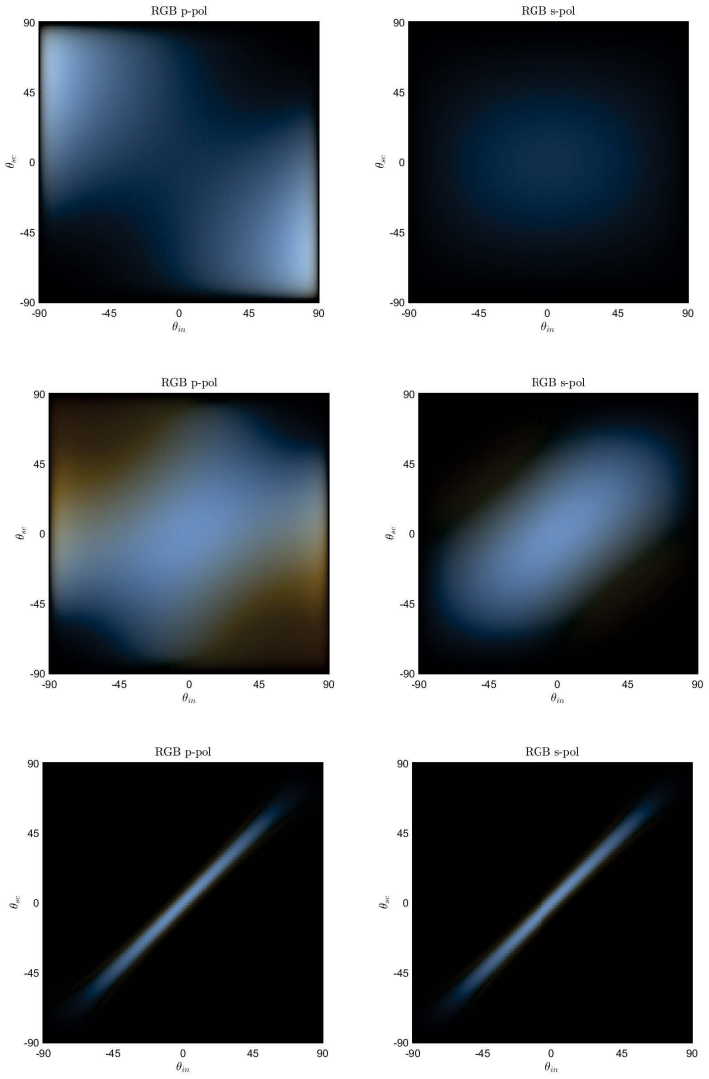

FIGURE 6.21: Colour of shallow aluminium profiles caused only by scattering. The profiles of each row have different correlation lengths: top row l_c = 20 nm, middle row l_c = 200 nm, and bottom row l_c = 2000 nm.

6.5 Conclusion

In this chapter we have presented the *C-method* and a numerical algorithm to determine the optimal convergence of this method for random and deep profiles. We have generated pseudo-random profiles using a method that relies on *Gaussian random field*, which is equivalent to the methodology that we used in chapter 4 for one dimension. In order to study the spectral and angular optical response of random profiles defined by certain statistical quantities: *root-mean square*, correlation length and period; we rely once again on Monte Carlo ensemble average in order to obtain representative results for such surfaces. Note that modal methods, like the C-method, have been generalized to two-dimensional profiles (Lalanne, 1997), or multi-layer structures with different profile interfaces (L. Li, 1994; L. Li, G. Granet, et al., 1996). For these methods the numerical approach presented here to improve convergence can also be applied, since it does not assume 1D profiles, but relies on minimizing the error propagation.

We validated our methodology comparing our results with published ones.

We analysed the effect of randomness for fixed profile depths. As it is well known in the literature the grooves height and period scales compared to the incident wavelength determine the level of scattering of the surface, and therefore the regime of the optical response. For surfaces in the scattering regime the level of randomness of the profile (the correlation length) greatly influences the angular optical response. We have found that by increasing the randomness, the reflectance decay has a flat response up to very high incident angles ~ 80 degrees. We think that this effect would be useful for solar absorbers.

To predict the angular response of any surface we have introduced the *effective slope approach*, which gives us the reference angle that bounds most of the scattering caused by the structure. This approximation can be useful to design profiles for optical angular selectivity.

Finally, we have studied the change of the gold colour due to surface roughness and compared it to aluminium surfaces. We conclude that shallow rough gold under p-polarization has a colour strongly dependent on the correlation length of the profile; showing pinkish colours for short correlation length and the more common yellow-reddish colour for larger l_c. On the other hand the colouring of Aluminium is more constant showing a blueish colouring. An interesting property, independent of the material, is that for shorter correlation lengths strong retro-reflection appears, while for larger correlation length most of the energy refracted is focused on the specular direction. As future work, we could focus on better Monte Carlo averaging which would enable a better understanding of the effect of the slope on the colour.

6.6 Addendum: Equivalent Metamaterial Interface

In this addendum of the present section an alternative method to study rough surfaces is suggested. The keystone of this idea is to find the permittivity and permeability of a metamaterial with flat interfaces that interacts with the light in the same way that the rough surface does. Thus, to achieve this goal transformation optics are used. Unfortunately we did not have time to implement this idea, but we present it because we think it is potentially very useful.

6.6.1 Space Transformation

The meaning of transformation optics is to transform Maxwell equations accordingly with a space transformation, and then to find the equivalent metamaterial that in the original coordinates interacts with the EMF in the same way that the original material in the transformed space. Therefore, the first step would be to find the desired space transformation. As the main aim is to relate the rough interface with a flat one a similar space transformation than in the C-Method is used. Nevertheless, this requires a space transformation that does not modify the whole space (like the one used before equation 6.9), but only a limited volume. Thus, to develop this approach the space transformation that will be used is the smart change of coordinates presented by Shcherbakov and Tishchenko (2013),

$$
\begin{aligned}
v &= x, \\
u &= \begin{cases} c\left(1 - \frac{|y|}{b}\right)\sin(Kx) + y, & |y| \leq b, \\ y, & |y| > b, \end{cases} \\
w &= z.
\end{aligned}
\tag{6.68}
$$

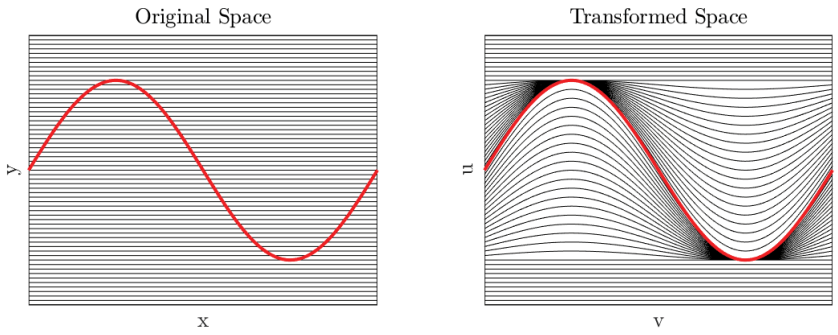

FIGURE 6.22: Green line represents the surface profile; (left) solid lines are parallel to the canonical basis vector ($\vec{e}_x$) of the original coordinate system, (right) solid lines are parallel to the canonical basis vector ($\vec{e}_v$) of the transformed coordinate system.

In general, following the same construction idea of the space transformation of eq. 6.68, we define a space transformation for any arbitrary continuous profile as shown in transformation 6.69.

$$\begin{aligned} v &= x, \\ u &= \begin{cases} c\left(1-\frac{|y|}{b}\right) f_K(x) + y, & |y| \leq b, \\ y, & |y| > b, \end{cases} \\ w &= z, \end{aligned} \tag{6.69}$$

where $f_K(x)$ is an arbitrary continuous function with periodicity K. Then, combining this definition and the method to generate a random profile that has been introduced in section 6.3, a space transformation as the one shown in figure 6.23 can be obtained.

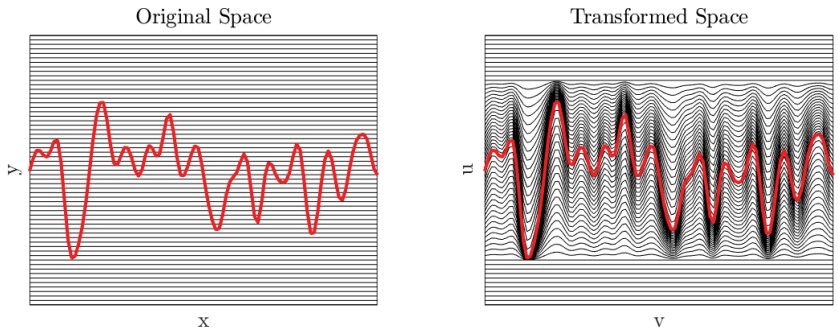

FIGURE 6.23: Green line represents random surface profile; (left) solid lines are parallel to the canonical basis vector ($\vec{e}_x$) of the original coordinate system, (right) solid lines are parallel to the canonical basis vector ($\vec{e}_v$) of the transformed coordinate system.

6.6.2 Metamaterial Permittivity and Permeability

In order to obtain the permittivity and permeability of the equivalent metamaterial the coordinate transformation introduced before (eq. 6.69) should be taken into account when solving Maxwell equations, therefore the general equations introduced in section 6.1 (eq. 6.13 & 6.14) can be applied considering the new metric tensor. Therefore, the permeability and permittivity tensors of the metamaterial will be obtained imposing the condition that they must be equal to the effective tensors that came from the Maxwell equations in the new coordinate system, in other words, the metamaterial tensors can be defined as follows,

$$\hat{\mu}_{meta} = \mu \hat{g}^{-1} \sqrt{det(\hat{g})}, \tag{6.70}$$

$$\hat{\epsilon}_{meta} = \epsilon \hat{g}^{-1} \sqrt{det(\hat{g})}, \tag{6.71}$$

where $\hat{g}$ is the metric tensor given by the coordinate transformation 6.69. It is important to notice that as the metric tensor depends on the periodic function $f_K(x)$, $\hat{g}$ will have different values for each point in the space. The problem of finding the resultant optical response of this metamaterial could be solved using a multilayer system where each slice will have a permittivity and permeability resultant of averaging the permittivity and permeability of the metamaterial over the period direction (x) and for fixed values of the vertical component y; therefore for each value of y, an effective layer permittivity and permeability will be found. Thus, with this defined new structure a transfer matrix formalism can be applied.

Formalisms limited to isotropic permeabilities are well known, but for our case would be relatively complicated due to non-orthogonal field directions and multiple

waves, so we expect that anisotropic μ will add significantly complexity to the implementation.

Chapter 7

Summary

In this thesis we have studied different kinds of optical coatings possessing some degree of randomness: metal sponges, randomly structured two-phase media, heterogeneous matrices and random rough surfaces. We have used several methods to create structures with a random morphology that resembles the real structures: molecular dynamics and Monte Carlo ensemble to create the mesoporous metal sponges; *Gaussian random fields* using different kernels to generate the two-phase structures or the random rough surfaces. To obtain the effective optical response we relied on Monte Carlo ensemble averaging.

In our study on mesoporous metal sponges we have shown a method to obtain the effective optical properties of these kind of structures, we found that they behave as lossy materials and lack the plasmon response of the bulk metal. Our findings agree with results experimentally measured of similar systems that can be found in the literature.

To improve our knowledge of column-like structures obtained experimentally using physical vapour deposition, we have developed a methodology to simulate them relying on the autocorrelation function of such samples. We used the cross-sections of the experimental autocorrelation function to select which kernels will offer an equivalent distribution on the anisotropy. Using these kernels and the *level-cut Gaussian random field* method we have obtained structures that are statistically similar. Once the structures were generated we analysed the optical response and the micro-structural parameters of these structures with a numerical extension of the method introduced by Brown and Sen and S. Torquato that instead relies on Monte Carlo ensemble average. Also we presented an algorithm to obtain the optimal bounds of the macroscopic permittivity (*leaf bounds*), which also allow us to obtain high order MSP. Using this framework we analysed single and mixed kernels and the MSP of second, third and forth order. We find that for a good sampling the depolarization factors ($\hat{\Upsilon}_2$) converge to the depolarization factors of an ellipse with the same anisotropy. The analysis on the third and fourth micro-structural parameters is more challenging; $\hat{\Upsilon}_3$ follows the fill factor giving values a bit smaller than $\hat{\Upsilon}_1$; the anisotropic MSP, $\Delta\hat{\Upsilon}_4$ has opposite sign

than the difference of the second order MSP, which indicates information on the structural anisotropy. The macroscopic permittivity of structures with similar anisotropy and fill factor is less sensitive to the specific generating kernel than we expected, only offering a small variance on the optical anisotropy. The effective permittivity of mixed kernels is more dependent on the degree of anisotropy and the generating kernels.

Paints are one of the more common coatings because of their versatility and efficiency. In our chapter on heterogeneous matrices we presented a generalized version of the four-flux method that allowed us to analyse and optimize paints. Our method allowed us to incorporate different size and material distributions of the components, and absorption caused by the matrix itself. We presented a matrix formalism to study multilayer paints, in particular we found that to optimize the reflectance in the IR the first layer should incorporate the bigger particles in order to scatter first IR wavelengths to avoid absorption.

The final work of this thesis has been in rough surfaces. As mentioned in the introduction, roughness effects are present in most coatings. We have used an optimized version of the C-method to analyse random structures generated using GRF, and a first order perturbation method to analyse the angular colour dependence of such profiles. Our findings include: the influence of the randomness decreases the reflectance for deep roughness a wide range of incident angles; an approximation to estimate angular dispersion based on the maximum slopes of the profiles enveloping function; and the effects on the colour of rough gold depending on the surface roughness, showing a whitish colour for incident s-polarization and a yellow-reddish colour for incident p-polarized light, and profiles with short correlation length have a strong retro-reflection.

7.1 Future Work

Several extensions have been proposed in individual chapters: here I will summarise the most important one and link some ideas together.

On random two-phase structures it would be interesting to extend our study on the micro-structural parameters of high order, I think that it is a particularly interesting topic that has only been extensively studied for isotropic structures, but computational limitations have prevented a deeper understanding of the high order MSP. With our framework it is straightforward to study anisotropy to high order. It would also be interesting to extend to scattering by exploiting the multi-interaction analogy to approaches used for rough surfaces.

Another objective that I have in mind is to incorporate angular dependence on the study of heterogeneous matrices. Our study on rough surfaces has shown the significant influence of the surface on the angular response. Thus I would like to

combine the C-method and our generalized four-flux method to be able to analyse realistic rough paints and their angular dependence.

Appendix A

Pseudo-Depolarization Factors

In this appendix I present unfinished research on an effective medium approximation that depends on the curvatures of the structure. I started this research to model the optical response of systems with complex morphology, like the metal sponges (chapter 3); nevertheless I was unable to complete it.

A.1 Curvature to depolarization approximation

Homogenizing some complex structure or physical property in order to solve a characteristic mathematical expression that represents a physic property of the structure under study is the key stone of *effective medium approximations* (EMA). In particular, in this work the interest resides in the electromagnetic properties of some material structure depending on its morphology and volume ratio of a particular material (fill factor).

Therefore, in order to work, EMA must include information regarding the geometry of the phases inside the matrix; therefore, a key considerations is the parametrization of distinct geometries. In particular, in effective medium models the anisotropy is typically represented by the depolarization factors that characterise the degree of anisotropy of an ellipsoid in comparison to a sphere. From this explanation it is easy to see how a problem can arise when the phases of the matrix are not convex independent particles, but instead they are a continuous network.This is the case of mesoporous sponges which their main phase percolates in a complex network making it extremely difficult to characterise. Nevertheless, it has been shown that the Gaussian and Mean curvatures are possible candidates to parametrise the morphology effect of these complex structures (Berk, 1987; Supansomboon et al., 2014; S. Torquato, 2002; S. Torquato and Donev, 2004). In particular, they indicated that curvature of mesoporous sponges undergoes very strong changes with the fill factor, and therefore the degree of anisotropy may change. Hence, we propose to study the relation of the anisotropy (depolarization factors) with the structure average Gaussian and Mean curvatures in order to acquire an insight on the optical response of these complex morphologies.

Thus, our goal is to express the structure anisotropy in terms of these averaged curvatures, instead of using the semi-axis as it is commonly used for convex structures. Following this idea, the first step will be to find a relation between the classic depolarization factors and our approximation (which can be easily expressed in terms of the curvature).

The *depolarization factors* are defined as:

$$L_i \equiv \frac{a_x a_y a_z}{2} \int_0^\infty \frac{ds}{(a_i^2+s)\sqrt{(a_x^2+s)(a_y^2+s)(a_z^2+s)}}, \tag{A.1}$$

where $i = \{x, y, z\}$ and R_i are the semi-axis of the ellipsoid. The *depolarization factors* satisfy $\sum_i L_i \equiv 1$.

In order to get a new insight, we present an approximation of these *depolarization factors*. Imposing a direct relation with the ellipsoid semi-axis (since these are always correlated with curvatures), and also, imposing the normalization condition of the *depolarization factors* ($\sum_i L_i \equiv 1$), the following expression is obtained:

$$\frac{1}{R} = \frac{1}{a_x} + \frac{1}{a_y} + \frac{1}{a_z}, \tag{A.2}$$

$$\tilde{L}_i = \frac{R}{a_i}. \tag{A.3}$$

It is easy to see that each *pseudo-depolarization factor* is a normalization of its semi-axis related to an effective radius R eq.(A.2), that comes from the well known *"parallel resistors equation"*. Using R to normalise each semi-axis ensures that $L_i \in [0, 1]$ since by definition $R < R_i, \forall i$. Moreover, it can bee seen that $\tilde{L}_i$ satisfies the sum condition of L_i, i.e.
$\sum_i^d \tilde{L}_i \equiv 1$.

Proof.

$$\begin{aligned} \tilde{L}_x + \tilde{L}_y + \tilde{L}_z &\equiv \frac{R}{a_x} + \frac{R}{a_y} + \frac{R}{a_z} \\ &= R(\frac{1}{a_x} + \frac{1}{a_y} + \frac{1}{a_z}) \\ &\equiv R(\frac{1}{R}) = 1 \end{aligned} \tag{A.4}$$

□

In the following lines, we will show that for most symmetrical examples, sphere ($3D$) or circle ($2D$), this approximation agrees coincides with the classical definition (eq.A.1).

Example A.1.1 (Sphere)**.** A sphere satisfies that $a_x = a_y = a_z$, then:

$$\frac{1}{R_S} = \frac{1}{a_x} + \frac{1}{a_x} + \frac{1}{a_x} = \frac{3}{a_x} \tag{A.5}$$

$$\tilde{L}_i = \tilde{L}_S = \frac{R_S}{a_x} = \frac{a_x}{3a_x} = \frac{1}{3}. \tag{A.6}$$

Example A.1.2 (Circle)**.** A circle satisfies that $a_x = a_y$, then:

$$\frac{1}{R_C} = \frac{1}{a_x} + \frac{1}{a_x} = \frac{2}{a_x} \tag{A.7}$$

$$\tilde{L}_i = \tilde{L}_C = \frac{R_C}{a_x} = \frac{a_x}{2a_x} = \frac{1}{2}. \tag{A.8}$$

In the following lines, we will compare the depolarization factors and our approximation (pseudo-depolarization factors) for different ellipsoids.

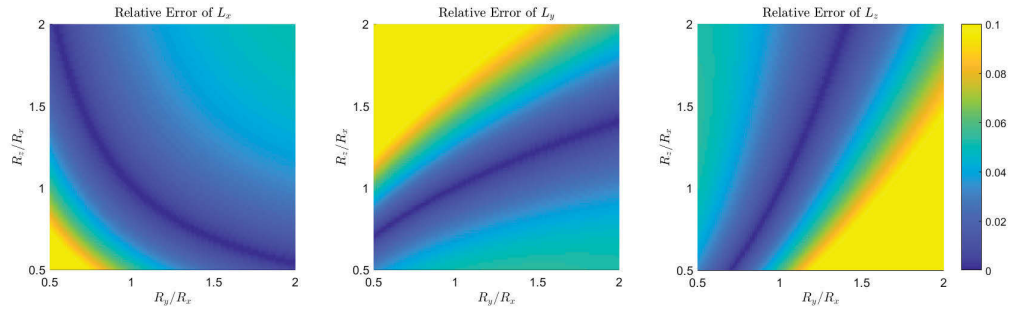

FIGURE A.1: Relative error between *depolarization* and *pseudo-depolarization factors* depending on the ratio between the semi-axis, up to double the length.

In figure A.1 we can see that this approximation is accurate when the level of anisotropy is not very large.

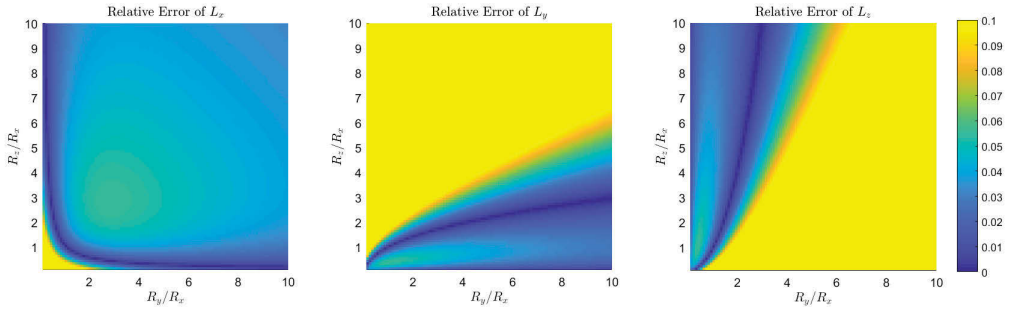

FIGURE A.2: Relative error between *depolarization* and *pseudo-depolarization factors* depending on the ratio between the semi-axis, semi-axis ratio up to 10 times larger.

In figure A.2 it can be seen clearly that for very elongated ellipsoids this breaks down.

As we could see, there is a big range of possible ellipsoidal shapes where we can use the *pseudo-depolarization factors*. So our next step is to try to relate this approximation with the curvatures (κ). The first way to proceed is simplify the problem, so we will suppose that we have a composite of fixed-size spheres, then as the curvature of a sphere is constant and it is the same for every direction, the curvature can be read as follows:

$$\kappa \equiv \frac{1}{r}. \tag{A.9}$$

Applying this definition, equation (A.3), and using that a sphere satisfies $R_1 = R_2 = R_3$, we obtain:

$$\tilde{L}_i(\kappa) = \tilde{L}(\kappa) = \frac{R}{a_x} = \kappa R. \tag{A.10}$$

We can appreciate from eq.(A.10), that if a dependent relationship exists between the curvature and the semi-axis, we can relate the curvature with the *pseudo-depolarization factors* as well.

The next step is to study a more flexible case, so we will study the curvature of an ellipse ($2D$) and relate it with our approximation. We can calculate the curvature of a curve using the parametric definition of an ellipse (A.12), which can be found through the ellipse definition (A.11).

$$\left(\frac{x}{a_x}\right)^2 + \left(\frac{y}{a_y}\right)^2 = 1, \tag{A.11}$$

$$y(x) = a_y\sqrt{1-\left(\frac{x}{a_x}\right)}. \tag{A.12}$$

Using the definition of the curvature for a $2D$ curve which is not parametrized by the *arclength* (A.13) and doing a little algebra we get the expression for the curvature of an ellipse (A.14).

$$\kappa(t) = \frac{||r'(t)\times r''(t)||}{||r'(t)^3||}, \tag{A.13}$$

$$\kappa(x) = \frac{|\ \frac{a_y}{a_x^2\sqrt{1-(x/a_x)^2}}\ |\ \left(1+\frac{x^2}{a_x^2|1-(x/a_x)^2|}\right)}{1+\frac{(a_y x)^2}{a_x^2|a_x^2-x^2|}\sqrt{1+\frac{(a_y x)^2}{a_x^2|a_x^2-x^2|}}}. \tag{A.14}$$

Equation (A.14) seems somewhat complicated and depends on the position, x. Nevertheless, the maximum and the minimum values of the curvature, that are achieved at $x=0, (\kappa(x=0)=\kappa_y)$ and $x=a_x, (\kappa(a_x)=\kappa_x)$, only depend on the semi-axis relation. To find κ_y is straightforward using equation (A.14) for $x=0$. Finding κ_x is more tricky using the same equation, but it is very easy if we parametrize the curvature in terms of y, i.e. $x(y)$. Thus, due to the symmetry between x and y and a_x and a_y, we can find $\kappa(y)$ just changing x for y and a_x for a_y in equation (A.14), then $\kappa_x = \kappa(y=0)$,

$$\kappa_x = \frac{a_x}{a_y^2}, \qquad \kappa_y = \frac{a_y}{a_x^2} \tag{A.15}$$

$$\kappa_x = \left(\frac{1}{L_x}-1\right)\frac{1}{a_y}, \qquad \kappa_y = \left(\frac{1}{L_y}-1\right)\frac{1}{a_x}, \tag{A.16}$$

where we have applied definitions (A.3) and (A.2). Using equations (A.16), the *pseudo-depolarization factors* (A.3) can be written in terms of the maximum and minimum curvature of the ellipse.

$$\begin{aligned} L_x &= \frac{1}{\kappa_x a_y + 1}, \\ L_y &= \frac{1}{\kappa_y a_x + 1}, \end{aligned} \tag{A.17}$$

and by construction these new definitions still satisfy $\sum_i L_i = 1$.

A.1.1 Pseudo-depolarization Factors of an Ellipsoid

In this section, it is presented the idea that I had to relate the pseudo-depolarization factors approximation with a surfaces with a close form (its boundaries can be defined by an equation). The main point of this method is to relate the geometrical anisotropy of certain body with the geometrical isotropy of a sphere. Therefore the method keystone is to find a change of variable that transform the original shape to a sphere, and the transformation that suffer each dimension is related to the geometrical depolarization factor.

Starting from the definition of an ellipsoid with semi-axis a, b, c:

$$\left(\frac{x}{a_x}\right)^2 + \left(\frac{y}{a_y}\right)^2 + \left(\frac{z}{a_z}\right)^2 = 1, \tag{A.18}$$

$$\left(\frac{R}{a_x}x\right)^2 + \left(\frac{R}{a_y}y\right)^2 + \left(\frac{R}{a_z}z\right)^2 = R^2, \tag{A.19}$$

where to obtain eq. A.19 we have multiplied eq. A.18 times a constant R^2. From equation A.19 is straightforward to see which change of variable will be needed to obtain a sphere:

$$\begin{cases} \tilde{x} &= L_x \cdot x, \\ \tilde{y} &= L_y \cdot y, \\ \tilde{z} &= L_z \cdot z, \end{cases} \tag{A.20}$$

where $L_i = R/a_i$ with $i \in \{x, y, z\}$. Consequently, from this relation (eq. A.19 the relative radius R introduced in equation A.3 is the radius of the equivalent sphere in the transformed space:

$$\tilde{x}^2 + \tilde{y}^2 + \tilde{z}^2 = R^2. \tag{A.21}$$

Similar that in the previous section we can express the depolarization factors in terms of the maximum curvatures. Nevertheless, it should be taken into account that

an ellipsoid is a surface, a two dimensional manifold that lives in the 3D space. Consequently, the meaningful curvatures would be the Gaussian (K) and Mean (H) curvatures at an extremal point on the surface. In the case of an ellipsoid, we can use the work done for the case of an ellipse, since both K and H depend on the maximum and minimum curvature for a given point, it is easy to see how in the extreme points the maximum and minimum curvatures are the curvatures of the two ellipses with same semi-axis as the ellipsoid. For instance, in the extreme point at $(0, a_y, 0)$ the ellipses that define the maximum and minimum curvatures are the ones with semi-axis (a_x, a_y) and (a_z, a_y), then using equation A.15, the Gaussian and Mean curvatures of an ellipsoid can be written as:

$$K = \kappa_M \cdot \kappa_m = \left(\frac{a_y}{a_x a_z}\right)^2, \tag{A.22}$$

$$H = \frac{1}{2}\left(\kappa_M + \kappa_m\right) = \frac{a_y}{2}\left(\frac{a_x^2 + a_z^2}{a_z^2 \cdot a_z^2}\right), \tag{A.23}$$

where κ_M and κ_m are, respectively, the maximum and minimum curvatures at a given point; the *principle curvatures*.

Gaussian and Mean Curvatures

In the following lines, using the expressions for the Gaussian and Mean curvatures of an ellipsoid, we will show how the pseudo-depolarization factors can be express in terms of these in their extremal values.

Using elliptical coordinates:

$$\begin{cases} x = a_x \cdot \cos\phi \sin\theta, \\ y = a_y \cdot \sin\phi \sin\theta, \\ z = a_z \cdot \cos\theta, \end{cases} \tag{A.24}$$

where $\phi \in [0, 2\pi]$ and $\theta \in [0, \pi]$. The Gaussian and Mean curvatures are defined as:

$$K = \frac{a_x^2 \cdot a_y^2 \cdot a_z^2}{\left(a_x^2 a_y^2 \cos^2\theta + a_z^2(a_y^2 \cos^2\phi + a_x^2 \sin^2\phi)\sin^2\phi\right)^2}, \tag{A.25}$$

$$H = \frac{a_x a_y a_z \cdot (3(a_x^2 + a_y^2) + 2a_z^2 + (a_x^2 + a_y^2 - 2a_z^2)\cos(2\theta) - 2(a_x^2 - a_y^2)\cos(2\phi)\sin^2\theta)}{8\left[a_x^2 a_y^2 \cos^2\theta + a_z^2(a_y^2 \cos^2\phi + a_x^2 \sin^2\phi)\sin^2\theta\right]^{3/2}}.$$

Then, without lose of generality we can assume that the longer semi-axis is c, and therefore the maximum curvatures are at the end of this semi-axis. Thus, at this point , $\theta = 0$, the Gaussian and Mean curvatures expressions yield to:

$$K = \left(\frac{a_z}{a_x \cdot a_y}\right)^2, \qquad H = \frac{a_z}{2}\left(\frac{a_x^2 + a_y^2}{a_x^2 \cdot a_y^2}\right). \tag{A.26}$$

As can be seen from previous relations, equations A.26, at the extreme point Gaussian and Mean curvatures get very simplified. Consequently, a easy relation between the curvatures at this characteristic point and the *pseudo-depolarization factors* can be obtained through basic algebraic operation. Thus, using the definition of the effective radius (eq. A.2) the *pseudo-depolarization factors* of an ellipsoid ($a_x = a_y$) can be expressed as:

$$L_{x,y} = \left(2 + \frac{1}{2\sqrt{K}}\right)^{-1}, \qquad L_z = \left(1 + 4\sqrt{K}\right)^{-1}. \tag{A.27}$$

It is very interesting to realise that the *pseudo-depol. factors* only depend on the Gaussian curvature at the critical point. Also, it seems logical to study how the *pseudo-depolarization factors* depend on the Gaussian curvature, thus figure A.3 shows this relation.

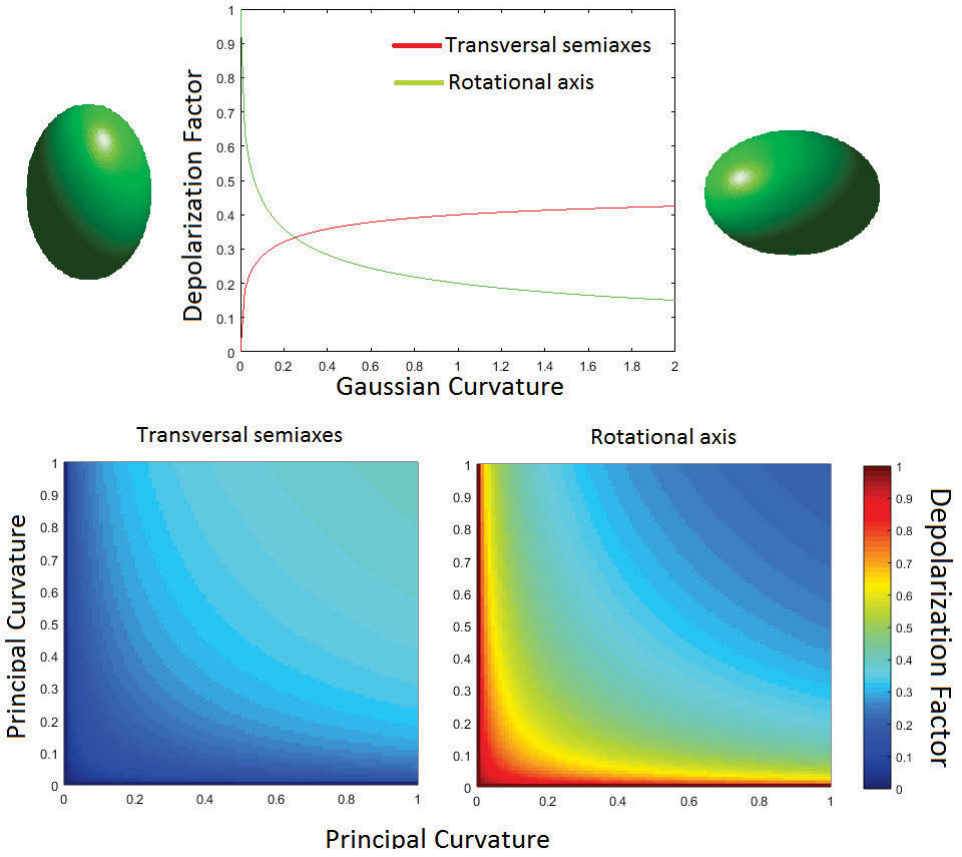

FIGURE A.3: This colormap represents the dependence of the *pseudo-depolarization factors* on the Gaussian curvature at the extreme point of $\theta = 0$.

A.1.2 Relative Extreme Curvatures: Field Enhancement

Another way to approach a regular surface is using relative maximum and minimum curvatures, since as we have seen in previous section, these curvatures depend directly on the semi-axis and for a general case can be defined from the derivatives on the surface. To make this particular analysis we will focus in prolate or oblate ellipsoids, i.e. ellipsoids with two identical semi-axis. For the sake of simplicity let's assume $a_x = a_y$ which implies identical depolarization in these directions, $L_x = L_y$. Thus, using the definitions of ellipse curvature (eq. A.14) and the effective radius (eq. A.2) the pseudo-depolarization factors can be written in terms of the curvatures.

$$\begin{aligned} \frac{a_x}{R} = 2 + \frac{a_x}{a_z} \quad &\Rightarrow \quad \kappa_x = \left(\frac{a_x}{R} - 2\right)\frac{1}{a_z}, \\ \frac{a_z}{R} = 1 + 2\frac{a_z}{a_x} \quad &\Rightarrow \quad \kappa_z = \left(\frac{a_z}{R} - 1\right)\frac{1}{2a_z}, \end{aligned} \tag{A.28}$$

also, as κ_x, κ_z depend on a_x, a_z, we can express the semi-axis in terms of the maximum and minimum curvatures as follows:

$$\begin{aligned} \frac{1}{a_z} &= \sqrt[3]{\kappa_x^2 \kappa_z}, \\ \frac{1}{a_x} &= \sqrt[3]{\kappa_z^2 \kappa_x}. \end{aligned} \tag{A.29}$$

Therefore, using this relation (eq. A.29) and equations A.28, the pseudo-depolarization factors can be defined in terms of the maximum and minimum curvatures yielding to the following expression:

$$\begin{aligned} L_x &= (\mathcal{C} + 2)^{-1}, \\ L_z &= \left(\frac{2}{\mathcal{C}} + 1\right)^{-1}, \end{aligned} \tag{A.30}$$

where we have defined $\mathcal{C} \equiv \sqrt[3]{\kappa_x/\kappa_z}$.

Has been shown by J. A. Stratton (1941) that the internal electric field of an ellipsoid excited by an external uniform field is uniform as well. This internal field depends on the permittivities of the surrounding medium and the ellipsoid itself, as well as on the ellipsoid geometry. Therefore, using definitions in equations A.30, we can analyse the internal field, and therefore its enhancement, due to the maximum and minimum curvatures of an oblate ellipsoid.

$$E_j^{in} = \frac{E_0}{1 + L_j(\epsilon_r^j - 1)}, \qquad j \in \{x, y, x\}, \tag{A.31}$$

where E_0 is the external uniform field and the relative permittivity has been introduced as $\epsilon_r^j \equiv \epsilon^j/\epsilon_0$ where ϵ^j are the diagonal terms of the permittivity tensor. Thus, we can find which relation the permittivities and the geometrical constant $\mathcal{C}$ have to

satisfy in order to produce a resonance in the internal field. A resonance will appear if the modulus of the denominator of equation A.31 is becomes zero. Let's write the permittivity using its real and imaginary part, i.e. $\epsilon_r = \epsilon'_r + i\epsilon''_r$, then:

$$||1 + L(\epsilon_r - 1)|| = 0, \tag{A.32}$$

$$\left(1 + L(\epsilon'_r - 1)\right)^2 + \left(L \cdot \epsilon''_r\right)^2 = 0, \tag{A.33}$$

where to simplify notation we have omitted the subscripts j. To make this example simpler we will consider a material that satisfies $(\epsilon''_r)^2 << 1$; then, equation A.33 gets simplified to the following real expression:

$$1 + L(\epsilon'_r - 1) = 0. \tag{A.34}$$

Therefore, using previous equation (A.34), for each coordinate the resonance condition yields to:

$$\begin{aligned} &x, y - axis: \\ &\qquad 1 + (\mathcal{C} + 2)^{-1} \cdot (\epsilon'_r - 1) = 0 \\ &\qquad \epsilon'_r = -(\mathcal{C} + 1). \end{aligned} \tag{A.35}$$

$$\begin{aligned} &z - axis: \\ &\qquad 1 + \left(\frac{2}{\mathcal{C}} + 1\right)^{-1} \cdot (\epsilon'_r - 1) = 0 \\ &\qquad \epsilon'_r = -2/\mathcal{C}. \end{aligned} \tag{A.36}$$

It is interesting to see that equations A.35 and A.36 agree with the well known resonant condition of a sphere ($\mathcal{C} = 1$) which is $\epsilon'_r = -2$.

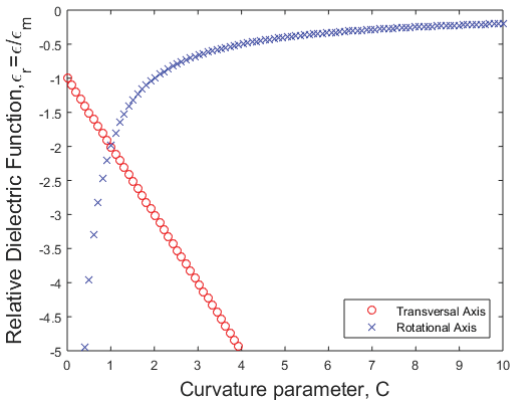

FIGURE A.4: This plot represents function A.35 and A.36, i.e. it shows the real relative permittivity (ϵ_r') in terms of the curvature parameter ($\mathcal{C}$) in order to obtain resonance for an oblate ellipsoid for the two distinct semi-axis.

A.1.3 Pseudo-depolarization Factors of an Hyperboloid

The methodology used to define the *pseudo-depolarization factors* can be applied for different defined surfaces. For instance, it is possible to study the equivalent concave surface of a spheroid, i.e. a hyperboloid with two equal semi-axis. Thus, the first step is to find the change of coordinates that transform the given surface to a sphere. Starting with the equation of a hyperboloid:

$$\left(\frac{x}{a_x}\right)^2 + \left(\frac{y}{a_y}\right)^2 - \left(\frac{z}{a_z}\right)^2 = 1. \tag{A.37}$$

Then, to convert this equation to a sphere we will apply the following change of variables:

$$\begin{cases} \tilde{x} &= \frac{R}{a_x}x = L_x \cdot x, \\ \tilde{y} &= \frac{R}{a_y}y = L_y \cdot y, \\ \tilde{z} &= i\frac{R}{a_z}z = L_z \cdot z. \end{cases} \tag{A.38}$$

Consequently, from this relation (eq. A.38 the relative radius R introduced in equation A.3 is the radius of the equivalent sphere in the transformed space:

$$\tilde{x}^2 + \tilde{y}^2 + \tilde{z}^2 = R^2. \tag{A.39}$$

Equivalently as we did for an ellipsoid we can relate the Gaussian and Mean curvatures at a critical point to the *pseudo-depol. factors* in order to obtain a simple relation.

$$\begin{cases} x = a_x \cos\phi \cosh\theta, \\ y = a_x \sin\phi \cosh\theta, \\ z = a_z \sinh\theta, \end{cases} \tag{A.40}$$

with $\theta \in (-\infty, \infty)$ and $\phi \in [0, 2\pi)$.

The Gaussian and Mean curvatures at any point of a hyperboloid ($a_x = a_y$) under the coordinate system defined in equation A.40 are the following:

$$\begin{aligned} K(\phi, u) &= -\frac{a_z^2}{\left(a_z^2 + (a_x^2 + a_z^2)u^2\right)^2}, \\ H(\phi, u) &= \frac{a_z^2\left(a_x^2(u^2-1) + a_z^2(u^2+1)\right)}{2a_x\left(a_z^2 + (a_x^2 + a_z^2)u^2\right)^{3/2}}, \end{aligned} \tag{A.41}$$

where $u = \sinh\theta$. As we did for the ellipsoid, we will use a characteristic point on the surface where their Gaussian and Mean curvatures are critical. For a hyperboloid, due to its concavity the extremal curvatures are located in the plane of $z = 0$ (following the notation given in eq. A.37), and in the particular case that we are studying, where $a_x = a_y$ the curvatures are constants along this plane by construction. Thus equations A.41 yield to

$$\begin{aligned} K(\phi, 0) &= -\frac{1}{a_z^2}, \\ H(\phi, 0) &= \frac{a_z^2 - a_x^2}{2a_x a_z}. \end{aligned} \tag{A.42}$$

Finally, in the same way that we proceed for en ellipsoid, using the definition of the effective radius, eq. A.2, and the expressions that we just derived for the Gaussian and Mean curvatures (eq. A.42), the *pseudo-depolarization factors* of a hyperboloid can be defined as:

$$\begin{aligned} L_{x,y} &= \left(2 - H + \sqrt{H^2+1}\right)^{-1}, \\ L_z &= i\left(\frac{2}{-H + \sqrt{H^2+1}} + 1\right)^{-1}. \end{aligned} \tag{A.43}$$

Oppositely to the expressions that we obtained for a prolate ellipsoid where the *pseudo-depol. factors* only depend on the Gaussian curvature, for the hyperboloid the

dependence is only on the Mean curvature. Figure A.5 shows this linearity with the principle curvatures, as expected for the only dependence on the Mean curvature.

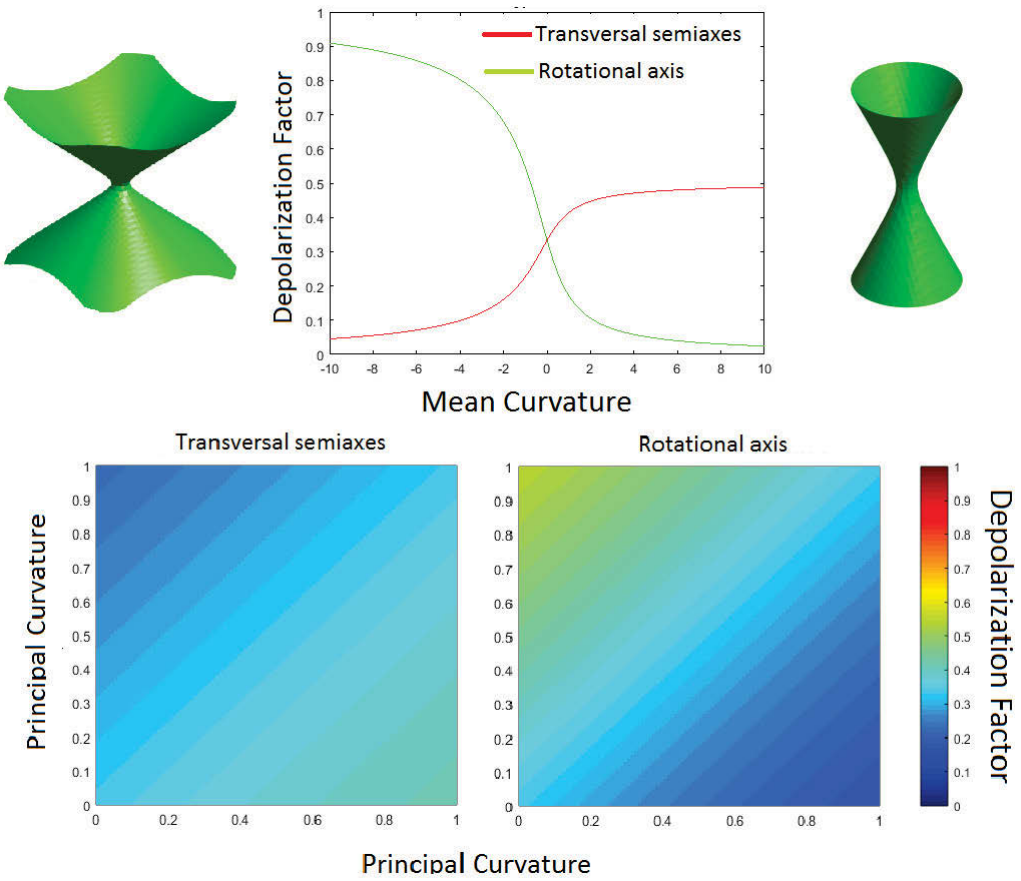

FIGURE A.5: This colormap show the dependence of the *pseudo-depol. factors* on the principal curvatures.

A.1.4 Pseudo-depolarization Factors of an Arbitrary Quadratic Coordinate Equation

An arbitrary geometry that can be expressed in a quadratic equation can be approximated by with this approach. Let's take the most general quadratic equation,

$$ax^2 + by^2 + cz^2 + 2Axy + 2Byz + 2Cxz = D, \tag{A.44}$$

we can express this equation in matrix form as follows,

$$\begin{pmatrix} x & y & z \end{pmatrix} \underbrace{\begin{pmatrix} a & A & C \\ A & b & B \\ C & B & c \end{pmatrix}}_{\Omega} \begin{pmatrix} x \\ y \\ z \end{pmatrix} = D. \tag{A.45}$$

Thus if Ω, constituent matrix, is diagonalisable, equation A.45 can be written in a simpler form,

$$\begin{pmatrix} x & y & z \end{pmatrix} \begin{pmatrix} \alpha & 0 & 0 \\ 0 & \beta & 0 \\ 0 & 0 & \gamma \end{pmatrix} \begin{pmatrix} x \\ y \\ z \end{pmatrix} = \Delta, \tag{A.46}$$

and therefore A.44 simplifies to the ellipse constituent equation,

$$\alpha x^2 + \beta y^2 + \gamma z^2 = \Delta, \tag{A.47}$$

from which we can apply the *pseudo-depolarization approach*.

A.2 Summary

With these preliminary results we have shown an approximation that works for structures with a low level of anisotropy. We can express easily the pseudo-depolarization factors in terms of the principle curvatures of the structure. In particular we have seen that the pseudo-depolarization factors of an ellipse depend on the extremal Gaussian curvature and for hyperboloids they depend on the extremal Mean curvature. This approach can be applied to any surface that can be expressed by a quadratic equation, as long as its constituent matrix can be diagonalized.

To further extend this work we need to analytically relate the pseudo-depolarization factors with other structural variables, e.g. the MSP ($\hat{\Upsilon}_i$) presented in chapter 4; and test our predictions for convex (described by ellipsoids) and concave structures (described by hyperboloids).

Appendix B

Supplementary Material

B.1 Four-Flux coefficients

The coefficients that appear in chapter 5 used to define reflectance and transmittance coefficients of our extended method are defined as follows[1]:

$$\tilde{C}_1 = e^{-2\sqrt{A_1}Z}(\alpha_3 - r_{di}^Z)\left[r_c^Z e^{-2\Gamma Z}(\alpha_2 - \alpha_1\alpha_3) + (\alpha_1 - \alpha_2\alpha_3)\right], \tag{B.1}$$

$$\tilde{C}_2 = (1 - \alpha_3 r_{di}^Z)\left[r_c^Z e^{-2\Gamma Z}(\alpha_1 - \alpha_2\alpha_3) + (\alpha_2 - \alpha_1\alpha_3)\right], \tag{B.2}$$

$$\tilde{C}_3 = \phi^{-1}\cdot(1 - \alpha_3^2)\left[r_c^Z(r_{di}^Z\alpha_2 - \alpha_1) + (r_{di}^Z\alpha_1 - \alpha_2)\right], \tag{B.3}$$

$$\tilde{C}_4 = \alpha_3(1 - \alpha_3 r_{di}^Z) - e^{-2\sqrt{A_1}Z}(\alpha_3 - r_{di}^Z). \tag{B.4}$$

$$\tilde{D}_1 = 1 - r_c^Z r_c^0 e^{-2\Gamma Z}, \tag{B.5}$$

$$\tilde{D}_2 = (1 - \alpha_3 r_{di}^Z)(1 - \alpha_3 r_{di}^0) - e^{-2\sqrt{A_1}Z}(\alpha_3 - r_{di}^Z)(\alpha_3 - r_{di}^0) \tag{B.6}$$

$$\tilde{B}_1 = e^{-(\Gamma + 2\sqrt{A_1})Z}(\alpha_3 - r_{di}^0)\left[r_c^Z(\alpha_1 - \alpha_2\alpha_3) + (\alpha_2 - \alpha_1\alpha_3)\right], \tag{B.7}$$

$$\tilde{B}_2 = e^{-\Gamma Z}(1 - \alpha_3 r_{di}^0)\left[r_c^Z(\alpha_2 - \alpha_1\alpha_3) + (\alpha_1 - \alpha_2\alpha_3)\right], \tag{B.8}$$

$$\tilde{B}_3 = e^{-\sqrt{A_1}Z}(1 - \alpha_3^2)\left[e^{-2\Gamma Z} r_c^Z(r_{di}^0\alpha_1 - \alpha_2) + (r_{di}^0\alpha_2 - \alpha_1)\right]. \tag{B.9}$$

where $\Gamma = K_{eff} + S_{eff}$ is the extinction parameter.

[1] Coefficients A_1, α_i are those introduced by Tonon et al., 2001.

The relation between the coefficients with and without tilde depends on the exponentials ϕ, φ and ψ defined as follows:

$$\varphi \equiv e^{\Gamma Z}, \tag{B.10}$$

$$\phi = \varphi \cdot \psi = e^{(\Gamma+\sqrt{A_1})Z}, \tag{B.11}$$

$$C_i = \phi \cdot \tilde{C}_i \qquad (i = 1, 2, 3), \tag{B.12}$$

$$C_4 = \psi \cdot \tilde{C}_4, \tag{B.13}$$

$$D_1 D_2 = \varphi \tilde{D}_1 \cdot \psi \tilde{D}_2 = \phi \cdot \tilde{D}_1 \tilde{D}_2. \tag{B.14}$$

B.2 Metric Space

The geometric operators: gradient, divergence and rotational, are linked to the space metric $\hat{g} = (g_{ij})$ as follows,

$$\nabla f = g^{ij} \frac{\partial f}{\partial q^i} \frac{\partial}{\partial q^j} \tag{B.15}$$

$$\nabla \cdot F = \frac{1}{det(g_{ij})} \frac{\partial}{\partial q^k} \left(\sqrt{det(g_{ij})} F^k \frac{\partial}{\partial q^k} \right) \tag{B.16}$$

$$\nabla \times F = \frac{1}{\sqrt{det(g_{ij})}} \nabla_q \times F \tag{B.17}$$

In chapter 6 we used these relations to obtain Maxwell's equations in the transformed space.

Bibliography

Abrahamson, I. G. (1964). "Orthant probabilities for the quadrivariate normal distribution". In: *Annals of Mathematical Statistics* 35.4, pp. 1685–1703.

Abramowitz, M., I. Stegun, and D. A. McQuarrie (Feb. 1966). "Handbook of Mathematical Functions". In: *American Journal of Physics* 34. Ed. by Milton Abramowitz and Irene Stegun, p. 177. ISSN: 0002-9505. DOI: 10.1119/1.1972842. URL: http://aapt.scitation.org/doi/10.1119/1.1972842.

Albin, N. (2006). "Optimality of the translation bounds for linear conducting composites in two and three dimensions". PhD thesis. University of Utah, Salt Lake City, UT.

Albin, N., A. Cherkaev, and V. Nesi (2007). "Multiphase laminates of extremal effective conductivity in two dimensions". In: *Journal of the Mechanics and Physics of Solids* 55.7, pp. 1513–1553. ISSN: 00225096. DOI: 10.1016/j.jmps.2006.12.003.

Alder, B. J. and T. E. Wainwright (Aug. 1959). "Studies in Molecular Dynamics. I. General Method". In: *The Journal of Chemical Physics* 31.2, pp. 459–466. ISSN: 0021-9606. DOI: 10.1063/1.1730376. URL: http://aip.scitation.org/doi/10.1063/1.1730376.

Allen, M. P. and D. J. Tildesley (2017). *Computer Simulation of Liquids*. Oxford University Press. ISBN: 9780198803201.

Arnold, M. D. (2005). "Growth and Patterning of Anisotropic Optical Coatings". PhD thesis. University of Otago, Dunedin, New Zealand.

— (2017). "Single-mode tuning of the plasmon resonance in high-density pillar arrays". In: *Journal of Physics Condensed Matter* 29. ISSN: 1361648X. DOI: 10.1088/1361-648X/aa57c8. URL: https://doi.org/10.1088/1361-648X/aa57c8.

Arnold, M. D. and M. G. Blaber (2009). "Optical performance and metallic absorption in nanoplasmonic systems". In: *Optics express* 17.5, pp. 3835–3847. ISSN: 1094-4087. DOI: 10.1364/oe.17.003835. URL: http://www.ncbi.nlm.nih.gov/pubmed/19259225.

Aspnes, D. E., J. B. Theeten, and F. Hottier (1979). "Investigation of effective-medium models of microscopic surface roughness by spectroscopic ellipsometry". In: *Physical Review B* 20.8, pp. 3292–3302. ISSN: 01631829. DOI: 10.1103/PhysRevB.20.3292.

Babar, Shaista and J. H. Weaver (Jan. 2015). "Optical constants of Cu, Ag, and Au revisited". In: *Applied Optics* 54.3, p. 477. ISSN: 1559-128X. DOI: 10.1364/AO.54.000477. URL: https://www.osapublishing.org/abstract.cfm?URI=ao-54-3-477.

Bale, Harold D. and Paul W. Schmidt (1984). "Small-Angle X-Ray-Scattering Investigation of Submicroscopic Porosity with Fractal Properties". In: *Physical Review Letters* 53.6, pp. 596–599. ISSN: 00319007. DOI: 10.1103/PhysRevLett.53.596.

Baneshi, Mehdi et al. (2012). "The effect of particles size distribution on aesthetic and thermal performances of polydisperse TiO 2 pigmented coatings: Comparison between numerical and experimental results". In: *Journal of Quantitative Spectroscopy and Radiative Transfer* 113.8, pp. 594–606. ISSN: 00224073. DOI: 10.1016/j.jqsrt.2012.02.006. URL: http://dx.doi.org/10.1016/j.jqsrt.2012.02.006.

Bardeen, J. M. et al. (1986). "The statisitcs of peaks of Gaussian random fields". In: *The Astrophysical Journal* 304, pp. 15–61.

Barman, S K (2000). "The solution of the radiative transfer equation for polarized light by the Chandrasekhar ' s discrete ordinate method". In: 66, pp. 509–517.

Beasley, J. K., J. T. Atkins, and Jr. Billmeyer (1967). *Scattering and Absorption of Light in Turbid Media*. Ed. by R. L. Rowell and R. S. Stein. New York: Gordon and Breach.

Beck, D. E. (1971). "Quantum-mechanical random-phase-approximation calculation of the surface-plasmon dispersion relation for a semi-infinite electron gas". In: *Physical Review B* 4.5, pp. 1555–1560. ISSN: 01631829. DOI: 10.1103/PhysRevB.4.1555.

Bergman, D. J. (1976). "Variational bounds on some bulk properties of a two-phase composite material". In: *Physical Review B* 14.4, pp. 1531–1542.

— (1978). "The dielectric constant of a composite material-A problem in classical physics". In: *Physics Reports* 43.9, pp. 377–407. ISSN: 03701573. DOI: 10.1016/0370-1573(78)90009-1.

— (1979). "Dielectric constant of a two-component granular composite: A practical scheme for calculating the pole spectrum". In: *Physical Review B* 19.4, pp. 2359–2368. ISSN: 01631829. DOI: 10.1103/PhysRevB.19.2359.

— (1980). "Exactly solvable microscopic geometries and rigorous bounds for the complex dielectric constant of a two-component composite material". In: *Physical Review Letters* 44.19, pp. 1285–1287. ISSN: 00319007. DOI: 10.1103/PhysRevLett.44.1285.

Berini, P. (2000). "Plasmon-polariton waves guided by thin lossy metal films of finite width: Bound modes of symmetric structures". In: *Physical Review B* 61.15, pp. 10484–10503. ISSN: 0163-1829. DOI: 10.1103/PhysRevB.61.10484.

Berk, N. F. (1987). "Scattering properties of a model bicontinuous structure with a well defined length scale". In: *Physical Review Letters* 58.25, pp. 2718–2721. ISSN: 00319007. DOI: 10.1103/PhysRevLett.58.2718.

— (1991). "Scattering properties of the leveled-wave model of random morphologies". In: *Physical Review A* 44.8, pp. 5069–5079.

Berryman, J. G. and G. W. Milton (1988). "Microgeometry of random composites and porous media". In: *Journal of Physics D: Applied Physics* 21.1, pp. 87–94. ISSN: 13616463. DOI: 10.1088/0022-3727/21/1/013.

Blumenfeld, Raphael and Salvatore Torquato (1993). "Coarse-graining procedure to generate and analyze heterogeneous materials: Theory". In: *Physical Review E* 48.6, pp. 4492–4500. ISSN: 1063651X. DOI: 10.1103/PhysRevE.48.4492.

Bohren, C. F. and D. R. Huffman (2007). *Absorption and Scattering of Light by Small Particles*. Weinheim: Wiley-VCH. ISBN: 9780471293408.

Bosman, M. et al. (2012). "Light splitting in nanoporous gold and silver". In: *ACS Nano* 6.1, pp. 319–326. ISSN: 19360851. DOI: 10.1021/nn203600n. URL: http://pubs.acs.org/doi/abs/10.1021/nn203600n.

Brouers, F. (2000). "Percolation threshold and conductivity in metal-insulator composite mean-field theories". In: *Journal of Physics C: Solid State Physics* 19.36, pp. 7183–7193. ISSN: 0022-3719. DOI: 10.1088/0022-3719/19/36/010.

Brown, W. F. (1955). "Solid Mixture Permittivities". In: *The Journal of Chemical Physics* 23.8, pp. 1514–1517. ISSN: 0021-9606. DOI: 10.1063/1.1742339. URL: http://aip.scitation.org/doi/10.1063/1.1742339.

Bruno, O. P. and F. Reitich (1993a). "Numerical solution of diffraction problems: a method of variation of boundaries". In: *Journal of the Optical Society of America A* 10.6, pp. 1168–1175. ISSN: 1084-7529. DOI: 10.1364/JOSAA.10.002551. URL: https://www.osapublishing.org/abstract.cfm?URI=josaa-10-12-2551.

— (1993b). "Numerical solution of diffraction problems: a method of variation of boundaries III Doubly periodic gratings". In: *Journal of the Optical Society of America A* 10.12, pp. 2551–2562. ISSN: 1084-7529. DOI: 10.1364/JOSAA.10.002551. URL: https://www.osapublishing.org/abstract.cfm?URI=josaa-10-12-2551.

— (1993c). "Numerical solution of diffraction problems: a method of variation of boundaries. II. Finitely conducting gratings, Pade approximants, and singularities". In: *Journal of the Optical Society of America A* 10.11, pp. 2307–2316. ISSN: 1084-7529. DOI: 10.1364/JOSAA.10.002551. URL: https://www.osapublishing.org/abstract.cfm?URI=josaa-10-12-2551.

Burke, J. J., G. I. Stegeman, and T. Tamir (1986). "Surface-polariton-like waves guided by thin, lossy metal films". In: *Physical Review B* 33.8, pp. 5186–5201. ISSN: 01631829. DOI: 10.1103/PhysRevB.33.5186.

Cahn, J. W. (Jan. 1965). "Phase Separation by Spinodal Decomposition in Isotropic Systems". In: *The Journal of Chemical Physics* 42.1, pp. 93–99. ISSN: 0021-9606. DOI: 10.1063/1.1695731. URL: http://aip.scitation.org/doi/10.1063/1.1695731.

Chai, J. et al. (2017). "Numerical simulation of white double-layer coating with different submicron particles on the spectral reflectance". In: *Journal of Quantitative Spectroscopy and Radiative Transfer* 189, pp. 176–180. ISSN: 00224073. DOI: 10.1016/j.jqsrt.2016.11.020. URL: http://linkinghub.elsevier.com/retrieve/pii/S0022407316301261.

Chandezon, J., M. T. Dupuis, et al. (1982). "Multicoated gratings: a differential formalism applicable in the entire optical region". In: *Journal of the Optical Society of America* 72.7, p. 839. ISSN: 0030-3941. DOI: 10.1364/JOSA.72.000839.

Chandezon, J., D. Maystre, and G. Raoult (1980). "A new theoretical method for diffraction gratings and its numerical application". In: *J. Optics (Paris)* 11.4, pp. 235–241.

Chandrasekhar, S. (1960). *Radiative Transfer*. New York: Dover.

Chen, X. et al. (2004). "Robust method to retrieve the constitutive effective parameters of metamaterials". In: *Physical Review E - Statistical Physics, Plasmas, Fluids, and Related Interdisciplinary Topics* 70.016608, pp. 1–7. ISSN: 1063651X. DOI: 10.1103/PhysRevE.70.016608.

Cherkaev, A. (2000). *Variational Methods for Structural Optimization*. Springer-Verlag.

Cherkaev, A. V. and L. V. Gibiansky (1996). "Extremal structures of multiphase heat conducting composites". In: *International Journal of Solids and Structures* 33.18, pp. 2609–2623. ISSN: 00207683. DOI: 10.1016/0020-7683(95)00176-X. URL: http://dx.doi.org/10.1016/0020-7683(95)00176-X.

Chou, Jeffrey B et al. (2014). "Design of wide-angle selective absorbers/emitters with dielectric filled metallic photonic crystals for energy applications." In: *Optics express* 22.S1, A144–A154. ISSN: 1094-4087. DOI: 10.1364/OE.22.00A144. URL: http://www.ncbi.nlm.nih.gov/pubmed/24921991.

Coilin, R. E. (1986). "Dyadic Green's Function Expansions in Spherical Coordinates". In: *Electromagnetics* 6.3, pp. 183–207. DOI: 10.1080/02726348608915211.

Cortie, M. B. et al. (2007). "Mesoporous gold sponge". In: *Australian Journal of Chemistry* 60.7, pp. 524–527. ISSN: 00049425. DOI: 10.1071/CH06372.

DeVoe, H. (1964). "Optical properties of molecular aggregates. II. Classical theory of the refraction, absorption, and optical activity of solutions and crystals". In: *J. Chem. Phys.* 41, pp. 393–400.

— (1965). "Optical properties of molecular aggregates. II. Classical theory of the refraction, absorption, and optical activity of solutions and crystals". In: *J. Chem. Phys.* 43, pp. 3199–3208.

Dlugach, Janna M et al. (2011). "Numerically exact computer simulations of light scattering by densely packed, random particulate media". In: *Journal of Quantitative Spectroscopy and Radiative Transfer* 112.13, pp. 2068–2078. ISSN: 00224073. DOI: 10.1016/j.jqsrt.2011.02.009. URL: http://dx.doi.org/10.1016/j.jqsrt.2011.02.009.

Dombrovsky, Leonid A., Jaona Randrianalisoa, and Dominique Baillis (2006). "Modified two-flux approximation for identification of radiative properties of absorbing and scattering media from directional-hemispherical measurements." In: *Journal of the Optical Society of America* 23.1, pp. 91–8. ISSN: 1084-7529. DOI: 10.1364/JOSAA.23.000091.

Draine, B. T. (1988). "The Discrete-Dipole Approximation and its Application to Interstellar Graphite Grains". In: *The Astrophysical Journal* 333, pp. 848–872.

Draine, B. T. and P. J. Flatau (1994). "Discrete-dipole approximation for scattering calculations". In: *Journal of the Optical Society of America A* 11.4, p. 1491. ISSN: 1084-7529. DOI: 10.1364/JOSAA.11.001491.

— (2008). "Discrete-dipole approximation for periodic targets: theory and tests." In: *Journal of the Optical Society of America. A, Optics, image science, and vision* 25.11, pp. 2693–2703. ISSN: 1084-7529. DOI: 10.1364/JOSAA.25.002693. arXiv: 0809.0338.

Earp, A. A. and G. B. Smith (2011). "Evolution of plasmonic response in growing silver thin films with pre-percolation non-local conduction and emittance drop". In: *Journal of Physics D: Applied Physics* 44.25, p. 255102. ISSN: 0022-3727. DOI: 10.1088/0022-3727/44/25/255102.

Edee, K et al. (2008). "Beam implementation in a nonorthogonal coordinate system: application to the scattering from random rough surfaces." In: *Journal of the Optical Society of America. A, Optics, image science, and vision* 25.3, pp. 796–804. ISSN: 1084-7529. DOI: 10.1364/JOSAA.25.000796.

Elias, M. and G. Elias (2002). "New and fast calculation for incoherent multiple scattering." In: *Journal of the Optical Society of America A.* 19.5, pp. 894–901.

Elias, Mady and Georges Elias (2004). "Radiative transfer in inhomogeneous stratified scattering media with use of the auxiliary function method." In: *Journal of the Optical Society of America. A* 21.4, pp. 580–9. ISSN: 1084-7529. DOI: 10.1364/JOSAA.21.000580. URL: http://www.ncbi.nlm.nih.gov/pubmed/15078030.

Engström, C. (2005). "Bounds on the effective tensor and the structural parameters for anisotropic two-phase composite material". In: *Journal of Physics D: Applied Physics* 38.19, pp. 3695–3702. ISSN: 00223727. DOI: 10.1088/0022-3727/38/19/019.

Fano, U. (Mar. 1941). "The Theory of Anomalous Diffraction Gratings and of Quasi-Stationary Waves on Metallic Surfaces (Sommerfeld's Waves)". In: *Journal of the Optical Society of America* 31.3, p. 213. ISSN: 0030-3941. DOI: 10.1364/JOSA.31.000213. URL: https://www.osapublishing.org/abstract.cfm?URI=josa-31-3-213.

Fukshansky, Leonid and Nina Kazarinova (1980). "Extension of the Kubelka-Munk theory of light propagation in intensely scattering materials to fluorescent media". In: *Journal of the Optical Society of America* 70.9, pp. 1101–1111. ISSN: 00303941. URL: http://www.opticsinfobase.org/abstract.cfm?uri=josa-70-9-1101.

Gali, M. A. and M. D. Arnold (Nov. 2018). "Recurrent approach to effective material properties with application to anisotropic binarized random fields". In: *(submitted to Physical Review B)*. arXiv: 1811.06163. URL: http://arxiv.org/abs/1811.06163.

Gali, M.A. et al. (2017). "Super-cool paints: Optimizing composition with a modified four-flux model". In: *Proceedings of SPIE - The International Society for Optical Engineering* 10369. ISSN: 1996756X. DOI: 10.1117/12.2273548.

Gali, Marc A. et al. (2017). "Extending the applicability of the four-flux radiative transfer method". In: *Applied Optics* 56.31, pp. 8699–8709. ISSN: 21553165. DOI: 10.1364/AO.56.008699.

Galí, Marc A. et al. (2015). "Plasmonic response in nanoporous metal: dependence on network topology". In: *Proc. SPIE 9668, Micro+Nano Materials, Devices, and Systems, 96683S*. DOI: 10.1117/12.2202278;.

Galinski, H. et al. (2011). "Dealloying of platinum-aluminum thin Films: Dynamics of pattern formation". In: *Physical Review Letters* 107.22, pp. 6–9. ISSN: 00319007. DOI: 10.1103/PhysRevLett.107.225503. arXiv: 1104.4944.

Garoli, D. et al. (2015). "Engineered/tailored nanoporous gold structures for infrared plasmonics". In: *Proc. of SPIE* 9547, 95470K. DOI: 10.1117/12.2186562. URL: http://proceedings.spiedigitallibrary.org/proceeding.aspx?doi=10.1117/12.2186562.

Gentle, A. R. and G. B. Smith (2007). *Angular selectivity: impact on optimised coatings for night sky radiative cooling*. Ed. by G. B. Smith, A. Lakhtakia, and C.C. Lee. SPIE-INT SOC OPTICAL ENGINEERING. DOI: 10.1117/12.825722.

— (2008). "Five layer narrow band position variable filters for sharp colours and ultra low emittance". In: *Applied Physics B: Lasers and Optics* 92.1, pp. 67–72. ISSN: 09462171. DOI: 10.1007/s00340-008-3060-0.

Gentle, A. R., S. D. Yambem, et al. (2015). "Optimized multilayer indium-free electrodes for organic photovoltaics". In: *Physica Status Solidi A* 212.2, pp. 348–355.

ISSN: 18626300. DOI: 10.1002/pssa.201431469. URL: http://doi.wiley.com/10.1002/pssa.201431469.

Gentle, J. E. (2009). *Computational Statistics*, p. 528. ISBN: 9780387759357. DOI: 10.1007/978-0-387-98144-4. arXiv: arXiv:1011.1669v3.

Genz, Alan and Frank Bretz (2009). *Computation of Multivariate Normal and t Probabilities*. Vol. 195. Lecture Notes in Statistics. Berlin, Heidelberg: Springer Berlin Heidelberg. ISBN: 978-3-642-01688-2. DOI: 10.1007/978-3-642-01689-9. URL: http://link.springer.com/10.1007/978-3-642-01689-9.

Golden, K. and G. Papanicolaou (1983). "Bounds for effective parameters of heterogeneous media by analytic continuation". In: *Communications in Mathematical Physics* 90.4, pp. 473–491. ISSN: 00103616. DOI: 10.1007/BF01216179.

Gonome, Hiroki et al. (2014). "Controlling the radiative properties of cool black-color coatings pigmented with CuO submicron particles". In: *Journal of Quantitative Spectroscopy and Radiative Transfer* 132, pp. 90–98. ISSN: 00224073. DOI: 10.1016/j.jqsrt.2013.02.027. URL: http://dx.doi.org/10.1016/j.jqsrt.2013.02.027.

Gotz, P. et al. (2008). "Normal vector method for the RCWA with automated vector field generation". In: *Optics Express* 16.22, pp. 17295–17301.

Granet, Gérard (1998). "Analysis of diffraction by surface-relief crossed gratings with use of the Chandezon method: application to multilayer crossed gratings". In: *Journal of the Optical Society of America A* 15.5, p. 1121. ISSN: 1084-7529. DOI: 10.1364/JOSAA.15.001121. URL: http://www.opticsinfobase.org/abstract.cfm?uri=JOSAA-15-5-1121%7B%5C%%7D5Cnhttp://www.opticsinfobase.org/abstract.cfm?URI=JOSAA-15-5-1121.

Granovsky, A., M. Kuzmichov, and J. P. Clerc (1999). "The Symmetrised Maxwell-Garnett Approximation for Magneto-Optical Spectra of Ferromagnetic Composites". In: *J. Magn. Soc. Japan*, pp. 382–384.

Hashin, Z. (1965). "On Elastic Materials Behaviour of Arbitrary of Fibre Reinforced Phase Transverse Geometry". In: *J. Mech. Phys. Solids* 13, pp. 119–134.

Hashin, Z. and S. Shtrikman (1962). "A Variational approach to the theory of the effective magnetic permeability of multiphase materials". In: *Journal of Applied Physics* 33.10, pp. 3125–3131. ISSN: 00218979. DOI: 10.1063/1.1728579.

Hébert, Mathieu and Jean-Marie Becker (2008). "Correspondence between continuous and discrete two-flux models for reflectance and transmittance of diffusing layers". In: *Journal of Optics A: Pure and Applied Optics* 10.035006, pp. 1–6. ISSN: 1464-4258. DOI: 10.1088/1464-4258/10/3/035006. URL: http://stacks.iop.org/1464-4258/10/i=3/a=035006?key=crossref.375ce61f67af0fb44cac3e351e71cc21

Hegge, T. S. et al. (2017). "The scattering of a scalar beam from isotropic and anisotropic two-dimensional randomly rough Dirichlet or Neumann surfaces: The full angular

intensity distributions". In: pp. 1–23. arXiv: 1712.05979. URL: http://arxiv.org/abs/1712.05979.

Hori, M. and F. Yonezawa (1975a). "Statistical theory of effective electrical, thermal, and magnetic properties of random heterogeneous materials. IV. Effective medium theory and cumulant expansion method". In: *Journal of Mathematical Physics* 16.2, pp. 352–364. ISSN: 00222488. DOI: 10.1063/1.522507. URL: http://link.aip.org/link/?JMP/16/352/1%7B%5C&%7DAgg=doi.

— (1975b). "Statistical theory of effective electrical, thermal, and magnetic properties of random heterogeneous materials. V. One- and two- dimensional systems". In: *Journal of Mathematical Physics* 16.2, pp. 365–377. ISSN: 00222488. DOI: 10.1063/1.522508. URL: http://link.aip.org/link/?JMP/16/365/1%7B%5C&%7DAgg=doi.

Isichenko, M. B. (1992). "Percolation, statistical topography, and transport in random media". In: *Reviews of Modern Physics* 64.4, pp. 961–1043.

Jahan, F. and G.B. Smith (1998). "Investigation of angular selective optical properties of silver/titanium oxide cermet thin films". In: *Thin Solid Films* 333.1-2, pp. 185–190. ISSN: 00406090. DOI: 10.1016/S0040-6090(98)00844-X.

Jalas, D. et al. (2014). "Effective medium model for the spectral properties of nanoporous gold in the visible". In: *Applied Physics Letters* 105.24, p. 241906. ISSN: 0003-6951. DOI: 10.1063/1.4904714. URL: http://scitation.aip.org/content/aip/journal/apl/105/24/10.1063/1.4904714.

Johnson, P. B. and R. W. Christy (1972). "Optical constants of the noble metals". In: *Phys Rev B* 6.12, pp. 4370–4379. ISSN: 01631829. DOI: 10.1103/PhysRevB.6.4370. arXiv: arXiv:1011.1669v3.

Keller, Joseph B. (1964). "A theorem on the conductivity of a composite medium". In: *Journal of Mathematical Physics* 5.4, pp. 548–549. ISSN: 00222488. DOI: 10.1063/1.1704146.

Kreibig, Uwe and Michael Vollmer (1995). *Optical Properties of Metal Clusters*. Springer.

Kubelka, Paul (1948). "New Contributions to the Optics of Intensely Light-Scattering Materials. Part I". In: *Journal of the Optical Society of America* 38.5, p. 448. ISSN: 0030-3941. DOI: 10.1364/JOSA.38.000448. URL: https://www.osapublishing.org/abstract.cfm?URI=josa-38-5-448.

— (1954). "New Contributions to the Optics of Intensely Light-Scattering Materials. Part II: Nonhomogeneous Layers". In: *Journal of the Optical Society of America* 44.4, p. 330. ISSN: 0030-3941. DOI: 10.1364/JOSA.38.000448. URL: https://www.osapublishing.org/abstract.cfm?URI=josa-38-5-448.

Laaksonen, K et al. (2014). "Nanoparticles of TiO2 and VO2 in dielectric media: Conditions for low optical scattering, and comparison between effective medium and

four-flux theories". In: *Solar Energy Materials and Solar Cells* 130, pp. 132–137. ISSN: 09270248. DOI: 10.1016/j.solmat.2014.06.036.

Lalanne, Philippe (1997). "Improved formulation of the coupled-wave method for two-dimensional gratings". In: *Journal of the Optical Society of America A* 14.7, p. 1592. ISSN: 1084-7529. DOI: 10.1364/JOSAA.14.001592. URL: https://www.osapublishing.org/abstract.cfm?URI=josaa-14-7-1592.

Lalanne, Philippe and G Michael Morris (1996). "Highly improved convergence of the coupled-wave method for TM polarization". In: *J. Opt. Soc. Am. A* 13.4, pp. 779–784.

Lang, X. et al. (2011). "Localized surface plasmon resonance of nanoporous gold". In: *Applied Physics Letters* 98.9, p. 93701. ISSN: 00036951. DOI: 10.1063/1.3560482. URL: http://scitation.aip.org/content/aip/journal/apl/98/9/10.1063/1.3560482.

Lapine, M., L. Jelinek, and R. Marqués (2012). "Surface mesoscopic effects in finite metamaterials". In: *Optics Express* 20.16, pp. 18297–18302. ISSN: 1094-4087. DOI: 10.1364/OE.20.018297.

Lee, Jeongwon et al. (2012). "Observation and differentiation of unique high-Q optical resonances near zero wave vector in macroscopic photonic crystal slabs". In: *Physical Review Letters* 109.6, pp. 1–5. ISSN: 00319007. DOI: 10.1103/PhysRevLett.109.067401.

Leonhardt, U. (June 2006). "Optical Conformal Mapping". In: *Science* 312.5781, pp. 1777–1780. ISSN: 0036-8075. DOI: 10.1126/science.1126493. URL: http://www.sciencemag.org/cgi/doi/10.1126/science.1126493.

Letnes, P. A. (2012). "Optical polarization effects of rough and structured surfaces". PhD thesis. Norwegian University of Science and Technology. ISBN: 9788247137710.

Letnes, P. A. et al. (2012). "Calculation of the Mueller matrix for scattering of light from two-dimensional rough surfaces". In: *Physical Review A - Atomic, Molecular, and Optical Physics* 86.3, pp. 1–5. ISSN: 10502947. DOI: 10.1103/PhysRevA.86.031803. arXiv: 1108.2599.

Li, Lifeng (1993). "A Modal Analysis of Lamellar Diffraction Gratings in Conical Mountings". In: *Journal of Modern Optics* 40.4, pp. 553–573. ISSN: 0950-0340. DOI: 10.1080/09500349314550631.

— (1994). "Multilayer-coated diffraction gratings: differential method of Chandezon et al. revisited". In: *Journal of the Optical Society of America A* 11.11, pp. 2816–2828. ISSN: 1084-7529. DOI: 10.1364/JOSAA.13.000543.

— (1996a). "Multilayer-coated diffraction gratings: differential method of Chandezon et al. revisited: errata". In: *Journal of the Optical Society of America A* 13.3, p. 543. ISSN: 1084-7529. DOI: 10.1364/JOSAA.13.000543.

Li, Lifeng (1996b). "Use of Fourier series in the analysis of discontinuous periodic structures". In: *J. Opt. Soc. Am. A* 13.9, pp. 1870–1876.

Li, Lifeng and Jean Chandezon (1996). "Improvement of the coordinate transformation method for surface-relief gratings with sharp edges". In: *Journal of the Optical Society of America A* 13.11, p. 2247. ISSN: 1084-7529. DOI: 10.1364/JOSAA.13.002247. URL: http://josaa.osa.org/abstract.cfm?URI=josaa-13-11-2247.

Li, Lifeng, Jean Chandezon, et al. (1999). "Method Made Easy for Optical Engineers". In: *Applied Optics* 38.2, pp. 304–313.

Li, Lifeng, G. Granet, et al. (1996). "Some topics in extending the C method to multilayer gratings of different profiles". In: *Pure and Applied Optics (Print edition) (United Kingdom)* 5.2, pp. 141–156. ISSN: 09639659. DOI: 10.1088/0963-9659/5/2/002.

Lloyd, G. E. R. (1970). *Early Greek Science: Thales to Aristotle*. New York: W.W. Norton & Co. ISBN: 0-393-00583-6.

— (1973). *Greek Science after Aristotle*. New York: W.W. Norton & Co. ISBN: 0-393-00780-4.

Lurie, K A and A V Cherkaev (1984). "Exact estimates of conductivity of composites formed by two isotropically conducting media taken in prescribed proportion". In: *Proceedings of the Royal Society of Edinbrugh*. Vol. 99A, pp. 71–87.

Maaroof, A. I., M. B. Cortie, A. Gentle, et al. (2007). "Mesoporous gold sponge as a prototype 'metamaterial'". In: *Physica B: Condensed Matter* 394.2, pp. 167–170. ISSN: 09214526. DOI: 10.1016/j.physb.2006.12.014.

Maaroof, A. I., M. B. Cortie, and G. B. Smith (2005). "Optical properties of mesoporous gold films". In: *Journal of Optics A: Pure and Applied Optics* 7, pp. 303–309. ISSN: 14644258. DOI: 10.1088/1464-4258/7/7/007.

Maaroof, A. I., A. Gentle, et al. (2007). "Bulk and surface plasmons in highly nanoporous gold films". In: *Journal of Physics D: Applied Physics* 40.18, pp. 5675–5682. ISSN: 0022-3727. DOI: 10.1088/0022-3727/40/18/024.

Madrazo, A. and A. A. Maradudin (Jan. 1997). "Numerical solutions of the reduced Rayleigh equation for the scattering of electromagnetic waves from rough dielectric films on perfectly conducting substrates". In: *Optics Communications* 134.1-6, pp. 251–263. ISSN: 00304018. DOI: 10.1016/S0030-4018(96)00402-6. URL: http://linkinghub.elsevier.com/retrieve/pii/S0030401896004026.

Maheu, B., J. N. Letoulouzan, and G. Gouesbet (1984). "Four-flux models to solve the scatering transfer equation in terms of Lorenz-Mie parameters". In: *Applied Optics* 23.19, pp. 3353–3362.

Maradudin, A. A. (2007). *Light Scattering and Nanoscale Surface Roughness*. Ed. by Alexei A. Maradudin. Nanostructure Science and Technology. Boston, MA: Springer US.

ISBN: 978-0-387-25580-4. DOI: 10.1007/978-0-387-35659-4. URL: http://link.springer.com/10.1007/978-0-387-35659-4.

Maradudin, A. A. and E. R. Mendez (1993). "Enhanced backscattering of light from weakly rough, random metal surfaces". In: *Applied Optics* 32.19, pp. 3335–3343.

Maradudin, A. A. and D. L. Mills (1975). "Scattering and absorption of electromagnetic radiation by a semi-infinite medium in the presence of surface roughness". In: *Physical Review B* 11.4, pp. 1392–1415. ISSN: 01631829. DOI: 10.1103/PhysRevB.11.1392.

Marvin, A., F. Toigo, and V. Celli (1975). "Light scattering from rough surfaces: General incidence angle and polarization". In: *Physical Review B* 11.8, pp. 2777–2782. ISSN: 01631829. DOI: 10.1103/PhysRevB.11.2777.

Mätzler, Christian (2002). "MATLAB Functions for Mie Scattering and Absorption". In: *IAP Research Report* 2002-08, pp. 1–18. ISSN: 03060012. DOI: 10.1039/b811392k. arXiv: arXiv:1011.1669v3. URL: http://arrc.ou.edu/%7B~%7Drockee/NRA%7B%5C_%7D2007%7B%5C_%7Dwebsite/Mie-scattering-Matlab.pdf.

Maystre, D. (Apr. 1978). "A new general integral theory for dielectric coated gratings". In: *Journal of the Optical Society of America* 68.4, p. 490. ISSN: 0030-3941. DOI: 10.1364/JOSA.68.000490. URL: https://www.osapublishing.org/abstract.cfm?URI=josa-68-4-490.

Mbise, G. et al. (1989). "Angular selectivity window coatings- theory and experiment". In: *Optical materials technology for energy efficiency and solar energy conversion VIII*. Ed. by C. G. Granqvist and C. M. Lampert. SPIE - INT SOC OPTICAL ENGINEERING, pp. 179–199. ISBN: 0-8194-0185-4.

McGurn, A. R., A. A. Maradudin, and V. Celli (Apr. 1985). "Localization effects in the scattering of light from a randomly rough grating". In: *Physical Review B* 31.8, pp. 4866–4871. ISSN: 0163-1829. DOI: 10.1103/PhysRevB.31.4866. URL: https://link.aps.org/doi/10.1103/PhysRevB.31.4866.

Mcgurn, A. R. and A.A. Maradudin (July 1996). "Perturbation theory results for the diffuse scattering of light from two-dimensional randomly rough metal surfaces". In: *Waves in Random Media* 6.3, pp. 251–267. ISSN: 0959-7174. DOI: 10.1088/0959-7174/6/3/006. URL: http://www.tandfonline.com/doi/abs/10.1088/0959-7174/6/3/006.

Mie, Gustav (1908). "Beiträge zur Optik trüber Medien, speziell kolloidaler Metallösungen". In: *Annalen der Physik* 330.3, pp. 377–445. ISSN: 00033804. DOI: 10.1002/andp.19083300302. URL: http://doi.wiley.com/10.1002/andp.19083300302.

Milton, G. W. (1981). "Bounds on the Complex Permittivity of a Two-Component Composite Material." In: *Journal of Applied Physics* 52.8, pp. 5286–5293. ISSN: 00218979. DOI: 10.1063/1.329385.

— (1982). "Bounds on the elastic and transport properties of two-component composites". In: *Journal of the Mechanics and Physics of Solids* 30.3, pp. 177–191.

— (1987a). "Multicomponent Composites, Electrical Networks and New Types of Continued Fractions I". In: *Comm. Math. Phys.* 111, pp. 281–327.

— (1987b). "Multicomponent Composites, Electrical Networks and New Types of Continued Fractions II". In: *Comm. Math. Phys.* 111, pp. 329–372.

— (2002). *The Theory of Composites*. Cambridge University Press.

Milton, G. W. and N. Phan-Thien (1982). "New Bounds on Effective Elastic Moduli of Two-Component Materials". In: *Proceedings of the Royal Society of London. Series A, Mathematical and Physical Sciences*. Vol. 380, pp. 305–331. ISBN: 00804630. DOI: 10.1098/rspa.1982.0044. URL: http://www.jstor.org/stable/2397305.

Milton, Graeme W., Marc Briane, and John R. Willis (2006). "On cloaking for elasticity and physical equations with a transformation invariant form". In: *New Journal of Physics* 8. ISSN: 13672630. DOI: 10.1088/1367-2630/8/10/248. arXiv: 1410.8184.

Miwa, T., A. J. Hayter, and S. Kuriki (2003). "The evaluation of general non-centred orthant probabilities". In: *J. R. Statist. Soc. B* 65, pp. 223–234.

Miwa, T., A. J. Hayter, and W. Liu (2000). "Calculations of level probabilities for normal random variables with unequal variances with applications to Bartholomew's test in unbalanced one-way models". In: *Computational Statistics & Data Analysis* 34, pp. 17–32.

Molenaar, R., J. J. Bosch, and J. R. Zijp (1999). "Determination of Kubelka–Munk scattering and absorption coefficients by diffuse illumination". In: *Applied Optics* 38.10, pp. 2068–2077.

Mudgett, P. S. and L. W. Richards (1971). "Multiple Scattering Calculations for Technology". In: *Applied Optics* 10.7, pp. 1485–1502. DOI: 10.1364/AO.10.001485.

Murat, F. and L. Tartar (1994). *On the Control of Coefficients in Partial Differential Equations*. Boston, MA: Birkhäuser.

Nicorovici, N. A., R. C. McPhedran, and G. W. Milton (1994). "Optical and dielectric properties of partially resonant composites". In: *Physical Review B* 49.12, pp. 8479–8482. ISSN: 01631829. DOI: 10.1103/PhysRevB.49.8479.

Niklasson, Gunnar A. (1987). "Comparison between four flux theory and multiple scattering theory". In: *Applied Optics* 26.19, pp. 4034–4036.

Nordam, T., P. A. Letnes, and I. Simonsen (2013). "Numerical simulations of scattering of light from two-dimensional rough surfaces using the reduced Rayleigh equation". In: *Frontiers in Physics* 1.7491, pp. 34–40. ISSN: 2296-424X. DOI: 10.3389/

fphy.2013.00008. arXiv: arXiv:1204.4984v2. URL: http://arxiv.org/abs/1204.4984%7B%5C%%7D5Cnhttp://www.arxiv.org/pdf/1204.4984.pdf%7B%5C%%7D5Cnhttp://journal.frontiersin.org/article/10.3389/fphy.2013.00008/abstract.

O'Donnell, K. A. (2001). "High-order perturbation theory for light scattering from a rough metal surface". In: *Journal of the Optical Society of America A* 18.7, p. 1507. ISSN: 1084-7529. DOI: 10.1364/JOSAA.18.001507. URL: https://www.osapublishing.org/abstract.cfm?URI=josaa-18-7-1507.

Olmon, Robert L. et al. (Dec. 2012). "Optical dielectric function of gold". In: *Physical Review B* 86.23, p. 235147. ISSN: 1098-0121. DOI: 10.1103/PhysRevB.86.235147. URL: https://link.aps.org/doi/10.1103/PhysRevB.86.235147.

Olsen, T. et al. (2011). "Dispersive and covalent interactions between graphene and metal surfaces from the random phase approximation". In: *Physical Review Letters* 107.15, pp. 1–5. ISSN: 00319007. DOI: 10.1103/PhysRevLett.107.156401. arXiv: 1106.5375.

Pendry, J. B. et al. (2012). "Transformation Optics and Subwavelength Control of Light". In: *Science* 337.6094, pp. 549–552. ISSN: 0036-8075. DOI: 10.1126/science.1220600.

Pitarke, J. M. and J. P. Perdew (2003). "Metal surface energy: Persistent cancellation of short-range correlation effects beyond the random phase approximation". In: *Physical Review B* 67.4, p. 045101. ISSN: 0163-1829. DOI: 10.1103/PhysRevB.67.045101. URL: https://link.aps.org/doi/10.1103/PhysRevB.67.045101.

Purcell, E. M. and C. R. Pennypacker (1973). "Scattering and Absorption of Light by Nonspherical Dielectric Grains". In: *The Astrophysical Journal* 186, pp. 705–714.

Quintanilla, J. (1999). "Microstructure functions for random media with impenetrable particles". In: *Physical Review E - Statistical Physics, Plasmas, Fluids, and Related Interdisciplinary Topics* 60.5, pp. 5788–5794. ISSN: 1063651X. DOI: 10.1103/PhysRevE.60.5788.

Quintanilla, John A. et al. (2007). "Versatility and robustness of Gaussian random fields for modelling random media". In: *Modelling and Simulation in Materials Science and Engineering* 15.4. ISSN: 09650393. DOI: 10.1088/0965-0393/15/4/S02.

Rahman, A. (Oct. 1964). "Correlations in the Motion of Atoms in Liquid Argon". In: *Physical Review* 136.2A, A405–A411. ISSN: 0031-899X. DOI: 10.1103/PhysRev.136.A405. URL: https://link.aps.org/doi/10.1103/PhysRev.136.A405.

Rakić, Aleksandar D. (Aug. 1995). "Algorithm for the determination of intrinsic optical constants of metal films: application to aluminum". In: *Applied Optics* 34.22,

p. 4755. ISSN: 0003-6935. DOI: 10.1364/AO.34.004755. URL: https://www.osapublishing.org/abstract.cfm?URI=ao-34-22-4755.

Rapaport, D. C. (1996). *The Art of Molecular Dynamics Simulation*. Cambridge University Press. ISBN: 0511816588.

Rayleigh, L. (July 1907). "III. Note on the remarkable case of diffraction spectra described by Prof. Wood". In: *The London, Edinburgh, and Dublin Philosophical Magazine and Journal of Science* 14.79, pp. 60–65. ISSN: 1941-5982. DOI: 10.1080/14786440709463661. URL: https://www.tandfonline.com/doi/full/10.1080/14786440709463661.

Rechtsman, M. C. and S. Torquato (2008). "Effective dielectric tensor for electromagnetic wave propagation in random media". In: *Journal of Applied Physics* 103.8, pp. 1–15. ISSN: 00218979. DOI: 10.1063/1.2906135. arXiv: 0709.1924.

Ren, X. et al. (2011). "Beyond the random-phase approximation for the electron correlation energy: The importance of single excitations". In: *Physical Review Letters* 106.15, pp. 16–19. ISSN: 00319007. DOI: 10.1103/PhysRevLett.106.153003. arXiv: 1011.2724.

Ren, Xinguo, Patrick Rinke, and Matthias Scheffler (2009). "Exploring the random phase approximation: Application to CO adsorbed on Cu(111)". In: *Physical Review B - Condensed Matter and Materials Physics* 80.4, pp. 1–8. ISSN: 10980121. DOI: 10.1103/PhysRevB.80.045402.

Rice, S.O. (1958). "Distribution of the Duration of Fades in Radio Transmission : Gaussian Noise Model". In: *The Bell System Technical Journal* 37.3, pp. 581–635.

Roberts, A. P. and M. A. Knackstedt (1996). "Structure-property correlations in model composite materials". In: *Physical Review E - Statistical Physics, Plasmas, Fluids, and Related Interdisciplinary Topics* 54.3, pp. 2313–2328. ISSN: 1063651X. DOI: 10.1103/PhysRevE.54.2313.

Roberts, A. P. and M. Teubner (1995). "Transport properties of heterogeneous materials derived from Gaussian random fields: Bonds and simulation". In: *Physical Review E* 51.5, pp. 4141–4154.

Roberts, A. P. and S. Torquato (1999). "Chord-distribution functions of three-dimensional random media: Approximate first-passage times of Gaussian processes". In: *Physical Review E - Statistical Physics, Plasmas, Fluids, and Related Interdisciplinary Topics* 59.5, pp. 4953–4963. ISSN: 1063651X. DOI: 10.1103/PhysRevE.59.4953. arXiv: 9901315 [cond-mat].

Rogers, C. A. (1961). "An asymptotic expansion for certain Schlafli functions". In: *J. London Math. Soc.* 36.1961, pp. 78–80.

Rozé, Claude, Thierry Girasole, Gerard Grehan, et al. (2001). "Average crossing parameter and forward scattering ratio values in four-flux model for multiple scattering media". In: *Optics Communications* 194, pp. 251–263.

Rozé, Claude, Thierry Girasole, and Anne Gaelle Tafforin (2001). "Multilayer four-flux model of scattering, emitting and absorbing media". In: *Atmospheric Environment* 35, pp. 5125–5130. ISSN: 13522310. DOI: 10.1016/S1352-2310(01)00328-4.

Schurig, D. et al. (Nov. 2006). "Metamaterial Electromagnetic Cloak at Microwave Frequencies". In: *Science* 314.5801, pp. 977–980. ISSN: 0036-8075. DOI: 10.1126/science.1133628. URL: http://www.sciencemag.org/cgi/doi/10.1126/science.1133628.

Sen, A. K. and S. Torquato (1988). "Series Expansions for Clustering in Continuum Percolation Models with Interactions". In: *Journal of Chemical Physics* 89.6, pp. 3799–3807. ISSN: 00219606. DOI: 10.1063/1.454904.

— (1989). "Effective Conductivity of Anisotropic 2-Phase Composite Media". In: *Physical Review B* 39.7, pp. 4504–4515.

Shcherbakov, Alexey A and Alexandre V Tishchenko (2013). "Efficient curvilinear coordinate method for grating diffraction simulation". In: *Optics Express* 21.21, pp. 25236–25247. ISSN: 1094-4087. DOI: 10.1364/OE.21.025236. URL: http://www.opticsinfobase.org/abstract.cfm?URI=oe-21-21-25236.

Shen, Yichen et al. (2014). "Metamaterial broadband angular selectivity". In: *Physical Review B* 90.12, pp. 1–5. ISSN: 1098-0121. DOI: 10.1103/PhysRevB.90.125422. URL: http://link.aps.org/doi/10.1103/PhysRevB.90.125422.

Siewert, C.E. (2000). "A concise and accurate solution to Chandrasekhar's basic problem in radiative transfer". In: *Journal of Quantitative Spectroscopy and Radiative Transfer* 64.2, pp. 109–130. ISSN: 00224073. DOI: 10.1016/S0022-4073(98)00144-7. URL: http://www.sciencedirect.com/science/article/pii/S0022407398001447.

Simonot, L. et al. (2016). "Multilayer four-flux matrix model accounting for directional-diffuse light transfers". In: *Applied Optics* 55.1, pp. 27–37. ISSN: 0003-6935. DOI: 10.1364/AO.55.000027. URL: http://www.osapublishing.org/viewmedia.cfm?uri=ao-55-1-27%7B%5C&%7Dseq=0%7B%5C&%7Dhtml=true.

Simonsen, I. et al. (2011). "Light scattering from anisotropic, randomly rough, perfectly conducting surfaces". In: *Computer Physics Communications* 182.9, pp. 1904–1908. ISSN: 00104655. DOI: 10.1016/j.cpc.2011.01.010. URL: http://dx.doi.org/10.1016/j.cpc.2011.01.010.

Slovick, Brian et al. (2017). "Transfer matrix method for four-flux radiative transfer". In: *Applied Optics* 56.21, pp. 5890–5896. ISSN: 1559-128X. DOI: 10.1364/AO.56.005890. arXiv: 1705.05453. URL: http://arxiv.org/abs/1705.05453.

Smith, G. B. (2002). "Nanostructured thin films - A critical review". In: *Complex mediums III: Veyond linear isotropic dielectrics*. Ed. by A. Lakhtakia, G. Dewar, and M. W.

McCall. SPIE-INT SOC OPTICAL ENGINEERING, pp. 207–221. DOI: 10.1117/12.472985.

Smith, G. B., a. Ben-David, and P. D. Swift (2001). "New type of TiN coating combining broad band visible transparency and solar control". In: *Renewable energy* 22.1, pp. 79–84. ISSN: 09601481. DOI: 10.1016/S0960-1481(00)00071-9.

Smith, G. B., A. R. Gentle, and A. I. Maaroof (Feb. 2007). "Metal-insulator nanocomposites which act optically like homogeneous conductors". In: *Journal of Nanophotonics* 1.1, p. 013507. ISSN: 1934-2608. DOI: 10.1117/1.2711706. URL: http://nanophotonics.spiedigitallibrary.org/article.aspx?doi=10.1117/1.2711706.

Smith, G. B. and C. G. Granqvist (2010). *Green Nanotechnology: Solutions for Sustainability and Energy in the Built Environment*. Boca Raton, USA: CRC Press.

Smith, G. B., A. I. Maaroof, R. S. Allan, et al. (2004). "Optical response of nanostructured metal/dielectric composites and multilayers". In: *Proc. of SPIE* 5508, pp. 192–205. DOI: 10.1117/12.555971. URL: http://proceedings.spiedigitallibrary.org/proceeding.aspx?doi=10.1117/12.555971.

Smith, G. B., A. I. Maaroof, and M. B. Cortie (2008). "Percolation in nanoporous gold and the principle of universality for two-dimensional to hyperdimensional networks". In: *Physical Review B - Condensed Matter and Materials Physics* 78.16, pp. 1–11. ISSN: 10980121. DOI: 10.1103/PhysRevB.78.165418.

Smith, G. B., A. Maaroof, et al. (2006). "Tuning plasma frequency for improved solar control glazing using mesoporous nanostructures". In: *Proc. of SPIE* 6197, 61970T. DOI: 10.1117/12.661198. URL: http://proceedings.spiedigitallibrary.org/proceeding.aspx?articleid=1325495%7B%5C&%7DresultClick=1.

Stauffer, D. and A. Aharony (1992). *Introduction to Percolation Theory*. 2nd. London: Taylor & Francis.

Stokes, G. G. (1851). "On the Composition and Resolution of Streams of Polarized Light from different Sources". In: *Transactions of the Cambridge Philosophical Society* 9, p. 399.

Stratton, J. A. (1941). *Electromagnetic Theory*. New York: McGraw-Hill.

Stratton, J. and L. Chu (1939). "Diffraction Theory of Electromagnetic Waves". In: *Physical Review* 56.1, pp. 99–107. ISSN: 0031-899X. DOI: 10.1103/PhysRev.56.99.

Supansomboon, S. et al. (2014). "Effect of precursor stoichiometry on the morphology of nanoporous platinum sponges". In: *ACS Applied Materials and Interfaces* 6.12, pp. 9411–9417. ISSN: 19448252. DOI: 10.1021/am501794y.

Tai, M C et al. (Mar. 2018). "Spontaneous growth of polarizing refractory metal 'nanofins'". In: *Nanotechnology* 29.10, p. 105702. ISSN: 0957-4484. DOI: 10.1088/1361-

6528/aaa639. URL: http://stacks.iop.org/0957-4484/29/i=10/a=105702?key=crossref.bff51d31d02cd253b75cc62c2a727063.

Tai, M. C., M. D. Arnold, et al. (Aug. 2017). "Optical anisotropy due to perpendicular azimuth serial bideposition". In: *Nanostructured Thin Films X*. Ed. by Tom G. Mackay, Akhlesh Lakhtakia, and Yi-Jun Jen. SPIE, p. 20. ISBN: 9781510611696. DOI: 10.1117/12.2273528. URL: https://www.spiedigitallibrary.org/conference-proceedings-of-spie/10356/2273528/Optical-anisotropy-due-to-perpendicular-azimuth-serial-bideposition/10.1117/12.2273528.full.

Tai, M. C., A. Gentle, M. D. Arnold, et al. (2016). "Optical in situ study of de-alloying kinetics in nanoporous gold sponges". In: *RSC Adv.* 6.89, pp. 85773–85778. ISSN: 2046-2069. DOI: 10.1039/C6RA18272K. URL: http://xlink.rsc.org/?DOI=C6RA18272K.

Tai, M. C., A. Gentle, K. S. de Silva, et al. (2015). "Thermal Stability of Nanoporous Raney Gold Catalyst". In: *Metals* 5.3, pp. 1197–1211. ISSN: 2075-4701. DOI: 10.3390/met5031197. URL: http://www.mdpi.com/2075-4701/5/3/1197/.

Tamm, I. Y. (1924). "Electrodynamics of an anisotropic medium in the special theory of relativity." In: *J. Russ. Phys. Chem. Soc.* 56.248.

Tang, K. and R. O. Buckius (2001). "A statistical model of wave scattering from random rough surfaces". In: *International Journal of Heat and Mass Transfer* 44.21, pp. 4059–4073. ISSN: 00179310. DOI: 10.1016/S0017-9310(01)00050-3.

Teubner, M. (1991). "Level surfaces of Gaussian random fields and microemulsions". In: *Europhysics Letters (EPL)* 14.5, pp. 403–408.

Tonon, C. et al. (2001). "Four-flux model for a multilayer, plane absorbing and scattering medium: application to the optical degradation of white paint in a space environment." In: *Applied Optics* 40.22, pp. 3718–3725. ISSN: 0003-6935. URL: http://www.ncbi.nlm.nih.gov/pubmed/18360405.

Torquato, S (1985). "Effective electrical conductivity of two-phase disordered composite media". In: *Journal of Applied Physics* 58, pp. 3790–3797. DOI: 10.1063/1.335593.

— (1985). "Bulk properties of two-phase disordered media. II. Effective conductivity of a dilute dispersion of penetrable spheres". In: *The Journal of Chemical Physics* 83.11, p. 4776. ISSN: 00219606. DOI: 10.1063/1.447497. URL: http://scitation.aip.org/content/aip/journal/jcp/81/11/10.1063/1.447497.

— (1986). "Microstructure Characterization and Bulk Properties of Disordered 2-Phase Media". In: *Journal of Statistical Physics* 45.5-6, pp. 843–873.

— (2002). *Random Heterogeneous Materials: Microstructure and Macroscopic Properties*. New York: Springer-Verlag.

Torquato, S. (2009). "Inverse optimization techniques for targeted self-assembly". In: *Soft Matter* 5.6, p. 1157. ISSN: 1744-683X. DOI: 10.1039/b814211b. arXiv: 0811.0040. URL: http://xlink.rsc.org/?DOI=b814211b.

Torquato, S. and A. Donev (2004). "Minimal surfaces and multifunctionality". In: *Proceedings of the Royal Society A: Mathematical, Physical and Engineering Sciences* 460.2047, pp. 1849–1856. ISSN: 1364-5021. DOI: 10.1098/rspa.2003.1269.

Torquato, S. and A. K. Sen (1990). "Conductivity tensor of anisotropic composite media from the microstructure". In: *Journal of Applied Physics* 67.3, pp. 1145–1155. ISSN: 00218979. DOI: 10.1063/1.345711.

Torquato, S. and G. Stell (1983). "Microstructure of two-phase random media. III. The n-point matrix probability functions for fully penetrable spheres". In: *The Journal of Chemical Physics* 79.3, pp. 1505–1510. ISSN: 00219606. DOI: 10.1063/1.445941. URL: https://doi.org/10.1063/1.445941.

Tsang, L., C. H. Chan, and K. Pak (1993). "Monte Carlo Simulation of a Two-Dimensional Random Rough Surface Using the Sparse-Matrix Flat-Surface Itertive Approach". In: *Electronics Letters* 29.13, pp. 1153–1154.

— (1994). "Backscattering enhancement of a two-dimensional random rough surface (three-dimensional scattering) based on Monte Carlo simulations Leung". In: *J. Opt. Soc. Am. A* 11.2, pp. 711–715.

Tsang, L., J. A. Kong, et al. (2000). *Scattering of Electromagnetic Waves: Numerical Simulations*. Ed. by J. A. Kong. Wiley Series in Remote Sensing, pp. 113–161.

van der Vaart, H. R. (Mar. 1953). "The content of certain spherical polyhedra for any number of dimensions". In: *Experientia* 9.3, pp. 88–89. ISSN: 0014-4754. DOI: 10.1007/BF02178328. URL: http://link.springer.com/10.1007/BF02178328.

— (1995). "The content of some classes of non-Euclidian polyhedra for any number of dimensions, with several applications, I, II". In: *Proc. Academie van Wetenschaffen*. Vol. 58. Amsterdam, pp. 199–221.

Vargas, W.E. and G.A. Niklasson (1997). "Pigment mass density and refractive index determination from optical measurements". In: *Journal of Physics Condensed Matter* 9, pp. 1661–1670. ISSN: 09538984. DOI: 10.1088/0953-8984/9/7/027.

Vargas, William E. (1998). "Generalized Four-Flux Radiative Transfer Model". In: *Applied Optics* 37.13, p. 2615. ISSN: 0003-6935. DOI: 10.1364/AO.37.002615. URL: https://www.osapublishing.org/ao/abstract.cfm?uri=ao-37-13-2615.

— (2000). "Optimization of the diffuse reflectance of pigmented coatings taking into account multiple scattering". In: *Journal of Applied Physics* 88.7, pp. 4079–4084. ISSN: 00218979. DOI: 10.1063/1.1289230. URL: http://link.aip.org/link/JAPIAU/v88/i7/p4079/s1%7B%5C&%7DAgg=doi.

Vargas, William E. and Gunnar A. Niklasson (1997a). "Applicability conditions of the Kubelka–Munk theory". In: *Applied Optics* 36.22, p. 5580. ISSN: 0003-6935. DOI: 10.1364/AO.36.005580. URL: https://www.osapublishing.org/abstract.cfm?URI=ao-36-22-5580.

— (1997b). "Forward-scattering ratios and average pathlength parameter in radiative transfer models". In: *Applied Optics* 36.16, pp. 3735–3738. ISSN: 0953-8984. DOI: 10.1088/0953-8984/9/42/021. URL: http://stacks.iop.org/0953-8984/9/i=42/a=021.

Vigdergauz, S. (1994). "Two-Dimensional Grained Composites of Extreme Rigidity". In: *Journal of Applied Mechanics* 61.2, p. 390. ISSN: 00218936. DOI: 10.1115/1.2901456. URL: http://appliedmechanics.asmedigitalcollection.asme.org/article.aspx?articleid=1411269.

Walsby, E. D. et al. (2005). "Growth and characterisation of birefringent films on textured silicon substrates". In: *Microelectronic Engineering* 78-79.1-4, pp. 436–441. ISSN: 01679317. DOI: 10.1016/j.mee.2004.12.055.

Wiener, O. (1912). "Die Theorie des Mischkörpers für das Feld der stationären Strömung". In: *Abh. Math. Phys. Kl. Kgl. Sachs. Ges.* 32, p. 509.

Willis, J. R. (1977). "Bounds and Self-Consistent Estimates for the Overall Properties of Anisotropic Composites". In: *J. Mech. Phys. Solids* 25, pp. 185–202.

Wood, R. W. (Sept. 1902). "XLII. On a remarkable case of uneven distribution of light in a diffraction grating spectrum". In: *The London, Edinburgh, and Dublin Philosophical Magazine and Journal of Science* 4.21, pp. 396–402. ISSN: 1941-5982. DOI: 10.1080/14786440209462857. URL: https://www.tandfonline.com/doi/full/10.1080/14786440209462857.

Yan, Zidan, John P. Perdew, and Stefan Kurth (2000). "Density functional for short-range correlation: Accuracy of the random-phase approximation for isoelectronic energy changes". In: *Physical Review B - Condensed Matter and Materials Physics* 61.24, pp. 16430–16439. ISSN: 1550235X. DOI: 10.1103/PhysRevB.61.16430.

Zhao, Jing et al. (2008). "Methods for Describing the Electromagnetic Properties of Silver and Gold Nanoparticles". In: *Accounts of Chemical Research* 41.12, pp. 1710/1720.

Zhou, Shiwei and Qing Li (2008). "A microstructure diagram for known bounds in conductivity". In: *Journal of Materials Research* 23.3, pp. 798–811. ISSN: 08842914. DOI: 10.1557/jmr.2008.0101.